ELECTRODEPOSITION AND CHARACTERIZATION OF SN-BI LEAD-FREE SOLDER ALLOYS

GOH YINGXIN

THESIS SUBMITTED IN FULFILMENT OF THE REQUIREMENT
FOR THE DEGREE OF
DOCTOR OF PHILOSOPHY

FACULTY OF ENGINEERING
UNIVERSITY OF MALAYA
KUALA LUMPUR

2015

UNIVERSITI MALAYA

ORIGINAL LITERARY WORK DECLARATION

Name of Candidate: GOH YINGXIN (I.C/Passport No:

Registration/Matric No: KHA 100056

Name of Degree: DOCTOR OF PHILOSOPHY

Title of Project Paper/Research Report/Dissertation/Thesis ("this Work"):

ELECTRODEPOSITION AND CHARACTERIZATION OF SN-BI LEAD-FREE SOLDER ALLOYS

Field of Study: NANO MATERIALS

I do solemnly and sincerely declare that:

(1) I am the sole author/writer of this Work;
(2) This Work is original;
(3) Any use of any work in which copyright exists was done by way of fair dealing and for permitted purposes and any excerpt or extract from, or reference to or reproduction of any copyright work has been disclosed expressly and sufficiently and the title of the Work and its authorship have been acknowledged in this Work;
(4) I do not have any actual knowledge nor do I ought reasonably to know that the making of this work constitutes an infringement of any copyright work;
(5) I hereby assign all and every rights in the copyright to this Work to the University of Malaya ("UM"), who henceforth shall be owner of the copyright in this Work and that any reproduction or use in any form or by any means whatsoever is prohibited without the written consent of UM having been first had and obtained;
(6) I am fully aware that if in the course of making this Work I have infringed any copyright whether intentionally or otherwise, I may be subject to legal action or any other action as may be determined by UM.

Candidate's Signature Date

Subscribed and solemnly declared before,

Witness's Signature Date

Name:

Designation:

ABSTRACT

Tin-bismuth eutectic alloy (Sn-58 wt.% Bi) is emerging as a potential lead-free solder alternative. The low melting temperature (138^{o}C) of this alloy makes it a suitable candidate for higher level interconnections and for soldering heat sensitive components. Demands for high density interconnections led to the development of electroplating technique in soldering. In this work, a methane sulfonic acid (MSA) based plating bath is developed for the electrodeposition of Sn-Bi solder alloys. Composition control of the alloy is hampered by the large potential gap between the two elements. Electrolyte additives were incorporated to assist the simultaneous deposition of Sn and Bi. The effects of hydroquinone (HQ) and gelatin on the electroplating characteristics of Sn–Bi alloys were investigated. The effects of current density on the deposition behavior and composition of Sn-Bi alloy were investigated by galvanostatic studies. Microstructure and composition characterizations of as-electrodeposited and reflowed Sn-Bi alloys obtained at different current densities were performed by field emission scanning electron microscopy (FESEM) coupled with energy dispersive X-ray spectroscopy (EDS). The melting temperature of the near-eutectic Sn–Bi deposit was obtained by differential scanning calorimetry (DSC). The crystallinity of Sn–Bi deposits was also characterized with X-ray diffraction (XRD). The application of electroplated Sn-Bi solder alloys as solder joint materials were evaluated through their shear behaviour. The effects of reflow temperature on the microstructure and shear strength of Sn-Bi/Cu solder joints were studied. In the plating bath without additives and with either one of the additives, polarization studies showed that Bi deposits at about −25 to −45mV; while Sn deposits at about −410 to −420mV. The addition of HQ has a mild adsorption effect on the electrode surface. On the other hand, gelatin possesses mild complexing effect on Bi deposition. The synergistic effect of HQ and gelatin imposed a strong

adsorption and complexing effect to reduce the large potential gap between Bi and Sn to only 243mV. With both HQ and gelatin added to the bath, co-deposition of Sn-Bi was achieved. Characterization of the electrodeposits indicated that Bi content in the alloys decreases with increasing current density. Near-eutectic Sn–60.75 wt.% Bi alloy was deposited from the bath containing both HQ and gelatin at a current density of 18mA cm^{-2}. The extrapolated onset temperature from DSC analysis is around 137.4◦C, which is close to the eutectic melting temperature. The microstructure of the bulk solder and morphology of the intermetallic compound (IMC) changes with reflow temperature. The shear strength and elastic energy release, *U* of the joints increases with increasing reflow temperature. Fractographs of the failed joints shows the variation of fracture mechanisms under different reflow conditions. At low reflow temperatures, solder joints mainly failed with dimpled fracture. However at high reflow temperatures, Bi-rich phase served as a boundary to block the deformation of Sn-rich phase, causing the fracture path to deviate from the shear direction and resulted in an increase in strength and *U* value.

ABSTRAK

Aloi eutectic Tin- bismuth (Sn -58 wt. % Bi) muncul sebagai alternatif pateri tanpa-Plumbum yang berpotensi. Suhu lebur rendah (138^{o}C) aloi ini menjadikannya calon yang sesuai bagi sambungan elektronik bertahap tinggi dan untuk pematerian komponen yang sensitif kepada haba. Keperluan untuk sambungan elektronik yang berketumpatan tinggi membawa kepada pembangunan teknik penyaduran dalam pematerian. Dalam karya ini , larutan penyaduran berasaskan asid metana sulfonik (MSA) disediakan untuk pengelektroenapan Sn -Bi aloi pateri. Kawalan komposisi aloi terjejas oleh jurang potensi besar antara kedua-dua elemen. Bahan tambahan elektrolit telah dimasukkan bagi membantu pemendapan serentak Sn dan Bi . Kesan-kesan hydroquinone (HQ) dan gelatin kepada ciri-ciri penyaduran aloi Sn -Bi telah disiasat . Kesan ketumpatan arus ke atas kelakuan pemendapan dan komposisi aloi Sn -Bi telah disiasat oleh kajian galvanostatic . Mikrostruktur dan komposisi pencirian aloi Sn -Bi disadur dan reflow yang didapati pada ketumpatan arus yang berbeza telah dilakukan oleh field emission scanning electron microscopy (FESEM) berserta dengan energy dispersive X-ray spectroscopy (EDS). Suhu lebur aloi Sn -Bi hampir-eutektik itu didapati dengan differential scanning calorimetry (DSC). Penghabluran deposit Sn -Bi juga dicirikan dengan X-ray diffraction (XRD). Penggunaan aloi Sn -Bi sebagai bahan pateri telah dinilai melalui sifat-sifat ricih mereka. Kesan suhu reflow pada mikrostruktur dan kekuatan ricih sambungan pateri Sn-Bi/Cu dikaji. Dalam larutan penyaduran tanpa tambahan dan dengan salah satu daripada bahan tambahan , kajian polarisasi menunjukkan bahawa penyaduran Bi berlaku pada kira-kira -25 hingga -45mV ; manakala penyaduran Sn pada kira-kira -410 hingga -420mV . Penambahan HQ mempunyai kesan penjerapan sederhana di permukaan elektrod. Sebaliknya, gelatin mempunyai kesan pengkompleks sederhana pada penyaduran Bi. Kesan sinergi HQ dan

gelatin yang mempunyai kesan penjerapan dan pengkompleksan yang kuat untuk mengurangkan jurang potensi besar antara Bi dan Sn kepada hanya 243mV. Dengan kedua-dua HQ dan gelatin ditambah ke larutan, penyaduran bersama Sn-Bi telah dicapai. Pencirian saduran menunjukkan bahawa kandungan Bi dalam aloi berkurangan dengan peningkatan ketumpatan arus . Aloi hampir-eutektik Sn-60.75 wt.% Bi didepositkan dari larutan yang mengandungi kedua-dua HQ dan gelatin pada ketumpatan arus 18mAcm^{-2}. Offset takat lebur daripada analisis DSC adalah sekitar 137.4^{o}C, yang terletak berhampiran dengan suhu lebur eutektik . Mikrostruktur pateri dan morfologi kompaun antara logam (IMC) berubah dengan suhu reflow. Kekuatan ricih dan pelepasan tenaga kenyal, *U* sambungan pateri meningkat dengan peningkatan suhu reflow. Fractographs sambungan yang patah menunjukkan variasi mekanisme patah di bawah keadaan reflow berbeza. Pada suhu reflow rendah, sambungan pateri gagal terutamanya dengan patah lekuk. Walau bagaimanapun pada suhu reflow tinggi, fasa kaya-Bi berkhidmat sebagai sempadan untuk menghalang ubah bentuk fasa kaya-Sn, menyebabkan corak patah menyimpang dari arah ricih dan menyebabkan peningkatan dalam kekuatan dan nilai *U*.

ACKNOWLEDGEMENTS

First and foremost, I would like to express my utmost gratitude to my supervisor, Prof. Dr. A.S.M.A. Haseeb for his guidance and support throughout my graduate studies. It has been a great pleasure working under his research group. Special thanks to Dr. Mohd Faizul Mohd Sabri, my co-supervisor, who also provided lots of useful insights on this study.

Many thanks to my fellow research group members for helping in miscellaneous research works. They were constantly offering assistance and valuable input into my research. I wish to thank science officers and lab technicians who helped to perform tests and analyses, particularly Mr. Mohd Nazarul Zaman for FESEM and EDX analysis, and Mr. Adhli Iskandar Putera for lap shear tests (Instron 5848 MicroTester).

I would also like to thank the Malaysian Ministry of Higher Education and University of Malaya for providing the funding for this project. Finally, I wish to thank my family members and friends for their unconditional support and encouragement to complete my Ph.D studies.

TABLE OF CONTENTS

LIST OF FIGURES

CHAPTER 3

CHAPTER 5

LIST OF TABLES

LIST OF SYMBOLS AND ABBREVIATIONS

Symbol/Abbreviation	Description
%	Percentage
A	Ampere
Å	Angstrom
Ag	Silver
Al	Aluminium
Au	Gold
BGA	Ball Grid Array
Bi	Bismuth
C	Coulomb/ Carbon
CFC	Complex formation constant
cm	Centimeter
CN^-	Cyanide ion
Cr	Chromium
Cu	Copper
DC	Direct current
E	Electrode potential
e^-	Electron
E_c	Electrochemical equivalent of electrodeposits
EDTA	Ethylenediamine-tetraacetic acid
EU	European Union
FC	Flip-Chip

g	Gram
g/L	Gram per liter
Gel	Gelatin
h	Hour
H^+	Hydrogen ion
H_2	Hydrogen
H_2O	Water
H_2SO_4	Sulfuric acid
HQ	Hydroquinone
HT	Heliotropin
I	Current
i	Current density
i_L	Limiting current density
IMC	Intermetallic Compounds
In	Indium
iNEMI	International Electronics Manufacturing Initiative
IrO_2-Ta_2O_5	Iridium-tantalum oxide
K	Potassium
kg	Kilogram
M	Metal/ Molar concentration
M_a	Active metal
mg	Milligram
mins	Minutes

ml	Milliliter
mm	Millimeter
M_n	Noble metal
MSA	Methane Sulfonic Acid
m_{th}	Theoretical weight of electrodeposits
mV	Millivolt
MW	Molecular weight
N_2	Nitrogen
N_2H_4	Molecular formula of Hydrazine
^{o}	Degree
O_2	Oxygen
^{o}C	Degree Celcius
OH^-	Hydroxide ion
OPPE	Iso-octyl phenoxy polyethoxy ethanol
Pb	Lead
Pb-free	Lead-free
PEG	Polyethylene glycol
PI	Pyrophosphate-Iodide
POELE	Poly Oxyethylene Lauryl Ether
PPG	Polypropylene glycol
Pt	Platinum
Q	Quantity of electricity
RoHS	Restriction of Hazardous Substances

rpm	Rotations per minute
s	Second (Unit Time)
Sb	Antimony
Sn	Tin
t	Time/ Solder thickness
TEA	Triethanolamine
Ti	Titanium
UBM	Under Bump Metallization
US$	United States Dollar
V	Volt
WEEE	Waste from Electrical and Electronic Equipment
wt.%	Weight Percentage
z	Ion charge
Zn	Zinc
ΔE	Overpotential
ε	Current efficiency
η_a	Activation polarization
η_c	Concentration polarization
η_o	Ohmic polarization
μm	Micrometer
FESEM	Field-emission scanning electron microscope
EDX	Energy dispersive X-ray spectroscope
DSC	Differential scanning calorimetry

XRD	X-Ray Diffraction
b	Overlap length of lap shear specimens
d	Substrate length of lap shear specimens
a	Substrate thickness of lap shear specimens
τ_{max}	Maximum shear stress
U	Elastic energy release
MPa	Megapascal
kJ m^{-3}	Kilojoule per meter cube (Unit for energy)
mA cm^{-2}	Milliampere per centimeter square (Unit of current density)
$C_6H_4(OH)_2$	Molecular formula of Hydroquinone

CHAPTER 1

INTRODUCTION

1.1 Introduction

In this work, the electrodeposition of Sn-Bi lead-free (Pb-free) alloys is studied. The increasing demand for lightweight and multifunctional devices requires encapsulation of maximum interconnections in minimum space. The electrodeposition technique is versatile enough to produce fine geometry interconnections of a large range of shapes and thicknesses. During the last few decades, electrodeposition of solder alloys has been studied extensively. Issues on solder alloy electrodeposition such as composition control, plating bath stability, and additive usages are addressed significantly in the reports (Joseph et al., 2006; H. S. Kim et al., 2014; J. H. Kim, Suh, & Kwon, 1996; Martyak & Seefeldt, 2004; M.-S. Suh, Park, & Kwon, 2006; Tsai & Hu, 2009a, 2009b; Tsai, Hu, & Lin, 2007; Xiao et al., 2003; J. Zhang, An, Chang, & Liu, 2008). For most of the Pb-free solder alloys such as Sn-Ag, Sn-Bi, Sn-Cu and Sn-Zn, the deposition behaviour is regular alloy deposition system where the more noble (more electropositive) element is preferentially reduced from the plating solution as expected from thermodynamics. The chemistry of the plating solutions has to be modified to irregular alloy co-deposition system with the aid of electrolyte additives for simultaneous alloy deposition to take place. Thus, the electrodeposition of Pb-free solder alloys is interesting because of the nature of the alloy deposition system requires right selection of electrolyte additives to modify the solution chemistry to attain alloy co-deposition.

The Pb-free concept came into the picture in the early 1990s when toxicity of Pb brings health and environmental concerns. To stamp out Pb from electronic devices, the widely utilized Sn-Pb solders have to be substituted by other alloy systems. The eutectic

Sn-58Bi alloy is suggested as one of the promising lead-free substitution candidates by the International Electronics Manufacturing Initiative (iNEMI) (Bradley, Handwerker, Bath, Parker, & Gedney, 2007). The Sn-58Bi alloy melts at 138^{o}C, which makes it a promising candidate for soldering components prone to thermal damage. In terms of the properties to be considered for solder materials such as joint strength, wettability and mechanical strength, Sn-58Bi alloy is comparable or even better than the traditional Pb-bearing solder alloys (Artaki et al., 1999; Bradley et al., 2007; Hua, Mei, & Glazer, 1998; Yen, Liou, Chen, Lin, & Huang, 2011). Attempts were made to electrodeposit Sn-Bi solder alloys in acidic baths due to the compatibility of acidic bath with photoresists (M. Fukuda, Imayoshi, & Matsumoto, 2001; Y.-G. Lee, Park, Lee, & Jung, 2011; M.-S. Suh et al., 2006; Tsai & Hu, 2009a, 2009b, 2011; Tsai et al., 2007; Tsai, Lien, & Hu, 2011). However, there are a few challenges faced during the development of a suitable plating bath for electrodeposition of Sn-Bi solder alloys. Belonging to the regular alloy deposition system group, the large difference in standard deposition potential of about 454 mV is the main hindrance for co-deposition of Sn-Bi alloys. Also, stannous ions tend to oxidize to stannic ions rapidly in acidic medium. The incorporation of electrolyte additives into the plating bath can significantly alleviate the two issues mentioned, but the selection of the right additive(s) is another challenging task.

Upon the development of a suitable plating bath, the properties of the electrodeposited alloy have to be characterized. One of the main concerns is the mechanical reliability of the soldered joints, as the joints are subjected to loadings throughout the service period. During soldering, intermetallic compounds (IMC) form which attributes to the bonding of solder joints. The morphology of IMC can vary with different soldering conditions, hence affecting the mechanical properties of the solder joints. When an electronic device is in service, it may be subjected to vibrational and

impact loads. Such loadings may deform the solder joints in the shear direction, which indicates that the shear strength of the solder joints is one of the most important mechanical properties to be considered. The lap shear test used in this work is a common technique to examine the shear deformation behaviour of a soldered joint. The shear behaviour reported in past literatures generally varies even for identical solder composition and substrate. This is due to the fact that the sample preparation and testing procedures are subjected to too many parameters for instance soldering conditions, substrate type, solder geometry, and testing conditions. The joint geometry effect is attempted to be minimized in this work by designing of the sample with reference to a few literature reports and standards (D1002-10, 2010; Shen, Chawla, Ege, & Deng, 2005; Siewert & Handwerker, 2002). Moreover, the interrelationships between IMC formation, shear strength and fracture mode for electrodeposited Sn-Bi/Cu joints are yet to be discussed. This work aims to investigate the effects of reflow temperature on the shear deformation behaviour of the joints, and the above mentioned interrelationships.

1.2 Objectives

The main objectives of the current work are as follows:

- To develop a plating bath for the co-deposition of Sn-Bi
- To investigate effects of additives on the behavior of plating solutions
- To optimize the plating parameters for electrodeposition of Sn-Bi
- To characterize the morphology and microstructure of electrodeposited alloys
- To investigate the shear behaviour of electrodeposited Sn-Bi/Cu solder joints

1.3 Scope and outline of work

The thesis contains six chapters. After a brief introduction in Chapter 1, Chapter 2 provides a comprehensive literature review on solder materials, solder deposition

techniques, principles of metal and alloy electrodeposition, electrolyte additives, and solder joint formations. Chapter 3 to Chapter 5 presents the main findings of this work. Chapter 3 presents the electrochemical studies on plating baths for Sn-Bi alloy deposition. The effects of hydroquinone (HQ) and gelatin on electrodeposition behaviour of Sn-Bi alloys are studied. Since Bi is the more noble element in the Sn-Bi system, the deposition potential of Bi has to be polarized to more active (more electronegative) potentials for co-deposition to take place. The effects of plating parameters such as agitation of solution and additive concentration on the polarization behaviour of solutions are investigated. A composition estimation method is suggested based on potentiodynamic and galvanostatic studies of the Sn-Bi plating solution containing both HQ and gelatin. The stability of plating bath after a storage period of 7-day is also evaluated.

Chapter 4 details out the electrodeposition of Sn-Bi alloys based on the developed plating bath. The alloy composition, morphology and microstructure of the electrodeposits are investigated. The applied current density is optimized to obtain the eutectic Sn-58Bi composition. Chapter 5 presents the shear deformation behaviour of electrodeposited Sn-Bi/Cu solder joints. As mentioned, solder interconnections are subjected to shear loads during service. Lap shear tests of solder joints can simulate such loadings. The IMC at the interface can exist in different morphology, which is related to the fracture mode of solder joints. The interrelationship between IMC morphology, shear strength and fracture mode is investigated. Finally, Chapter 6 summarizes the result of this thesis work and recommends future work that can be carried out to bring the research on electrodeposition of Sn-Bi solder alloys to the fore.

CHAPTER 2

LITERATURE REVIEW

2.1 Solder materials

Solders are well known as fusible metals or alloys with a melting point below 425ºC used for metallurgical joining of electronic materials and components (Abtew & Selvaduray, 2000). With the introduction of silicon chip and printed circuit boards, the importance of solder materials to function as both the electrical and mechanical attachment has lead to considerable research in this area. Solder materials used in the electronic packaging field are usually tin (Sn)-based alloys. Common alloying elements include lead (Pb), silver (Ag), copper (Cu), bismuth (Bi), zinc (Zn) and indium (In). Further details on Pb-Sn solders and other Pb-free solders used in electronic packaging will be discussed later.

There are several physical forms of solder materials such as bar, ingot, sheet, powder, balls and paste (C. Han, 2009). Among them, solder paste is the most common form used in the electronic packaging industry. Solder paste consists of solder powder suspended in flux and optional additives. The tacky nature of solder paste enables it to function as temporary glue during component placement and soldering steps. The solder paste technology is well developed for the automated production of consistent and reliable solder joints.

When the ball grid array (BGA) and flip-chip (FC) technology emerged in the electronic packaging field, solder balls/bumps gained considerable interest. Figure 2.1 shows a schematic diagram of typical configurations of a flip-chip package. The basic alloy for solder bumps at the die level contains high temperature or high Pb content

solders where Sn-37Pb has been the common composition. On the other hand, on the underside of the carrier substrate (which may involve board level soldering), a near eutectic and low temperature solder is preferred in order to take into account the temperature tolerance level of board materials. Usually, Bi or In containing solders are used in such applications.

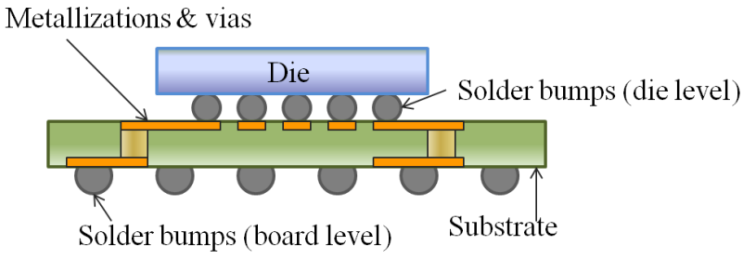

Figure 2.1 Schematic cross-sectional view of a flip-chip package.

2.1.1 Sn-Pb solder

Sn-Pb alloys have been used as interconnection materials for more than five decades (Suganuma, 2001). This is because of the technical advantages provided by Sn-37Pb alloy such as low cost, low eutectic melting point of 183^{o}C, good solderability and availability to operate in a wide range of service conditions (Suganuma, 2001). Lead (Pb), being a readily available element, is also capable of reducing surface tension of pure tin (Sn). Pb also serves as a solvent metal to enable rapid diffusion of other joint constituents (e.g.: Sn and Cu) to form reliable intermetallic bonds. With such a long history, the knowledge base about the metallurgical and mechanical behaviour of this alloy is very well established and refined to an extent that it used to dominate the worldwide soldering industry.

In the late 1970s, concerns were first raised about the potential of Pb poisoning from solder joints used in plumbing of potable water conduit (Vianco, 2000). An accumulation of Pb in the human body may cause damage to the blood and central

nervous system. The move to eliminate Pb from electronics solders initiated in the early 1990s. The basis for the proposal to ban Pb-bearing solders in the electronics industry is the ever increasing amount of discarded electronic products in landfills. The Pb content in the devices may leach into municipal water supplies, posing threat to human health and environment.

Attempts to introduce legislations to limit the use of Pb were first made in the United States. The proposal included the Lead Exposure Reduction Act of 1991 and Lead Exposure Act of 1992 (Abtew & Selvaduray, 2000). The proposal of these acts prohibits the sale or distribution in commerce of packaging or products if they include any additive to which lead has been intentionally introduced. Although the bills were not passed, such proposal generated a great momentum worldwide in developing Pb-free solders. In Europe, the primary legislative action is the Waste from Electrical and Electronic Equipment (WEEE) and Restriction of Hazardous Substances (RoHS) directive. This directive has been in force since August 2004. More than four years later only about a third of electrical and electronic waste is reported to be treated in line with these laws and the other two thirds is going to landfill and potentially to sub-standard treatment sites in or outside the European Union. On June 7, 2012, this directive is revised with new waste collection targets agreed. The existing binding EU collection target is 4 kg of WEEE per capita, representing about 2 million tons per year, out of around 10 million tonnes of WEEE generated per year in the EU. By 2020, it is estimated that the volume of WEEE will increase to 12 million tons. In Japan, the use of Pb is not banned yet. However, it is controlled strictly in such ways that Pb or Pb containing products are prohibited from being sent to landfills and waste disposal sites. Manufacturers will have to either attain 100% recycling of Pb, or opt for Pb-free alternatives.

2.1.2 Selection criteria of Pb-free solders

Institutions, laboratories and manufacturers are conducting continuous and aggressive research on Pb-free solder alternatives. There are several criteria for the selection of suitable Pb-free alloys. The first step in finding a suitable substituting alloy system is to look for nontoxic and low-melting element(s) to substitute lead. Ternary alloys (or less) are preferred because when more elements are involved control difficulties may occur (Bradley et al., 2007). The present and future availability of these elements is one of the main criteria in the selection of a Pb-free solution. Arguments over the long-term availability of Bi arose when it is claimed to be the by-product of Pb-mining (Miric & Grusd, 1998; Suraski & Seelig, 2001). However it appears there are still bulk deposits of Bi which are not currently mined due to its low market price. Scarcity of In limits the wide use of this element in the soldering field (Suraski & Seelig, 2001; Zeng & Tu, 2002). As with Bi, Sb is also identified as the by-product of Pb-mining. Sb also adversely affect wettability of solders when used in large amount (Miric & Grusd, 1998).

Cost is another important factor to be taken into account. Generally lead-free systems cost about 2-2.5 times higher than the Sn-Pb system (Abtew & Selvaduray, 2000; Suganuma, 2001). Although the cost increase lowered the pace of Pb-free solder development, possible legislation of Pb-ban causes an inevitable driving force to exist. Besides, the amount of solders on a circuit board of a consumer electrical product is small and hence the apparent price of the product will not be affected much. However, in the point of value engineering, content of costly elements such as Ag and Au should be minimized to an extent where the manufacturing cost impact will be negligible.

Current assembly manufacturing lines are optimized for the fabrication of Sn-Pb systems. The selection of Pb-free solder alloys should take into account their

compatibility with the equipments and processing conditions including flux systems and operating temperatures. The melting temperature of eutectic Sn-Pb is 183^{o}C and typical reflowing temperature is 230^{o}C. Inauspiciously, melting temperatures of typical Pb-free systems are about 30-50^{o}C higher than eutectic Sn-Pb which causes processing limitations. Reliability of the fabricated Pb-free solders is also expected to be no poorer than the Sn-Pb system which is a very challenging task in this research field. Properties such as wettability, mechanical strength, thermal fatigue resistance and creep resistance of the solder joints are often taken into consideration. Considering the criteria mentioned above, researchers and institutions came up with a list of Pb-free alloys with great potential as substitution for Pb-bearing solders. A brief description of the Pb-free alloys is provided in the next section.

2.1.3 Pb-free solder alloys

A large number of Pb-free solder alloys have been proposed but none came in as a drop-in replacement for Sn-Pb solders. Abtew and Selvaduray (2000) identified 69 alloys from the literature, where Sn being the major constituent, while Bi and In are the major alloying elements. The International Electronics Manufacturing Initiative (iNEMI) also came up with a Lead-Free Assembly Project in 2007 to further assist the implementation of Pb-free soldering into electronics manufacturing by providing reliable and sufficient data. A few alloys of interest will be discussed here.

Sn-9Zn is one of the alloys of interest due to its eutectic melting temperature (198^{o}C) that is close to that of eutectic Sn-Pb. Zn is reported to have the ability to suppress tin whisker growth (Abtew & Selvaduray, 2000). The eutectic microstructure of this alloy is also very similar to Sn-Pb, consisting of Sn-rich and Zn-rich lamellar structures. However, Zn-containing alloys oxidize easily, show severe drossing during

wave soldering, and are prone to corrosion with maximum paste shelf life measured in weeks only (Bradley et al., 2007; Miric & Grusd, 1998). Given these drawbacks, the suitability of this alloy as a potential replacement for Sn-Pb solders is doubtful.

The eutectic Sn-3.5Ag alloy has a relatively higher melting temperature of 221^{o}C. The microstructure of this alloy is different from the eutectic Sn-Pb alloy as it consist eutectic dispersion of Ag_3Sn intermetallics embedded within the Sn matrix. The much higher Sn content (96.5Sn compared to 63Sn) tends to accelerate the growth of Cu_6Sn_5 intermetallic compound (IMC) on Cu base metal (Miric & Grusd, 1998). The good mechanical properties of this alloy make it a potential Pb-free candidate. However, since cost considerations should also be taken into account, the use of Ag-containing alloys should be minimal to reduce the overall processing costs.

Similarly, the Sn-0.7Cu eutectic alloy is a Sn-rich alloy with eutectic temperature of 227^{o}C. The microstructure is also similar as the Sn-3.5Ag alloy where Cu_6Sn_5 intermetallics are embedded within the Sn matrix. The main concern of this alloy is also the excessive IMC growth when in contact with Cu metallization. Also, both Sn-3.5Ag and Sn-0.7Cu alloys have very high Sn content and may be prone to Sn whisker growth. However, the service environments which will induce whisker growth are still not clear.

As of now, the Sn-Ag-Cu ternary alloys are the most promising candidates as lead-free replacement. The true eutectic composition determined experimentally is Sn-3.58±0.05Ag-0.96±0.04Cu at 217.2±0.2°C (Moon & Boettinger, 2004). However, there are a few compositions commonly used in the industries such as Sn-3.8Ag-0.7Cu, Sn-3.5Ag-0.7Cu, and Sn-4Ag-0.5Cu, with melting ranges near 217-227°C (Bradley et al.,

2007; Miric & Grusd, 1998; Suganuma, 2001). It is reported that there is no significant difference in the wetting characteristics and mechanical reliability among these different compositions. These alloys are suitable to be used at high operating temperatures of up to 175^{o}C (Miric & Grusd, 1998). But for devices prone to thermal damage and for multi-level packaging, alternative alloys with lower melting temperature are still required.

The Sn-58Bi eutectic alloy, which is the alloy investigated in this work, has a low eutectic melting point of 138^{o}C. This alloy was not of interest when the Pb-free concept first came into the picture. This is because during the transition to Pb-free solders, there would still be Pb contaminants remaining in the existing production line. In the presence of Pb contamination, the Sn-Bi solder reacts with Pb and form ternary eutectic of composition Sn-51.5Bi-33Pb (Moon, Boettinger, Kattner, Handwerker, & Lee, 2001) with a very low melting temperature of 96^{o}C. Hence, above this temperature, the solder melts and which leads to premature failure of the solder joints.

However, decades after the transition period, the Sn-58Bi solder alloy is gaining considerable attention. According to the Sn-Bi phase diagram (B. J. Lee, Oh, & Shim, 1996), Sn has very low solubility (0.11 wt.%) in Bi at the eutectic solidification temperature, hence the Bi phase is essentially pure Bi. On the other hand, Bi has a maximum solubility of 21 wt.% in Sn. The microstructure of this alloy is very similar to that of Sn-37Pb, which is a two phase lamellar structure. The comparisons between Sn-58Bi and Sn-37Pb alloys are summarized below:

1) **Cost:** The raw metal cost per kg (excluding fabrication costs) as of December 2012 (Source: London Metal Exchange (LME) website))

Lead (Pb) : US$ 1.791/kg

Tin (Sn) : US$ 17.981/kg

Bismuth (Bi) : US$ 13.311/kg

By calculating the ratio needed to produce the eutectic alloy, the raw metal cost is about US$ 11.99/kg for Sn-37Pb alloy; and about US$ 15.27/kg for Sn-58Bi alloy. This price difference is considered to be acceptable because Sn-58Bi requires a lower manufacturing temperature which reduces the fabrication cost. Also, the price stated above is per kg of raw metal which the cost effect is rather minimal for mass production.

2) **Wetting:** The wetting angle of Sn-58Bi solders on Cu substrate evaluated experimentally in the past literatures falls in the range of 30- 37^{o} (Mei & Morris, 1992; Vianco, 2000). Compared to wetting angle of Sn-37Pb solders (14 - 27 ^{o}), the wettability of Sn-58Bi is slightly inferior but it is still considered within the acceptable range. However, Hua et al. (1998) reported that the wetting behaviour is highly dependent on the solder, substrate, and flux system. The flux system used to compare wetting angles in other literature may be developed specially for Sn-37Pb and needs to be activated at a higher temperature. In their work, new fluxes specially designed for Sn-58Bi alloys were used and wetting angle of this solder was improved to 15^{o}.

3) **General mechanical properties:** Hua et al. (1998) reported that the shear strength, measured at room temperature and at a strain rate of 4 x 10^{-3}/s, of Sn-58Bi alloy is 33.3 MPa, which is higher than that of Sn-37Pb (14.6MPa). However when temperature is increased to 110^{o}C, the shear strength of Sn-58Bi decreases to 12.3MPa while the strength of Sn-37Pb remains the same. In other works, it is reported that the Sn-58Bi can outperform Sn-Pb solders in thermal cycling tests at 0/100^{o}C and -55/+125^{o}C for Organic Solderability Preservative (OSP) boards (Artaki et al., 1999; Bradley et al.,

2007). Even at a test temperature of 125^{o}C which is near to the Sn-58Bi melting point (138^{o}C), Sn-58Bi can still perform beyond expectation. Most of the reports available on the aging of Sn-58Bi alloy came to the conclusion that the strength of Sn-58Bi/Cu joints increase dramatically with aging time (Felton, Raeder, & Knorr, 1993; Hua et al., 1998; Raeder, Felton, Tanzi, & Knorr, 1994). This is believed to be related to the bismuth stratification effect upon aging. However till now, no clear explanations on this phenomenon are available.

2.2 Solder deposition technologies

There are a variety of solder deposition techniques available today. Physical deposition methods such as evaporation, or solid phase deposition methods such as robotic ball placement and stencil printing have been applied in the soldering field (Kloeser et al., 2000; Morris & Wojcik, 1991; Rinne, 1997). Another method with long history in the electronic packaging field is the electrodeposition method (Rinne, 1997; Ruythooren et al., 2000). These technologies will be discussed further in the following sub-sections.

2.2.1 Evaporation

Evaporation is one of the oldest techniques used to produce metals or alloys thin films. This deposition technique consists of simple processing steps, starting with the heating up of metal source to high temperature. The vapour generated is transported to the target substrate, usually in vacuum to avoid interference of gas molecules, and impinges on the substrate surface. Then, the evaporant condenses to a solid film on the substrate, followed by the nucleation and growth process.

The source material must be heated to a sufficiently high temperature to produce the desired vapour pressure for deposition to happen. The heat source may be resistive heating elements, electron beam, laser beam, or arc discharge. Thermal evaporation

using direct resistance heating is the cheapest and easiest option. However, this technique is limited to metals or low melting point materials with maximum heating temperature of about 1800^{o}C. Also, the container of source material may evaporate together which contaminates the deposited film. Electron beam evaporation is a much better option, despite the higher cost, because a wide spectrum of materials including dielectrics can be melted due to the higher maximum heating temperature (3000^{o}C). Impurity level of electron beam evaporated film is also much lower because the beam is targeted directly to the surface of evaporant.

In the electronic packaging industry, the evaporation technique is mainly used for deposition of under bump metallization (UBM) layers and solder bumps through a patterned mask. A relatively thick metal mask is clamped mechanically to the wafer at a fixed spacing. Common evaporated materials include Cr, Cr-Cu, Cr-Ge, Au, Sn-Pb, Sn-Cu and Sn-Au (C. Han, 2009). However, this technique is not widely applied due to the following disadvantages (Datta, Osaka, & Schultze, 2005; Qin, Wilcox, & Liu, 2010):

- Low efficiency. This technique only offers 5% of efficiency, where 95% of evaporated materials may end up condensing on the chamber walls and metal masks.
- High cost. The evaporating equipment requires a vacuum system which is expensive and the metal mask has very low lifespan.
- Low precision. For fine pitch patterns, precision in alignment is difficult to achieve due to the high metal mask thickness.

2.2.2 Solid phase deposition

The solid phase deposition of solders involves positioning of solid solder over the bond pad and followed by the reflow process to form solder bumps. The robotic solder ball

placement technique is one of the solid phase deposition techniques developed in the late 1990s. Pre-formed solder balls are singulated, placed on bond pads or UBM layers, and reflowed instantly upon placement by a short laser pulse. A schematic diagram of the process is shown in Figure 2.2. The laser current can be optimized easily to achieve good wetting yet not causing damage to the bond pad. With an average deposition speed of 7 balls per second and fast turnover cycle, this technique has gained considerable attention in the industry for flip-chip and all sorts of fluxless applications (Motulla et al., 1997). This technique can also be used for the repair of defective solder bumps due to its high flexibility (Motulla et al., 1997).

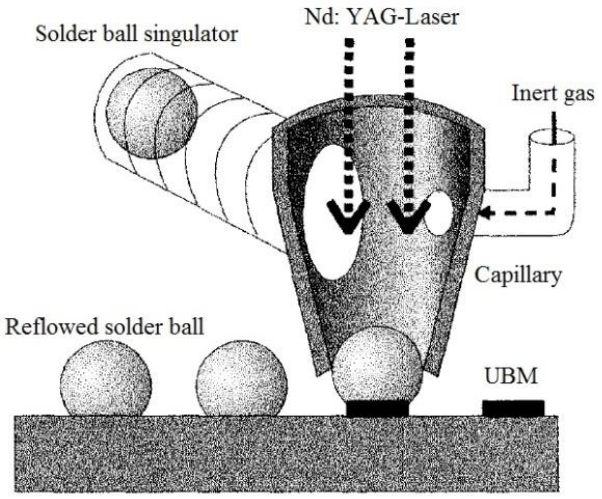

Figure 2.2 Schematic illustration of robotic ball placement process (Rinne, 1997).

Another economical and well-established solid phase deposition technique would be stencil printing. This technology has been practised in massive scale in the soldering industry, and is illustrated in Figure 2.3. A travelling squeegee applies pressure along the stencil mask and printing solder paste onto the bond pads or UBM layers. Motulla et al. (1997) prepared a cost comparison model between the robotic ball placement and stencil printing technique, which includes capitals and setup costs . The model shows that stencil printing process cost 5 times more than robotic ball placement

for low wafer yield calculations, and the breakeven point between these two techniques will be at about 35,000 wafers per year. Hence stencil printing is the economical method for extremely high production volume. However, this process is affected by many factors (Kloeser et al., 2000; Morris & Wojcik, 1991; Xiao et al., 2003):

- Printing parameters: printing speed, separation speed, alignment, downward pressure,
- Stencils: stencil materials, aperture size and quality, smoothness of aperture walls, and
- Solder paste: powder size, particle distribution, rheology.

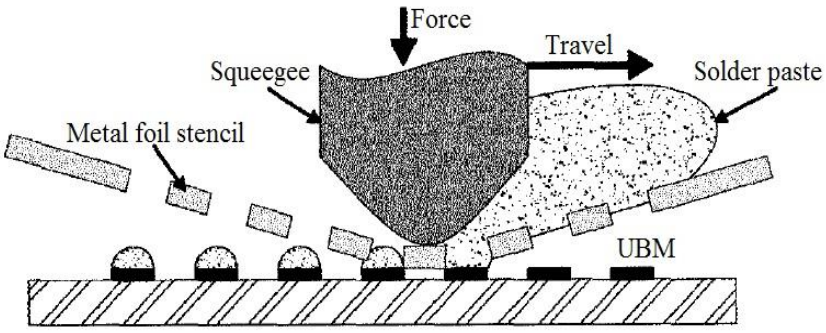

Figure 2.3 Schematic illustration of stencil printing technique (Rinne, 1997).

The stencil printing process offers a high speed, high yield and low cost method for solder deposition. However, it is rather difficult for this technique to yield precise and uniform solder geometry, especially for pitch sizes finer than 150 μm. The stencil thickness has to be lower than the aperture size in order for the solder paste to remain on the bond pad and not to wet a large area of the stencil. The printing equipments and stencil design has to undergo major changes in order to meet the fine pitch which is uneconomical and impractical. Hence for pitch sizes lower than 150 μm, an alternative solder deposition technique has to be used.

2.2.3 Electrodeposition

In year 1805, Luigi Brugnatelli from Italy invented the electrodeposition technique and electroplated gold using the Voltaic Pile discovered by Allessandro Volta in 1800. Since then, the technique is mainly used for the deposition of gold and silver in cyanide bath for decorative coatings purpose throughout the next half of the century. As scientists gained more knowledge on the science of electrochemistry, the application of this technique moved on to non-decorative and protective coatings for manufacturing and engineering purposes. However, no significant development was seen until the emergence of the electronics industry in 1940s. This has marked a milestone in the technical improvements of the whole plating process such as development of safer cyanide-free baths, improvements in hardware and chemical formulas etc. The developments of electrodeposition in electronics are summarized as follows:

1936→ printed circuit board

1960s→ surface mount technology, soldering

1980s→ through hole technology, Cu interconnects

1990→ first electrodeposited Damascene Cu wafer

As discussed earlier, both evaporation and solid deposition techniques (robotic ball placement and stencil printing) have limitations in terms of cost and feasibility for fine pitch bumping, respectively. The electrodeposition technique offers significant advantages over the three techniques discussed earlier. Electrodeposition does not require complex equipment or setup as no vacuum is required. The whole process can be performed at room temperature or near room temperature thus reducing cost and problems with thermal stress (Ruythooren et al., 2000). For microelectronics related applications, especially when fine geometry and high aspect ratio structures are

involved, electrodeposition could be the reliable option (C. Han, 2009; Ruythooren et al., 2000). Most electroplating systems are able to operate at about 90% efficiency which fulfils the economical aspect (Ruythooren et al., 2000). In short, this technique could yield high throughput, good precision and uniformity, and theoretically no pitch limitations.

For electrodeposition of single metals, plating baths and the overall process can be rather easy. The deposition rate can be determined from Faraday's law, while the electrochemical reactions can be predicted from the Nernst's equation. However, for electrodeposition of alloys, the reactions become much more complex and difficult to predict. The complexity of the process further increases with inclusion of electrolyte additives in the form of antioxidants, chelating agents, surfactants and grain refiners. To cope with these variables, electroplating equipment for wafers have to include advanced electrolyte flow designs with proper recycling and conditioning systems to monitor the plating conditions. A schematic diagram of electrodeposition setup with essential components is shown in Figure 2.4. Detailed electrodeposition principles of metals and alloys will be discussed in ***Section 2.3***.

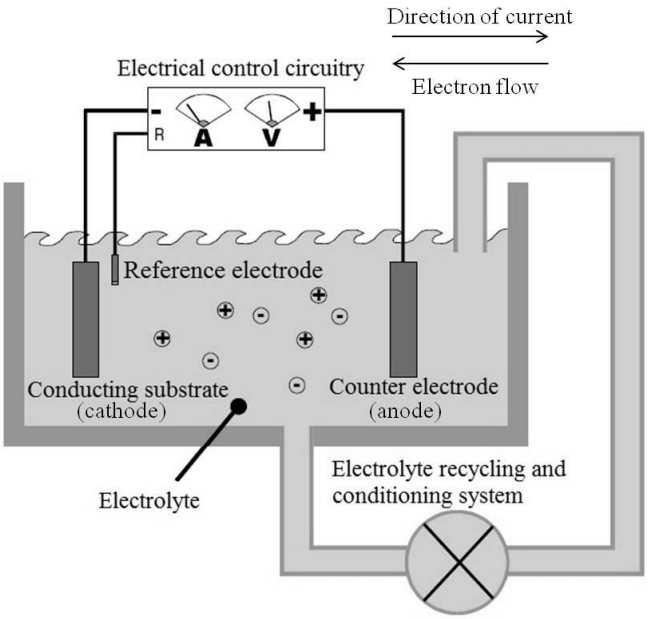

Figure 2.4 Schematic illustration of electrodeposition setup (Ruythooren et al., 2000).

Comparisons between techniques discussed above are tabulated (Table 2.1). If cost is the main concern, stencil printing or robotic ball placement are appropriate options for mass production. To meet the demands for fine pitch bumping, electrodeposition appears to be the best option available as it is compatible to photolithography patterning. However, when it comes to lead-free solder, complexity of this process can be challenging due to the large deposition potential gaps between Sn and lead-free substituting elements (Ag, Bi, Cu, Zn). The electrodeposition issues of Sn and Sn alloys will be discussed in Section 2.4.

Table 2.1 Comparisons of solder deposition processes (Yaakup, Zakaria, Hashim, & Isnin, 2008).

Techniques	Complexity	Cost	Pitch size (μm)	Precision (±μm)	Lead-free challenge
Evaporation	Medium	High	25-50	5	High
Stencil Printing	Low	Low—Medium	> 150	10	Low
Robotic Ball Placement	Low	Low—Medium	> 150	10	Low
Electrodeposition	High	Medium	25-50	0.5	Medium—High

2.3 Principles of electrodeposition of metal and metal alloys

2.3.1 Electrodeposition of metal

Electrodeposition occurs during electrolysis in a conducting solution, known as the 'electrolyte'. As illustrated in Figure 2.4 (***Section 2.2***), the anode and cathode are immersed in the electrolyte and connected to a direct current (DC) source, and a reference electrode is connected for electrolyte monitoring purposes. The current enters the electrolyte via anode (counter electrode), and leaves the electrolyte via the cathode (conducting substrate). During electrolysis, ions existing in the solution carry the current. The current capacity is dependent on ion concentration and mobility in the

solution (Tan, 1993). The ions responsible for current transport in the electrolyte may or may not take part in the electrode reactions (Raub & Müller, 1967). For example, cations transporting to the cathode may not be discharged, or may participate slightly in the discharging process. Neutral molecules which do not migrate under the influence of current may be decisive for the discharge process. Furthermore, anions migrating to the anode may also play a vital role in the discharge process. The quantitative aspects of the overall reactions are governed by the Faraday's law.

2.3.1.1 Electrode reactions

During metal deposition, cations build up at the cathode surface upon the application of current. The cathodic reaction for metal deposition follows the general equation:

$$M^{z+} + ze^- \rightarrow M \qquad (2\text{-}1)$$

This reaction is often accompanied by hydrogen discharge. In acidic solutions, hydrogen evolution follows the equation:

$$2H^+ + 2e^- \rightarrow H_2 \qquad (2\text{-}2)$$

While in neutral or basic solutions, hydrogen evolution follows the equation:

$$2H_2O + 2e^- \rightarrow H_2 + 2OH^- \qquad (2\text{-}3)$$

The discharge and incorporation of hydrogen into metal deposits can be a main cause of pores in electrodeposits. Although other gases adhering to the cathode can also cause such defects but cathodically discharged hydrogen is usually responsible (Raub & Müller, 1967). The discharge reaction of hydrogen also lowers the overall current efficiency (Tan, 1993).

On the other hand, if a soluble anode is used in the electrodeposition process, the oxidation reaction will take place according to the equation:

$$M \rightarrow M^{z+} + ze^- \qquad (2\text{-}4)$$

Such reactions are also termed as metal dissolution. An insoluble anode will not send ions into the electrolyte so that the metal is not dissolved. The anodic reactions on insoluble anodes are dependent on the electrolyte compositions. For alkaline plating bath, oxygen evolution takes place as follows:

$$4OH^- \rightarrow 2H_2O + O_2 + 4e^- \qquad (2\text{-}5)$$

In acidic electrolytes, the oxygen evolution reaction follows the equation:

$$2H_2O \rightarrow 4H^+ + O_2 + 4e^- \qquad (2\text{-}6)$$

2.3.1.2 Current

The electrolysis process is governed by the Faraday's law, which may be expressed as follows:

$$m_{th} = E_cQ = E_cIt \qquad (2\text{-}7)$$

where m_{th} is the theoretical weight of deposits, the quantity of electricity is given by $Q = It$, where I is current (in amperes, A) and *t* is time (in seconds, s). E_c is the electrochemical equivalent of the deposited element in g/ Ah. The equivalent weight of an element is given by its atomic weight divided by its valence in the compound present; and the electrochemical equivalent is the equivalent weight deposited per unit electricity. Calculations of electrochemical equivalents for bismuth and tin is shown as examples:

$$E_{c\,(Bi^{3+})} = \frac{208.98}{96500\ X\ 3} = 0.722\,\frac{mg}{C}\ \ or\ 2.599\ \frac{g}{A\,h}$$

$$E_{c\,(Sn^{2+})} = \frac{118.71}{96500\ X\ 2} = 0.615\ \frac{mg}{C}\ \ or\ 2.214\ \frac{g}{A\,h}$$

This concept can be applied to alloys as well by assuming the deposition rate of both metal ions is the same, and is not influenced by electrolyte additives. Let the alloy be made up of two metals, having electrochemical equivalent of E_1 and E_2, and with weight fractions of f_1 and f_2. The electrochemical equivalent of an alloy with the respective fractions is given by:

$$E_{c,a} = \frac{E_1 E_2}{f_1 E_2 + f_2 E_1} \qquad (2\text{-}8)$$

So, for example, the estimated electrochemical equivalent a solder alloy plating of 42% Sn -58% Bi will be:

$$E_{c,\ 42Sn-58Bi} = \frac{(0.615\ X\ 0.722)}{(0.42\ X\ 0.722)+(0.58\ X\ 0.615)} = 0.673\ \frac{mg}{C}$$

Upon obtaining the estimated weight of deposits using Equation 2-9, the current efficiency of the particular electrodeposition process can be defined. Current efficiency, ε is the proportion of current that is used for the electrodeposition reaction, and it is equivalent to:

$$\varepsilon\ (\%) = \frac{Actual\ deposit\ weight}{Theoretical\ deposit\ weight}\ X\ 100 \qquad (2\text{-}9)$$

The current efficiency is 100% when no other side reactions take place. Possible side reactions during metal deposition include hydrogen discharge, oxide layer reductions, and deposition of impurities.

2.3.1.3 Polarization

When two electrodes are immersed in the electrolyte, the electrochemical equilibrium of the electrodes is defined as dynamic equilibrium. The potential-determining ions move in both the positive and negative directions at an equal rate to attain equilibrium. As electrolysis process starts, the potential of anode and cathode changes. This change in electrode potential is known as polarization of the electrodes. The difference between

the electrode potential with and without current application is termed the overpotential, ΔE:

$$\Delta E = E_i - E^o \qquad (2\text{-}10)$$

where, E_i is the electrode potential with current applied, and E^o is the electrode potential without current applied. Overpotential refers to the potential-determining reaction while polarization refers to the electrode itself. The overpotential is produced by inhibiting factors of various kinds which affect the reaction at electrodes. Depending on the types and sites of inhibition, different kinds of overpotential or polarization can be distinguished (Raub & Müller, 1967).

The total polarization occurring at the electrode can be divided into different reactions, being the activation polarization, η_a, concentration polarization, η_c, and the Ohmic polarization, η_o. The activation polarization is due to the inhibition of potential-determining ions from passing through the electrolytic double layer. An initial activation potential has to be achieved to overcome kinetic barriers of the discharge reactions. Once the barrier has been overcome, a small change in potential will produce a large change in current, and the process is now diffusion-controlled.

The concentration polarization is caused by changes in local concentration of ions. It can be divided into reaction polarization and diffusion polarization. Reaction polarization is due to inhibition of reactions preceding the electrode reactions; such as hydration/dehydration and complex formation/decomposition reactions. For example, the discharge-determining step proceeds through complex decomposition, the formation rate of the charged complex from the parent ion may control the supply of complex to the cathode. Diffusion polarization is caused by the inhibition of ions or complex

diffusion towards the diffusion boundary layer. When electrodeposition or discharge of ions has initiated, there will be a given time where ions at the boundary are consumed faster than the replenishment of ions, and a diffusion layer is formed at the immediate vicinity of the cathode. The concentration of ions at the diffusion layer is lower than in the bulk electrolyte. The rate of reduction reaction will then be limited by diffusion of ions through the boundary layer, and the limiting rate is the limiting current density, i_L. The i_L is the highest possible current density for a given electrode reaction due to its dependence on the diffusion velocity of ions involved. Ohmic polarization, also known as resistance polarization, is due to the inhibition of transport of an ion through a layer contiguous to the Ohmic potential drop, for example an oxide film or an adsorbed film. The Ohmic polarization disappears in a few microseconds upon the current breaks through the resistivity limit. Since the resistivity of the films inhibits the passage of ions, some may consider the Ohmic polarization as a part of the activation polarization.

Polarization curves are of special interest for the theoretical interpretation of electrode processes in an electrolyte. When current is applied to the electrode, potential of working electrode is displaced and can be measured as a function of current density. The working electrode can be anode or cathode, depending on the polarity of current source. For electrodeposition, the cathodic potential and current density is of main interest. A typical cathodic potential-current density curve is shown in Figure 2.5. Increasing the potential with time causes the number of ions discharged to increase, hence resulting in an increase in the cathodic current. The concentration difference between the cathode surface and the bulk solution increases. Finally it may occur that all the ions near the cathode surface has been discharged, and ions arrived at the cathode by diffusion are then immediately discharged. With further increase of potential, current cannot increase further because the discharge process is governed by the diffusion rate

of ions. Thus, the cathodic limiting current density, i_L, is attained. As mentioned earlier, this is the highest possible current density for a given electrode reaction, and can only be exceeded when the potential for other reactions has been reached, e.g. that of hydrogen discharge.

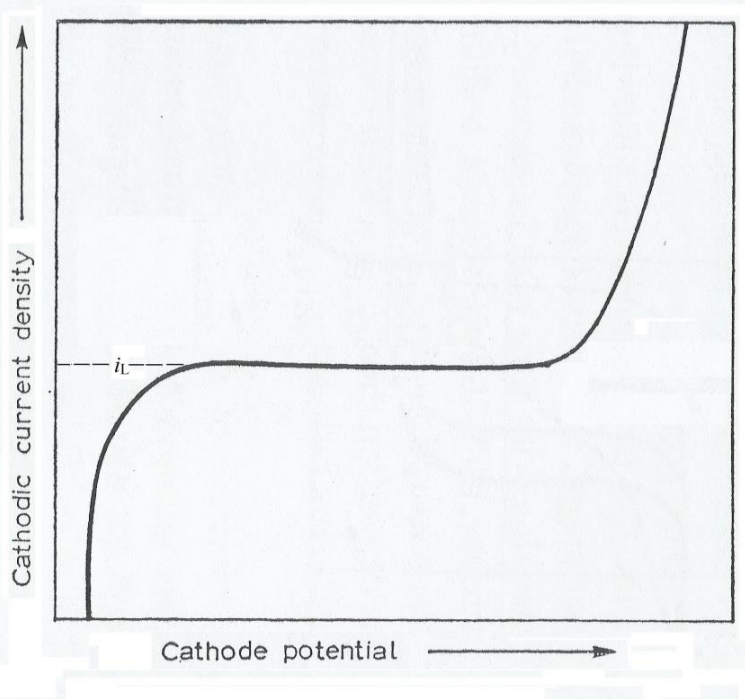

Figure 2.5 Cathode potential-current density curve with limiting current density (Raub & Müller, 1967).

For some simple solutions e.g. lead nitrate, silver nitrate, the polarization curves are nearly vertical (nearly parallel with the current density Y-axis) (Tan, 1993). This implies a small polarization effect, where the increase in cathodic potential is small for a large increase in current density. Large cathodic polarization refers to a significant increase in potential for a small increase in current density. Large polarization effect is usually caused by by-reactions in the electrolyte such as dissociation of complex ions to produce metal ions. Electrolytes with large polarization generally have better deposition rate. However polarization is not the sole factor affecting the deposition behaviour. The electrodeposition process is also influenced by the nature of additives and plating parameters.

2.3.1.4 Mechanism of electrodeposition

The electrodeposition process of metals may appear as simple as the discharge of metal ions in solution upon receiving electrons. But the actual deposition mechanism is much more complex and it is not yet possible to explain the process fully in terms of physical or chemical theory. Some simplified mechanisms will be discussed in this section although there are still numerous knowledge gaps in this area.

Metal ions (cations) in electrolytes can appear in simple form as well as complex form. In a simple salt solution, cations are present in hydrated form and have the same valency as free cations. The hydrated metal ions in aqueous solution exhibit various structural configurations, depending on the size and electronic properties of the metal ion. For example, metal ions with d^4 and d^9 valence shell electron configuration (e.g. Cr(II) and Cu(II) respectively) have Jahn-Teller distorted aqua complexes; while metal ions with $d^{10}s^2$ valence shell electron configuration (e.g. Sn(II), Pb(II), Bi(III)) may have a stereochemically active or inactive electron lone pair (Persson, 2010).

Thus the preliminary reaction in the deposition process is the removal of water molecules, which occurs at the diffusion layer (Figure 2.6). The energy required for ion dehydration depends on the nature of the ions, where high removal energy gives rise to high activation polarization. The hydrated ion transports towards the cathode under influence of electrical field, as well as by diffusion and convection. As ions migrate through the diffusion layer, the electrical field strength is not yet strong enough to dehydrate the cations. The water molecules are only aligned by the field. As the cations diffuse through the electric double layer, loosely bound water molecules are removed and become components of the double layer. The cations are then neutralised and adsorbed on the cathode as ad-atoms, which then diffuses across the surface to a growth point and incorporated into the crystal lattice of the cathode.

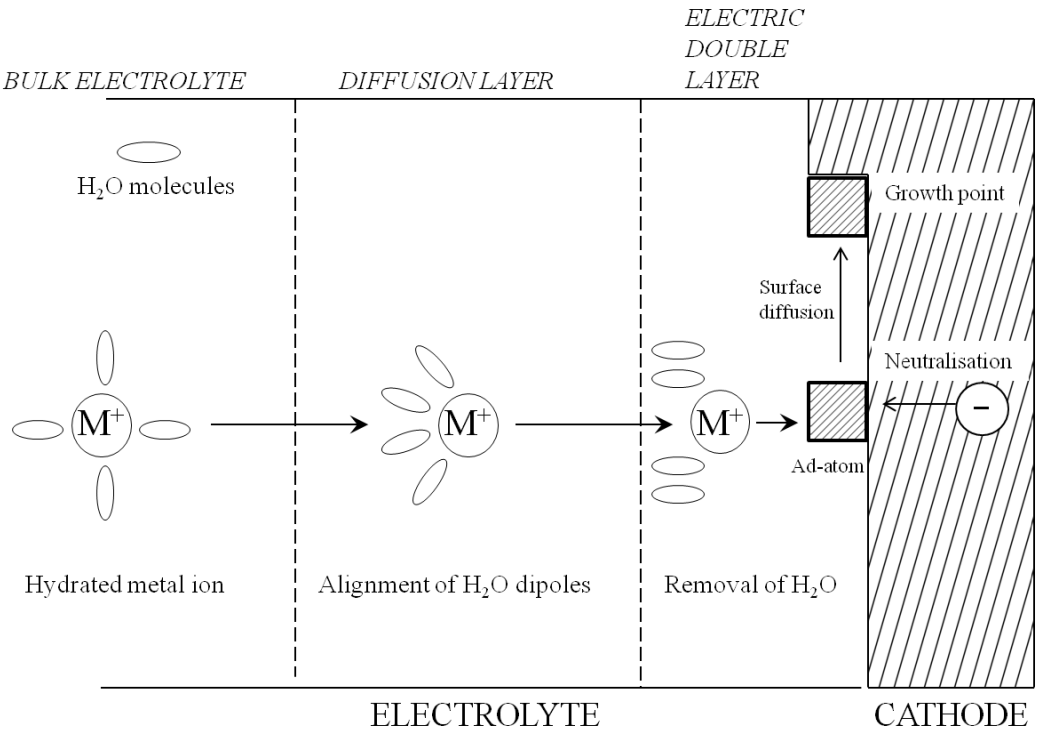

Figure 2.6 Schematic illustration of electrodeposition of metal from simple salt solution (Raub & Müller, 1967; Tan, 1993).

However, in most practical electroplating baths, the metal ions are present in complex form. The metal ions to be deposited are bounded by negatively charged complex ions, and complex metal ions have higher stability than hydrated metal ions. The exact composition of complexes in the electrolyte in many cases is unknown. A very common complex ion deposition is the silver cyanide system, and will be used as an example for discussion here. A few possible discharge mechanisms have been suggested for complex metal ions (Raub & Müller, 1967):

- Decomposition of complex into its components

$$[Ag(CN)_2]^- \rightarrow Ag^+ + 2\ CN^- \qquad (2\text{-}11)$$

$$Ag^+ + e^- \rightarrow Ag \qquad (2\text{-}12)$$

- Primary deposition of an alkali metal and secondary discharge of the metal to be deposited by charge exchange with alkali metal atom.

$$K^+ + e^- \rightarrow K \qquad (2\text{-}13)$$

$$[Ag(CN)_2]^- + K \rightarrow Ag + K^+ + 2\ CN^- \qquad (2\text{-}14)$$

- Discharge from complexes with lower coordination number. The direct discharge of complexes with high coordination numbers, which usually predominates in the bath, is not possible. The discharge can only take place following the partial splitting off of the anions in complex with the formation of complexes with lower coordination number or of neutral molecules.

2.3.2 Electrodeposition of metal alloys

The electrodeposition of metal alloys is often referred to as the co-deposition of two or more metals (Brenner, 1963). Brenner has distinguished alloy electrodeposition into five categories:

1. Regular alloy co-deposition: The composition of the deposit is controlled by mass transfer/diffusion of the more noble component towards the cathode. The more noble element in the plating bath is preferentially discharged and can be explained by solution thermodynamics. This deposition mode is likely to occur in baths with uncomplexed metal ions having very large potential difference.

2. Irregular alloy co-deposition: The equilibrium potentials of metal ions are shifted due to solution chemistry. The deposition process is not clearly diffusion controlled, but

under cathodic potential control. This is often the case for alloy electrodeposition from complexed solutions, such as the cyanide plating bath for copper-zinc deposition. Generally, metals with a potential difference of less than 200 mV (based on standard e.m.f. series) may be co-deposited from simple salt solutions. For metals with larger potential gap, simultaneous deposition of the metals is possible only with suitable bath formulation. Usually, a complexing agent has to be used to reduce the potential gap between two elements.

3. Equilibrium co-deposition: This plating process is characterized by the similar or extremely small difference in standard equilibrium potentials of different metal ions in the solution, for example the tin-lead system. The ion concentration of the solution gives the ratio of deposited metal directly.

4. Anomalous alloy deposition: This refers to the plating system where the less noble metal is deposited preferentially. Deposition of mutual alloys of iron, nickel, and cobalt exhibits such behaviour.

5. Induced alloy co-deposition: This applies to systems where the metal ion cannot be deposited as single metals from aqueous solutions. Examples are molybdenum, germanium or tungsten, which can only be deposited together with iron group metals.

The first three categories mentioned above are normal systems, where the deposition behaviours can be estimated from polarization curves. Examples of polarization curves are shown in Figure 2.7. If metal M_n has a far more noble potential than metal M_a (Figure 2.7(a)), only metal M_n will be deposited if the current i_p is applied. For the applied current, the cathode potential, E_p, correspond only to the

deposition of M_n. Figure 2.7(b) shows that when the polarization curves of two metals are close enough, an applied current of i_p corresponds to the potential E_p which allows deposition of both metals. The composition of M_n can be estimated from the ratio of $\frac{i_p - i_a}{i_p}$, while the composition of metal M_a can be estimated as $\frac{i_a}{i_p}$. The most favourable condition for alloy co-deposition is when the curves are identical. This phenomenon is extremely rare in practice. Instead, some polarization curves intersect with each other as seen in Figure 2.7(c). Simultaneous deposition of the metals will take place at the cathode potential E_p. At cathodic potentials more electropositive than E_p, the proportion of metal M_n deposited will be greater than M_a; while at potentials more electronegative than E_p it will be otherwise.

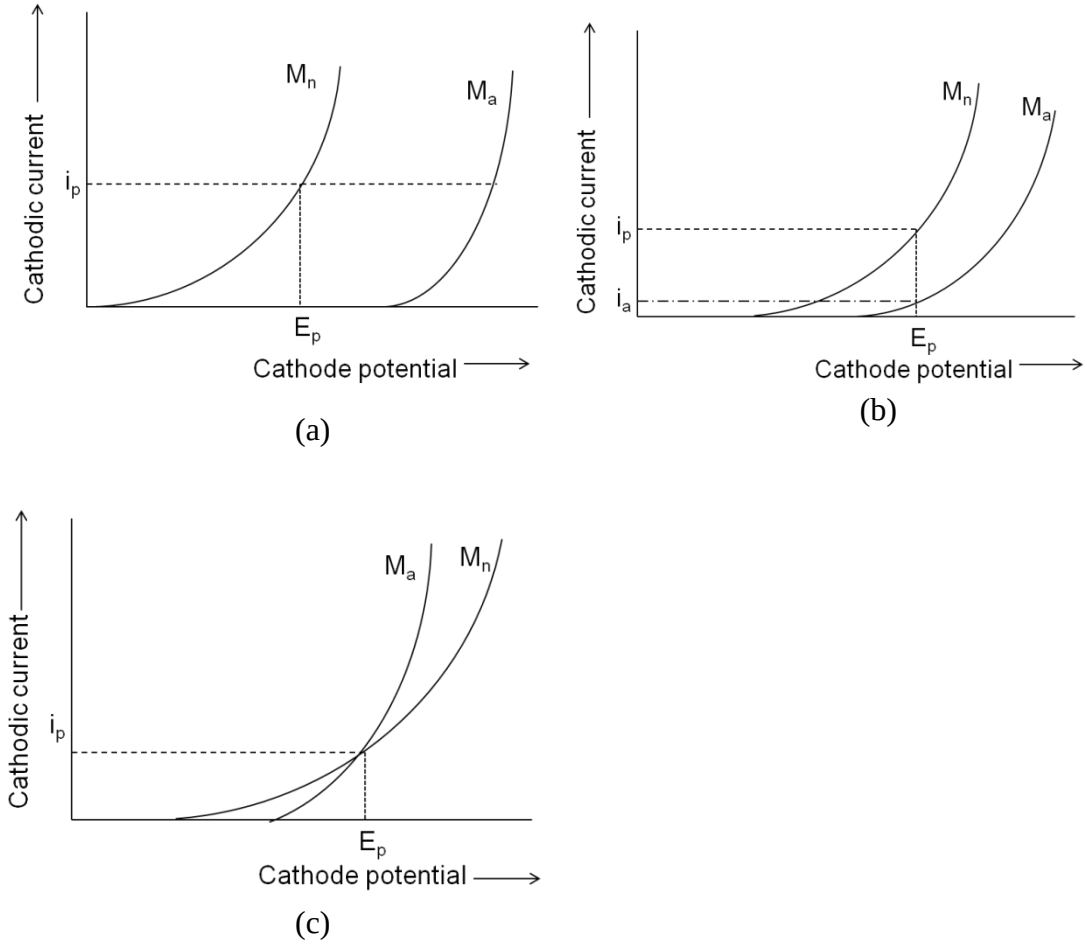

Figure 2.7 Cathodic polarization curves of metal M_n and M_a with potentials (a) far apart, (b) close, and (c) intersecting (Tan, 1993).

However, the predictions from polarization curves are not always accurate because the deposition process is also affected by many other operating variables. The alloy composition is dependent on operating variables such as the current density, solution/cathode agitation, metal ion concentration, solution pH, temperature and the incorporation of electrolyte additives. A major change in one variable will need a significant change of another variable to maintain a given deposit composition. Since Sn and Sn-based alloys are of main concern in this work, the details of these factors affecting the electrodeposition process will be discussed in the next section.

2.4 Electrodeposition of Sn and Sn alloys

The electrodeposition of solders dates back to 1950s when tin-lead (Sn-Pb) solders were still dominating the electronics industry. Co-deposition of Sn-Pb solders has been quite successful (Field & Weill, 1951; J. H. Kim et al., 1996; Kohl, 1982; Lin & Liu, 1999) which can be attributed to the small difference in standard reduction potential between the two elements (Sn^{2+}/Sn: −0.137 V and Pb^{2+}/Pb: −0.125 V). With rising emphasis to restrict the usage of toxic Pb in electronic applications, electroplating of alternative binary systems such as Sn-Ag (Ezawa et al., 2001; J. Y. Kim, Yu, Lee, & Lee, 2004; Neveu, Lallemand, Poupon, & Mekhalif, 2006; Qin, Wilcox, & Liu, 2008; Venkatasamy, Riemer, & Tabakovic, 2011), Sn-Bi (M. Fukuda et al., 2001; Y.-G. Lee et al., 2011; M.-S. Suh et al., 2006; Tsai & Hu, 2011), Sn-Cu (C. Han, 2009; A. Survila, Mockus, Kanapeckaite, Brazinskiene, & Juskenas, 2012), as well as ternary systems such as Sn-Ag-Cu (Joseph & Phatak, 2011; Qin et al., 2010; J. Zhang, An, & Chang, 2009) are being pursued.

Electrodeposition of binary and ternary Pb-free solder alloys is obstructed by the inability to deliver exact alloy compositions for soldering requirements. This is mainly

due to the large potential difference between Sn and the other substituting elements such as Ag, Bi, Cu and Zn, as shown in Figure 2.8. In bimetallic or trimetallic plating baths, the more electropositive element will be preferentially plated out. One way to overcome this difficulty is to utilize the sequential deposition technique. Multiple layers of single metal are deposited from different baths and composition is controlled by varying the thickness ratio of the layers (Bonafede, Huffman, & Palmer, 2006; Ishii, Aoyama, & Tokumitsu, 2001). The metal stack is then annealed to allow composition homogenization through interdiffusion. This method is used in the electrodeposition of Sn-Au solder alloys (Bonafede et al., 2006; Ishii et al., 2001) as the redox potential of Au is far too noble compared to Sn (Au^{3+}/Au: +1.52 V; Au^{+}/Au: +1.83 V). Other Sn-based solder alloys deposited sequentially are those containing Ag, Bi, and Cu, such as Sn-Ag (Cabruja, Bigas, Ullan, Pellegrini, & Lozano, 2007; Ezawa et al., 2001), Sn-Ag-Cu (C. F. Han, Liu, & Ivey, 2009), and Sn-Bi-Cu-Ag (Joseph et al., 2006).

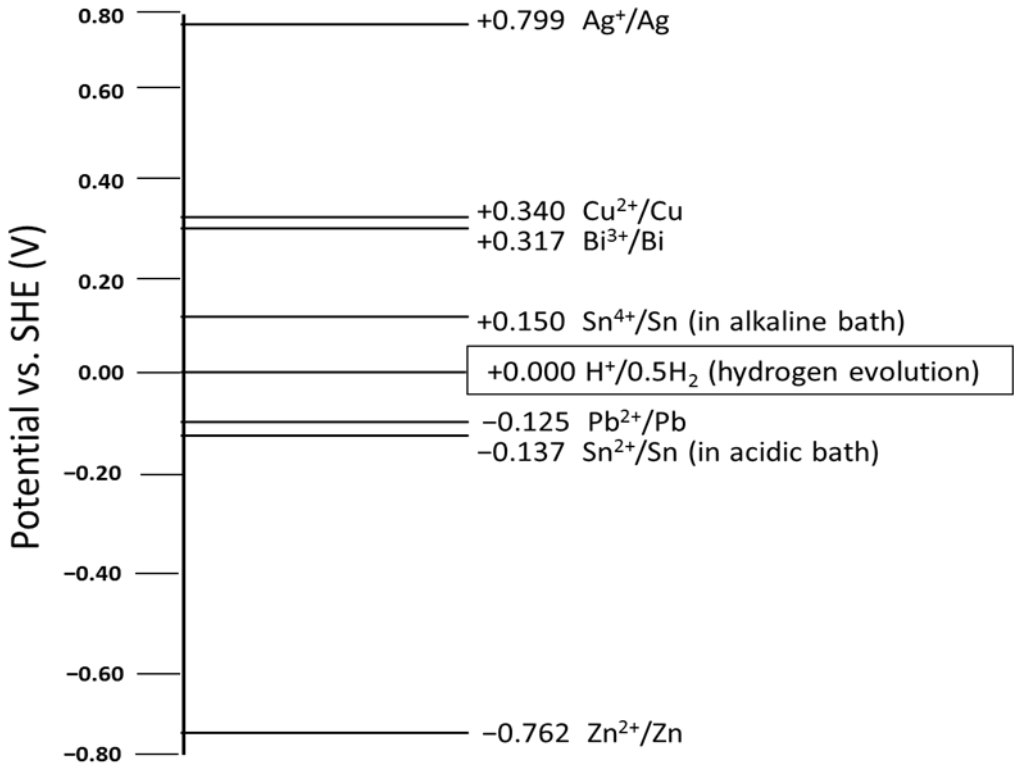

Figure 2.8 Aqueous redox potentials of Pb-free substitution elements vs. standard hydrogen electrode (SHE) (Kühlkamp).

However, this technique possesses drawbacks such as 1) separate baths have to be prepared to deposit elements individually which is time consuming, 2) the tendency of cross contamination between plating baths (Djurfors & Ivey, 2001; Yaakup et al., 2008), 3) post-deposition annealing causes segregation of Sn to the surface of alloy resulting in formation of oxide (Cabruja et al., 2007; Djurfors & Ivey, 2001), and 4) low homogeneity in composition within layers and sharp boundaries may exist (Bicelli, Bozzini, Mele, & D'Urzo, 2008). Figure 2.9 shows cross-sectional micrograph of as-plated multiple Sn-Au layers and post-annealed solder bump. Near eutectic Sn-Au solder bumps are achieved after reflow but still there are homogeneity issues within the bump (light area 7.07 wt% Sn; dark area 16.27 wt% Sn).

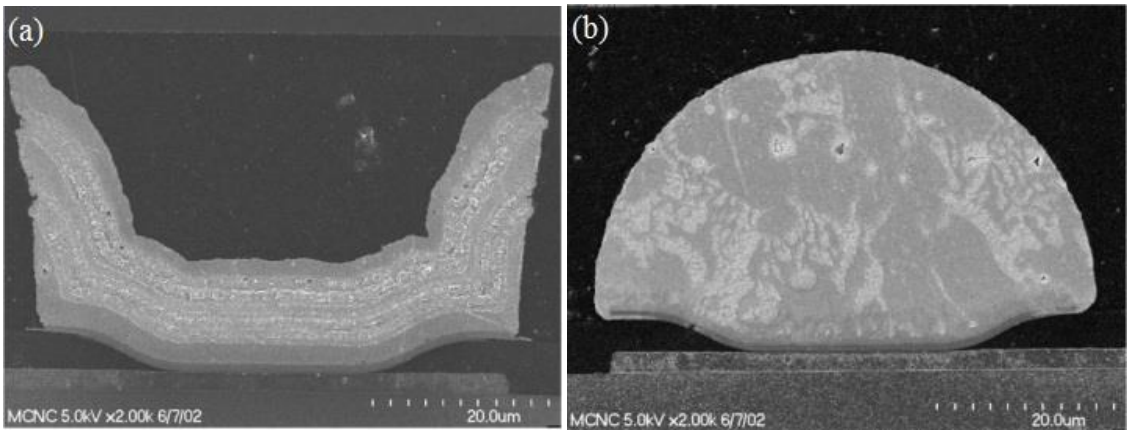

Figure 2.9 Cross – section of Au/Sn/Au/Sn/Au (a) as-plated sample and (b) reflowed sample (Bonafede et al., 2006).

Co-deposition of all elements in a single bath is a better option. But the achievement of desired alloy composition remains a problem, although researchers suggested a few measures that can allow the deposition of alloys near desired composition.

2.4.1 Composition control of deposits

A widely accepted way is to add suitable chelating agent(s) to the bath to alter the deposition potentials of individual metal ions. The selection of chelating agents is usually based on the element that has more noble electrode potential, since they are preferentially deposited. A chelating agent forms bonds selectively with the more noble element to form complexes. The metal ions in complex form will need a higher activation potential to be released. Hence the deposition potential is shifted to a more electronegative value (Joseph et al., 2006; Tan, 1993). The potential gap between both elements will then be brought closer. Examples of some commonly used chelating agents for Pb-free solder alloy deposition include thiourea, ethylenediamine-tetraacetic acid (EDTA), and pyrophosphate-iodide for Ag (Joseph & Phatak, 2008, 2010; J. Y. Kim et al., 2004; Qin et al., 2008; Qin et al., 2010); polycarboxylic acids, citric acid, and EDTA for Bi (Joseph et al., 2006; Tsai & Hu, 2009a, 2009b, 2011; Tsai et al., 2007); and thiourea, and triethanolamine (TEA) for Cu (Mitsunobu Fukuda, Imayoshi, & Matsumoto, 2002; J. Zhang et al., 2008). Figure 2.10 shows the effect of thiourea in shifting the deposition potential thereby suppressing the preferential deposition of Ag and Cu. Figures 2.9(a) and 2.9(b) respectively show that the deposition potentials for Ag and Cu are shifted much nearer to the deposition potential of Sn when thiourea is added. This indicates the chelating effect of thiourea with Ag and Cu ions. On the other hand the deposition potential of Sn is barely affected by thiourea (Figure 2.10(c)). The successful suppression of preferential deposition of Ag and Cu from the plating bath has made ternary alloy co-deposition possible (Mitsunobu Fukuda et al., 2002). The bonding mechanism between chelating agents and metal ions will be discussed further in ***Section 2.4.3.1***.

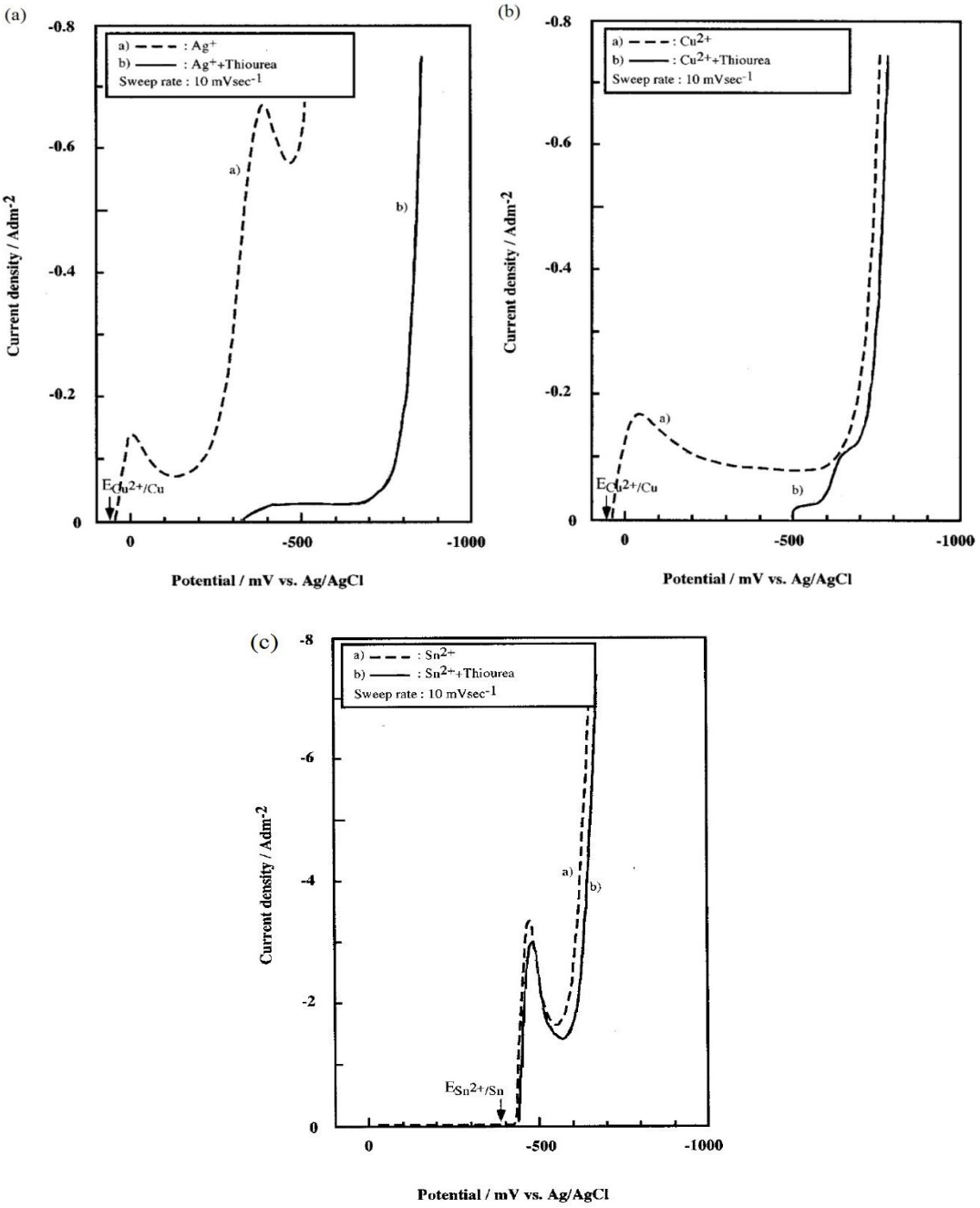

Figure 2.10 Polarization curves of (a) Ag, (b) Cu, and (c) Sn deposition in 2 M H_2SO_4 solutions (adapted from(Mitsunobu Fukuda et al., 2002)).

The addition of chelating agent(s) alone may not be sufficient to obtain the desired composition. Investigations reveal that the composition of the deposited alloy depends on deposition current density, composition of plating solutions and electrolyte flow (Kiumi, Takeda, Yoshioka, Kuriyama, & Saito, 2005). Optimization of these relevant plating parameters is done in practice to achieve the desired composition. Figure 2.11 summarizes the data on the effect of current density on the composition of

Pb-free solder found in the recent literatures. It is observed in Figure 2.11(a) that the amount of Ag in the deposit generally decreases as the current density increases. This can be attributed to the more noble reduction potential of Ag^+ as compared to Sn^{2+}. Lower overpotential (at low current densities) favors reduction of more electropositive species; while higher overpotential (at high current densities) favors less preferred reactions, such as reduction of Sn^{2+}, while deposition of Ag becomes diffusion limited(Chen et al., 2008; Tan, 1993). Neveu et al. (2006) and Chen et al. (2008) observed a slight increase in Ag content with increased current density at some intermediate values which may be attributed to an increased current efficiency of Ag over Sn at that particular current density (J. Y. Kim et al., 2004).

In the case of Sn-Bi alloy deposition, Fukuda et al. (2001) and Lee et al. (2011) found that Bi content tends to decrease with current density (Figure 2.11(b)). Conversely, Suh et al. (2006) found an increase in Bi content with increasing current density. On the other hand, the variation of the Bi content of the deposits reported by Medvedev et al. (2003) was negligible, from 0.63 to 0.94 wt.%. The decrease in the content of the more noble Bi matches the previous argument for the co-deposition of Sn-Ag. However, the reason for sudden increase in Bi content showed by Fukuda et al. (2001) is not known. The increase in Bi content as found by Suh et al. (2006) may be attributed to the effects of chelating additives added to the plating bath that have shifted the deposition potential of Bi to more electronegative than Sn, hence causing Sn to be the more noble element (M.-S. Suh et al., 2006).

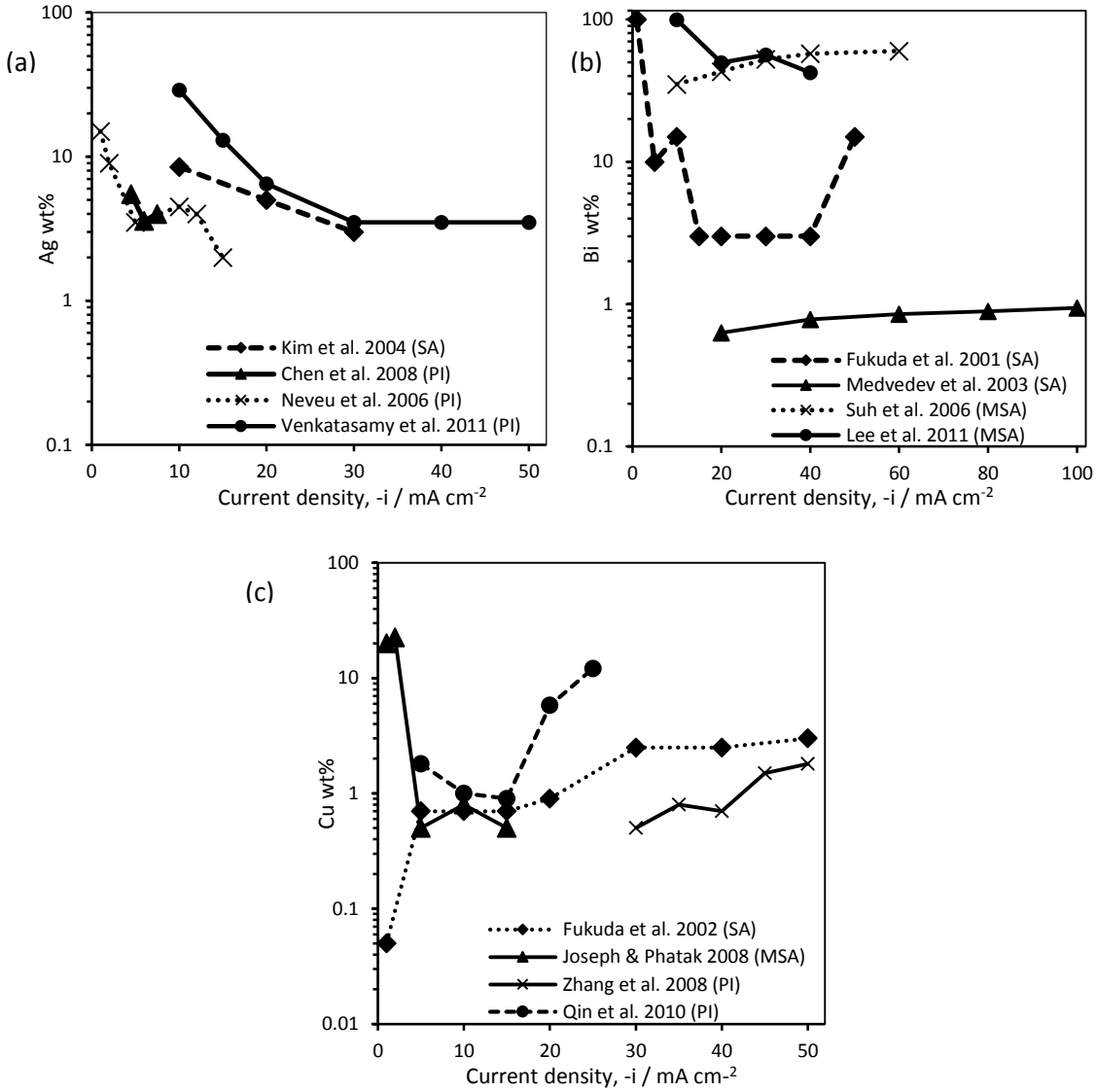

Figure 2.11 (a) Ag wt% variation vs. current density for Sn-Ag plating solutions; (b) Bi wt% variation vs. current density for Sn-Bi plating solutions; (c) Cu wt% variation vs. current density for Sn-Ag-Cu plating solutions (denotation: SA- Sulfuric Acid bath; PI- Pyrophosphate-Iodide bath; MSA- Methane Sulfonic Acid bath).

The Bi content in the deposited alloy is also a function of the type of background electrolyte used and the amount of Bi salt incorporated. Both Suh et al.(2006) and Lee et al. (2011) use methane sulfonic acid (MSA) as background electrolyte hence the Bi content do not differ much. Although Fukuda et al. (2001) and Medvedev et al. (2003) use similar background electrolyte, but there is a big difference in the Bi content obtained. This may result from the small amount of Bi salt added by Medvedev et al. (2003), 0.002M, which is 10 times less than the amount Fukuda et al. (2001) added. For ternary alloy Sn-Ag-Cu deposition, the content of Ag (not shown here) shows similar

trend as in the deposition of binary Sn-Ag as depicted in Figure 2.11(a). The Cu content generally showed an increasing trend (Figure 2.11(c)), which may be related to the decrease in Ag reduction rate, as the reduction potential of Ag is more noble compared to Cu. By summing up the contents of noble elements (Ag wt% + Cu wt%) in the ternary system, a decreasing trend is still observed, which fulfilled the theoretical deposition behavior. However, there is an exception showed by Joseph and Phatak (2008) using methane sulfonic acid (MSA) bath, where a decreasing trend is observed. The reason is not fully understood.

Besides current density and bath composition, agitation is another important plating parameter that has an impact on the alloy composition. Qin et al. (2010) investigated the electrodeposition of Sn-Ag-Cu under static and stirring conditions. From Figure 2.12(a) and 2.12(b), the results show that at low current density region (5-15 mA cm^{-2}), stirring of the plating solution enhances the deposition of both more noble elements (Ag and Cu) significantly. Thereafter, the contents of Ag and Cu decrease with increasing current density. This fits in well to the theory discussed previously where higher current densities favor less preferred reactions, which is the reduction reaction of Sn^{2+} in this case (Chen et al., 2008; Tan, 1993). However, there is an abnormal hike in Cu content at 20 and 25 mA cm^{-2} under static conditions. The sudden increase in Cu content may be attributed to the exposure of Cu cathode due to nodular and porous microstructure of deposits when approaching the limiting current density (Figure 2.12(c)). Deposits tend to be burnt and spongy around or above the limiting current density hence are less adhesive (Tan, 1993). With stirring, the limiting current density can be extended several fold and compact deposits (Figure 2.12(d)) can be obtained over a wider current density range (from the range of 5-15 mA cm^{-2} to 5-70 mA cm^{-2}). Moreover, the extended limiting current density resulted in relatively lower

overpotential at low current densities. Hence the reduction reaction of more noble elements becomes highly favorable and contents of Ag and Cu in the deposits increased significantly in the low current density region. It is demonstrated here that stirring of plating solution boosts the deposition of more noble elements at low current densities and improvement in microstructures can also be achieved.

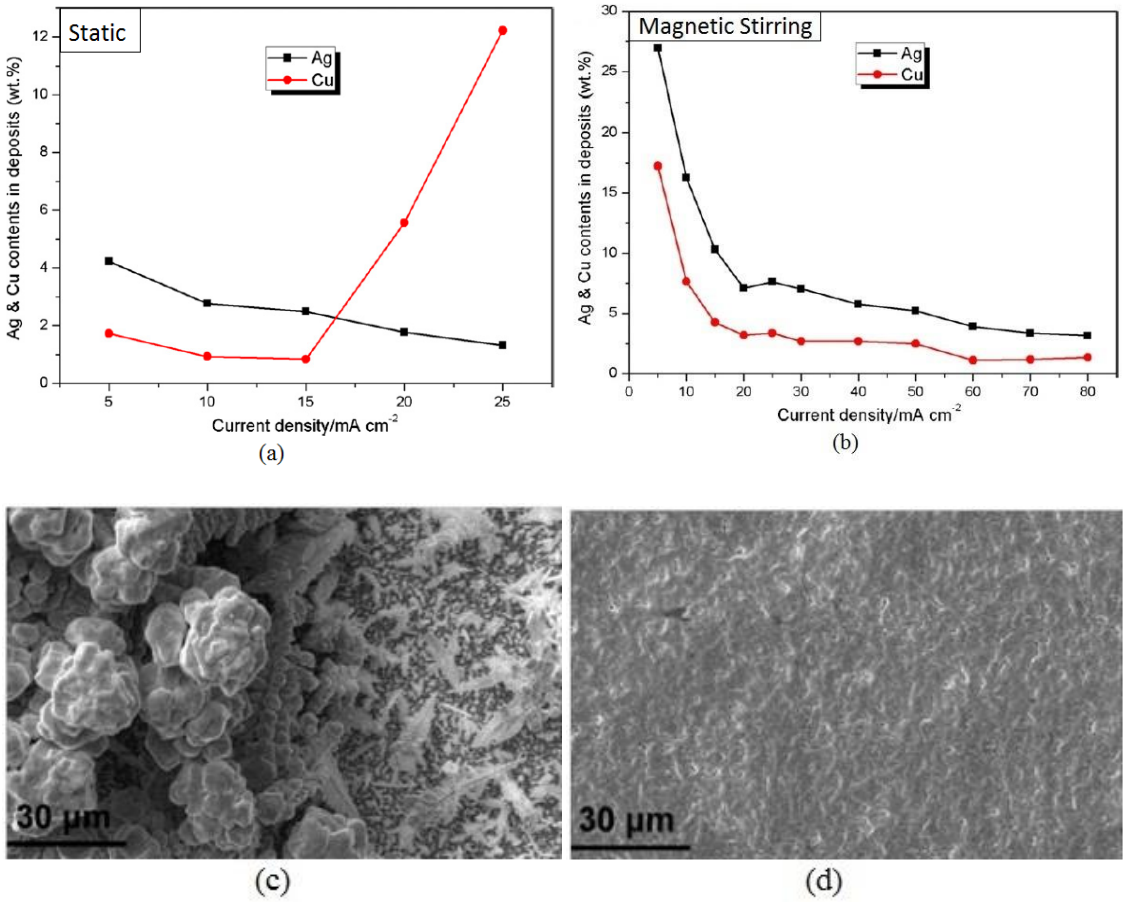

Figure 2.12 Ag and Cu contents (wt %) in the electrodeposited Sn-Ag-Cu films vs. current density (a) without stirring and (b) stirring with magnetic stirrer at 300rpm; (c) exposure of Cu cathode at 25 mA cm^{-2}; (d) compact deposits obtained at 70 mA cm^{-2} under stirring condition (Qin et al., 2010).

Joseph et al. (2006) demonstrated a similar trend where stirring facilitates the deposition of more noble Bi at a low current density of 5 mA cm^{-2}. Figure 2.13 shows the composition of deposits under static and stirred conditions. The Sn content of the deposits decreased drastically when agitation was applied while the content of the more noble Bi increased to 90 wt%. However, the Cu content of the deposits, which is even more noble than Bi, did not show much difference. This may be attributed to the low

amount of Cu salt that was present in the plating bath. From the electrochemical point of view, limiting current density increases when stirring is applied. Hence the deposition rate of element with more noble deposition potential is enhanced. But from the practical point of view, stirring might increase the amount of dissolved oxygen in the plating bath, causing oxidation and decrease in concentration of Sn ions. It is difficult to determine which mechanism is dominant unless measurements on Sn ions concentration under both static and stirring conditions are conducted.

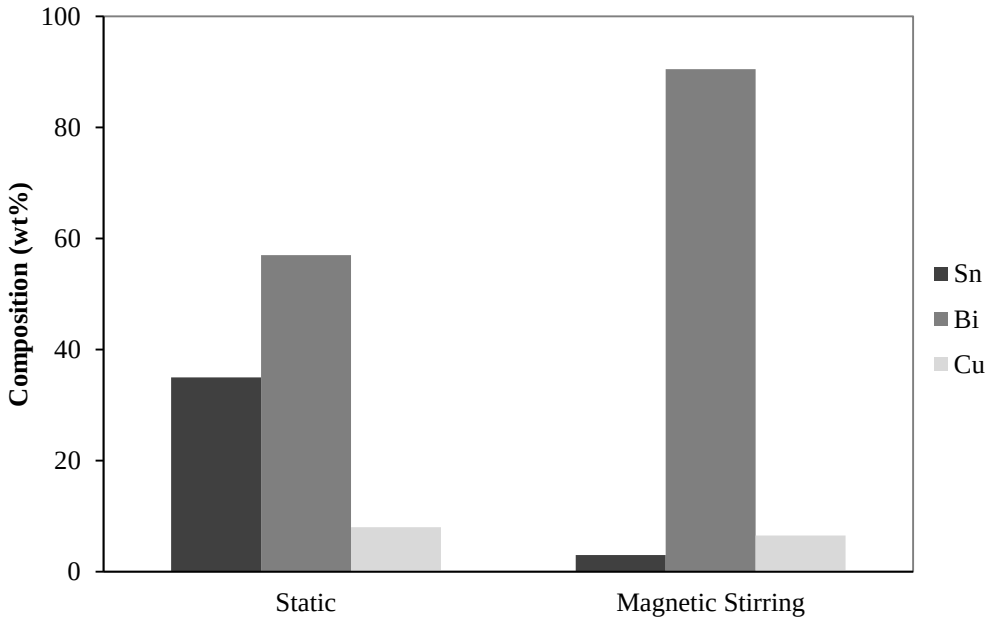

Figure 2.13 Composition variation of Sn-Bi-Cu alloy with stirring conditions at 5 mA cm^{-2} (Joseph et al., 2006).

2.4.2 Plating bath stability

This section focuses on the stannous ions oxidation problem in electroplating baths and the methods that were applied to significantly alleviate this issue. However, prior to the discussion on plating bath stability, it will be worthwhile to look at the brief summary of commonly used plating baths for the electrodeposition of Sn-based solder alloys as described in the next section.

2.4.2.1 Common plating baths for electrodeposition of Sn-based alloys

Electrodeposition of Sn and Sn-based alloys can be done in either alkaline or acidic solutions. Alkaline solutions possess some attractive qualities such as they are non-corrosive and do not require additives as the Sn^{4+} ions already exist in a stable state (He, Liu, & Ivey, 2007; Qin et al., 2010). A good example would be the pyrophosphate-iodide bath where stannic ions are formed immediately and the bath remains clear and stable for a time period as long as one year (C. Han, 2009; Neveu et al., 2006; Qin et al., 2008). The pyrophosphate-iodide electrolyte system is widely used in the electrodeposition of Sn-Ag solder alloys (Chen et al., 2008; Neveu et al., 2006; Venkatasamy et al., 2011). The large difference in standard potential between Sn and Ag (0.649 V) (Refer Figure 2.8) requires plating bath with chemical nature that allows formation of stable Ag complexes(Schlesinger & Paunovic, 2010). However, the stannic ions cause the process to consume twice as much electrical charge compared to plating the same amount of Sn in acidic solutions which contain stannous ions (He et al., 2007; Sun & Ivey, 1999). Other drawbacks of alkaline baths are the passivation of anode under low current densities, high processing temperature of up to 65^{o}C, and possibility of degrading photoresists. Particularly, the latter drawback may limit the use of alkaline baths for the deposition of Pb-free solder into micropatterns.

Acidic plating baths, on the other hand, are compatible with photoresists. They also offer advantages such as large plating current density range and ability to operate at room temperature. Some major acidic electrolyte systems for Sn alloy plating include sulfuric acid electrolyte, citric acid electrolyte and methane sulfonic acid (MSA) electrolyte. The most advantageous features of sulfuric acid systems are low cost, high throwing power, and 100% cathode efficiency is achievable. However, sulfuric acid based plating baths are less appropriate for deposition of Ag and Bi containing alloys as

they can form insoluble precipitates (M.-S. Suh et al., 2006). Citric acid electrolytes are extensively used for Sn alloys co-deposition as citric acid itself acts as a complexing agent for many metallic ions (Tsai & Hu, 2009a, 2009b, 2011; Tsai et al., 2007; Tsai et al., 2011). However, the addition of wetting agents or surfactants to these plating baths can be considered as a must to improve the adhesion and suppress dendritic growth of the deposits. The usefulness of MSA in electroplating was well known for several decades but only gained commercial acceptability in the 1980s (Schlesinger & Paunovic, 2010). It is a reducing acid which can also act as a complexing agent, has high solubility for salts of nearly all Pb-free substituting metal, and ease of effluent treatment. Numerous MSA-based plating baths were formulated for the electrodeposition of Pb-free Sn-based alloys and many patents have been granted. Table 2.2 summarizes the pros and cons of common electroplating baths and Sn alloys that were successfully plated from the baths.

Table 2.2 Comparison between different electrolyte systems in electrodeposition of Sn-based alloys.

	Background electrolyte	**Advantages**	*Disadvantages*	Alloys deposited	References
Alkaline	Pyrophosphate-Iodide	• **High stability** • **Able to form stable complexes with noble metals**	• *Narrow operating temperature range* • *Requires more control and maintenance* • *May degrade photoresists*	Sn-Ag Sn-Ag-Cu	(Chen et al., 2008; C. Han, 2009; Neveu et al., 2006)
Acidic	Sulfuric Acid	• **Low cost** • **Easy bath preparation** • **High cathode efficiency (~100%)** • **Composition control possible through manipulation of parameters (current density, salt concentration, current type)**	• *Corrosive to plating equipments* • *Rapid oxidation of Sn(II) ions* • *Surfactant addition is necessary to improve surface morphology* • *Ag and Bi ions form insoluble precipitates*	Sn-Ag Sn-Bi Sn-Cu Sn-Zn Sn-Bi-Cu Sn-Ag-Cu	(Arici, Nazir, & Aksu, 2011; M. Fukuda et al., 2001; Mitsunobu Fukuda et al., 2002; Joseph et al., 2006; J. Y. Kim et al., 2004; Medvedev, Makrushin, & Dubenkov, 2003; Schlesinger & Paunovic, 2010; A. Survila, Mockus, Kanapeckaite, Jasulaitiene, & Juskenas, 2009)
	Citric Acid	• **Donor ligands form complexes readily with many metallic ions (e.g. Sn^{2+}, Bi^{3+}, Cu^{2+}, Ag^{+}, etc.)** • **Mild acidic nature**	• *Surfactants must be added to improve deposits adhesion and suppress dendritic growth*	Sn-Bi Sn-Ag Sn-Cu Sn-Ag-Cu	(Tsai & Hu, 2009a, 2009b, 2011; Tsai et al., 2007; Tsai et al., 2011)
	Methane Sulfonic Acid	• **Less corrosive** • **Reducing nature minimizes oxidation of Sn ions** • **High solubility for Pb-free candidate salts** • **More environmental friendly due to easy effluent treatment**	• *Performance can only be improved with addition of electrolyte additives* • *Sn(IV) ions exist in metastannic acid form (colloidal) hence causing problems to plating bath*	Sn-Ag Sn-Bi Sn-Cu Sn-Ag-Cu	(Joseph & Phatak, 2008, 2010; Y.-G. Lee et al., 2011; Low & Walsh, 2008a; Schlesinger & Paunovic, 2010; M.-S. Suh et al., 2006)

2.4.2.2 *Stability of acidic plating baths*

As mentioned in Section 2.4.2.1, alkaline plating baths generally have very high bath stability. On the other hand, stability issues arise for acidic plating baths that are preferred due to their compatibility with photoresists. The major problem with acidic plating baths is the spontaneous oxidation of stannous ions to stannic ions (Kunihiro, Morimitsu, & Matsunaga, 2000; Low & Walsh, 2008c; Martyak & Seefeldt, 2004; Sun & Ivey, 1999; J. Zhang et al., 2008) due to the chemical reaction given by Equation 2-14.

$$2Sn^{2+} + O_2 + 4H^+ \rightarrow 2Sn^{4+} + 2H_2O \qquad (2\text{-}15)$$

Stannic ions tend to precipitate as stannic compounds in the form of white particles and lead to an increase in turbidity due to sludge formation.

Researchers attempted to solve this problem by adopting three approaches: 1) incorporating antioxidant into the plating bath (e.g.: Hydroquinone, Catechol) (Kunihiro et al., 2000; Low & Walsh, 2008c; Martyak & Seefeldt, 2004; Sun & Ivey, 1999; J. Zhang et al., 2009; J. Zhang et al., 2008), 2) using an anode with low oxygen overpotential (Kunihiro et al., 2000), and 3) adding a reducing agent (e.g.: Hydrazine) (Venkatasamy et al., 2011). An antioxidant functions by consuming dissolved oxygen in the bath hence prevents the oxidation process. For example, the oxygen removal mechanism of hydroquinone follows the following reaction (Low & Walsh, 2008c):

$$2C_6H_4(OH)_2 + O_2 \rightarrow 2C_6H_4O_2 + 2H_2O \qquad (2\text{-}16)$$

However, for electrodeposition at high current densities, the oxidation process depends on the oxygen evolution potential and antioxidant alone may not be sufficient

to suppress oxidation. Kunihiro et al. (2000) found that the simultaneous use of an antioxidant and an anode with low oxygen overpotential can help to maintain the bath stability. Kunihiro et al. (2000) studied the effects of the use of two different types of anodes which are platinum (Pt) and iridium-tantalum oxide (IrO_2-Ta_2O_5) coated Ti in the presence of catechol as antioxidant. IrO_2-Ta_2O_5/Ti has lower oxygen overpotential compared with Pt. They recorded the variation of Sn^{2+} and Sn^{4+} contents of the bath as a function of electrolysis time. Kunihiro et al. (2000) observed that at low current density (25 mA cm^{-2}), the plating bath remained stable when Pt was used as anode. But at high current density (250 mA cm^{-2}), the bath rapidly degraded with deposition time as indicated by the sharp reduction in Sn^{2+} concentration after about five hours of electrolysis, when Pt electrode was used (Figure 2.14). This was in spite of the fact that the bath contained catechol as antioxidant. However, no reduction in Sn^{2+} content and hence no degradation was observed when IrO_2-Ta_2O_5/Ti was used as anode.

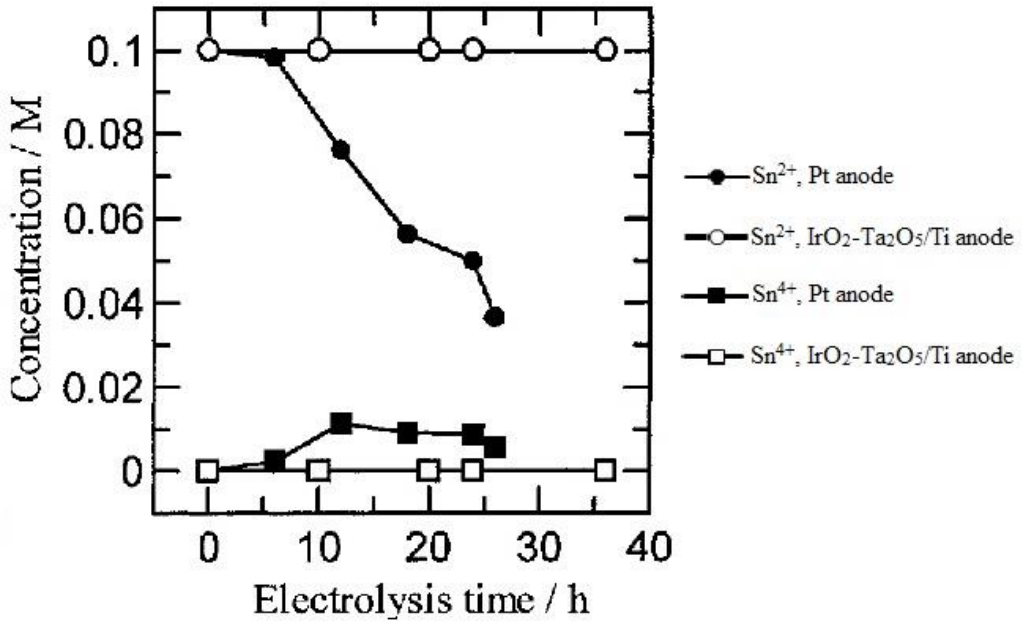

Figure 2.14 Concentration changes of Sn^{2+} and Sn^{4+} ions during electrodeposition at 250 mA cm^{-2} (Kunihiro et al., 2000).

On the other hand, reducing agent such as hydrazine acts as both oxygen scavenger and also reduces the Sn^{4+} species formed back to the desired Sn^{2+} species (Low & Walsh, 2008c; Venkatasamy et al., 2011). Hydrazine oxidizes to nitrogen gas and water while releasing electrons via:

$$N_2H_4 + O_2 \rightarrow N_2 + 2H_2O + 2e^- \quad (2\text{-}17)$$

The electrons released from hydrazine oxidation then reduce the Sn^{4+} species in the electrolyte via:

$$Sn^{4+} + 2e^- \rightarrow Sn^{2+} \quad (2\text{-}18)$$

Bath stability can be monitored by physical observation of bath turbidity (Joseph & Phatak, 2010) as well as by electrochemical measurements of peak and limiting current densities (Low & Walsh, 2008c). It can also be done by monitoring the Sn^{2+} content in the bath as has been discussed in Figure 2.14. A stable plating bath should be clear and transparent. The change in bath color and increase of turbidity over storage time under atmospheric conditions indicates the spontaneous oxidation of remaining stannous ions in the bath. The degradation of stannous-containing plating bath usually trails the following path: from clear and transparent, to yellowish and transparent, to yellowish and turbid with precipitates, and precipitates settling down (Joseph & Phatak, 2010). Electrochemical measurements on percentage reduction of peak and limiting current density of the bath can give a more accurate picture on bath stability because the exact amount of remaining stannous ions can be estimated. Figure 2.15 illustrates the percentage decrease in limiting current density with storage time and also the effect of various concentrations of hydroquinone in suppressing stannous oxidation in a methane sulfonic acid plating bath as observed by Low and Walsh (2008c).

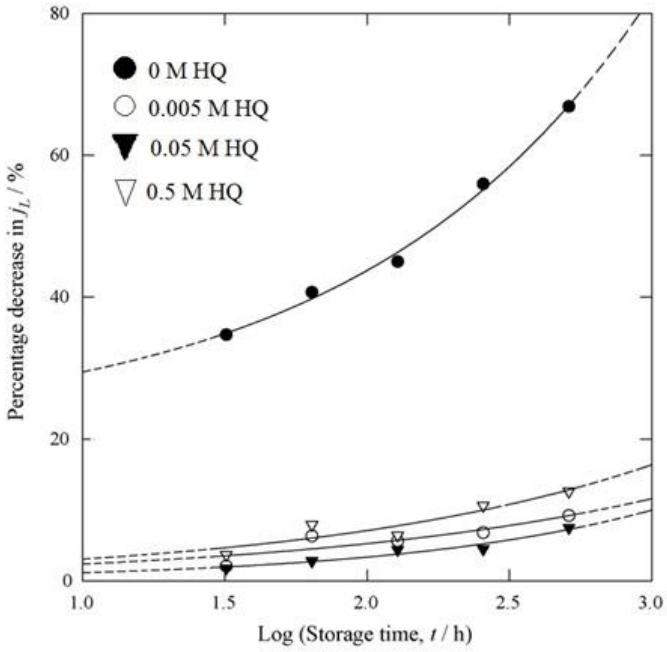

Figure 2.15 Percentage decrease in limiting current density with storage time (Low & Walsh, 2008c).

The reduction in limiting current density indicates that there are less stannous ions available in the bath. It is seen in Figure 2.15 that a small amount of hydroquinone is effective in maintaining the limiting current density and hence the stability of the bath. Without the aid of antioxidants, stannous oxidation takes place almost immediately and develops in a rapid manner which results in poor bath stability. This can bring detrimental effects to the electrodeposition process such as much lower current efficiency (Bi et al., 2009), deposits produced might be loosely adhered (Tsai et al., 2007), and dendrites may form due to the presence of Sn^{4+} species (Venkatasamy et al., 2011).

2.4.3 Electrolyte additives

Electrolyte additives are routinely used in the plating baths of Sn and Sn-based solder alloys, to obtain desirable deposits. Various categories of additives can be identified, namely 1) chelating (complexing) agents; 2) antioxidants (oxidation inhibitors); 3) surfactants (surface-active agents); and 4) grain refiners and brighteners. The role of

antioxidants are vital in acidic plating baths to act as oxygen scavenger hence avoiding stannous (Sn^{2+}) to stannic (Sn^{4+}) oxidation. Surfactants adsorb on electrode surfaces to help eliminate gas bubbles hence improve properties of deposits. Compositional control can be aided by adding chelating agents; while improvements in microstructure are achieved by grain refiners and brighteners.

Without the aid of the additives mentioned above, it is difficult to attain a stable and repeatable plating solution for the electrodeposition of solder alloys. The main problem regarding the selection of additives lies on the uncertainty on electrochemical changes of plating baths made by the additives. Also, the incorporation of electrolyte additives increases the cost and complexity of the plating bath and chances of contaminating the electrodeposits. The properties of additives commonly used by researchers in the electroplating of Sn-based Pb-free solder will be reviewed here to provide a clearer picture on the functioning mechanism of additives in the plating baths.

2.4.3.1 Chelating agent

Chelating agents, also known as complexing agents, are organic compounds that have at least two functional electron donor groups capable of bonding to the metal atom. They are usually amino polycarboxylates, hydroxy carboxylates, and organophosphonates (Knepper, 2003). A chelate or complex is the term given to the formation of a ring between a multiply-charged metal ion and the chelating agent. The stability of the complex formed is affected by a few factors:

a) Number of donor atoms in the chelating agent: chelating agents with higher number of donor atoms tend to form stronger complexes (Knepper, 2003; Stavila, Davidovich, Gulea, & Whitmire, 2006),

b) Complex formation constant (CFC): This expresses the chelate strength for a certain metal ion and a certain chelating agent. Chelating agents can be categorized according to their CFCs; weak chelators (CFC < 5); intermediate chelators (CFC 5-12); strong chelators (CFC > 12) (Anderegg, Arnaud-Neu, Delgado, Felcman, & Popov, 2005; Knepper, 2003; Schowanek, McAvoy, Versteeg, & Hanstveit, 1996),

c) Properties of the metal ions: strongly hydrolyzed cations like Al^{3+}, Bi^{3+}, In^{3+} and Zr^{4+} are strongly complexed by chelating agents (Anderegg et al., 2005; Knepper, 2003; Schowanek et al., 1996), and

d) pH value: chelating strength is pH dependent, e.g.: at low pH values, iron complexes with amino polycarboxylate chelating agents are more stable compared to calcium and magnesium complexes. Hence, pH can be used as a means to increase complexing selectivity for one ion over another (Knepper, 2003; Schowanek et al., 1996).

Figure 2.16(a) shows the structure of an amino polycarboxylate chelating agent, ethylenediamine-tetraacetic acid (EDTA), and Figure 2.16(b) illustrates the formation of a chelate. It consists of six donor groups (two amino groups and four acetic groups, as shaded in Figure 2.16(a)) and hence is able to form strong complexes with most metal ions. However, its chelating strength is pH dependent (e.g. Bi-EDTA complexes have CFCs of 17.73 and 25.68 in the pH range of 0.6-1.4 and 1.5-10 respectively).

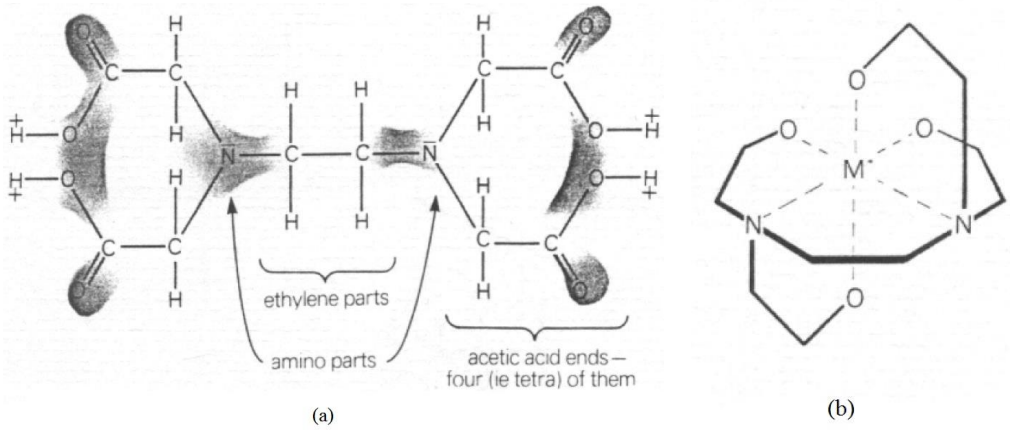

Figure 2.16 (a) Structure of an EDTA molecule and (b) the formation of a chelate.

In the electroplating of Sn-based Pb-free solder alloys, chelating agents play an important role in facilitating the co-deposition of alloying elements in a single bath. As explained in the previous section (***2.4.1 Composition Control of Deposits***), the more noble elements need to be chelated since they otherwise are preferentially deposited. Appropriate type and amount of chelating agents should be selected based on the metal ion to be chelated and the bath pH so as to achieve a selective chelating effect. Table 2.3 presents CFCs of commonly used chelating agents with Pb-free substitution elements.

Table 2.3 Complex formation constants (CFCs) of chelating agents metal ions at 0.1 M and 25^{o}C (Knepper, 2003; Stavila et al., 2006).

	Ag^{+}	Bi^{3+}	Cu^{2+}	Zn^{2+}
EDTA	**7.3**	**27.8***	**18.8**	**16.4**
NTA	**5.2**	**18.2***	**12.9**	**10.7**
DTPA	**-**	**30.7***	**21.4**	**18.3**
EGTA	**6.9**	**23.8***	**17.9**	**14.5**
HEDTA	**6.7**	**22.3***	**17.6**	**14.5**

EDTA: Ethylenediamine-tetraacetic acid
NTA: Nitrilotriacetic acid
DTPA: diethyl triamine-pentaacetic acid
EGTA: Ethyleneglycol-O, O'-bis(2-aminoethyl)-N, N, N', N'-tetraacetic acid
HEDTA: N-(2-Hydroxyethyl)ethylenediamine-N, N', N'-triacetic acid
**CFC at 20^{o}C.*

For instance, among all ions chelated with EDTA, Bi^{3+} has the highest CFC. This implies that Bi^{3+} will form stronger chelates with EDTA and will also be preferentially chelated when other ions are present. The Ag^{+} generally forms weak chelates with amino polycarboxylates hence could not be sufficiently chelated by them. Other compounds like thiourea can successfully chelate Ag^{+} (Mitsunobu Fukuda et al., 2002; Joseph & Phatak, 2008, 2010; J. Y. Kim et al., 2004) but the CFC is not known.

2.4.3.2 Antioxidants

An antioxidant is usually an organic ring compound with a radical group (e.g.: NH_2, NO_2, OH) attached in the ortho- or para- position (Duffy, 1981). Figure 2.17 illustrates chemical structures of typical antioxidants and structure of two commonly used antioxidants in acidic plating baths, catechol and hydroquinone. Hydroquinone is the para-isomer of catechol and both of them fulfill the chemical structure needed to be an oxygen scavenger.

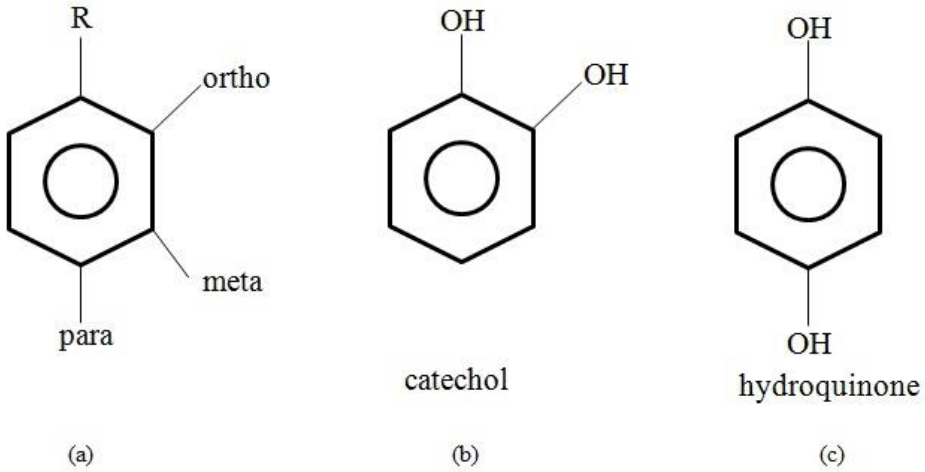

Figure 2.17 (a) Organic ring compound with radical group, R, attached and nomenclature of ring position; (b) Structure of catechol with two –OH groups attached in ortho- and para- position; (c) Structure of hydroquinone with two –OH groups attached in para- position.

Antioxidants are widely utilized to maintain plating bath stability hence extending the lifespan of the bath. They function by removing dissolved oxygen in solutions hence inhibiting oxidation of easily oxidized species in the plating bath, for instance, the stannous ions. The functioning mechanism of an antioxidant has been discussed in the previous section (***2.4.2.2 Stability of acidic plating baths***).

2.4.3.3 Surfactants

Surfactants are molecules composed of a polar hydrophilic head and a non-polar hydrophobic tail. They can be anionic, cationic, nonionic or zwitterionic, depending on the charge of their head group(Malik, Hashim, Nabi, AL-Thabaiti, & Khan, 2011; Salager, 2002). On the other hand, they are also commonly classified according to their tail composition, which can be hydrocarbon-based, polyether-based, fluorocarbon-based (fluorosurfactants), or siloxane-based(Low & Walsh, 2008b; Yan et al., 2004). The most widely used surfactants are polyether-based. This is attributed to their availability, suitability in improving Sn plating, and the resultant surface tension is closely related to hydrocarbon-chain length (Arvydas Survila & Bražinskienė, 2007; A. Survila, Mockus, Kanapeckaitė, & Samulevičienė, 2005). Fluorosurfactants are also particularly advantageous in electroplating due to their chemical stability, cost effectiveness and allows high operating temperature (Low & Walsh, 2008b; Malik et al., 2011; Vittal, Gomathi, & Kim, 2006).

Changes caused by surfactant molecules can be due to: 1) physical adsorption or chemisorptions onto the electrode surface; or 2) alteration of solution viscosity. Surfactants are used in electroplating aiming at the following beneficial effects (Low & Walsh, 2008b; Vittal et al., 2006):

- widening of the operating range with respect to pH, temperature and current density by altering electrode polarization,
- modification of the crystal size of deposits hence enhances surface brightness
- facilitates detachment of gas bubbles from the cathode and prevents void formation, and
- cleaning of the metal surface as a preparatory step to plating.

Table 2.4 summarizes the effects of various surfactants used by researchers in the electroplating of Sn-based solder alloys. Generally, surfactants reduce the peak current density by adsorbing and forming a blocking layer on the surface. This suppresses the formation of active sites for deposition. The behavior of ionic surfactants (anionic and cationic) is concentration and potential dependent (J.-Y. Lee, Kim, Chang, Tae Kim, & Park, 2004; Low & Walsh, 2008b; Neveu et al., 2006). On the other hand, the activity of polyether based surfactants is molecular weight dependent and easily affected by other substances in the solution. For example, the inhibitive effect of polyethylene glycol (PEG) are enhanced with increasing molecular weight (Chen et al., 2008) and existence of other compounds such as polypropylene glycol (PPG), phenolphthalein, and sorbitol (Martyak & Seefeldt, 2004; Neveu et al., 2006).

Table 2.4 Recent examples of surfactants used in Sn-based plating baths.

Metal/ Alloy	Background Electrolyte	Surfactant	Surfactant Class Head/Tail	Effects	Reference
Sn	Methane Sulfonic Acid (MSA)	Polyethylene Glycol (PEG) (Molecular weight: MW 600) Polypropylene Glycol (PPG) (425)	N / PE	PEG- Suppresses H_2 evolution and shifts deposition potential in cathodic direction PPG + Phenophthalein- enhance adsorption of PEG, produces matte Sn deposits (synergetic effect)	Martyak and Seefeldt, 2004
	MSA	DuPont™ ForaFac®	C^+ / FS	Inhibits Sn reduction Shifted hydrogen evolution reaction to more negative potential (suppresses H_2 evolution) Deposition potential remains the same indicating no complexes formed with Sn ions	Low and Walsh, 2008b
	Sulfuric Acid (SA)	Sintanol DS-10	N / PE	Inhibits Sn reduction Surface activity suppressed in halides (Cl^-, Br^-, I^-) containing solution	Survila et al., 2005
	Phenol Sulfonic Acid (PSA)	Ethoxylated α-Naphtholsulfonic Acid (ENSA)	A^- / HC	Inhibits Sn reduction at low concentrations Facilitates Sn reduction at high concentrations	Lee et al., 2004
Sn-Bi	SA	Poly Oxyethylene Lauryl Ether (POELE)	N / PE	Inhibits Bi deposition Suppresses H_2 evolution Produces smoothing effect on deposits	Fukuda et al., 2001
	Citric Acid (CA)	PEG 400	N / PE	Inhibits Bi deposition Suppresses H_2 evolution No significant influence on Sn deposition	Tsai et al., 2007
Sn-Cu	SA	Sintanol DS-10	N / PE	Inhibits Sn reduction over a wide range of potential No significant effect on Cu reduction	Survila et al., 2009
	MSA	DuPont™ ForaFac®	C^+ / FS	Shifted Cu deposition potential to more negative, Sn and Cu reduction potential closer Current density reduced at more noble potentials; Current density increased when potential more negative because potential high enough to allow movement of metal ions	Low and Walsh, 2008c
	SA	PEG 194-40000	N / PE	Current density falls drastically with increasing PEG molecular weight Formation of adsorption layer on Sn much more slower than on Cu	Survila, 2011
Sn-Ag	Pyrophosphate- Iodide (PI)	PEG 200-4000	N / PE	Inhibits preferential deposition of Ag PEG with higher molecular weight (4000) provides more coverage of active sites compared to PEG with low molecular weight (200)	Chen et al., 2008
	PI	Triton X-100 Sorbitol Sodium Gluconate	N / PE A^- / HC	Triton X-100- Suppress cathodic peak for SnAg co-deposition Sorbitol & Sodium Gluconate - Inhibition of current density at high negative potentials, slow down cationic diffusion to cathode	Neveu et al., 2006
	PI	PEG 600	N / PE	Inhibits preferential deposition of Ag Shift deposition potential of Sn in cathodic direction	Ventkatasamy et al., 2011
Sn-Ag-Cu	MSA	Iso-octyl phenoxy polyethoxy ethanol (OPPE) (Commercial name: Triton X-100)	N / PE	Links with metal ion to prevent precipitation, improve bath stability from 2 hrs to 1 week Reduce current density Refined, compact, and uniform microstructure	Joseph and Phatak, 2010
	SA	Poly Oxyethylene Lauryl Ether (POELE)	N / PE	Inhibits Sn reduction Suppresses H_2 evolution Produces smoothing effect on deposits	Fukuda et al., 2002

C^+: Cationic; A^-: Anionic; N: Nonionic; HC: hydrocarbon based; PE: polyether based; FS: fluorosurfactant

2.4.3.4 Grain refiners and brighteners

The properties of electrodeposited solder alloys are strongly related to their microstructure. In some cases of electroplating of Sn-containing solder alloys, the usage of surfactant alone could not produce smooth enough deposits (Joseph & Phatak, 2008, 2010). Dendritic or rough structures are still observed. To further improve the smoothness of the deposits, grain refiners may have to be added into the plating bath. Similar to surfactants, grain refiners are organic molecules that adsorb on surfaces to impair the surface activity and increase cathodic polarization (Suganuma, 2003; Tzeng, Lin, Wang, & Wan, 1996; J. Zhang et al., 2008). This results in increased nucleation rate and hence a reduction in grain size which lead to a smooth surface. Figure 2.18 shows a typical example of Sn-Ag-Cu deposition. Rough deposits are still seen with the addition of surfactant, iso-octyl phenoxy ethanol (OPPE) as shown in Figure 2.18(b). Upon the addition of gelatin as grain refiner, the grains are far more compact and fine with grain size ranging from 3-4 μm (Figure 2.18(c)). Examples of grain refiners used in Sn and Sn-alloy plating baths are gelatin, phenolphthalein, and β-naphthol (Joseph & Phatak, 2010; Martyak & Seefeldt, 2004; Sekar, Eagammai, & Jayakrishnan, 2010; Suganuma, 2003).

Surfactants and grain refiners only produce matte or satin bright finishes. To obtain a mirror bright finish, brighteners need to be added to the plating bath. Brighteners are aromatic ring-containing organic molecules that behave the same way as surfactants and grain refiners, with the exception that they are very much smaller in size (Suganuma, 2003). With larger surface areas, they can adsorb stronger on surfaces, thus able to further reduce the size of surface features to smaller than the wavelength of visible light (0.4-0.7 μm) so that light is not scattered or absorbed but reflected (Suganuma, 2003). Brighteners commonly used in the electrodeposition of Sn and Sn-

based alloys are benzaldehyde, formaldehyde, propionaldehyde, formalin, and heliotropin (Medvedev et al., 2003; A. Survila et al., 2009; Tzeng et al., 1996; J. Zhang et al., 2009; J. Zhang et al., 2008).

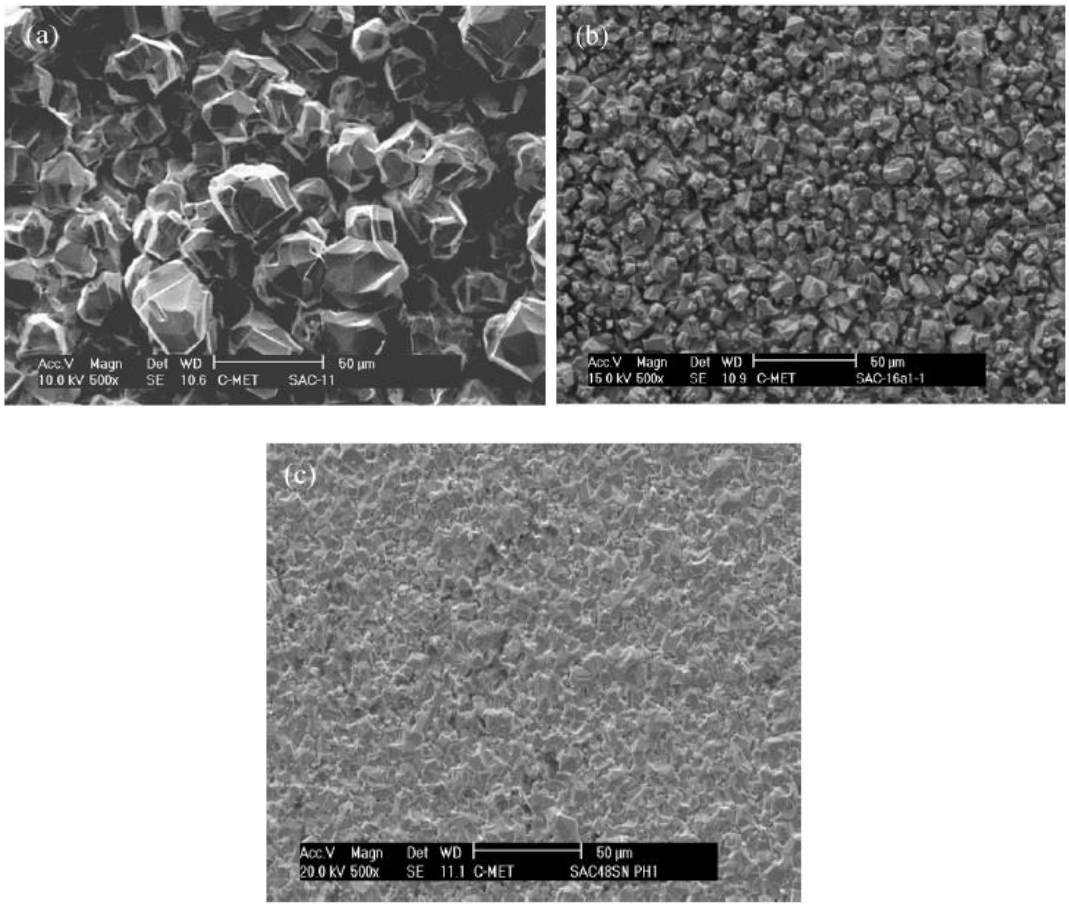

Figure 2.18 SEM micrographs of Sn-Ag-Cu deposited in thiourea-containing methane sulfonic acid bath: (a) without additives; (b) with OPPE; (c) with OPPE and gelatin (Joseph & Phatak, 2010).

However, the effects of brighteners are not significant when used alone in the plating bath. Thus their usage is always accompanied by the addition of other additives such as chelating agent, surfactants and grain refiners to give a synergistic effect (Medvedev et al., 2003; A. Survila et al., 2009; J. Zhang et al., 2009; J. Zhang et al., 2008). Zhang et al. (2008) demonstrated that triethanolamine (TEA) as a chelating agent for Cu, and heliotropin (HT) as a brightener, produce satisfactory fine-grained and bright deposits when used together rather than individually as shown in Figure 2.19(d).

Figure 2.19(b) shows that the addition of TEA results in compact deposits but with large grains of 7-12 μm in size. The addition of HT results in flat and fine grains of 3-8 μm in diameter but lack compactness and smoothness (Figure 2.19(c)). Combination of both additives gives desirable deposits that are smoother, more compact, and fine grained with sizes less than 1 μm.

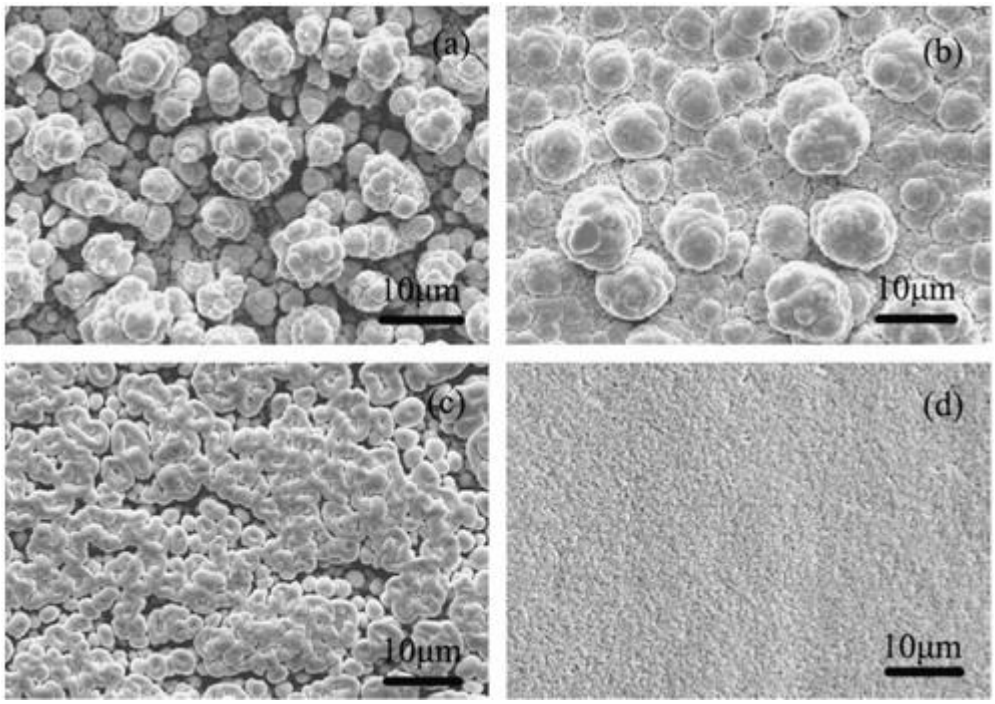

Figure 2.19 SEM micrographs of Sn-Ag-Cu deposited in pyrophosphate-iodide bath: (a) without additives; (b) with TEA; (c) with HT; (d) with TEA and HT (J. Zhang et al., 2008).

Due to the small molecule size of brighteners, they tend to be trapped in the deposits hence resulting in organic impurities. The organic elements exist can be carbon, nitrogen, sulfur, and oxygen. The gas compounds of the organic impurities may be released during soldering process and are detrimental to the properties of solder joints (J. Zhang et al., 2008). Investigations showed that bright deposits have much higher carbon content (0.05−0.4 wt%) compared with matte and satin bright deposits (0.001−0.005 wt%) (Suganuma, 2003; J. Zhang et al., 2008; Y. Zhang & Abys, 1999). Therefore, the

necessity of adding brighteners into plating baths should be considered and, in cases where they are added, thorough cleaning of the deposits with water is essential.

2.5 Solder joint formation and its strength

The electronic packaging industry is widely utilizing Sn-based alloys as interconnection materials. Hence, the interfacial reaction between Sn and the metallization layer is an essential process for metallurgical bond formation. The metallization typically used for solder interconnects is Cu, and is readily wet by Sn when the surface is oxide free. Intermetallic compounds (IMC) of Cu-Sn are generally formed by liquid-solid reactions and/or solid state diffusion, either during the soldering operation or during service. Excessive formation of Cu-Sn IMCs is not desirable as their brittle nature may bring adverse effects to the mechanical reliability of joints. This section discusses the IMC formation and the effects of IMC on shear strength of the solder joints.

2.5.1 Intermetallic compound (IMC) formation

When molten Sn-based solders come into contact with Cu surfaces, the joint is achieved by the interfacial reaction between Cu and Sn forming IMC (K. N. Tu & Thompson, 1982). According to thermodynamics (Figure 2.20), the first IMC phase to form at the interface is Cu_6Sn_5, and subsequently the second IMC phase Cu_3Sn is formed between Cu and Cu_6Sn_5. Since Cu_6Sn_5 phase is formed preferentially when in contact with molten solder, the morphology is irregular due to the liquid-solid reaction. While Cu_3Sn layer is rather planar, uniform and thinner, which reflects the solid state diffusion of Cu and/or Sn through the Cu_6Sn_5 layer. The morphology of IMC may differ for different Sn-based alloys due to different reaction kinetics.

The amount of IMC formed at the interface depends on the solubility of the solder elements in the base metal and also on the reflow time and temperature.

Intermetallics are formed in the body of the solder as it solidifies and as the base metal, dissolved in the molten solder, precipitates out. Subsequent growth of intermetallics during storage and operational service occurs through a solid-state diffusion process. The melting temperature of most solders is relatively low so that in general the operational temperature seen by the solder joint is a relatively high homologous temperature (T_o/T_m) which contributes to the rather rapid solid state reaction of tin and copper to form IMC, also resulting in low mechanical strength values and creep resistance.

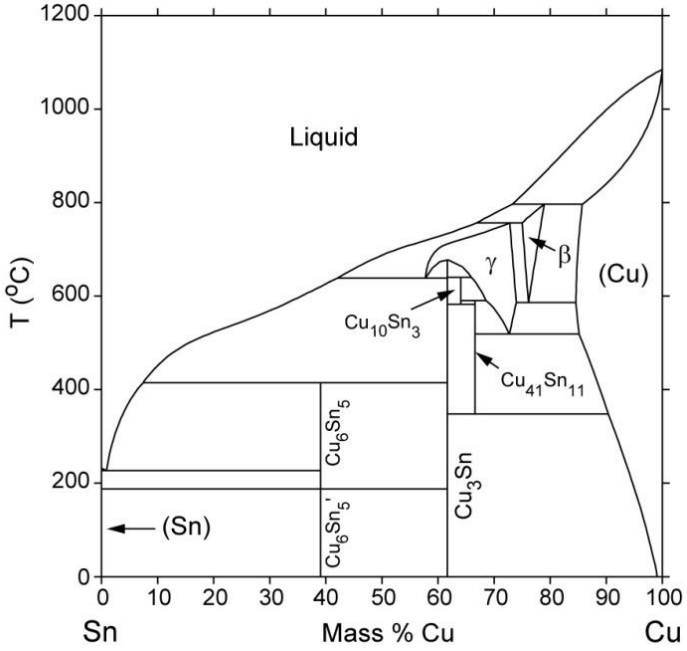

Figure 2.20 Cu-Sn binary phase diagram.

The formation and growth of IMC is an important factor which dictates the strength and lifespan of solder interconnections. Should the interconnections fail mechanically, the functionality of the electronic device may also be adversely affected. The relationship between IMC formation and the solder joint strength is the key issue to be indentified in order to understand the deformation behaviour of solder joints. The strengths of Sn-based solder joints are discussed in the next section.

2.5.2 Shear strength of Sn-based solder joints

Interconnections in electronic devices experience loads when in service or when under impact. The solder connections are prone to shear loading rather than tensile loading under most circumstances. Thus, the shear properties of solder materials determine the suitability of the material to be used in electronic packages. The mechanical properties of the solder joints are highly dependent on the solder composition, substrate material, flux, soldering conditions, joint geometry, and testing conditions (Miao, Duh, & Chiou, 2000; Tomlinson & Fullylove, 1992). Researchers came up with a few methods to simulate the loading conditions when the interconnections are in service, or experience external impact.

Investigation of thermal fatigue behaviour is one method to evaluate the strain induced when interconnections are in service. Solder joints are subjected to thermal shock, and the resultant shear strain is the sum of linear thermal expansion of the carrier substrate and the differential thermal expansion between the solder and carrier substrate (Sidhu & Chawla, 2008). Tu et al. (1997) conducted a thermal fatigue test on Sn-37Pb/ Cu solder joints. The reflowed specimens were subjected to thermal cycling between -35^{o}C to 125^{o}C with frequency of two cycles per hour until failure. It is reported that the thermal shock resulted in growth of IMC layer, and the lifetime of solder joints monotonically decrease with increasing IMC thickness. The authors claimed that the thickening and flattening of the IMC layers are less resistant to crack formation compared to prism-like IMC structures(P. L. Tu, Chan, & Lai, 1997). In another work, Sn-6Bi-2Ag-0.5Cu/Cu solder joints prepared by mechanical alloying were exposed to thermal shock environment of -25^{o}C to 125^{o}C for up to 1000 cycles (Huang, Wu, Lai, & Chan, 2000). These solder joints exhibited higher shear strength than Sn-37Pb and Sn-3.5Ag tested under the same conditions, probably due to the dispersion strengthening of

small Bi particles and fine Ag_3Sn phase present in the solder alloy. The shear strength of Sn-6Bi-2Ag-0.5Cu/Cu solder joints decreased with increasing thermal shock cycles due to the increasing number of voids which lead to crack initiation. The solder joints fail within the bulk solder and at the IMC/solder interface under all conditions (Huang et al., 2000).

Another widely utilized test method which also simulates real life loading of the solder joints would be the lap shear test. Testing at high strain rates can simulate impact loading, while at low strain rates simulate vibrational loading. Tomlinson and Fullylove (1992) measured the shear strengths of copper and brass lap joints soldered with six commercial Sn-based solders, at 20^{o}C and 100 ^{o}C, each with a strain rate of 0.05 and 50mm min^{-1}. The solders studied were pure Sn, Sn-1Cu, Sn-3.5Ag, Sn-5Sb, Sn-57Bi and Sn-2Ag-36Pb. Generally, Ag containing solders gave highest strength values, while Sn-57Bi solder showed good ductility but did not follow the general pattern of shear behaviour under different test conditions. The shear strength and deformation behaviour of Sn-3.5Ag/Cu lap joints were also studied by Deng et al. (2005). From both experimental and finite element analysis, the authors concluded that the shear strength of solder joints is controlled primarily by the solder strength rather than IMC thickness. However, IMC thickness determined the fracture mode of the joints (Schlesinger & Paunovic, 2010).

Recent interests in the Sn-58wt.%Bi alloy as potential solder material has prompted investigations on the soldered Sn-Bi joints. Suh et al. (2008) investigated the effects of intermetallic compound (IMC) growth on the shear strength of electrodeposited Sn-Bi solder joints. Aging period of less than 24h resulted in an increase in maximum shear stress because the prism-like IMC with high surface

roughness binds strongly to the bulk solder alloy, hence giving rise to shearing resistance at the solder/IMC interface. However as aging period increases, the maximum shear stress of the Sn-Bi solder joints decrease due to the increase in IMC thickness and flatness. Tomlinson and Fullylove (1992) found out that at room temperature and low strain rate, the shear strength of Sn-57Bi solder is comparable to that of Sn-3.5Ag and Sn-5Sb solders. However, at 100^{o}C and high strain rate, the shear properties of Sn-57Bi solder deteriorates. Raeder et al. (1994) found that the shear strength of Sn-Bi/Cu solder joints is similar to that of Sn-Pb. It is also reported in the same work that an aging period of 30 days results in stratification of Bi-rich phase at the interface, which in turn increases the strength of the solder joints. In the as-reflowed joints, fracture occurs through separation of the IMC/Sn-rich phase. After aging, Bi-rich phase formed at the solder/IMC interface upon consumption of Sn during IMC growth. In the aged samples, fracture occurs by cleavage through the Bi-rich phase, resulting in an increase in joint strength and ductility. The Bi stratification effect was also observed when Bi is added to Sn-Ag-Cu solders (Zhao, Cheng, Qi, & Chi, 2009). Zhao et al. (2009) suggested that the Bi stratification suppressed the diffusion of Cu hence retarding IMC growth.

2.6 Summary

With the emphasis to stamp out Pb from electronic components and devices, Sn-Pb alloy can no longer be used as a solder material. Aggressive research on Pb-free solder alloys have been conducted. In earlier studies, research focuses very strongly on Sn-Ag-Cu ternary alloy, where the alloy offers superior mechanical properties compared to Pb-bearing alloys. However, the melting range of this alloy is 217-227^{o}C and this temperature is considered too high for devices prone to thermal damage. The eutectic Sn-58Bi alloy is also suggested to be one of the promising lead-free substitution

candidates by the International Electronics Manufacturing Initiative (iNEMI). This is attributed mainly to the low melting point of this solder alloy (138^{o}C), which makes it suitable for low temperature soldering of heat sensitive components. This alloy was not of interest when the Pb-free concept was first introduced. Because during the transition from Sn-Pb to Pb-free solders, there would still be Pb contaminants in existing production lines. Sn-Bi can form a very brittle ternary compound with Pb, having a very low melting point of 96^{o}C. Above this temperature, the ternary compound melts and leads to joint failure. But as the Pb-free concept is now established, Sn-58Bi alloy is worth studying for heat sensitive applications.

Besides selection of a good solder material, suitable solder deposition technique is also required to cost-effectively mass produce the alloy of interest. The recent trend in the electronics world is miniaturization, lightweight, and multifunctional. This requires encapsulation of maximum interconnections in minimum space. Electrodeposition is the best technique available to produce fine geometry solder interconnections. Coupled with the photolithography process, the electrodeposition technique can produce fine pitch solder bumps of any arrays, and theoretically no pitch limitations.

Unfortunately, the main issues with electrodeposition of Pb-free solder alloys is the large deposition potential gap between Sn and potential Pb-free substituition elements. Composition control of the solder alloys is hard to achieve. Also, to take into account of the compatibility with photolithography process, acidic plating baths are preferred. Sn^{2+} ions are prone to oxidize to Sn^{4+} ions in acidic bath, and then precipitate as stannic compounds. The two issues mentioned above can seriously affect the efficiency and applicability of the electrodeposition technique. The usage of electrolyte additives such as antioxidants, chelating agents or surfactants may alleviate

electrodeposition issues. However, with uncountable organic and inorganic electrolyte additives available, it is also a tough task to select which additive may be suitable for a certain plating bath. Screening trials such as some preliminary polarization studies have to be done for the selection of additives. The additive should also be easily available and less costly in order to fulfil economical aspects.

In addition to the development of a plating bath for the co-deposition of Sn-Bi alloys, the shear properties of the electroplated solder joints should also gain considerable focus. Solder joints are subjected to thermal and mechanical loading during service. The lap-shear tests are widely used to investigate the shear, creep and thermal fatigue behaviour of solder joints, as the deformation mode simulates the real life loading of the interconnections. Intermetallic compounds (IMC) formed at the solder/substrate interface can highly affect the strength and fracture mode of the solder joints. To better understand the shear and deformation behaviour of Sn-Bi/Cu solder joints, the interrelationships between IMC formation, shear strength and fracture mode of the solder joints are of great interest.

CHAPTER 3

ELECTROCHEMICAL STUDIES ON SN-BI ALLOY DEPOSITION

3.1 Background

A number of baths have been developed for the electrodeposition of Sn and Sn-based Pb-free solder alloys as discussed in the previous chapter. For the electrodeposition of Sn-Bi alloys, most of the plating baths are acidic as can be seen in the summary in Table 2.2 (***Section 2.4.2.1***). Such acidic solutions are also chemically compatible with the photoresist masked substrates, which fulfils the demand for fine geometry electrodeposition. Tsai et al. (2007) developed a citric acid based plating bath with ethylenediaminetetraacetic acid (EDTA) and polyethylene glycol (PEG, MW400) as complexing agents. The synergistic effects between these additives were found to improve the adhesion and suppress dendrite formation. Dendrite-free 30Sn-70Bi electrodeposits with good adhesion were successfully deposited from this plating bath. The authors further optimized the electroplating parameters, by making the following amendments in their later work (Tsai & Hu, 2009b):

1) Changing the Sn metal salt from $SnCl_4 \cdot nH_2O$ (Sn^{4+}) to $SnCl_2 \cdot n$H2O (Sn^{2+});

2) Increasing the concentration of Sn from 0.1M to 0.15M;

3) Reducing the concentration of Bi from 0.1M to 0.05M;

4) Reducing the concentration of citric acid from 0.4M to 0.3M;

5) Reducing the concentration of EDTA from 0.1M to 0.05M;

6) Changing the pH of the plating bath from pH 6.0 to pH 2.0; and

7) Reducing the current density from 100 mA cm^{-2} to 20 mA cm^{-2}.

This optimization resulted in the electrodeposition of near eutectic 44Sn-56Bi electrodeposits.

Methane sulfonic acid (MSA) is another medium studied by a number of researchers for the electrodeposition of Sn-Bi alloys (Y.-G. Lee et al., 2011; M.-S. Suh et al., 2006). In general, MSA is much less toxic than many other acids such as fluoroboric and fluorosilicic acid. Also, MSA offers benefits such as good metal salt solubility, good conductivity, and readily biodegradable compared to nitric acid and acetic acid (Gernon, Wu, Buszta, & Janney, 1999). From the reports available, eutectic Sn-Bi electrodeposits can be obtained when commercial electroplating additives are used in the MSA bath. Suh et al. (2006) included a commercial additive (Talin HSM 96) in their plating bath, and varied a few plating parameters such as Sn concentration, pulsed current frequency and duty cycle to obtain Sn-Bi electrodeposits of varying composition. Eutectic Sn-Bi alloy was obtained at a current density of 4A dm^{-2} (40mA cm^{-2}) when the Sn content of the plating bath was 25.3wt.%. Sn content in the deposit increased with increasing pulse frequency and decreasing duty cycle. In addition, the Sn–Bi deposits became finer with decreasing pulse frequency and increasing duty cycle. Lee et al. (2011) did not reveal the name or nature of the electroplating additive they used. From the polarization curve recorded in their plating bath, it is seen that from −0.07 V to −0.45 V, Bi deposition is the dominating reaction, while beyond −0.5V, Sn-Bi co-deposition took place.

The benign nature of MSA makes it a promising electroplating medium for the electrodeposition of eutectic Sn-Bi alloys. The main objective of this study is to develop a simple MSA-based plating bath. The key target is to utilize non-commercial and easily available additives, and also minimize the number of additives to develop a plating bath as environmentally benign as possible. To meet this goal, a number of commonly used organic additives were selected and screened beforehand. Finally,

hydroquinone (HQ) and gelatin turned out to be potential candidates to improve the quality of plating bath and electrodeposits. The primary function of HQ is to inhibit Sn^{2+} oxidation. It is reported that HQ can retain 48 g/L out of 50 g/L of Sn^{2+} in a MSA-based plating bath (Schlesinger & Paunovic, 2010). Gelatin, a widely utilized leveling and grain refining agent in electrodeposition of metals and alloys, is known to improve the morphology of deposits through adsorption onto active growth sites (Brown & Hope, 1995; Joseph & Phatak, 2010; Lien, Hu, Tsai, & Shan-Hill Wang, 2012; Sekar et al., 2010; Tsai et al., 2011). The individual and synergistic effects of HQ and gelatin on the polarization behavior of the Sn-Bi plating solution were studied.

3.2 Experimental

Prior to the electrochemical analysis of plating baths, trial screenings of the effects of additives were performed. An additive was chosen from each category of electrolyte additives mentioned in ***Section 2.4.3*** for the screening test. Based on literatures, ethylenediamine-tetraacetic acid (EDTA), hydroquinone (HQ) polyethylene glycol (PEG, MW 400), and gelatin were selected for the screening potentiodynamic studies. Preliminary results of polarization scans suggested that incorporation of HQ and gelatin have higher potential of altering the deposition behaviour of Sn-Bi. Thus the effects of only these two additives were studied in this work. More details of the screening tests were presented in the results section.

The composition of the MSA-based plating bath developed is shown in Table 3.1, which mainly consisted $SnSO_4$ and Bi_2O_3 with HQ and gelatin as additives. When the individual effects of the metal ions or additives were investigated, the other constituents were omitted and the concentration remains. The solutions were prepared at room temperature with 300ml of distilled water, where MSA was first added to the

water. The acid solution was magnetically stirred at 80rpm, while other constituents were added sequentially to the solution with intervals of 15 mins to allow complete dissolution of the chemicals.

Table 3.1 Electroplating bath constituents for polarization studies and electrodeposition of Sn-Bi alloys.

Chemicals	Concentration
Methane sulfonic acid (CH_3SO_3H) (99.5%, Sigma Aldrich, USA)	120 ml/L
Tin sulfate ($SnSO_4$) (95-98%, R&M Chemicals, UK)	30 g/L
Bismuth oxide (Bi_2O_3) (99%, R&M Chemicals, UK)	9 g/L
Hydroquinone (95-98%, R&M Chemicals, UK)	5 g/L
Gelatin (R&M Chemicals, UK)	2 g/L

Electrochemical polarization studies of the plating solutions were performed at room temperature with a potentio/galvanostat, PC14/300 (Gamry Instruments). All plating solutions were filtered prior to the studies which were carried out in a single-compartment cell. The volume of the plating solution was kept at 300ml. The working electrode was 0.3mm thick Cu sheet, degreased with soap water, etched with 10% sulfuric acid for 20 s and rinsed thoroughly with distilled water. The Cu sheets were covered with insulation tape with an area of 1 cm^2 exposed. Pt wire served as the counter electrode. A Ag/AgCl electrode was utilized as the reference electrode. The reference electrode was placed in a Luggin capillary to minimize errors due to IR drop across the electrolyte.

3.3 Results and discussion

3.3.1 Screening tests for additive selection

Referring to the standard redox potentials of Sn and Bi (Figure 2.8), it is known that Bi is the more electropositive element and Sn is the more electronegative element. To significantly reduce the deposition potential gap between the elements, chelating or complexing of the more electropositive element (Bi in this case) is essential to shift the electrode potential to more electronegative values. A preliminary screening test is performed to select the suitable additives to alter the deposition potential of Bi. As mentioned in the literature review, electrolyte additives can be categorized into 1) chelating (complexing) agents; 2) antioxidants (oxidation inhibitors); 3) surfactants (surface-active agents); and 4) grain refiners and brighteners (***Section 2.4.3***). Based on the local availability and past literature, one additive is selected from each category for screening purpose. Ethylenediamine-tetraacetic acid (EDTA) is selected as chelating (complexing agent), hydroquinone (HQ) as antioxidant, polyethylene glycol (PEG) as surfactant, and gelatin as grain refiner.

Figure 3.1 shows the polarization curves of Bi-MSA solutions, where the effects of the individual additives are studied. An inset diagram near the deposition potential of Bi is provided. It can be seen that all of the additives shifted the deposition potential of Bi to more electronegative values. However, the addition of HQ (curve (d), Figure 3.1) and gelatin (curve (e), Figure 3.1) demonstrated a greater shift, compared to PEG (curve (a), Figure 3.1) and EDTA (curve (b), Figure 3.1). When the electrode potential is polarized to more negative than -500mV, the abrupt rise in current density is attributed to hydrogen evolution reaction (will be explained in latter sections). It is also obvious that both HQ and gelatin have the ability to suppress the undesirable hydrogen evolution reaction to more electronegative potentials, where the increase in current density takes

place beyond -700 mV (curve (d) and (e), Figure 3.1). Therefore, only HQ and gelatin are selected for further electrochemical studies of Sn-Bi plating baths.

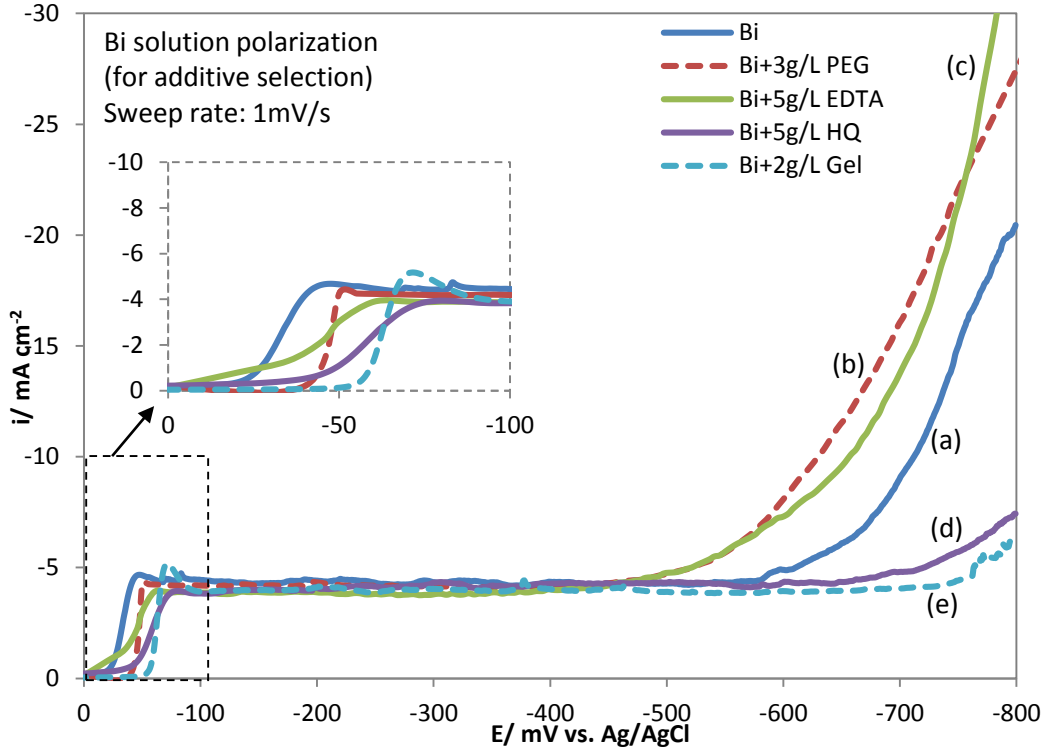

Figure 3.1 Polarization curves for Bi-MSA solutions (a) without additives, (b) with 3g/L PEG, (c) with 5g/L EDTA, (d) with 5g/L HQ, and (e) with 2g/L gelatin.

3.3.2 Polarization studies in Sn-MSA solution

The potentiodynamic method with a sweep rate of 1 mV/s is used to study the polarization behaviour of Sn in methanesulfonic acid (MSA) solution. The bath contained 120 ml/L of MSA and 30 g/L of $SnSO_4$. In the plating bath without additives, no reactions were observed at potentials from the open circuit potential (OCP) of this solution up to −430 mV (curve (a), Figure 3.2). At −430 mV, an abrupt increase in current density to a value of about −12.5 mA cm^{-2} is observed prior to a change in slope. The current density increases at a much slower pace as the potential approaches −490 mV. The current density again increases abruptly to very high values, accompanied by aggressive gas evolution at the electrode surface.

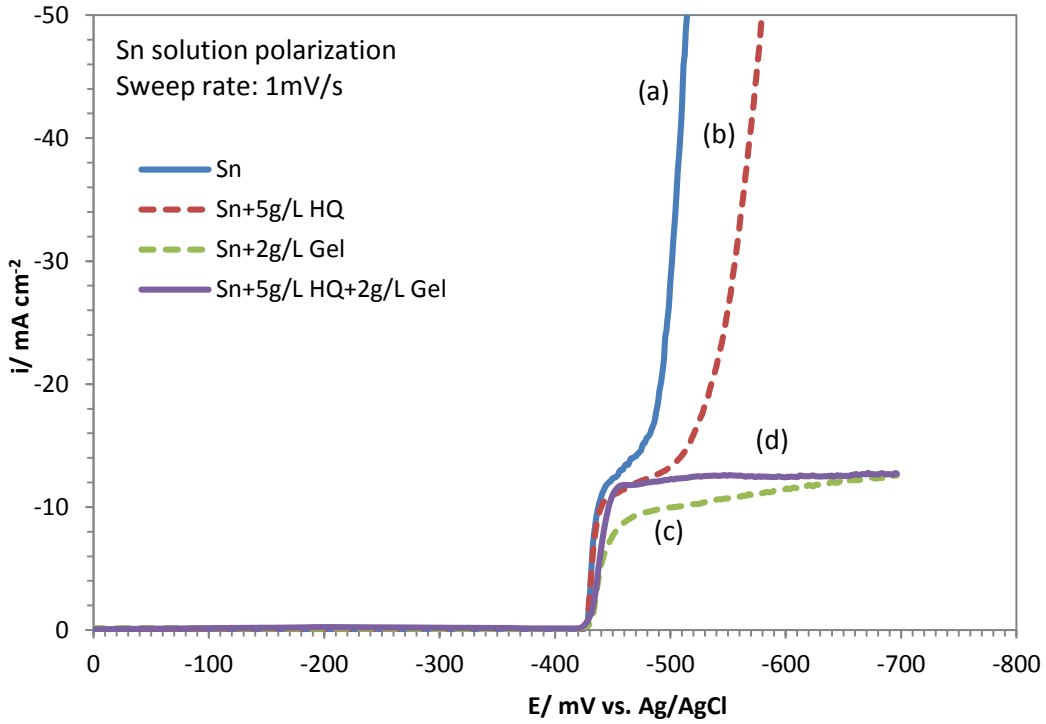

Figure 3.2 Polarization curves for Sn-MSA solutions (a) without additives, (b) with HQ, (c) with gelatin, (d) with HQ and gelatin.

When potential is applied to the cathode, the current density response of the solution is recorded. Metal ions migrate to the surface of cathode under the influence of attractive charges. An increase in the potential causes the number of ions discharged to increase with unit time. The maximum current density is associated with the complete consumption of metal ions at the cathode surface (Low & Walsh, 2008b, 2008c; Neveu et al., 2006). The concentration difference between the cathode and the bulk solution increases, therefore the rate of diffusion of ions increases. Finally it may occur that the ions are discharged and deposited immediately upon arrival at the cathode surface. With further increase of potential, the current density cannot increase further because the number of ions discharged is determined by the diffusion rate (Raub & Müller, 1967). This will result in a plateau in the polarization curve, and the plateau current density value is termed as the limiting current density, i_L. This value can only be exceeded when another cathodic reaction has been reached, such as discharge of other ionic species or hydrogen discharge. A decrease or drop in current density may also occur after the

maximum current density when the mass transfer of ions in the plating bath is unable to replenish the ions at a rate sufficient to keep up with the reduction rate of ions (Martyak & Seefeldt, 2004).

As has been observed, Sn deposition starts at about −430 mV in the MSA-Sn solution used in this study. The deposition process is slightly limited by diffusion rate of Sn^{2+} ions up to −490 mV, and then discharge and desorption of hydrogen from the metal surface takes place simultaneously with stannous reduction. There is no obvious i_L plateau observed for this MSA-Sn solution because the diffusion-limited Sn deposition process is rapidly replaced by the hydrogen evolution reaction. The co-deposition of hydrogen has great influence on the deposition mechanism and properties of the electrodeposits. The discharge and incorporation of hydrogen into metal deposits can be a main cause of pores in electrodeposits. Such adhering hydrogen bubbles may also screen the underlying metal from the applied current so that the deposits only grows slowly, thus producing depressions or pits in the surface. Although other gases adhering to the cathode can also cause such defects but cathodically discharged hydrogen is usually responsible (Raub & Müller, 1967). The discharge reaction of hydrogen also lowers the overall current efficiency (Tan, 1993). Thus, the suppression of hydrogen discharge is a must to ensure high efficiency electrodeposition and metal deposits of superior quality.

The addition of HQ to the MSA-Sn solution resulted in a slight decrease in the diffusion-limited current density and a delay in occurrence of the high current density "tail" (curve (b), Figure 3.2). The decrease in diffusion-limited current density with HQ addition is suggested to be caused by the adsorption of HQ on electrode surface, resulting in a reduced surface activity. Such a reduction in current brought about by HQ

has been observed earlier during Sn deposition (Low & Walsh, 2008c). Similar observations was also made for surfactants like polyoxyethylenelaurylether (POELE) (Mitsunobu Fukuda et al., 2002) and iso-octyl phenoxy polyethoxy ethanol (OPPE) (Joseph & Phatak, 2008) during Sn-Ag-Cu deposition. The adsorption effect is further confirmed by the suppression of the hydrogen evolution "tail" by HQ where the reaction is postponed to a more electronegative potential of about −500 mV. It is reported that HQ and similar quinone compounds are capable of adsorbing to metal electrodes through different modes, e.g. flat or edgewise chemisorption (Hou, Han, Niu, & Lin, 2006; Soriaga, White, Song, & Hubbard, 1984). The schematic adsorption pattern is shown in Figure 3.3. The adsorption orientation is dependent on many factors such as pH value, adsorbate concentration, temperature, electrode potential and surface atom orientation. These factors also influence one another and affect the electron transfer (Hou et al., 2006). The flat adsorption of HQ will result in a higher blocking area than edgewise adsorption. Judging from the mild decrease in current density, HQ adsorption in the MSA-Sn solution may be of edgewise adsorption.

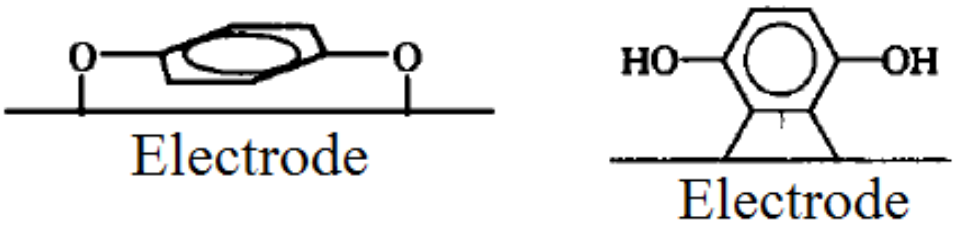

(a) (b)

Figure 3.3 Adsorbed hydroquinone (HQ) molecules with (a) flat orientation and (b) edgewise orientation (Hou et al., 2006).

Upon the addition of 2 g/L of gelatin to the Sn-MSA plating bath, the current density at the deposition potential of Sn has been lowered to about −6.5 mA cm^{-2} with respect to the plating bath without additives. The current density then increases slowly to −12.5 mA cm^{-2} with increasing cathodic polarization (curve (c), Figure 3.2). This

indicates that gelatin has a strong adsorption effect on Sn deposition thus slowing down the deposition rate. The adsorption effect is also evident with the suppression of hydrogen evolution. The general structure of a gelatin molecule comprised of a series of different amino acids linked by peptide bonds. A representative molecular structure is shown in Figure 3.4, but the actual molecular arrangement and amino acid type depends strongly on the source of gelatin. Since there are numerous organic ring compounds available for adsorption in the gelatin molecule, the coverage area is much higher than HQ. Gelatin thus impedes electron transfer at the electrode surface to a greater extent (Brown & Hope, 1995; Meudre et al., 2014). With both HQ and gelatin added to the Sn plating solution, the current density at the deposition potential is close to that of the case when only HQ is added (curve (d), Figure 3.2). The suppression of current density at the deposition potential by gelatin addition alone is no longer observed. This implies that the combination of HQ and gelatin has increased the amount of Sn ions to be deposited near the cathode surface. The suppression of hydrogen evolution is still observed, indicating that a strong adsorption effect of gelatin still takes place. With both additives incorporated in the plating bath, the limiting current density plateau of Sn deposition is observed to be around −12.0 mA cm^{-2}. With further increase of potential, the current density cannot increase further because the number of ions being discharged is determined exclusively by the diffusion rate. The limiting current density can only be exceeded when the potential of another cathodic reaction has been reached, such as that of hydrogen discharge.

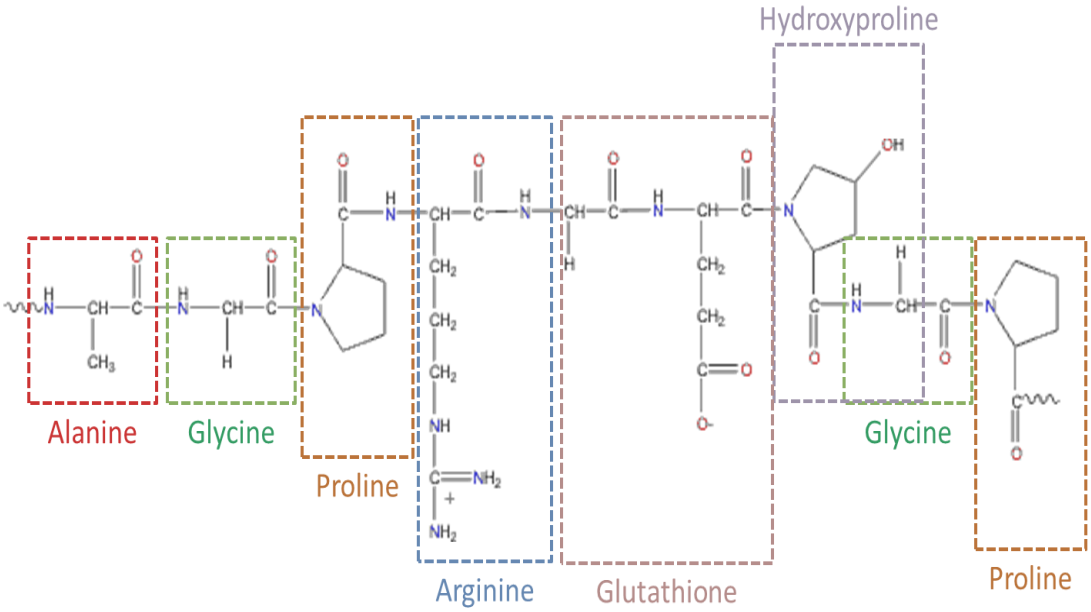

Figure 3.4 Representative structure of gelatin (Spray Drying of Blood and Gelatin (Animal), GEA Process Engineering Inc. website, Retrieved 08 March 2014, from http://www.niroinc.com/food_chemical/spray_drying_gelatin.asp).

3.3.3 Polarization studies in Bi-MSA solution

This plating bath contains 120 ml/L of MSA, 9 g/L of Bi_2O_3, and optional addition of 5 g/L of HQ and 2g/L of gelatin. Polarization studies show that without additives, the nucleation process of Bi ions initiates at about −20 mV (curve (a), Figure 3.5). The reduction peak of Bi is seen at −36 mV, with peak current density of −4.5 mA cm^{-2}. The limiting current density plateau extends to a large potential range. Thereafter, hydrogen evolution initiates at about −600 mV, which is more electronegative compared to the Sn plating bath. In polarization studies, the metal ions in the plating bath will be deposited when the deposition potential of the metal is achieved. The cathode which is initially the substrate material, will behave like the deposited metal for potentials more electronegative than the deposition potential. This is why the hydrogen discharge potentials in Sn and Bi solutions are different. Bi has a higher hydrogen overvoltage compared to Sn (Raub & Müller, 1967).

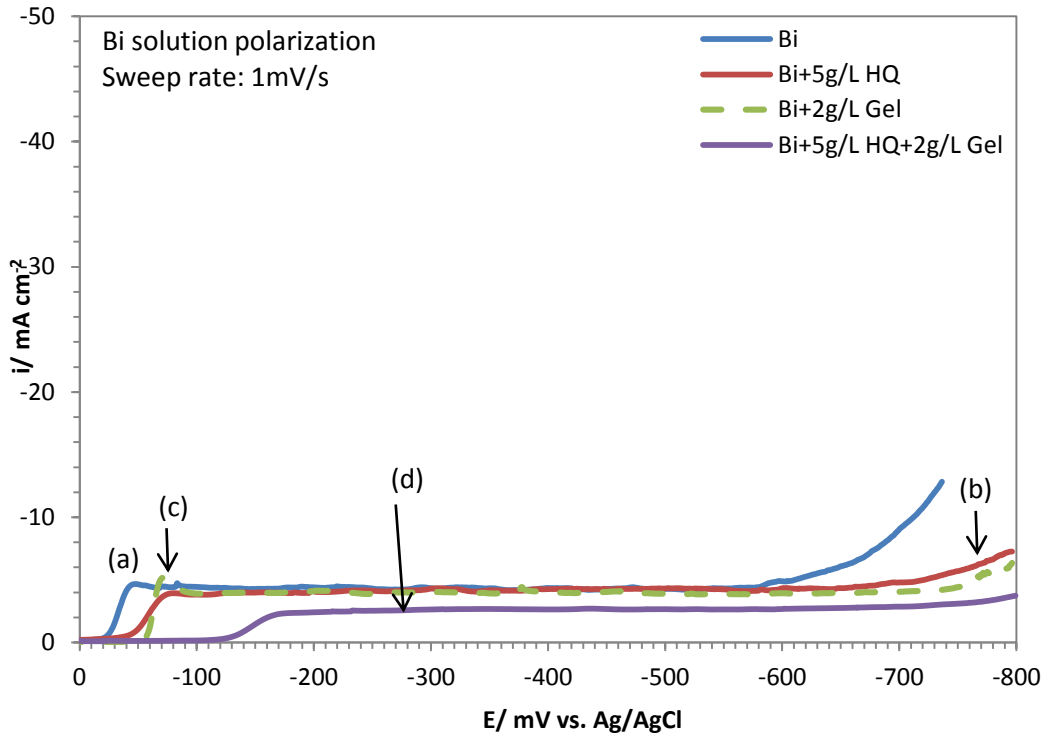

Figure 3.5 Polarization curves for Bi-MSA solutions (a) without additives, (b) with HQ, (c) with gelatin, (d) with HQ and gelatin.

The initiation of Bi deposition shifts to a potential of −40 mV when HQ is added to the plating bath, as seen in curve (b) of Figure 3.5. It is reported that HQ is capable of forming complexes with metal ions such as Sn^{2+}, and prevents the oxidation of the metal species (Schlesinger & Paunovic, 2010). In this Bi-MSA-HQ solution, the shift in deposition potential of Bi may suggest that there is a complexation reaction happening between HQ and Bi ions (Schlesinger & Paunovic, 2010). The Bi(III) ion has a $d^{10}s^2$ electron configuration with a lone s^2 electron pair. In aqueous solution, the hydrated Bi(III) ions are eight-coordinate in a distorted square antiprismatic fashion as shown in Figure 3.6(a). Although Sn(II) ion has $d^{10}s^2$ electron configuration as well, the lone s^2 electron pair occupies nearly half the sphere of the ion. The water molecule attached to the trans position to the lone pair is more strongly coordinated than the other four water molecules in the equatorial plane. The hydrated Sn(II) ion then has a stereochemically active electron pair as shown in Figure 3.6(b) (Persson, 2010). The high tendency for Bi(III) to hydrolyze can be an indication of the ease of these ions to form complexes

when additives with donor atoms present in aqueous solution (Stavila et al., 2006). The minor shift in deposition potential (about 30mV) suggests that these complexes have rather low stability and decomposes with slight increase in electrode potential. The hydrogen evolution reaction is also seen to be suppressed with addition of HQ, where an increase in current density is observed only after −700 mV. This implies that HQ also serves as an adsorption agent on the substrate in the Bi-MSA plating bath. Curve (c) of Figure 3.5 illustrates that the deposition behavior of Bi when gelatin is introduced to the bath is very similar to that of Bi-MSA-HQ plating bath. Gelatin is also suggested to impose mild complexing effect on Bi ions and adsorbs on electrode surface.

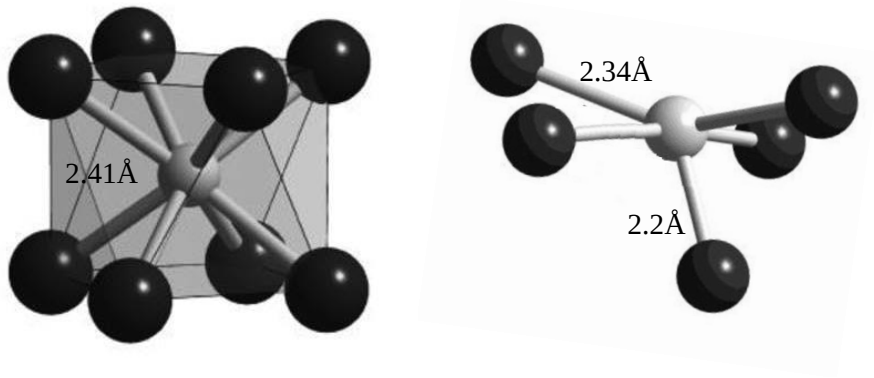

Figure 3.6 (a) Square antiprism structure of hydrated Bi(III) ions, holo-directed; and (b) irregular structure of hydrated Sn(II) ions, hemi-directed (Persson, 2010).

When both HQ and gelatin is added to the Bi-MSA solution, a huge shift in deposition potential is observed (curve (d), Figure 3.5). Deposition initiates at about −130 mV, and reaches the limiting current density at about −170 mV. Limiting current density of Bi deposition is reduced to −2.5 mA cm^{-2}. The increased number of donor atoms of ligands and the increased number of chelating rings formed usually results in higher complex stability (Stavila et al., 2006). Ion complexes with higher stability usually have deposition potentials polarized to more electronegative direction and lower

limiting current density due to the change in deposition behaviors of ions. The main reason is the slower reaction rate of complex ions discharge, where the complexes have to be decomposed into components before the ions can be discharged (Raub & Müller, 1967). With both HQ and gelatin present in the plating bath, increased number of donor atoms of ligands has imposed a stronger complexing effect, which is evident by the huge leap in deposition potential. The synergistic complexing effect of HQ and gelatin has successfully shifted the deposition potential of Bi much closer to that of Sn (Refer to curve (d), Figure 3.2). This shift is desirable because co-deposition of Sn-Bi alloy can only be achieved when their deposition potentials are near.

3.3.4 Polarization studies in Sn-Bi-MSA solution

The polarization curves of Sn and Bi allow the understanding of deposition behaviour of individual metal ions in the MSA-based plating solution. However, these do not represent the actual deposition behaviour when both ions are present simultaneously in a single plating bath. Figure 3.7 depicts the polarization curves for Sn-Bi plating solutions, with and without additives. Without additives, the potential gap between the two elements is 429 mV (curve (a), Figure 3.7). There is difficulty for co-deposition of alloys to commence if the reduction potential difference is not within 200 mV (Schlesinger & Paunovic, 2010). The addition of HQ is expected to reduce the potential gap between the two elements, judging from the negative shift of Bi reduction potential (curve (b), Figure 3.5). However, the addition of HQ into the plating bath does not shift the deposition potential of Bi ions in this bimetallic plating solution, as seen in curve (b) of Figure 3.7. It is observed that the addition of HQ has a more pronounced effect on the deposition behaviour of Sn, where the deposition current density is suppressed and the hydrogen discharge reaction has been polarized to more electronegative potentials. It may be suggested that when both metal ions are present in

the plating bath, HQ preferentially suppresses the deposition current density of Sn and hydrogen evolution, rather than shifting the deposition potential of Bi.

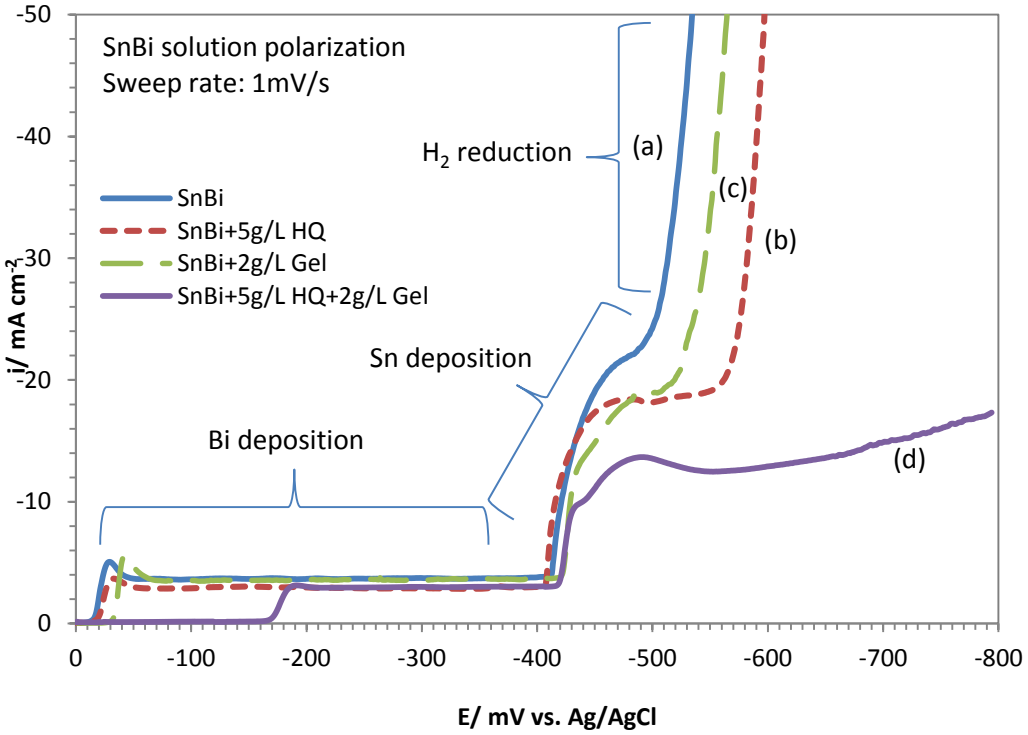

Figure 3.7 Polarization curves for Sn-Bi-MSA solutions (a) without additives, (b) with HQ, (c) with gelatin, (d) with HQ and gelatin.

A different trend is observed when gelatin is added to the Sn-Bi bimetallic plating bath (curve (c), Figure 3.7). The strong suppression of current density and hydrogen evolution by gelatin observed in Sn plating bath (curve (c), Figure 3.2) is no longer observed in the Sn-Bi plating bath. On the other hand, the mild shift in deposition potential of Bi still exists. This suggests that in the Sn-Bi bimetallic bath, HQ tends to modify the deposition behaviour of Sn, while gelatin tends to modify the deposition behaviour of Bi.

When both HQ and gelatin are added to the plating bath, there is a substantial reduction in the potential gap (curve (d), Figure 3.7). The potential difference between the deposition peaks of the elements has been decreased to 255 mV. This trend has

already observed in the Bi-MSA solution where synergistic effects of HQ and gelatin have shifted the deposition potential of Bi to a more electronegative potential (curve (d), Figure 3.5). Huge shift in deposition potential of Bi and strong suppression in current densities are observed in this bimetallic plating bath with both HQ and gelatin as additives. HQ is suggested to serve as adsorption agent in this bimetallic plating bath, probably adsorbing in flat orientation as strong suppression of hydrogen evolution is observed (Hou et al., 2006). In addition, there are numerous amide nitrogen atoms in gelatin available for both adsorption on electrode surface and complexation with metal ions (Brown & Hope, 1995). The reduced deposition potential gap between two elements suggests that co-deposition of alloy is possible in this plating bath with both additives incorporated (Mitsunobu Fukuda et al., 2002; Schlesinger & Paunovic, 2010). More effective suppression of hydrogen evolution reaction also indicates that this combination of additives is capable of hindering the electrode surface activity, thus reducing active sites for Sn and Bi deposition. With this, uniform and compact alloy deposits are expected from this plating bath.

3.3.5 Effects of agitation

The polarization curves in the previous section were obtained under the condition where the solution was static, or unstirred. In that way, the behaviour of metal ions could be predicted more accurately. However in practical applications, agitation of solution or rotation of electrode has to be applied in order to increase the diffusion rate of ions and to ensure uniform deposition (Raub & Müller, 1967; Schlesinger & Paunovic, 2010; Tan, 1993). The effects of agitation of Sn solution are studied and polarization curves are presented in Figure 3.8. Magnetic stirring of 80rpm is applied to the 300ml solution. From curve (b) of Figure 3.8, it is observed that the limiting current plateau for Sn deposition is no longer observed when the solution is agitated. The

agitation of solution has also promoted the hydrogen discharge reaction to take place at a more noble electrode potential.

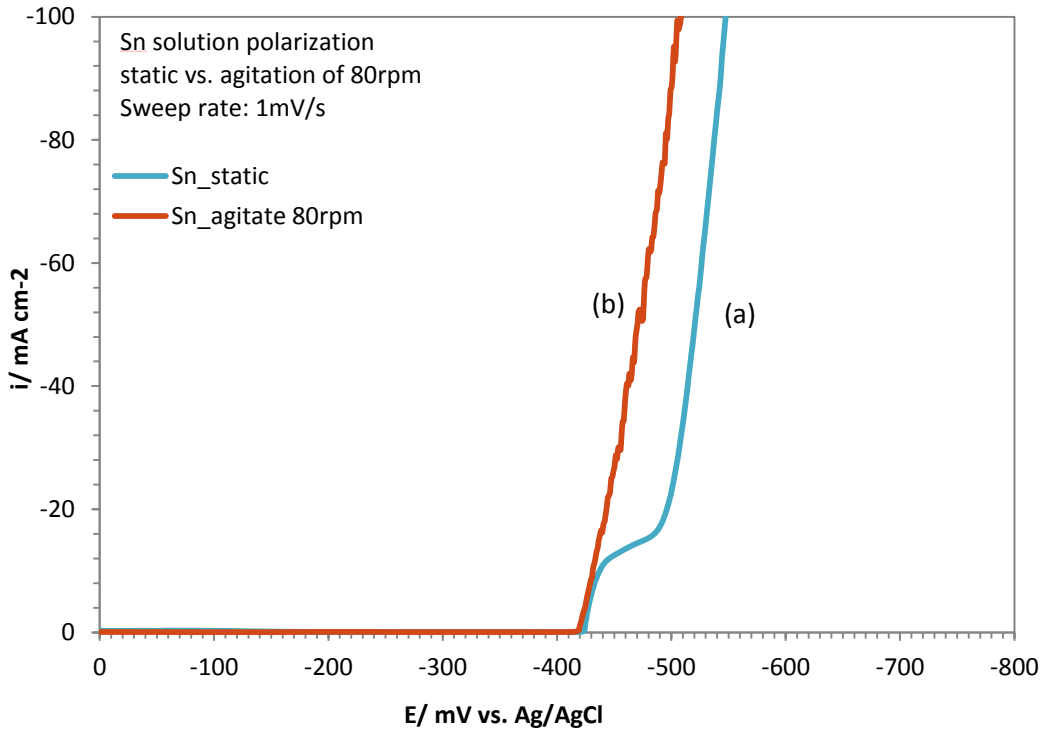

Figure 3.8 Polarization curves for Sn solution under (a) static and (b) agitation of 80rpm.

The cathodic hydrogen discharge in acid solutions can be resolved into the following partial reactions (Raub & Müller, 1967):

(a) Transport of hydrogen ions to double layer,

(b) Discharge of hydrogen ion at electrode through acceptance of electron where Volmer reaction takes place (i.e. transition from solvation bond (solv) to adsorption bond (ad)):

$$H^{+}_{solv} + e^{-} \rightarrow H_{ad} \qquad (3\text{-}1)$$

(c) Formation of molecular hydrogen H_2 on the cathode surface with retention of adsorption bond, and this step can proceed through the Tafel reaction:

$$H_{ad} + H_{ad} \rightarrow H_{2,ad} \qquad (3\text{-}2)$$

or the Heyrovsky reaction:

$$H^+_{solv} + H_{ad} + e^- \rightarrow H_{2,ad} \quad (3\text{-}3)$$

(d) Desorption of the adsorbed hydrogen molecule $H_{2,ad}$ from the cathode surface,

(e) Removal of the molecular hydrogen H_2 by diffusion within the solution or as gaseous hydrogen.

The polarization of hydrogen, like all polarization process, varies with the operation conditions. It is dependent on factors like temperature, cathode metal, hydrogen pressure, pH and composition of electrolyte. The transport process to the double layer (step (a)) is of no significance because abundant hydrogen ions are available in aqueous solution. The main governing factors of hydrogen deposition would be the discharge reactions enumerated under (b) and (c). Generally, in quiescent electrolytes, hydrogen discharge takes place through the Volmer reaction (Equation 3-1) and then the Tafel reaction (Equation 3-2). However when agitation is applied, the mechanism of hydrogen discharge may take place through the Heyrovsky reaction (Equation 3-3) which then affects the hydrogen polarization behaviour.

Another possibility for the alteration of hydrogen polarization behaviour would be the effects of cathode surface material. Under quiescent conditions, the deposition of Sn takes place at about -430 mV (Figure 3.8(a)). The cathode, originally a Cu substrate, then behaves like a Sn substrate for potentials beyond -430 mV. The hydrogen discharge reaction then takes place on the Sn substrate when potential reaches about -500 mV. The application of agitation, whether by magnetically stirring of the solution or with a rotating disc electrode, will inevitably increase the limiting current density of an electrode reaction due to the reduction of diffusion layer thickness (Tan, 1993). A few factors such as lack of surfactant or wetting agent, with improper metal concentration, and high current density may result in rapid and explosive growth of Sn dendrites (Schlesinger & Paunovic, 2010). The outward growth of Sn dendrites usually

result in porous and poorly adhering films. Under such circumstances, the electrode behaves more like a Cu substrate rather than a Sn substrate. The hydrogen overvoltage for Cu (750 mV at 10mA cm^{-2} in 1N HCl) is lower than for Sn (980 mV at 10mA cm^{-2} in 1N HCl) (Raub & Müller, 1967). Hence, with a lower overvoltage, hydrogen discharge reaction takes place at a more noble electrode potential. The same trend is observed for Sn solution with addition of HQ (Figure 3.9). The mild suppression of current density by HQ has been eliminated when stirring of solution is applied.

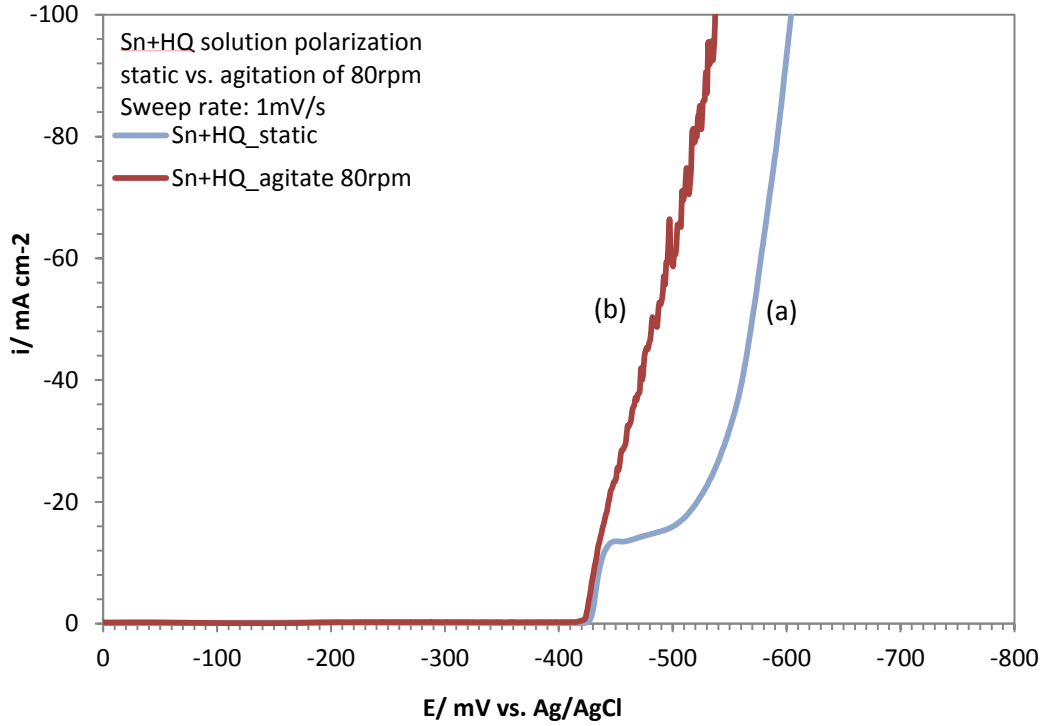

Figure 3.9 Polarization curves for Sn+HQ solution under (a) static condition and (b) agitation at 80rpm.

For the case of gelatin addition, the strong suppression of hydrogen evolution is still pronounced even when stirring is applied (Figure 3.10). It is also seen that the limiting current density for Sn deposition in this bath has increase by about threefold. In the limiting current region, deposition process depends solely on the diffusion rate of ions. The agitation of solution increases the diffusion rate of ions, hence resulting in an increment in limiting current density. Figure 3.11 shows the polarization curves of

Sn+HQ+Gelatin solution, under static and stirred conditions. Similarly, the limiting current density increases by about threefold. Comparing curve (b) in Figure 3.11 and that in 3.9, it can be noted that the limiting current plateau with addition of both HQ and gelatin has less fluctuations than for only gelatin addition. This implies that the diffusion of ions in the Sn+HQ+Gelatin plating bath is more stable than in the Sn+Gelatin plating bath. This may be due to the anti oxidation effects of HQ, which reduces the amount of tin (IV) oxide precipitates suspended in the plating bath. These oxide precipitates increased the turbidity of the plating bath and may also impede ion movements when present in large amount.

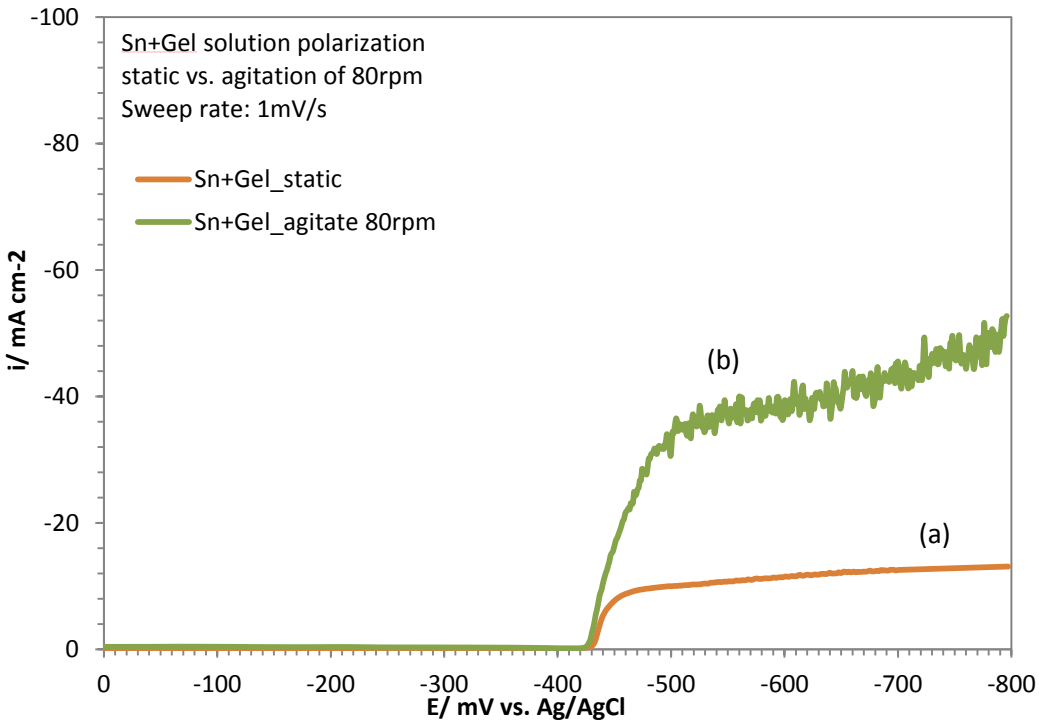

Figure 3.10 Polarization curves for Sn+Gelatin solution under (a) static condition and (b) agitation at 80rpm.

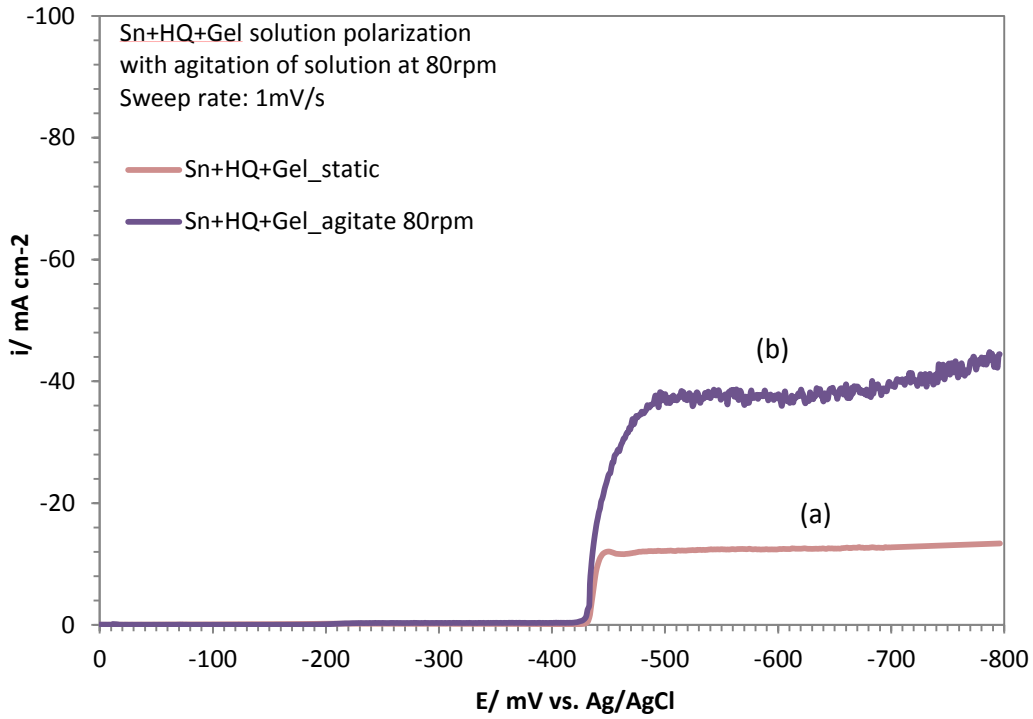

Figure 3.11 Polarization curves for Sn+HQ+Gelatin solution under (a) static condition and (b) agitation at 80rpm.

The effects of agitation of Bi solution were also studied in a similar manner and polarization curves are presented in Figure 3.12. There is about 3.5 times increment in the limiting current density for Bi deposition upon agitation (curve (b), Figure 3.12), and hydrogen discharge reaction is shifted to a more noble electrode potential. The change in hydrogen discharge mechanism (from Tafel to Heyrovsky reaction) could be the main reason for change in hydrogen polarization behaviour. For Bi solutions containing HQ and with solution agitation, the limiting current density increases by threefold (curve (b), Figure 3.13). Hydrogen discharge reaction is shifted to more noble potential, but to a lesser extent compared to the cases without additives. This implies that HQ possesses stronger suppression capability in Bi solutions than in Sn solutions.

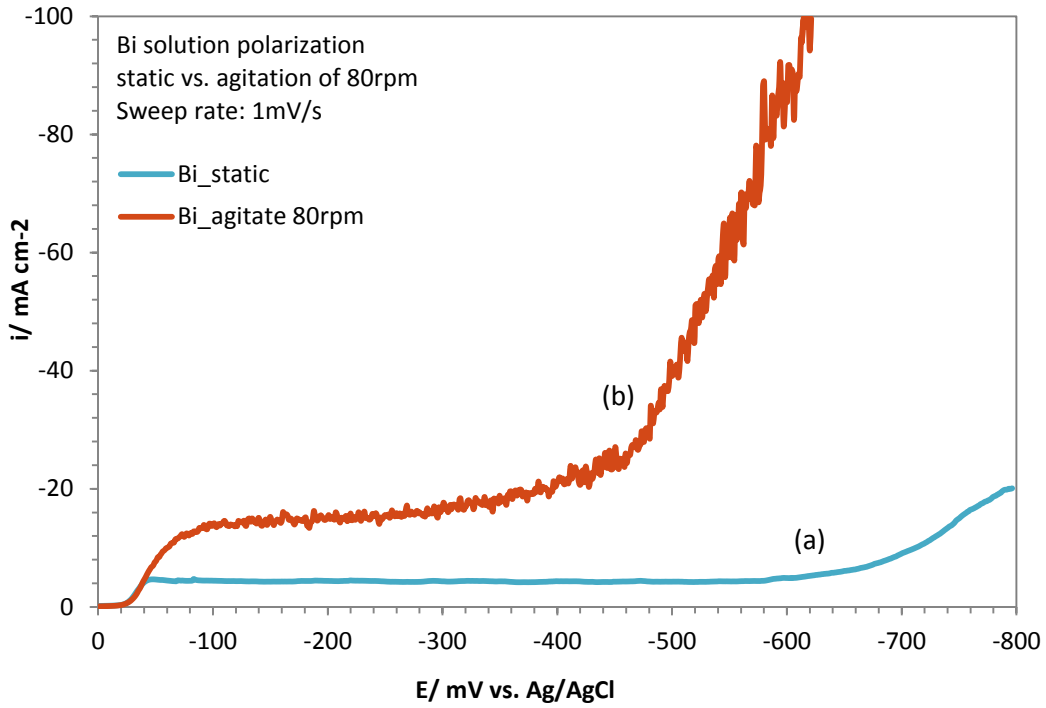

Figure 3.12 Polarization curves for Bi solution under (a) static condition and (b) agitation at 80rpm.

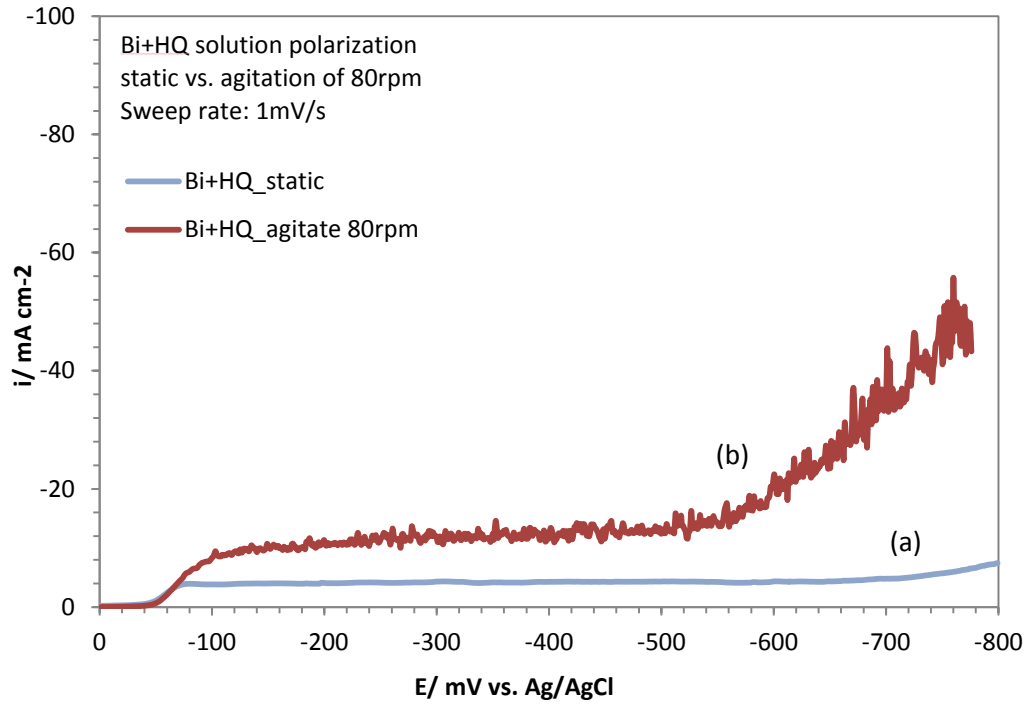

Figure 3.13 Polarization curves for Bi+HQ solution under (a) static condition and (b) agitation at 80rpm.

The Bi plating solution containing gelatin as the only addition (Figure 3.14) and with both HQ and gelatin added (Figure 3.15) shows a threeefold increase in the limiting current density for Bi deposition upon agitation of the plating solution. Other

features, especially the shift in Bi deposition potential by HQ and gelatin, remain unchanged.

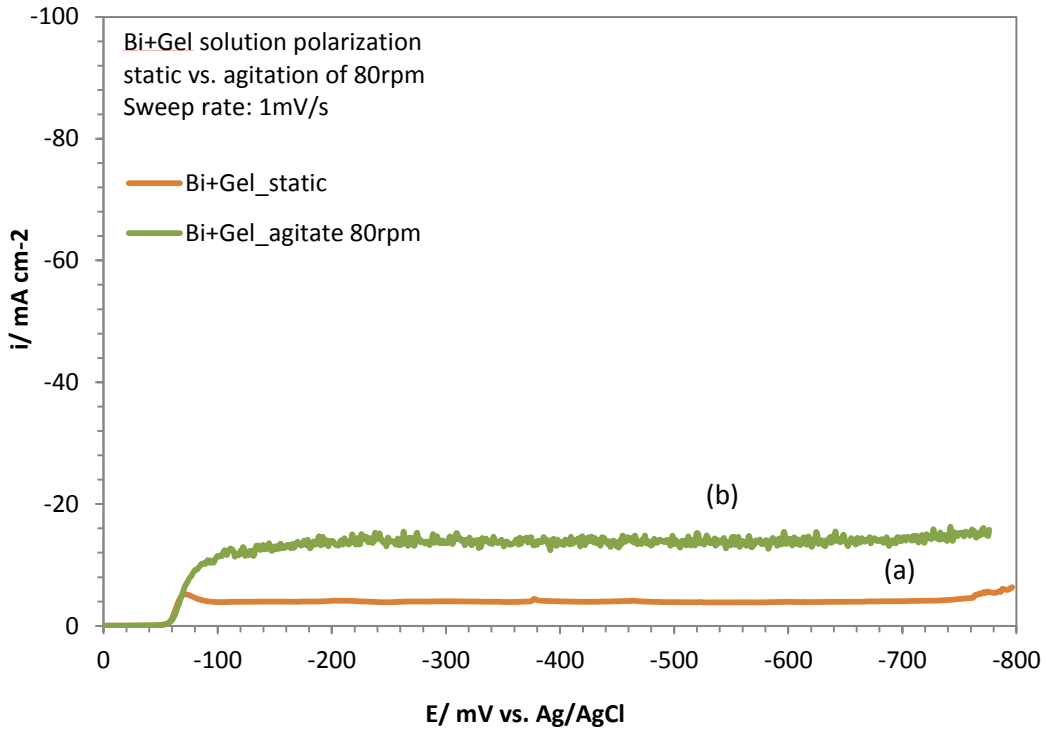

Figure 3.14 Polarization curves for Bi+Gelatin solution under (a) static condition and (b) agitation at 80rpm.

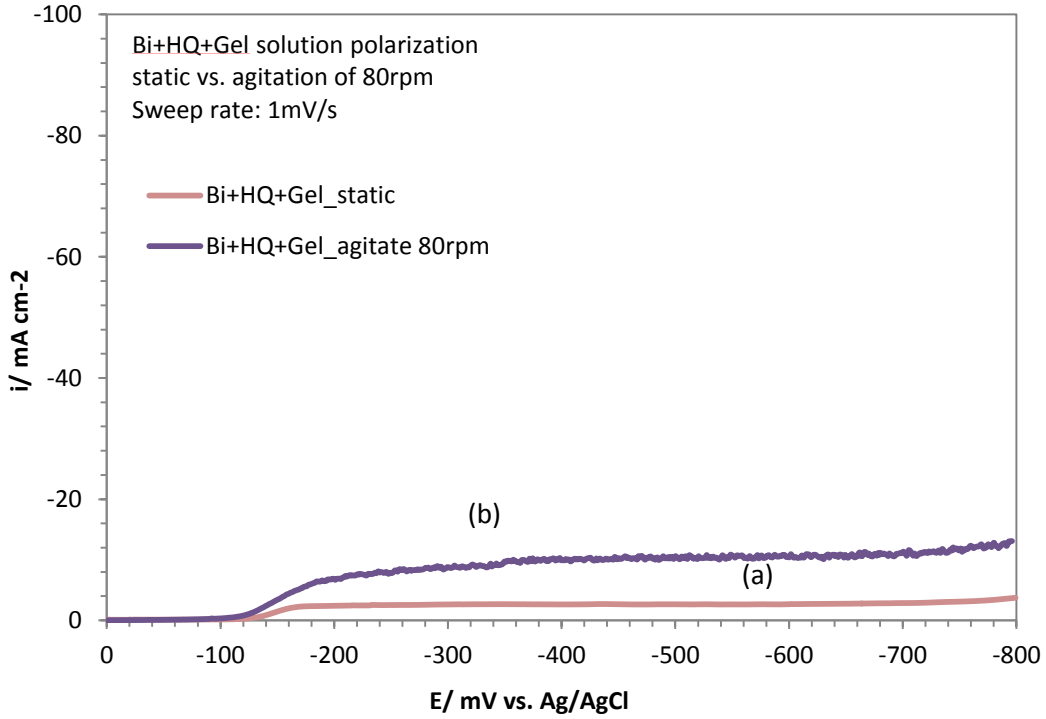

Figure 3.15 Polarization curves for Bi+HQ+Gelatin solution under (a) static condition and (b) agitation at 80rpm.

For Sn-Bi bimetallic plating baths, the behaviour is almost similar to that of individual metal plating baths when agitation is applied (Figure 3.16). The limiting current density of Bi increases threefold with stirring of the solution, while hydrogen evolution takes place simultaneously with Sn deposition. Similar trend is observed for baths with HQ (Figure 3.17) or gelatin (Figure 3.18) added, where the mild adsorption effect of these additives is seen to be eliminated upon stirring. For bimetallic bath with both HQ and gelatin incorporated, the huge shift in Bi deposition potential which reduces the potential gap between the two elements is still observed (Figure 3.19). Both the limiting current density for Bi and Sn deposition is seen to increase by about threefold. However, the suppression of current density is not as strong as measured under quiescent state, as observed in the increase in current density beyond -600mV (curve (b), Figure 3.19).

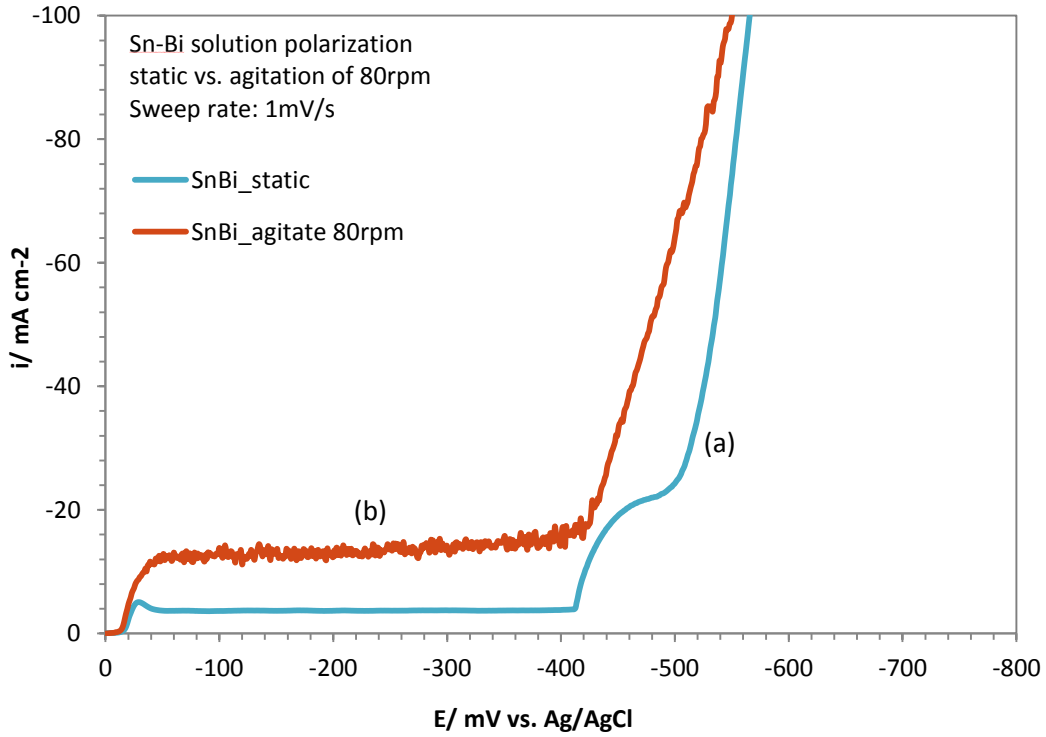

Figure 3.16 Polarization curves for Sn-Bi solution under (a) static condition and (b) agitation at 80rpm.

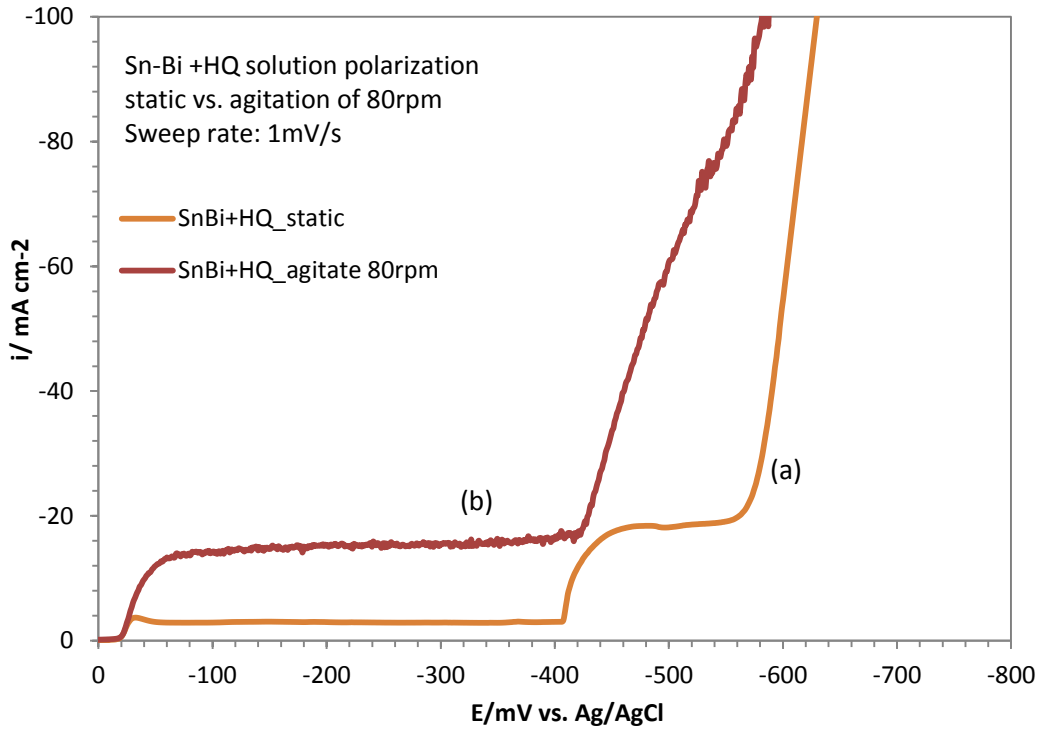

Figure 3.17 Polarization curves for Sn-Bi+HQ solution under (a) static condition and (b) agitation at 80rpm.

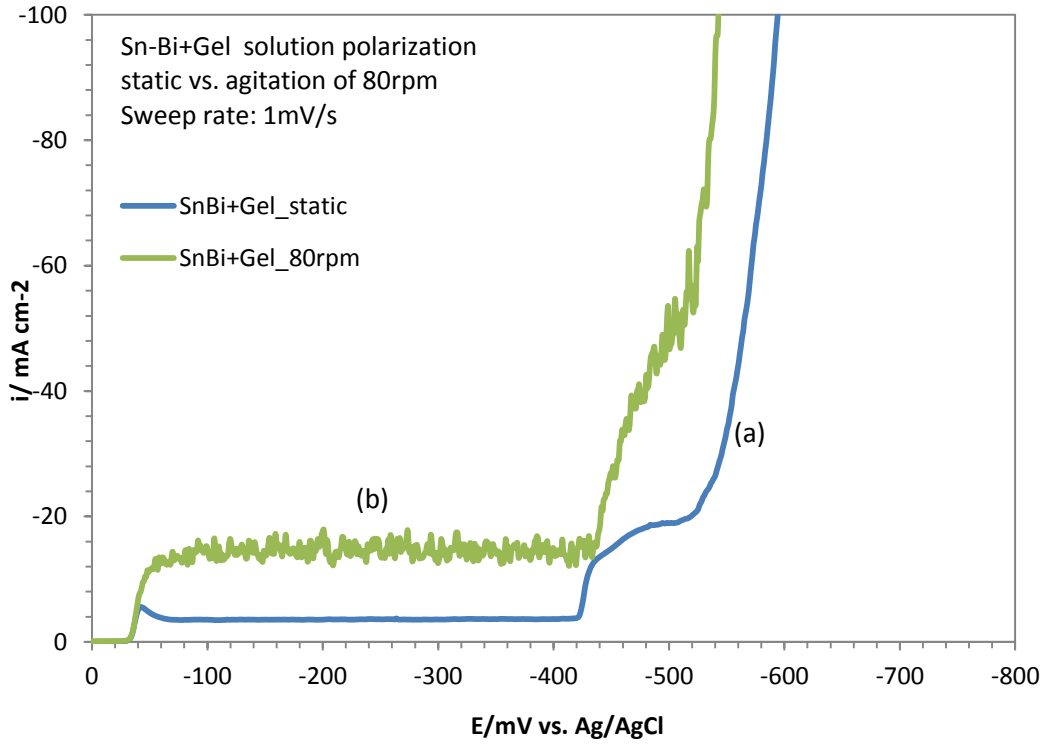

Figure 3.18 Polarization curves for Sn-Bi+Gelatin solution under (a) static condition and (b) agitation at 80rpm.

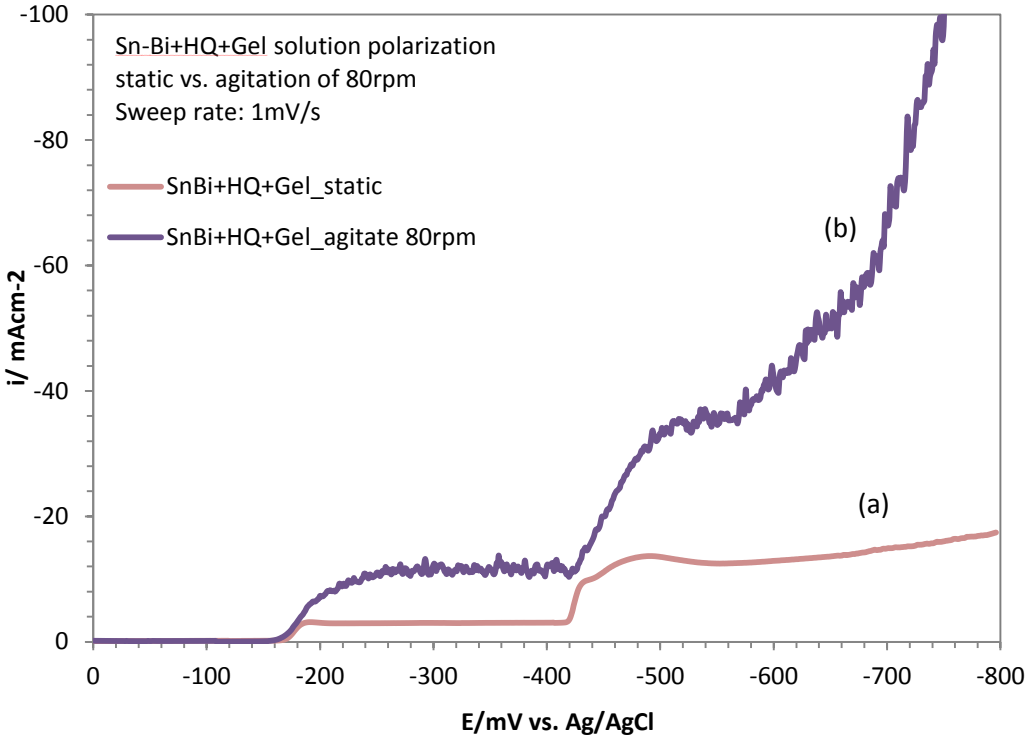

Figure 3.19 Polarization curves for Sn-Bi+HQ+Gelatin solution under (a) static condition and (b) agitation at 80rpm.

From the above observations, the application of stirring is capable of increasing the limiting current density for the deposition of alloys. Hence, it is expected to obtain a higher current efficiency when stirring is done. However, a particular drawback is that the hydrogen discharge mechanism is altered with agitation of solution. Generally, agitation promoted the hydrogen evolution reaction to take place at a more noble electrode potentials. If electrodeposition is performed at high current density, the deposition process may take place simultaneously with hydrogen discharge which may result in electrodeposits of inferior quality. The deposition potentials and complexing effects are not affected by agitation of solution.

3.3.6 Effects of additive concentration

The amount of additives in the plating bath has been increased (double the amount of previously studied baths) to observe the effects of additive concentration in the plating bath. Figure 3.20 shows polarization curves of plating baths with varying amount of HQ,

with and without the addition of gelatin. It has already been observed in previous studies that 5g/L of HQ imposes mild adsorption effect. The increase of HQ amount to 10g/L has shifted the deposition potential of Bi slightly and increased limiting current density of Sn deposition (curve (c), Figure 3.20). In the plating bath containing only Bi, HQ is found to impose mild complexing effect which shifted the deposition potential of Bi slightly (curve (b), Figure 3.5). But this effect is no longer observed in the bimetallic Sn-Bi plating bath. It is suggested that HQ preferentially adsorbs on the electrode surface when Sn is present, and hence there are insufficient amount of HQ available for complexing with Bi. By doubling up the amount of HQ in the plating bath, both shifting in Bi deposition potential and suppression of hydrogen evolution exists, which is in agreement with previous discussions.

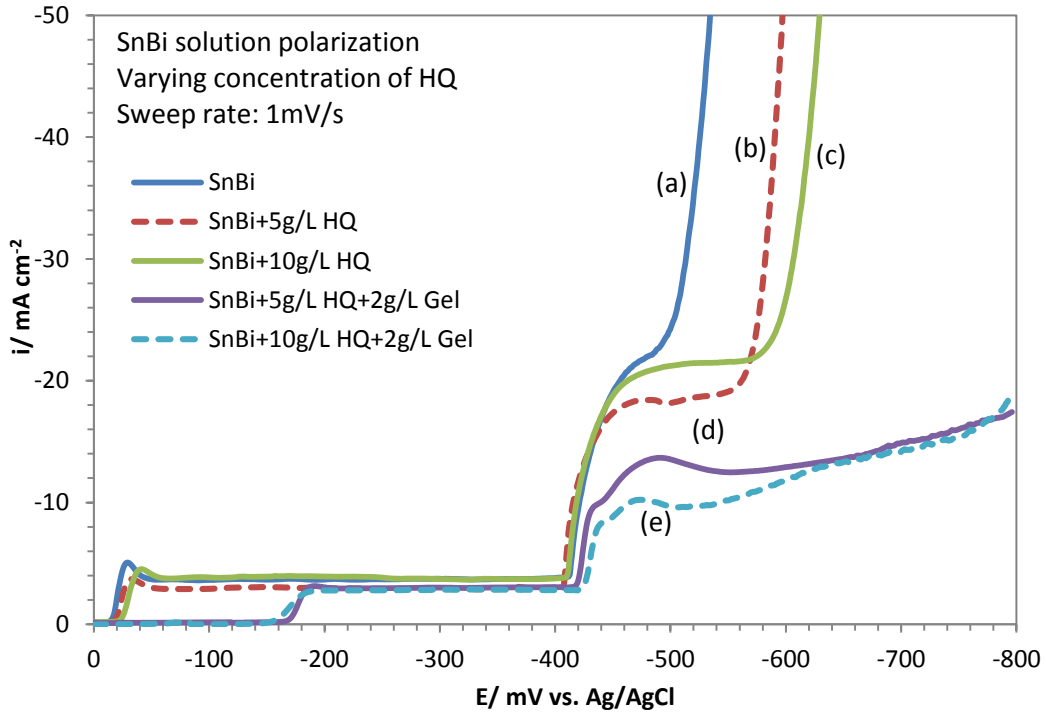

Figure 3.20 Polarization curves for Sn-Bi solution (a) without additives, (b) with 5g/L HQ, (c) with 10g/L HQ, (d) with 5g/L HQ and 2g/L gelatin, and (e) with 10g/L HQ and 2g/L gelatin.

In the plating bath containing both HQ and gelatin, doubling up the amount of HQ does not change the complexing effect on Bi ions but has suppressed the current density of Sn (curve (e), Figure 3.20). The increased amount of HQ has increased the adsorption coverage area which slows down the deposition rate of Sn. The deposition rate then increases slowly and eventually achieved a same limiting current density compared to the plating bath with less amount of HQ (curve (d), Figure 3.20).

Figure 3.21 shows the effects of varying amount of gelatin on the polarization behaviour of Sn-Bi plating baths, with and without the addition of HQ. With 2g/L of gelatin, we have observed a mild shift in deposition potential of Bi (curve (b), Figure 3.21). The increase in amount of gelatin to 4g/L shows that the mild shift of deposition potential is retained, while the hydrogen evolution reaction has been suppressed to much more electronegative potentials. It can be inferred that when sufficient amount of gelatin is added, it can function as both complexing and adsorption agent. However the complexing effect is still not enough to close the huge deposition potential gap between the two metals. As has been mentioned previously, with the addition of both HQ and gelatin to the plating bath, both complexing and adsoprtion effect is achieved. The increase of gelatin amount to 4g/L in the Sn-Bi plating bath containing HQ does not yield pronounced effect on the deposition behaviour (curve (e), Figure 3.21). From the polarization studies conducted on varying amount of additives, it can be concluded that the additive content of 5g/L HQ and 2g/L gelatin is still the optimum amount to be added to the Sn-Bi plating bath.

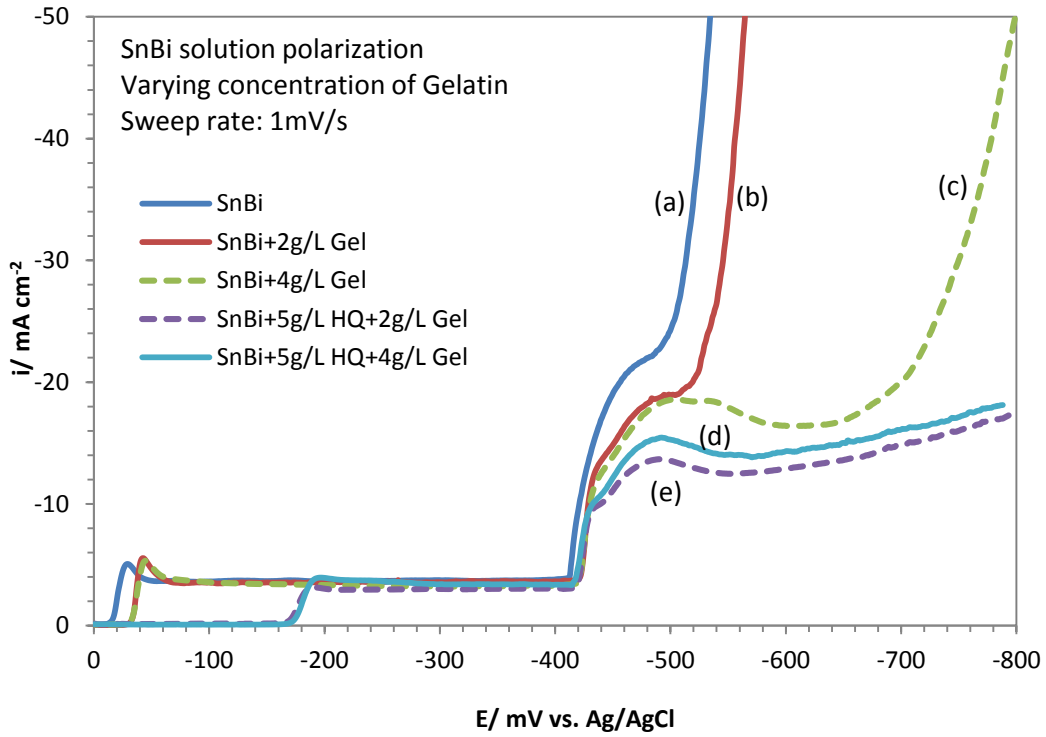

Figure 3.21 Polarization curves for Sn-Bi solution (a) without additives, (b) with 2g/L gelatin, (c) with 4g/L gelatin, (d) with 5g/L HQ and 2g/L gelatin, and (e) with 5g/L HQ and 4g/L gelatin.

3.3.7 Composition estimation from galvanostatic and polarization curves

From the literature survey mentioned in ***Section 2.3.2***, the composition of an alloy can actually be estimated from the polarization curves from the ratio of applied current density to the limiting current density of a metal. The effects of applied current density on the composition of alloy will be discussed in detail in the next chapter, while this section focuses on the electrochemical behaviour of the plating solution upon the application of a constant current density, namely the galvanostatic studies. Galvanostatic studies were performed in agitated Sn-Bi solutions with both HQ and gelatin added to observe the deposition behaviour of the alloy at different applied current densities. A constant current density was applied for 60mins, while data of the electrode potential was collected. Figure 3.22 depicts the cathode potential vs. deposition time curve of Sn-Bi+HQ+gelatin solution agitated at 80rpm.

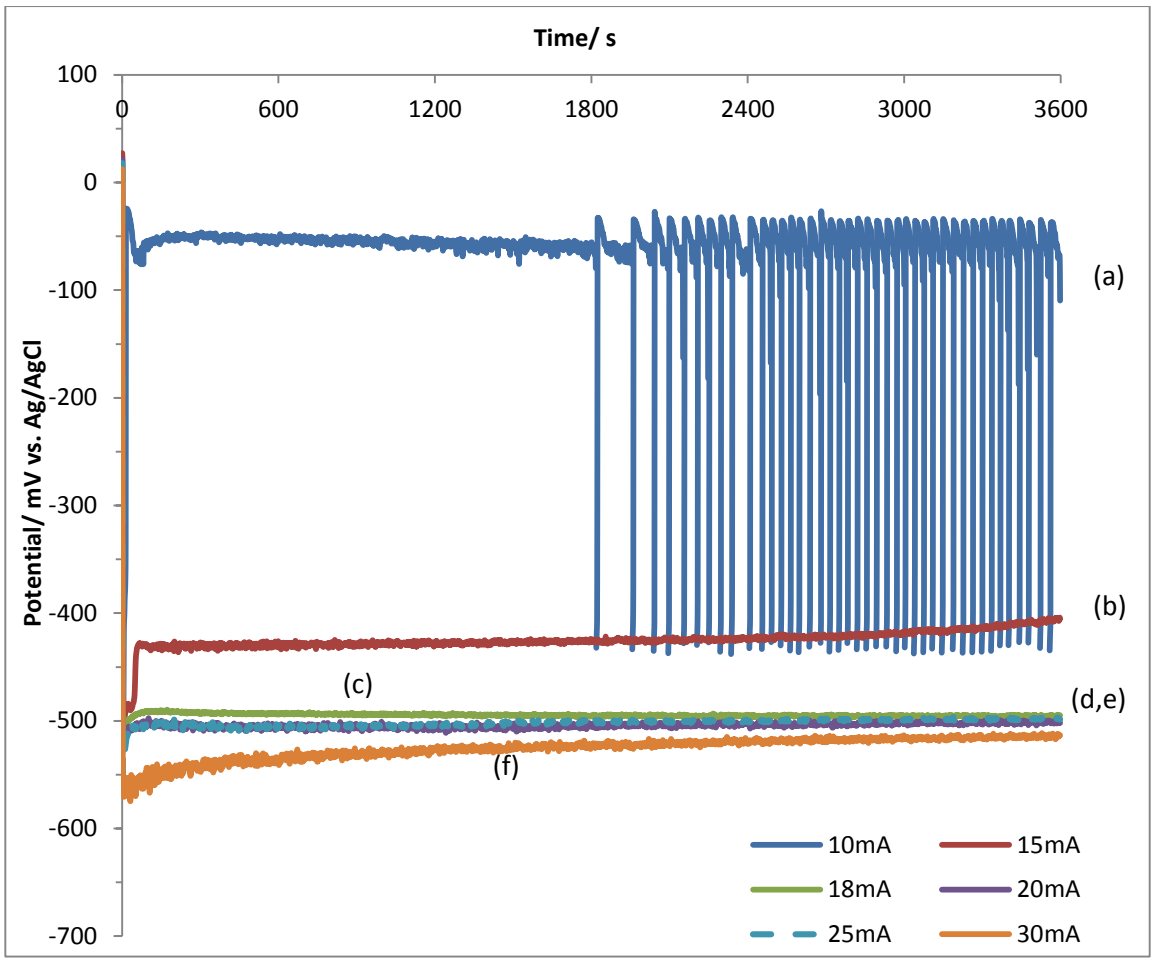

Figure 3.22 Potential vs. time curve for agitated Sn-Bi+HQ+gelatin solution obtained at applied current density of (a) 10 mA cm^{-2}, (b) 15 mA cm^{-2}, (c) 18 mA cm^{-2}, (d) 20 mA cm^{-2}, (e) 25 mA cm^{-2}, and (f) 30 mA cm^{-2}.

At a current density of 10 $mAcm^{-2}$, it is seen that there is a small overpotential of about -75mV before the deposition process takes place at around -51mV for about 25mins (curve (a), Figure 3.22). After that, fluctuation of potential is observed from -33mV to -425mV for the remaining deposition period. Experiments were repeated several times and it was found that the fluctuations did not occur constantly at the later stage of deposition, but took place randomly at different deposition stages. It may be due to the fact that the applied current density is too near to the limiting current density of Bi which is about -10.2 $mAcm^{-2}$ (Figure 3.23). The surface area of the substrate or deposited film may vary throughout the deposition process due to changes in surface roughness. Since current density is the applied current over the substrate area, slight

variations in the area may result in changes to the actual current density at the electrode surface. Such variations are expected to be the cause of electrode potential fluctuations. As seen from the polarization curve of agitated Sn-Bi+HQ+gelatin solution (curve (b), Figure 3.19), it is expected that electrode potentials more noble than -425mV will yield only Bi deposits, while beyond -425mV the co-deposition is expected to take place. Hence from the potential vs. deposition time curve of current density of -10 $mAcm^{-2}$, the deposition expected to yield Bi rich deposits.

Curve (b) of Figure 3.22 shows that when -15 $mAcm^{-2}$ is applied, there is an overpotential of about -480mV before the overall deposition takes place at about -430mV. With increasing applied current density (curve (c-f), Figure 3.22), the overpotential value increases and deposition process takes place at more electronegative potentials. The expected compositions of the electrodeposits at each current density are calculated from the polarization curve as shown in Figure 3.23. For example, when the applied current is -30 $mAcm^{-2}$, and the limiting current density of Bi is taken to be -10.2 $mAcm^{-2}$, the estimated composition of Bi present in the electrodeposits will be $\frac{-10.2}{-30}\ X\ 100\% = 34\%$. Estimated compositions of several applied current densities are calculated and tabulated in Table 3.2. The composition of electrodeposits will be characterized with energy dispersive x-ray spectroscopy (EDS) and results are presented in the next chapter.

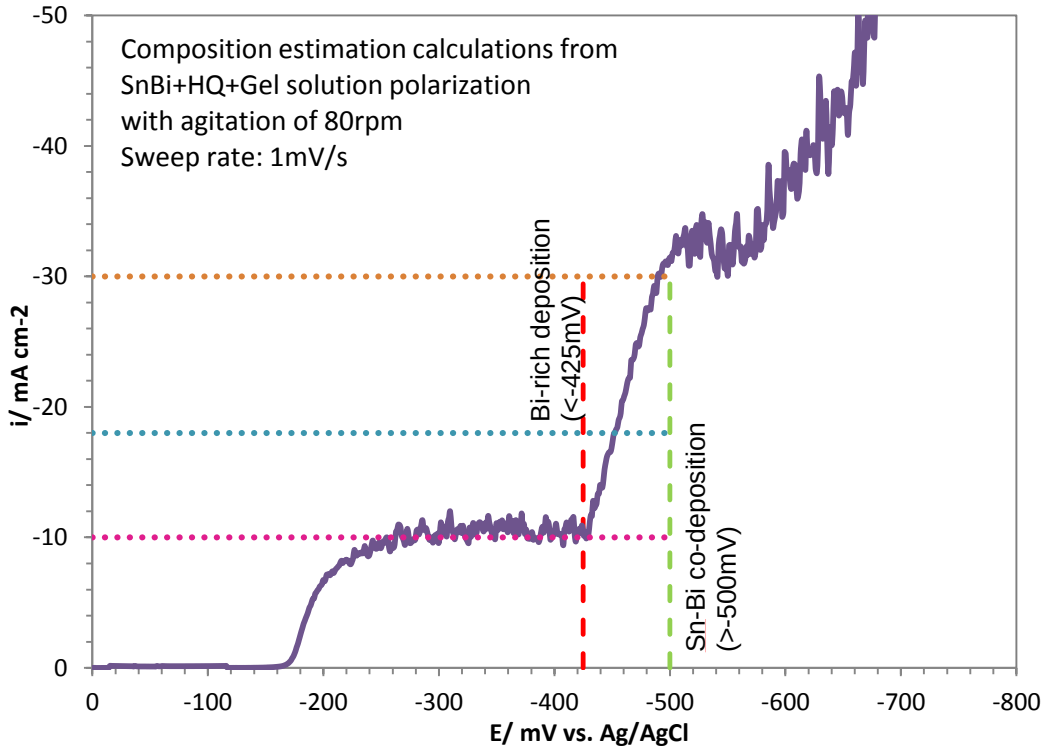

Figure 3.23 Composition estimation from polarization curve for Sn-Bi+HQ+gelatin solution agitated at 80rpm (limiting current density of Bi: -10.2 $mAcm^{-2}$).

Table 3.2 Estimated compositions of alloys at various applied current density.

Applied current density ($mA\ cm^{-2}$)	Percentage of Bi in alloy (wt. %)	Percentage of Sn in alloy (wt. %)
10	100.0	-
15	68.0	32.0
18	56.7	43.3
20	51.0	49.0
25	40.8	59.2
30	34.0	66.0

3.3.8 Plating bath stability

One of the issues with acidic plating baths would be the stability or reusability of the plating solutions after some storage period. The changes or degradation of the plating bath can be observed through the physical appearance, which is the turbidity of the plating bath. However, physical appearance can be subjective. A more practical way is

to monitor the limiting current densities (i_L) of elements present in the bath, as the i_L is a good representative of ion concentration in the plating bath. A study has been conducted to evaluate the stability of Sn-Bi plating bath over a storage period of 7 days, with and without additives. 2.5L of freshly prepared plating baths were stored in air tight glass bottles at room temperature, and 300ml of the solution was collected for potentiodynamic polarization analysis every day. Figure 3.24 shows the changes in i_L of Sn and Bi with storage time.

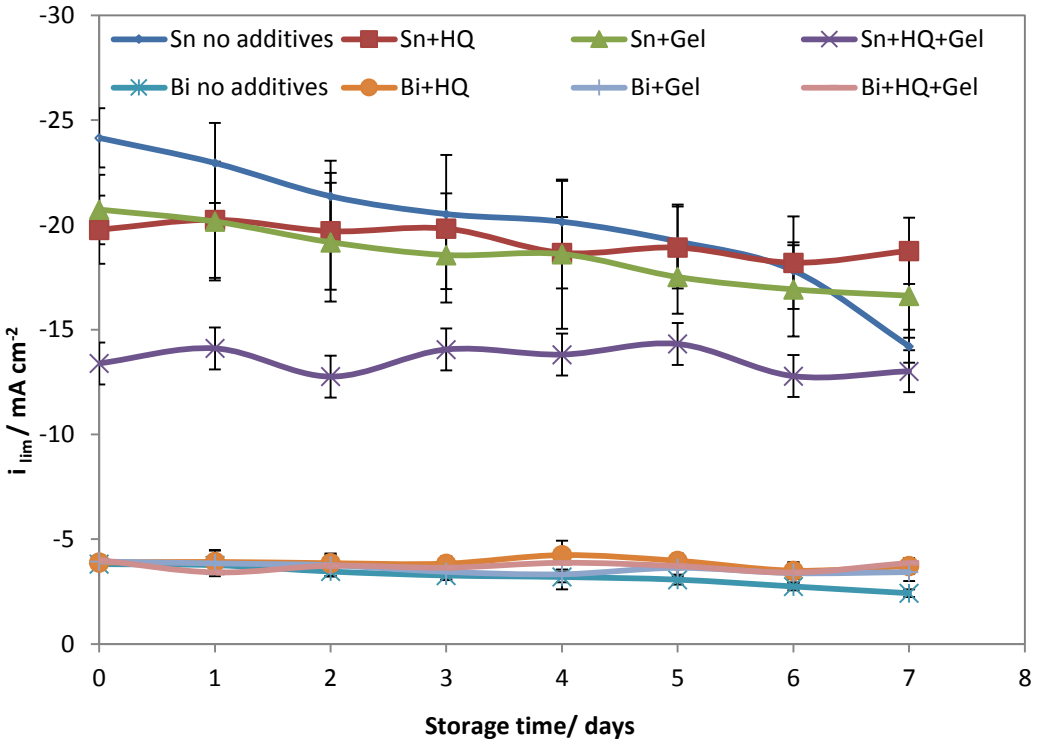

Figure 3.24 Limiting current density of Sn and Bi vs. storage time of plating solution.

It may be noted that there are some fluctuations in measurements which may be caused by experimental variations from day to day. The variations in measurements are presented as error bars in Figure 3.24. The percentage decrease in i_L for Sn-Bi plating baths are presented in the form of charts (Figure 3.25) to give a clearer picture. It is seen that the Sn bath experiences a sharp drop in i_L over the 7 day storage period with a percentage decrease of 41.2% (bar (a), Figure 3.25). The i_L of Bi has also decreased

from -3.81 mA cm^{-2} for the freshly prepared solution to -2.42 mA cm^{-2} by the 7th day of storage, where the decrease is 36.4% (bar (e), Figure 3.25). The metal ions are suggested to have oxidized in the plating bath and settle in the form of hydroxide precipitates. This is also evident by the increased turbidity of the plating bath.

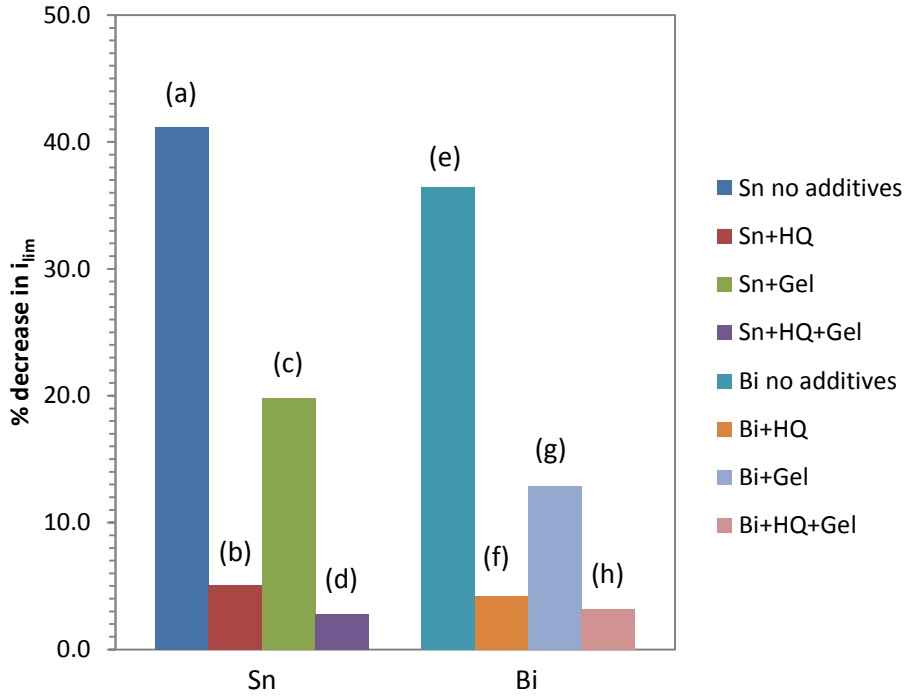

Figure 3.25 Percentage decrease of limiting current density of Sn and Bi after 7 days of storage of plating solution.

With the addition of HQ to the plating bath, the i_L of Sn is slightly lower due to the adsorption effects. There are also some fluctuations in the data collected which may be due to minor variations in surface roughness of the electrode which then affected the adsorption of HQ. However, the i_L for both Sn and Bi ions is observed to have very minor changes throughout the 7-day storage period with the addition of HQ. The i_L of Sn and Bi marked an insignificant decrease of 5.1% and 4.2% respectively with HQ added (bar (b) and (f), Figure 3.25). This has suggested the effectiveness of HQ to serve as antioxidant in the Sn-Bi acidic plating bath.

Gelatin comprises numerous organic amino acid chains, which are also prone to degradation. From Figure 3.25(c), the inclusion of gelatin into the plating bath has resulted in a decrease of the i_L of Sn by 19.8% after 7-days. However, the decrease in i_L of Bi is 12.9%. Possible reason where Bi ions do not degrade as rapidly as Sn ions may be the mild complexing effect of gelatin with Bi (curve (c), Figure 3.7). It can be inferred that complex ions can remain stable in a stored plating bath for a longer period compared to simple ions.

The addition of both HQ and gelatin to the bimetallic Sn-Bi plating bath results in an insignificant reduction in i_L after a storage period of 7 days. The i_L of Sn and Bi marked an insignificant decrease of 2.8% and 3.2% respectively (Figure 3.25(d) and (h)). Again, it is suggested that with complexing of ions, the ions are less prone to oxidation or precipitation even after prolonged period of plating bath storage. The synergistic effects of HQ and gelatin have suggested possible co-deposition of Sn-Bi alloys, and also improved the lifespan of the MSA-based Sn-Bi plating bath.

3.4 Chapter conclusions

The effects of two additives, hydroquinone (HQ) and gelatin, on the electrochemical behaviour of Sn-Bi plating bath is studied in this chapter. It is found that HQ possess mild suppression effect on the current densities of Sn, possibly through edgewise adsorption. This suppression effect is eliminated upon stirring of the solution. In Bi-MSA solution, HQ shifted the deposition potential of Bi to more electronegative values. But this effect is no longer observed in the bimetallic Sn-Bi plating bath, where possibly some amount of HQ served to suppress the deposition current density of Sn. Doubling up the amount of HQ in Sn-Bi plating bath again brings up the shifting of Bi deposition potential, suggesting that with sufficient quantity of HQ present, both suppression and

shift of deposition potential take place simultaneously. Strong suppression of current density and hydrogen evolution by gelatin is observed for both single metal Sn and Bi solutions. This effect persists even when stirring is applied to the solution. However, gelatin only shows mild shift in deposition potential of Bi in the Sn-Bi bimetallic plating bath, and the suppression of hydrogen evolution reaction is not observed. It is suggested that in the Sn-Bi solution, HQ tends to modify the deposition behaviour of Sn while gelatin tends to modify the deposition behaviour of Bi. The incorporation of both electrolyte additives HQ and gelatin into the plating bath has imposed a synergistic effect, where a huge shift in Bi deposition potential and strong suppression of hydrogen evolution is achieved. This synergistic effect is desirable because the deposition potential gap between the two elements has been reduced from 429mV (without additives) to 255mV (with both HQ and gelatin added). This combination of additives has also improved the MSA-based Sn-Bi plating bath stability by minimizing the oxidation of ions present in the bath. The Sn-Bi alloy composition is estimated from the polarization curve of Sn-Bi+HQ+gelatin plating bath. The plating bath will be put into practice and actual alloy composition will be characterized by EDS, where results are discussed in the upcoming chapter.

CHAPTER 4

ELECTRODEPOSITION AND CHARACTERIZATION OF SN-BI ALLOYS

4.1 Background

The ever-rising demand for slim, lightweight and high-speed devices has prompted the development of fine pitch solder interconnections. The electrodeposition technique has outdone all other solder deposition techniques in the fabrication of fine geometry solder bumps of due to its cost-effectiveness in mass production. Co-deposition of Sn-Pb solders has been quite successful in the past (Field & Weill, 1951; J. H. Kim et al., 1996; Kohl, 1982; Lin & Liu, 1999) which can be attributed to the small difference in standard reduction potential between the two elements (Sn^{2+}/Sn: −0.137 V and Pb^{2+}/Pb: −0.125 V). However, legislations stamped out the usage of toxic Pb in electronic applications. This leads to extensive research on electrodeposition of alternative Pb-free solder systems. These systems are usually binary or ternary alloys of Sn containing Ag, Bi, Cu, and Zn. Among them, Sn-Ag-Cu alloys are recognized as the most promising candidate by the industry, due to their superior mechanical properties and solderability. However, this solder is not suitable for higher hierarchy level interconnections and heat-sensitive electronic components due to its high melting point (217^{o}C) that requires high reflow temperature. A low melting temperature alloy is essential to meet such standards and Sn-58 wt.% Bi eutectic alloy can be a promising candidate.

With a low melting temperature of 138^{o}C, Sn-Bi solders are gaining considerable attention in the electronics industry. The advantages of Sn-Bi solder include good joint strength, excellent creep resistance, low coefficient of thermal expansion (1.5 X 10^{-5} / ^{o}C), good wettability, and low cost (M. Fukuda et al., 2001; Y.-G. Lee et al., 2011; Tsai & Hu, 2009a, 2009b, 2011; Tsai et al., 2007; Tsai et al., 2011;

Yen et al., 2011). Attempts were made to co-deposit Sn-Bi solder in acidic baths due to the compatibility of acidic bath with photoresists (M. Fukuda et al., 2001; Y.-G. Lee et al., 2011; M.-S. Suh et al., 2006; Tsai & Hu, 2009a, 2009b, 2011; Tsai et al., 2007; Tsai et al., 2011). However, the electrodeposition of Sn-Bi solder involves a few challenges. Firstly, exact eutectic composition is difficult to achieve due to the large potential difference between Sn and Bi (Sn^{2+}/Sn: −0.137 V and Bi^{3+}/Bi: +0.317 V). Secondly, oxidation of stannous ions in acidic medium degrades the stability of plating bath. The addition of electrolyte additives can significantly alleviate these two issues, but the complexity of the plating bath and the process will further increase. These electrochemical aspects have been addressed in the previous chapter (Chapter 3). From electrochemistry point of view, the addition of both HQ and gelatin shows potential for co-deposition of Sn-Bi alloy. The application of the plating bath and resulting electrodeposits will be characterized and discussed in this chapter.

4.2 Experimental

Sn-Bi deposits were electroplated onto 0.3 mm-thick 3 × 3 cm^2 Cu sheets and Pt wire was used as anode. The Cu sheets were degreased with soap water, etched with 10% sulfuric acid for 20s and rinsed thoroughly with distilled water prior to plating. The pre-treated substrates were vertically placed in a 300ml single-compartment cell. The composition of the MSA-based plating bath was as shown in Table 3.1 (***Section 3.2***), which mainly consisted $SnSO_4$ and Bi_2O_3 with HQ and gelatin as additives. The pH of the solution was maintained at 1±0.5. The direct current for electrodeposition was obtained from a DC power supply and the distance between electrodes was maintained at 5 cm. The electrodeposition process was carried out at room temperature, where the plating bath temperature was about 28−30^oC. Current density used was in the range of 10−30 mA cm^{-2}. Magnetic stirring of 80 rpm was applied during deposition to prevent

gas bubbles from being trapped on the cathode surface and to promote mass transfer of metal ions. After the deposition process, the plated substrates were removed immediately from the bath (within ~3seconds after turning off the power supply) to avoid dissolution of deposits at open circuit potential. Post-deposition rinsing was done with running distilled water and the deposits are then dried with a blower.

Surface morphologies of the electrodeposits were examined by a field-emission scanning electron microscope (FESEM) (Zeiss Auriga® Ultra-60). The average composition of deposit was obtained by performing semi-quantitative energy dispersive X-ray spectroscope (EDX) (Zeiss Auriga® Ultra-60 EDAX detector) analysis at 5 different locations on the surface of the deposits on areas measuring $60 \times 60\ \mu m^2$. The melting temperature of the near-eutectic Sn-Bi deposit was obtained by differential scanning calorimetry (DSC) (Mettler Toledo). The crystallinity of Sn-Bi deposits was also characterized with X-Ray Diffraction (XRD) (Siemens D-5000). Cross sectional analysis of the as-electrodeposited and reflowed alloys were also examined by FESEM. Reflow of the electrodeposits Sn-Bi films were done in a reflow oven (C.I.F. Forced Convection FT02). During reflow, all samples were preheated at $100^{o}C$ for 120 s. The samples were then held at $170^{o}C$ for 45 s before cooling in the reflow oven to room temperature.

4.3 Results and discussion

4.3.1 Optimization of MSA-based plating solution for Sn-Bi electrodeposition

4.3.1.1 Additive-free Sn-Bi electrodeposition

The electrochemical studies of the additive-free plating bath shows that there is a large deposition potential gap between Bi and Sn metal ions (curve (a), Figure 3.7). It may be worth mentioning that the attempts to electrodeposit from the Sn-Bi plating baths without additives and with HQ yield spongy and non-adherent deposits at all current densities. The amount of loose deposits formed increase with increasing plating time and current density. The loose deposits fall off easily during the post-deposition rinsing process. This phenomenon was encountered during electrodeposition of Sn-Bi alloys in other plating baths (Tsai & Hu, 2009b; Tsai et al., 2007; Tsai et al., 2011) but the actual cause could not be identified. In this work, we attempted to investigate the loose deposit formation mechanism. The plating bath without additives is utilized for this investigation. Deposits obtained at different plating time is collected for FESEM analysis in order to distinguish the deposition modes happening at different stages.

Firstly, a Cu substrate is plated for 10 minutes at 10 mA cm^{-2} where small amount of powdery substances start to form. After the removal of the first substrate, a new substrate is inserted and plating was done for 30 minutes. Post-deposition cleaning was done by immersing the samples in distilled water carefully to retain as much of the loose deposits as possible. Figure 4.1(a) shows the surface morphology of the first sample plated for 10 minutes. Figure 4.1(a) reveals three distinct features found in the first sample: (i) rough and uneven substance loosely attached to deposits, (ii) porous and non-uniform deposits magnified in Figure 4.1(b), and (iii) dendrites. EDX spot analyses of the three features are tabulated (Table 4.1), where position (i) is high in Sn and O content while (ii) and (iii) are Bi rich with traces of Sn. When plating is done for 30

minutes, Bi dendrites are found to grow in size (Figure 4.1(c)). The magnified micrograph reveals that the deposits beneath the dendrites became coarser with many sharp edges (Figure 4.1(d)). Similar to previous EDX results, the Bi dendrites and deposits beneath dendrites are rich in Bi. The rough deposits (position (i), Figure 4.1(a)) are no longer found in the deposits plated for 30 minutes.

There is aggressive formation of Bi dendrites in the early stages of deposition. The sharp edges of the dendrites have increased the surface area which in turn lowered the current density. This impeded the reduction of Sn ions, as low current densities do not favor the deposition of more electronegative elements. The Sn ions around the electrode that failed to be reduced are then suspected to have oxidized, probably by the oxygen produced at the insoluble Pt anode. This is supported by the high O content in the rough substances found at the early stage of deposition (position (i), Figure 4.1(a)). As plating time increases, the Bi dendrites grew larger in size ((Figure 4.1(c)) and cause greater hindrance for proper deposition. The mass of non-adherent oxidized Sn grew with plating time and could no longer sustain on the substrate.

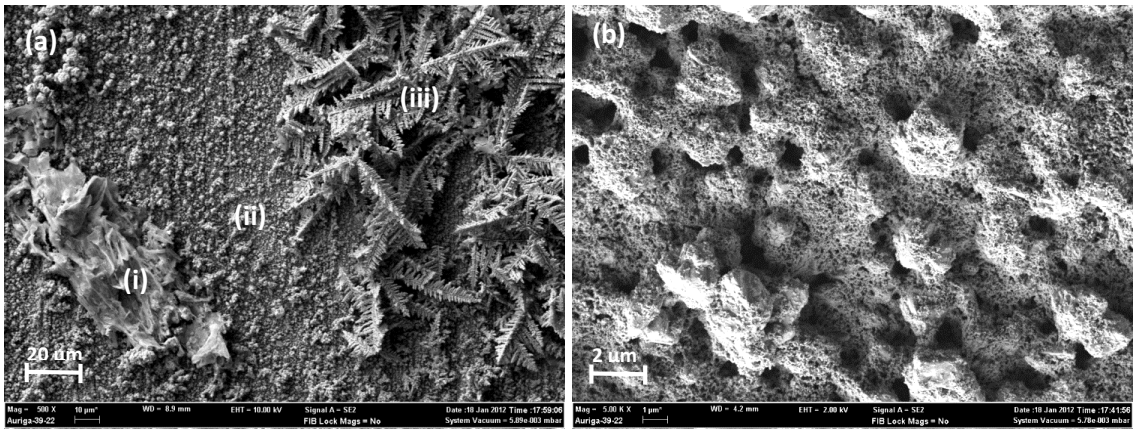

Figure 4.1 Surface morphology of deposits plated for 10 minutes in additive-free Sn-Bi plating bath at 10 mA cm^{-2} :(a) (i) rough substance with high Sn and O content, (ii) porous Bi rich deposits, (iii) Bi dendrites, and (b) magnified micrograph of part (a)(ii); Surface morphology of deposits plated for 30 minutes (c) larger Bi dendrites and (d) magnified micrograph of deposits beneath dendrite.

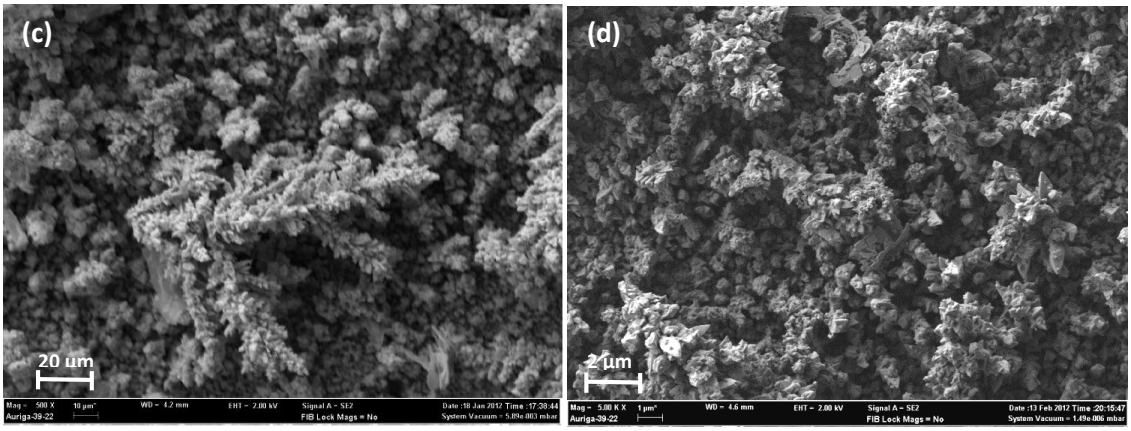

Figure 4.1 continued.

Table 4.1 Composition of unique features found in Figure 4.1(a).

Element/Spot	(i)	(ii)	(iii)
Sn (wt. %)	54.90	1.88	3.03
Bi (wt. %)	21.64	98.12	96.97
O (wt. %)	22.68	-	-
C (wt. %)	1.39	-	-

Figure 4.2 shows the representative micrograph of surface morphology of 60mins deposition in the additive-free Sn-Bi plating bath at 10 mA cm^{-2}. The surface is rather rough which matches the morphology seen in the early deposition stage, where there is formation of dendrites. The dendrite then grows with increasing deposition time and resulted in rocky surface morphology. EDX analysis of this sample shows that the composition is pure Bi.

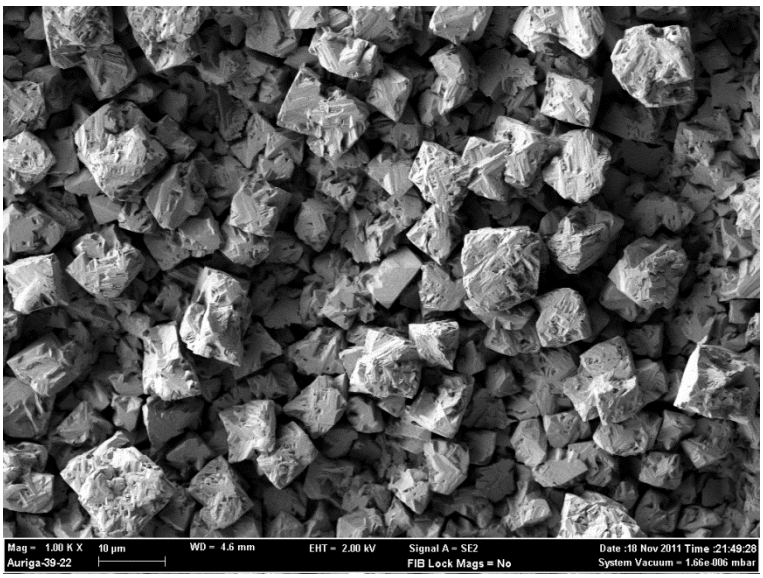

Figure 4.2 Surface morphology of deposits obtained at 10 mA cm^{-2} from additive-free Sn-Bi plating bath (deposition time: 60 minutes).

4.3.1.2 Effect of HQ addition on Sn-Bi electrodeposition

Electrodeposition from the bimetallic plating bath containing HQ also yields loose deposits. However, the surface morphology of deposits after 60mins of deposition yields finer and more rounded structure (Figure 4.3). EDX analysis of the electrodeposits also indicates the occurrence of only pure Bi. From previous electrochemical studies on plating bath containing HQ, it is observed that the addition of HQ did not reduce the deposition potential gap between Sn and Bi (curve (b), Figure 3.7), but possesses mild suppression effect on hydrogen evolution reaction. The large deposition potential gap of between two elements may not allow the alloy co-deposition to take place, hence only the more noble Bi is deposited preferentially. However, the suppression effect of HQ has improved the surface morphology of electrodeposits compared to the electrodeposits from the plating bath without additives.

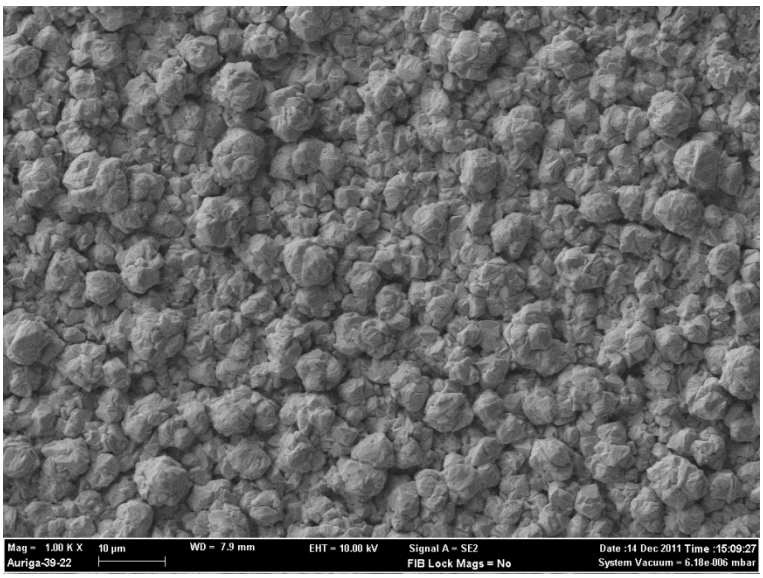

Figure 4.3 Surface morphology of deposits obtained at 10 mA cm^{-2} from Sn-Bi+5g/L HQ plating bath (deposition time: 60 minutes).

4.3.1.3 Effect of HQ and gelatin addition on Sn-Bi electrodeposition

Polarization curves of Sn-Bi+HQ+gelatin plating solutions reveals that there is a significant reduce of deposition potential gap between the two elements (curve (d), Figure 3.7). This suggests that it is possible for alloy co-deposition to take place. FESEM micrograph of electrodeposits obtained from this plating bath containing both additives at an applied current density of 10 mA cm^{-2} shows relatively smooth metallic deposits (Figure 4.4). EDX analysis also indicated both Sn and Bi were present in the deposits, with an average composition of Sn-84.25wt.%Bi. As discussed in the previous chapter, lower current densities favor the electrodeposition of more noble element. It is expected that the Sn composition will increase with increasing applied current density. The effects of current density on composition and morphology of electrodeposits are presented in the next section.

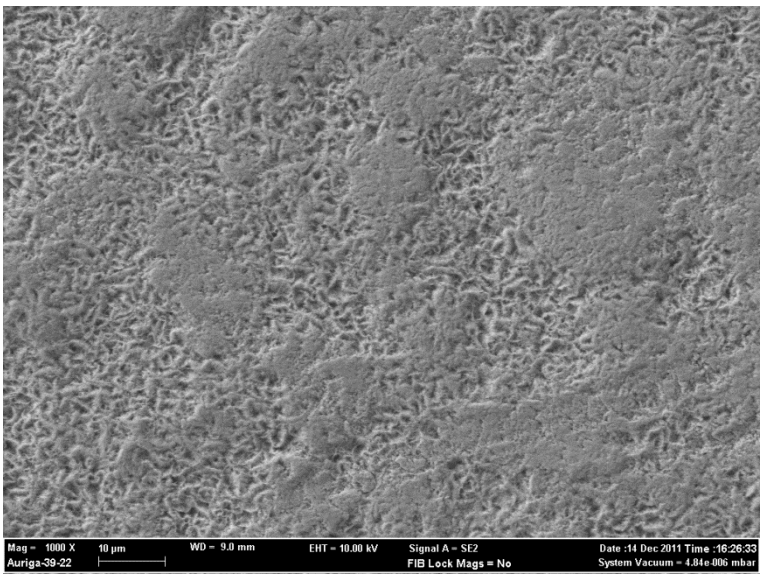

Figure 4.4 Surface morphology of deposits obtained at 10 mA cm^{-2} from Sn-Bi+5g/L HQ+2g/L gelatin plating bath (deposition time: 60 minutes).

4.3.1.4 Effects of current density

From earlier results, the formation of loose deposits in additive-free and HQ-containing bath is suggested to be related to the preferential deposition of Bi with rough surface morphology at early stages of electrodeposition (***Section 4.3.1.1***). However, the loose deposits are obtained at an applied current density of 10 mA cm^{-2}, where ambiguity may arise that current density is too low hence the overpotential is not sufficient for deposition of the more active element Sn. In this section, current density is varied from 10-30 mA cm^{-2} to investigate its effect on the morphology and composition of the electrodeposits. Figure 4.5 (a)-(c) show the FESEM micrographs of deposits obtained after 60 minutes at different current densities of 10, 20, and 30 mA cm^{-2} in Sn-Bi plating solution without additives. As mentioned earlier, loose deposits form during the electrodeposition process and which fell off during post-deposition cleaning of the electrodeposits. The micrographs only represent the deposits that are still adhered to the Cu substrate. EDX analyses shows that the composition of all adhering deposits obtained from this plating bath within the current density range 10-30 mA cm^{-2} are pure

Bi. It was then further seen that even at higher current densities, Sn ions with more electronegative deposition potential still fails to deposit. With the deposition potentials too far apart, increasing the current density is not sufficient to achieve the overpotential needed for Sn deposition to take place. Also, when the applied current density is much higher than the limiting current density of Bi (-10.2 mA cm^{-2}), there is a high tendency for burnt and spongy deposits to form (Tan, 1993). This is consistent with the observation during electrodeposition in additive-free bath, where the amount of loose deposits increases with increasing current density. This leads to a substantial decrease in current efficiency, which is calculated by weight of electrodeposits utilizing Equation (2-8) and (2-9) and presented in Figure 4.6.

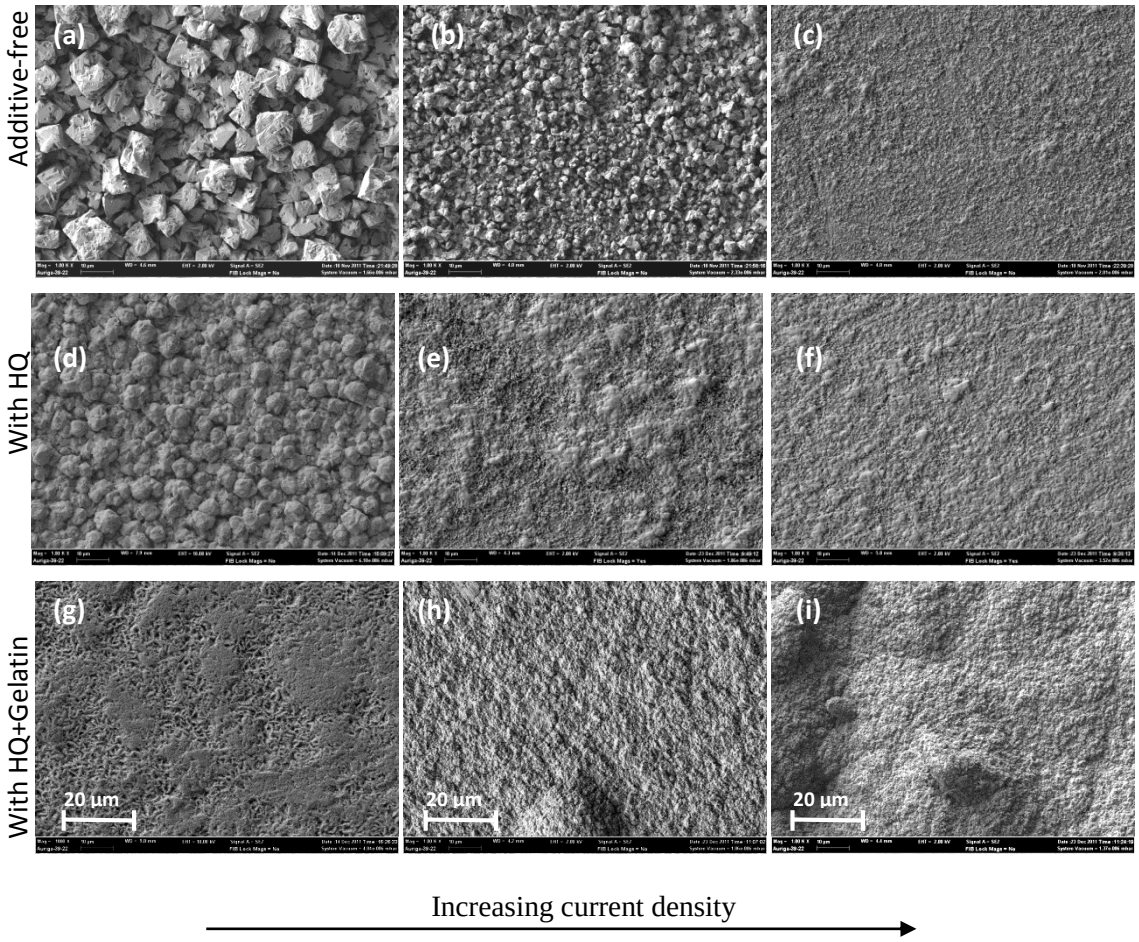

Figure 4.5 Surface morphology of deposits prepared from Sn-Bi plating solutions: without additives at (a) 10 mA cm^{-2}, (b) 20 mA cm^{-2}, (c) 30 mA cm^{-2}; with HQ at (d) 10 mA cm^{-2}, (e) 20 mA cm^{-2}, (f) 30 mA cm^{-2} ; and with HQ and gelatin at (g) 10 mA cm^{-2}, (h) 20 mA cm^{-2}, (i) 30 mA cm^{-2}.

The variation in current density resulted in morphological changes of the deposits. Generally, the Bi deposits obtained from additive-free plating baths are coarse and rocky. But there is a trend where the crystal structure of the Bi deposits becomes finer as the current density increases (from Figure 4.5 (a)-(c)). This is because at higher current densities (high overpotential), the rate of nucleation is greater than the growth rate of the fresh nuclei at the initial stage of deposition (J. Y. Kim et al., 2004; Mallik et al., 2014; Sharma, Bhattacharya, Das, & Das, 2014). Hence, finer and more compact crystals are expected at higher applied current densities.

The topography micrographs of electrodeposits from HQ-containing Sn-Bi plating baths after 60 minutes deposition at different current densities of 10, 20, and 30 mA cm^{-2} are shown in Figure 4.5 (d)-(f). Similarly, the micrographs only represent the surface of adherent deposits. Compared to deposits from additive-free plating bath, the HQ addition to the plating bath has resulted in rounded and finer surface features. The adsorption effect of HQ reduced the active sites for crystal growth hence resulted in deposits with finer crystal structures (Figure 4.5(d)-(f)) compared to the deposits from additive-free bath (Figure 4.5(a)-(c)). From the EDX analyses, the composition of adhering deposits obtained from this Sn-Bi+HQ plating bath within the current density range 10-30 mA cm^{-2} are pure Bi. As the addition of HQ did not reduce the deposition potential gap between Sn and Bi, this composition is within expectations.

The surface morphology of the electrodeposits obtained from the plating bath containing both HQ and gelatin becomes finer and more compact with increasing current density (Figure 4.5(g)-(i)). This can be attributed to the synergistic effects of HQ and gelatin which formed complexes with Bi ions to allow co-deposition, and also adsorb strongly on the electrode surface to suppress the nuclei growth significantly. The

current efficiencies in this HQ and gelatin containing plating bath are higher than in previous cases (without additives and with HQ), and the efficiencies are generally near to 100% as shown in Figure 4.6. This indicates that proper electrodeposition is achieved in this plating bath where loose deposits no longer form.

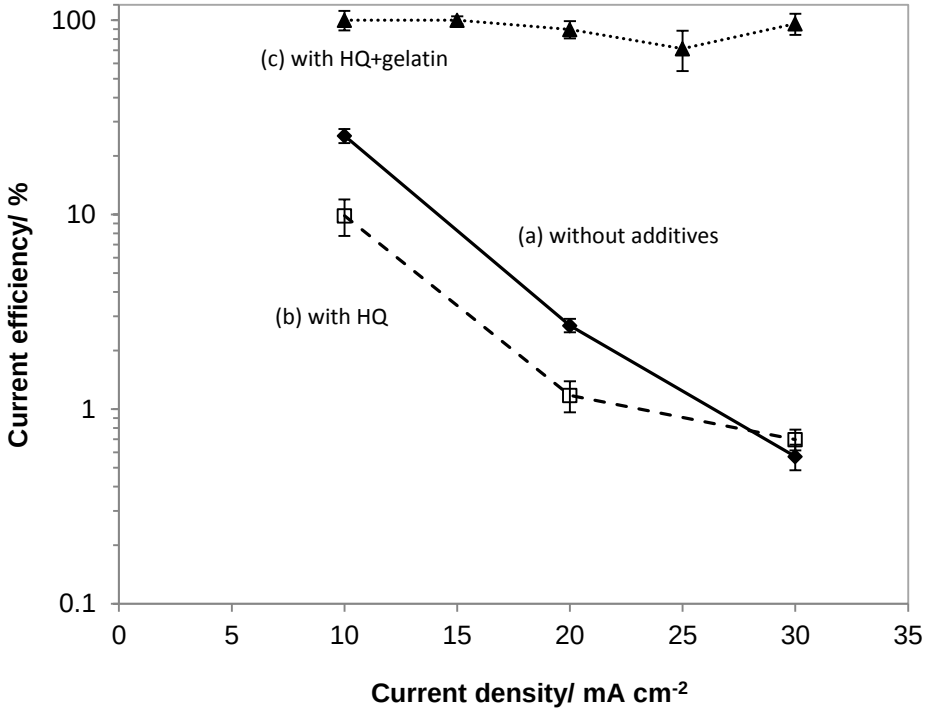

Figure 4.6 Current efficiency (calculated by weight of deposits) of Sn-Bi plating baths (a) without additives, (b) with HQ, and (c) with HQ+gelatin.

However, the electron micrographs of Sn-Bi deposits obtained at high current density of 20 and 30 mA cm^{-2} (Figure 4.5 (h) and (i)) is taken at higher magnifications and on smoother areas. At lower magnifications, it is observed that at current densities above 20 mA cm^{-2}, there are large overplated crystals and dendrites growing out of the smooth and uniform surface, where representative micrographs are shown in Figure 4.7. This phenomenon seemed to occur at a later stage where there is a possibility of gelatin depletion. It is reported that gelatin undergoes decomposition via acid hydrolysis in electrolytes (Brown & Hope, 1995; Saban, Scott, & Cassidy, 1992). Saban et al. (1992) showed that gelatin undergoes decomposition after about 40-80 minutes of plating time

in a sulfuric acid based Cu plating bath, depending on the mass transfer rate of the electrolyte solution. The decomposition of gelatin may result in a decrease in adsorption coverage area. The electrode surface not covered by gelatin adsorption bonds will become preferential nucleation and growth sites for the metal ions, hence resulting in outward growth of deposits at selected areas.

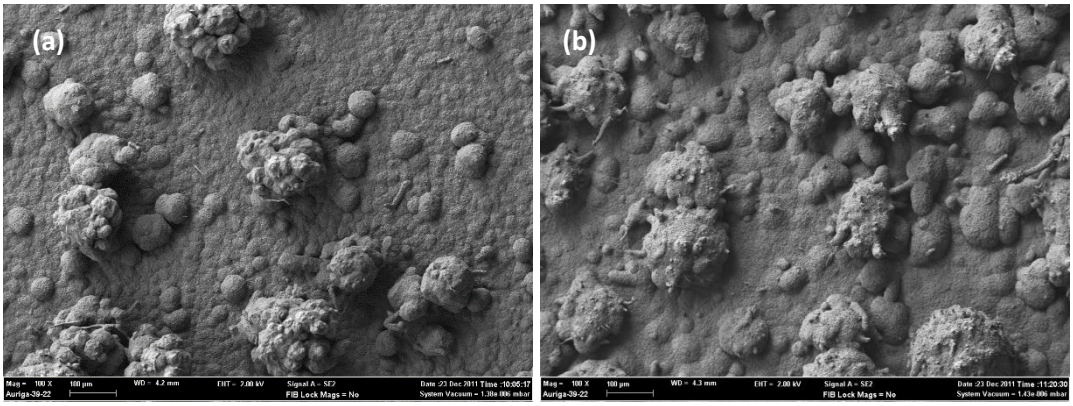

Figure 4.7 Surface morphology of deposits from Sn-Bi+HQ+gelatin plating solution at current density of (a) 20 mA cm^{-2}, and (b) 30 mA cm^{-2}.

EDX analyses were carried out on the deposits and the average composition is taken from smooth surfaces without large crystals. Curve (a) in Figure 4.8 shows the Bi content in deposits versus current density obtained experimentally from the plating bath containing both HQ and gelatin. The Bi content decreases with increasing current density. This is consistent with the general rule for co-deposition of alloys where the more noble metal is preferentially deposited at lower current densities. In ***Section 3.3.7***, the estimation of alloy compositions from the polarization curves has been suggested and the estimated values are tabulated in Table 3.2. To compare the estimated compositions with experimental data, the estimated alloy composition from polarization curve of Sn-Bi+HQ+gelatin plating solutions is plotted in curve (b), Figure 4.8. The trend exhibited by both the experimental and estimated data is rather similar, where the experimental data shows some deviation. The applied current density of 10-30 mA cm^{-2} in intervals of 5 mA cm^{-2} did not yield the eutectic Sn-Bi alloy composition. To obtain

the desired eutectic alloy composition of Sn-58wt.% Bi, a current density of 18 mA cm^{-2} is applied based on the estimation from polarization curves.

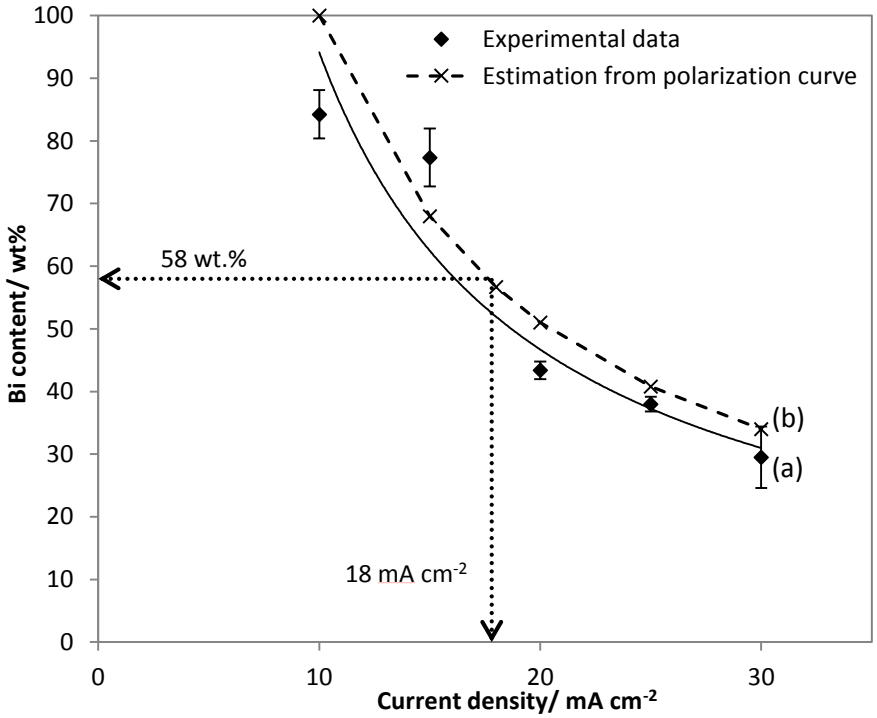

Figure 4.8 Bi content in electrodeposits (a) from experimental results and (b) estimated from polarization curve vs. applied current density.

4.3.2 Electrodeposition of Sn-Bi eutectic alloys

Sn-Bi electrodeposits are deposited at 18 mA cm^{-2} for 60 minutes in the plating bath containing both HQ and gelatin as additives. The electrodeposits were characterized under FESEM/EDX, DSC, and XRD. The topography micrograph of the electrodeposits shows smooth and uniform structures without large crystals (Figure 4.9(a)), which is similar to deposits at lower current densities (Figure 4.5(g)). A representative EDX spectrum of the electrodpeosits is shown in Figure 4.9(b). The average chemical composition obtained from three samples electroplated at this current density is Sn-60.75 wt.% Bi, which is close enough to the eutectic (Sn-58 wt.% Bi) composition. The current density of 18 mA cm^{-2} is found to be the optimum current density which yields smooth and uniform microstructures and near-eutectic composition.

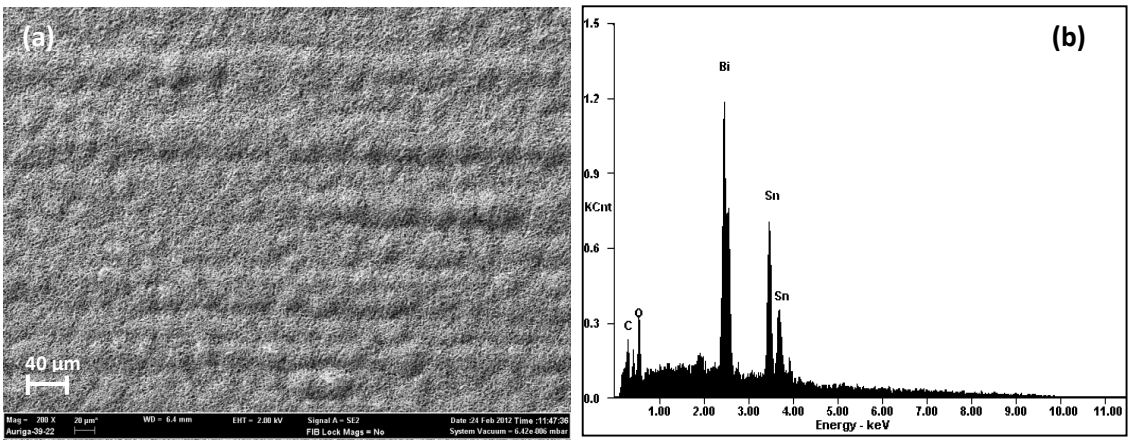

Figure 4.9 (a) Surface morphology of electrodeposits obtained at current density of 18mA cm^{-2} from Sn-Bi+HQ+gelatin plating solution, and (b) representative EDX spectrum of the electrodeposits.

The melting point is a physical property that can further indicate the composition of the electrodeposited alloy. The electrodeposited Sn-Bi thin film was scraped carefully from the substrate and was subjected to DSC analysis. The extrapolated onset temperature from DSC analysis of this near-eutectic Sn-Bi solder alloy suggests that the melting temperature is around 137.4^{o}C (Figure 4.10), which is near the eutectic melting temperature (138^{o}C).

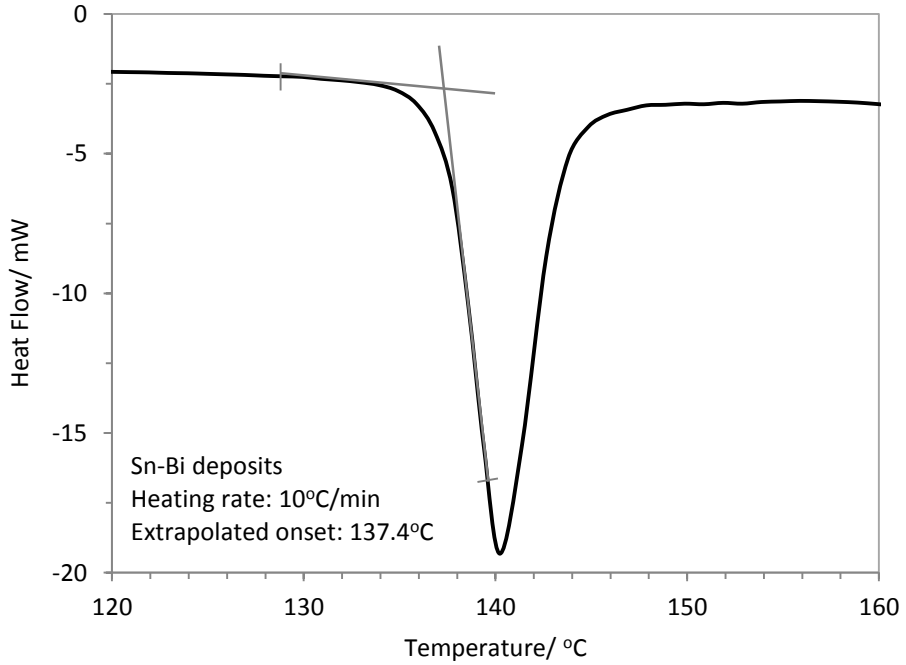

Figure 4.10 DSC curve of Sn-60.75 wt.% Bi electrodeposits.

Further characterization on the crystallinity of the electrodeposits is performed by XRD analysis. Figure 4.11 shows XRD spectrum of samples prepared at 18 mA cm^{-2} (the near-eutectic Sn-Bi alloy) and at 30 mA cm^{-2} (Sn-29.51 wt.% Bi with large crystals). The patterns mainly show sharp peaks belonging to Sn and Bi. The sharp peaks in the XRD patterns of the near-eutectic Sn-Bi alloy prepared at 18 mA cm^{-2} and Sn-29.51 wt.% Bi alloy prepared at 30 mA cm^{-2} indicate that the deposits obtained under the experimental conditions possess good crystallinity. Compared to Sn peaks, Bi peaks are more prominent in deposits obtained at 18 mA cm^{-2} and less prominent in that obtained at 30 mA cm^{-2}. This is consistent with the composition of the deposits. The preferred orientation of Sn and Bi metal is (211) and (012) respectively for the near-eutectic Sn-Bi alloy (spectrum (a), Figure 4.11); while it is (200) and (122) respectively for the Sn-rich alloy (spectrum (b), Figure 4.11). It is known that the crystal orientation of the Sn-Bi electrodeposits is highly dependent on the alloy composition as well as the crystal orientation of substrates (Tsai & Hu, 2009b). Since the Cu substrates used in this work is of commercial grade, it is difficult to compare the preferred crystal orientation of electrodeposited Sn-Bi alloys.

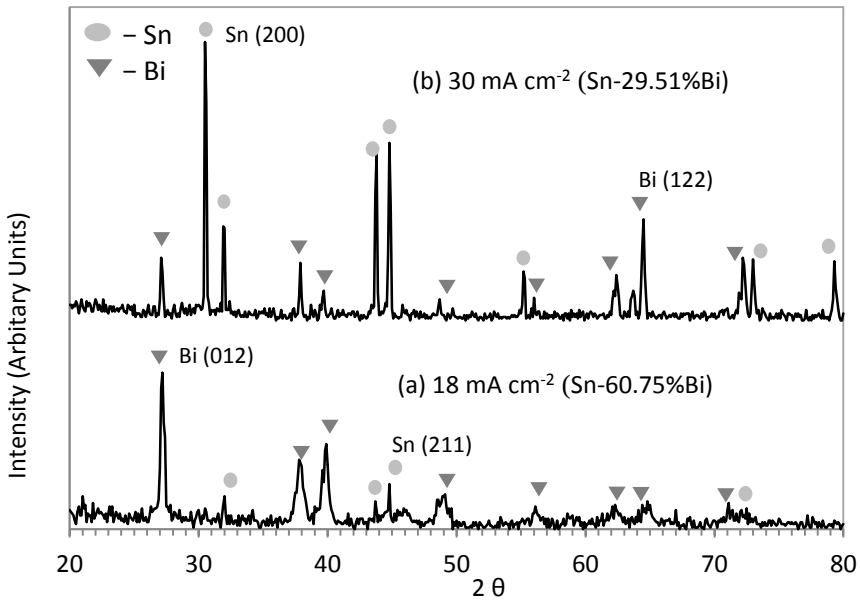

Figure 4.11 XRD spectrum of deposits prepared at (a) 18 mA cm^{-2} (Sn-60.75 wt.% Bi) and (b) 30 mA cm^{-2} (Sn-29.51 wt.% Bi).

4.3.3 Microstructure of Electrodeposited Sn-Bi alloys

4.3.3.1 Microstructure of as-electroplated Sn-Bi alloy films

The cross-sectional areas of as-electrodeposited Sn-Bi films under different current densities are characterized by FESEM (with backscattered electron detector) to analyze the microstructure of the alloys. Samples electrodeposited for 60 minutes at current densities of 10, 18, and 30 mA cm^{-2}, which represented low, optimum, and high current densities respectively, are selected for this investigation. Figure 4.12(a), (b) and (c) shows the cross-sectional views of Sn-Bi films deposited at 10, 18, and 30 mA cm^{-2} respectively; while Figure 4.12(d), (e) and (f) are the magnified micrographs near the solder/substrate interface of the samples. Generally, the Sn-Bi alloys show two distinct features where the brighter phase is Bi and the darker phase is Sn. The Bi atoms have higher molecular weight of 208.98 g/mol compared to Sn (118.71 g/mol) have caused stronger backscattering of electrons, thus appear brighter in the micrographs. The Sn-Bi alloy phase diagram does not show any intermetallic phase. The elements do not dissolve in each other, and exist as two phase alloy. No obvious reactions happen between the as-electrodeposited alloys and the Cu substrate as there are no intermetallic compounds (IMC) seen at the Sn-Bi/Cu interface. Micro-voids are observed in all cases.

From Figure 4.12(a), the Sn-Bi film electrodeposited at 10 mA cm^{-2} shows good uniformity. The magnified micrograph of the deposits obtained at 10 mA cm^{-2} (Figure 4.12(d)) shows that there is a bright layer formed at the Sn-Bi/Cu interface, where EDX point analysis shows that it is pure Bi. This is in agreement with the galvanostatic studies outcome discussed in ***Section 3.3.7***. At 10 mA cm^{-2}, electrodeposition started at a potential of about -50 mV, where at such noble potential only pure Bi deposition will take place (curve (a), Figure 3.22). At some point of the deposition (varies for every experiment), fluctuations of deposition potential is observed between -30mV and -

430mV. Since the current applied is dependent on the surface area of the electrode, the changes in surface roughness will affect the area of the substrate thus causing a slight change in current density. This has caused the potential value to fluctuate and hence resulted in Sn-Bi co-deposition instead of pure Bi deposition, which is why pure Bi is not obtained as predicted from the polarization curves. This also explains the microstructure of the as-electrodeposited film, where a Bi-rich layer is first deposited and then followed by the co-deposition of Sn-Bi. From Figure 4.12(d), it can be seen that there are numerous black spots which are actually voids. With current efficiency of nearly 100%, such voids are not caused by hydrogen gas bubbles entrapped in the deposits. These voids are possibly caused by inclusion of additives or oxide particles.

The Sn-Bi alloys electrodeposited at 18 mA cm^{-2} shows good surface uniformity (Figure 4.12(b)). The magnified micrograph of the as-electrodeposited Sn-60.75wt.% alloy (Figure 4.12(e)) shows the alloy exist in two phases where the Bi rich phase is embedded in the Sn matrix. Previous analysis of the topography of Sn-Bi alloys deposited at 30 mA cm^{-2} shows large amount of outward growing crystal structures (Figure 4.7(b)), and the cross-sectional view of the deposits is in agreement with previous observations. Figure 4.12(c) shows the electron micrograph of the alloy deposited at 30 mA cm^{-2}. It is observed that there is proper deposition up to about 40 μm of thickness, before the outward growth takes place at certain locations of the film (labelled X and Y in Figure 4.12(c)). At higher current densities (higher overpotentials), additives near the electrode surface deplete at a higher rate. When adsorption bonds at the electrode surface no longer exist, growth of nuclei can no longer be suppressed to a lower rate and such outward growing crystal structures will be observed. The magnified view of the alloy film also shows two-phase structure.

10 mA cm^{-2}

18 mA cm^{-2}

30 mA cm^{-2}

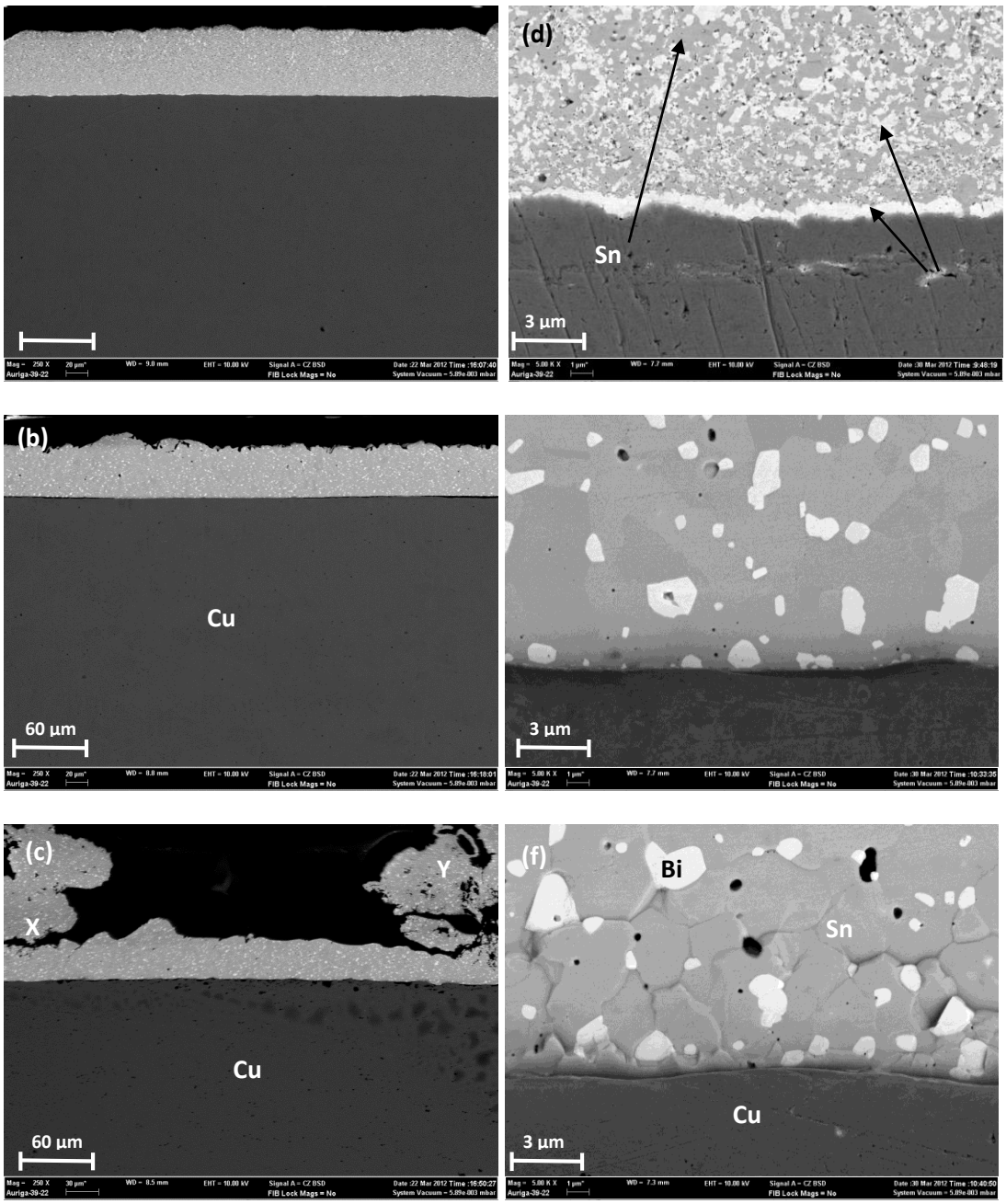

Figure 4.12 Micrographs of cross-sectional areas of Sn-Bi alloy films electrodeposited at a current density of (a) 10 mA cm^{-2}, (b) 18 mA cm^{-2}, and (c) 30 mA cm^{-2}; (d), (e) and (f) are the respective magnified view near the alloy/substrate interface.

4.3.3.2 Microstructure of reflowed Sn-Bi alloy films

The electrodeposited Sn-Bi alloys are reflowed at 170^{o}C and the microstructures are investigated. The micrographs of reflowed alloys deposited at different current densities are presented in Figure 4.13. The microstructure of the reflowed alloy deposited at 10 mA cm^{-2} is shown in Figure 4.13(a). The alloy is rich in Bi phase (lighter regions) with Sn phase (darker regions) embedded. The as-electrodeposited sample shows that there

are lots of microvoids present, and during reflow the microvoids coalesce to form large voids in the alloy. The magnified micrograph near the interface shows formation of intermetallics. EDX point analysis suggests that Cu_6Sn_5 is formed with the weight percent ratio of 39.07% Cu and 60.93% Sn. The EDX point analysis results are shown in Figure 4.14.

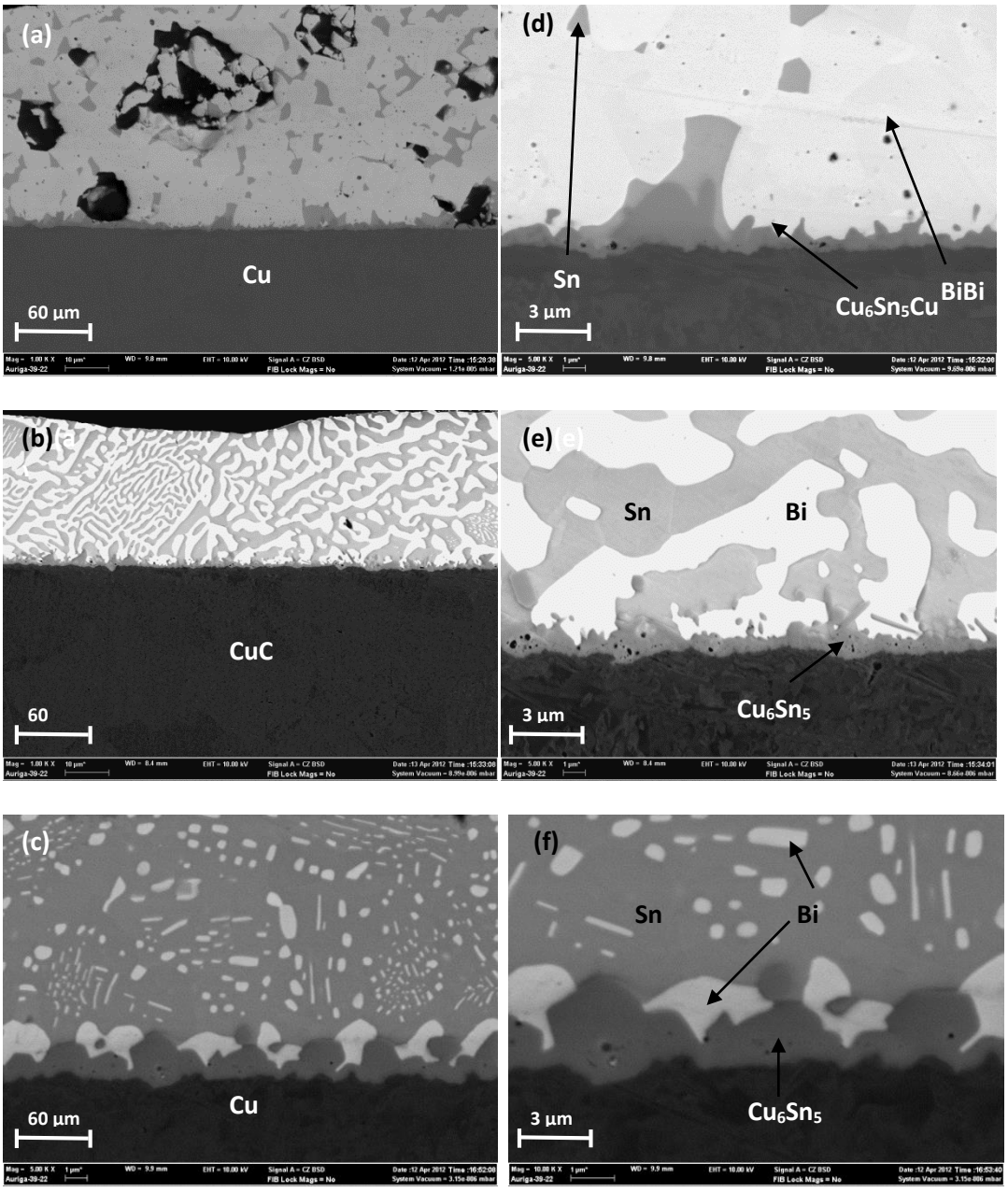

Figure 4.13 Micrographs of cross-sectional areas of reflowed Sn-Bi alloy films electrodeposited at a current density of (a) 10 mA cm^{-2}, (b) 18 mA cm^{-2}, and (c) 30 mA cm^{-2}; (d), (e) and (f) are the respective magnified view near the reflowed alloy/substrate interface.

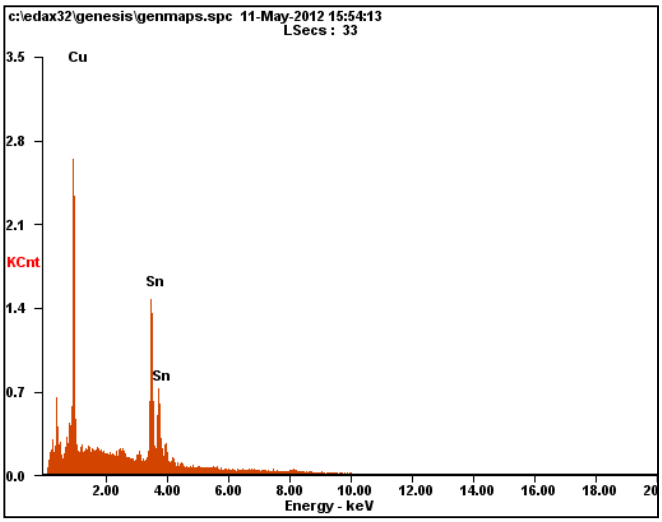

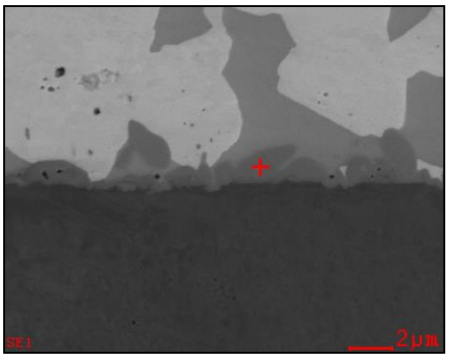

Element	*Wt%*	*At%*
CuL	39.07	54.49
SnL	60.93	45.51
Matrix	Correction	ZAF

Figure 4.14 EDX spectrum for the respective point analysis at the interface of reflowed alloy/substrate interface.

The microstructure of the reflowed near-eutectic Sn-Bi alloy deposited at 18 mA cm^{-2} is presented in Figure 4.13(b). The reflowed sample shows a homogeneous distribution of the Bi-rich light phase and Sn-rich dark phase regions. The microstructure is near eutectic as expected from the phase diagram and very similar to microstructure of metallurgically prepared eutectic Sn-Bi alloys. Magnified micrograph of this sample shows formation of Cu_6Sn_5 IMC.

The sample electrodeposited at 30 mA cm^{-2} yields a different microstructure after reflow, despite having a similar microstructure with 18 mA cm^{-2} sample in the as-electrodeposited form. The reflowed alloy shows majority of Sn-rich phases, with Bi phases embedded within the Sn matrix as well as segregated near the interface (Figure 4.13(c) and (f)). The segregation of Bi may be due to the consumption of Sn near the interface during the IMC formation, hence leaving behind Bi rich phases near the IMC layer.

4.4 Chapter conclusions

The large deposition potential gap between Sn and Bi is the main hindrance to proper metal deposition. Without the aid of additives, or with only HQ added, the deposition potential gap was too big and only the more noble element Bi was deposited. The synergistic effects of HQ and gelatin made co-deposition of Sn-Bi achievable. The crystal structure of electrodeposits got finer with increasing current density. Large outward growing crystals formed at higher current densities, which were attributed to the breaking of adsorption bonds at the electrode surface. Composition control of electrodeposits was achieved by manipulating the applied current density. Current efficiency of the Sn-Bi+5g/L HQ+2g/L gelatin plating bath was nearly 100%. Near-eutectic dendrite-free Sn-60.75wt.% Bi alloy was produced at an applied current density of 18mA cm^{-2}. The microstructure of the near-eutectic alloy was very similar to the ones obtained by metallurgical processing.

CHAPTER 5

SHEAR STRENGTH AND FRACTURE BEHAVIOUR OF ELECTRODEPOSITED SN-BI/CU SOLDER JOINTS

5.1 Background

Solder interconnections play a key role not only as conductive electrical paths, but also as mechanical bonds between different elements of the electronic device. Thus, solder materials have to provide good metallurgical bonding while offering the necessary conduction and mechanical strength. With the continual reduction in package size, the reliability of solder joints is gaining considerable attention. Interfacial reactions between the solder material and the substrate dictate the bonding strength of the joint. The interfacial reactions between Sn-Bi and Cu substrates have been studied, attributable to the recent interest in Sn-58Bi as a substituting alloy for Pb-bearing solders (Hu, Li, Li, & Min, 2013; Q. K. Zhang, Zou, & Zhang, 2011; Zou, Zhang, & Zhang, 2012). Understanding the interfacial reactions of the solder joints is essential as previous reports claim that the intermetallic compound (IMC) determines the fracture mode of the joints (Schlesinger & Paunovic, 2010; M. Yang et al., 2010). Also, the Cu_6Sn_5 IMC that forms at the interface can have different morphologies under different thermal conditions which also affects the shear strength of the solder joints (M. Yang et al., 2010). However, discussions on the interrelationships between solder microstructure, IMC formation, shear strength, and fracture mode for the Sn-Bi/Cu system are not yet available.

The lap-shear tests are is widely utilized to evaluate the shear, creep and thermal fatigue behaviour of Sn-based solder joints because the general deformation mode in such tests simulates the real life loading of the interconnections (Shen et al., 2005). The shear stress is taken as the axial load applied divided by the solder joint area; while

shear strain is the applied displacement divided by the solder thickness. Complex deformation fields are involved in such loading conditions, therefore the shear strain value can only be taken as a rough estimation (Shen et al., 2005). The shear behaviour reported in different studies generally varies even for identical solder composition and substrate combinations. For instance, some reports showed that aging of Sn-58Bi/Cu joints increased the shear strength (Felton et al., 1993; Raeder et al., 1994); while the work by other authors showed a decreased strength (M. S. Suh, Park, & Kwon, 2008). This may be due to the variance in soldering conditions, joint geometry, and testing conditions (Miao et al., 2000; Schlesinger & Paunovic, 2010; Tomlinson & Fullylove, 1992; L. M. Yang, Zhang, & Zhang, 2012). The effects of joint geometry on the shear behaviour of solder joints are seldom reported. Poor geometry design may result in a large variance between far-field and nominal response of the shear behaviour of solder joints. The far-field response refers to the shear response measured by the equipment for the overall substrate-solder assembly; while the nominal response refers to the actual shear response in the solder. In this work, the joint geometry was designed with reference to a few literature and standards (D1002-10, 2010; Shen et al., 2005; Siewert & Handwerker, 2002), to minimize the deformation and bending of Cu substrate during lap shear tests, allowing more reliable far-field displacement data collection. Shen et al. (2005) conducted an analysis based on numerical modeling by finite element analysis to compare the effects of solder joint geometry on the accuracy of responses obtained from shear tests. A schematic diagram of solder-substrate assembly is presented in Figure 5.1 to define the typical parameters involved in lap shear tests. Some preliminary tests were conducted in this work based on the key findings of Shen et al. (2005), and the following effects were taken into account:

- *Effects of solder thickness, t:* for larger solder thickness, far-field response is closer to nominal response; while for smaller solder thickness, substrate carries most deformation. In this work, the target solder thickness is set at a nominal value of 50μm to simulate the miniaturization of interconnections. The solder thickness effect will be discussed further in this chapter.

- *Effects of overlap length, b:* large overlap length results in a prolonged elastic regime in measurements; for a large $\frac{\text{solder thickness}}{\text{overlap length}}$ ratio, far-field response is closer to nominal response. The overlap length in this work is set at 5 mm, resulting in a ratio value of 0.01. This is to take into account applicability of overlap geometry during sample preparation. Samples with overlap lengths smaller than 5 mm are too fragile to be handled, and may damage before the lap shear tests are conducted.

- *Effects of substrate thickness and length (excluding overlap length),* $\frac{a}{d}$*:* substrate should be as thick as possible to achieve response close to nominal response; for a large $\frac{\text{substrate thickness}}{\text{substrate length}}$ ratio, far-field response is closer to nominal response. Thickness of substrate in this work is 5 mm and substrate length is 15 mm, giving a ratio of 0.33. The grip area has to be set at about 3 times the overlap length away from the joints to minimize the gripping effect during measurements.

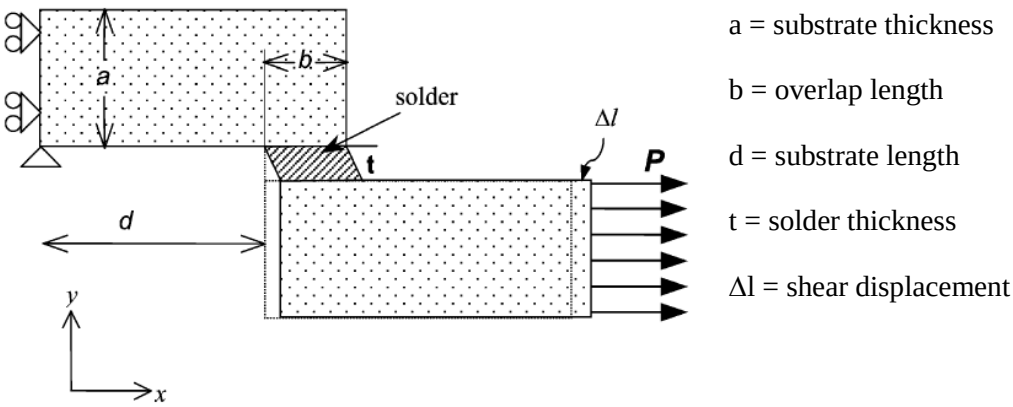

Figure 5.1 Schematic of solder–substrate assembly and definition of parameters associated with the lap-shear test (Shen et al., 2005).

5.2 Experimental

Lap shear specimens were prepared by joining two pieces of commercially pure 35mm X 35mm Cu plates of 5mm thickness, with an overlap length of 5mm. The eutectic Sn-Bi solder alloy was electroplated onto both the Cu plates using the previously developed electroplating bath and optimized parameters as described in Chapter 4. The electroplating bath was composed of 120ml/L of methane sulfonic acid (CH_3SO_3H), 30g/L of $SnSO_4$, 9g/L of Bi_2O_3, 5g/L of hydroquinone and 2g/L of gelatin. The electroplating was performed at a current density of 18mA cm^{-2} for a plating time of 30 mins which resulted in a solder thickness of 25µm on one face of the Cu plate. Water-soluble flux was applied on both electroplated Cu substrates prior to reflow. The two electroplated Cu plates were aligned and a slight pressure of about 0.5 MPa was applied. Reflow of the joints were performed with a reflow oven (C.I.F. Forced Convection FT02) and a schematic reflow profile is shown in Figure 5.2. The joints were pre-heated to a temperature of 150^{o}C and held for 3 minutes, and then reflowed at three different temperatures of 200^{o}C, 230^{o}C and 260^{o}C for 10 minutes. A higher reflow temperature and long reflow period was applied to provide sufficient time for heat re-distribution due to the large size of the Cu substrate in this case. The samples were cooled in the

oven for 15 mins (default mode of the reflow oven) and later removed to be cooled at room temperature.

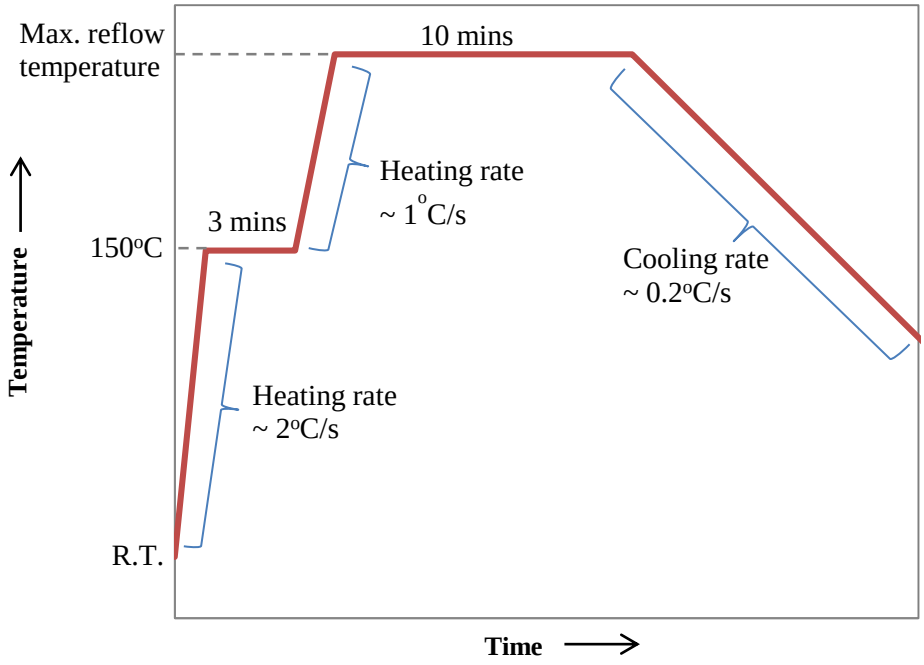

Figure 5.2 Schematic reflow profile (R.T. = room temperature; Maximum reflow temperature is 200°C, 230°C or 260°C).

Figure 5.3 shows the schematic diagram of the reflowed solder joints. The reflowed joints (Figure 5.3(a)) were cut into strips of 5 mm width using electric discharge machining (EDM). Seven samples were produced after cutting the joined Cu plates as illustrated in Figure 5.3(b). The preparation of at least five shear samples from a single bulk sample was in accordance to ASTM D1002-10. Specimens situated at the middle (numbered 2 to 6 in Figure 5.3(a)) were mechanically tested, while the specimens at both ends (numbered 1 and 7) were used for microstructure investigations. Lap shear tests were performed on the specimens using the Instron 5848 MicroTester. Cross sectional samples of as-reflowed Sn-Bi solder alloy joints were polished using standard metallurgraphic procedures down to 0.04 µm colloidal silica suspensions. All cross-sectional samples were examined under a field emission scanning electron microscope (FESEM) (Auriga Zeiss Ultra-60) in the backscattered electron mode. The

lap shear specimens were loaded to failure at a strain rate of 4×10^{-4} /s. The failed solder joints were kept carefully without damaging the fracture surface. Fractography was performed with FESEM (Quanta FEG 450) coupled with energy dispersive X-ray spectroscopy (EDX) (Oxford Instruments X-Max). Cross sectional analysis of failed samples was performed with FESEM (Hitachi SU8030).

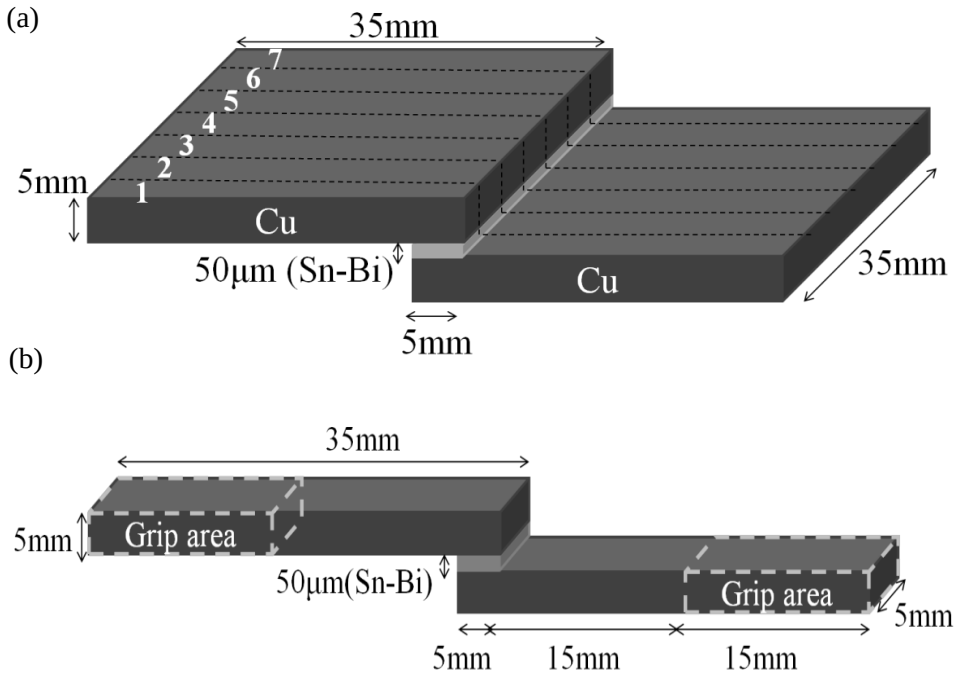

Figure 5.3 Schematic diagram of (a) as-reflowed solder joint and (b) solder joint of 5 mm width machined with EDM.

5.3 Results and discussion

5.3.1 Effects of reflow temperature on microstructure of solder joints

Representative micrographs of Cu/Sn-Bi/Cu solder joints reflowed at 200^{o}C, 230^{o}C, and 260^{o}C are shown in Figure 5.4(a), (b) and (c) respectively. EDX point analysis showed that the lighter shade (white) regions are Bi-rich phase while the darker shade (greyish) regions are Sn-rich phase. EDX area analysis was also performed on five randomly selected areas measuring 20 x 20 µm on the cross sectional sample and the average composition is found to be Sn-59.8wt.%Bi, which is near to the eutectic composition.

Micrographs taken at higher magnification at the Sn-Bi/Cu interface of the joints reflowed at 200^{o}C, 230^{o}C, and 260^{o}C are shown in Figure 5.4(d), (e) and (f) respectively. Under high magnification, the morphology of the interfacial IMC is seen to be different. Figure 5.4(d) shows that the Cu_6Sn_5 morphology formed at a reflow temperature of 200^{o}C is of prism-type. While the reflow temperature of 230^{o}C and 260^{o}C yields scallop-type IMC morphology (Figure 5.4(e) & 5.4(f)). The nucleation and growth of IMC is highly dependent on the soldering temperature, cooling rate and concentration of Cu and Sn (Gu, Qu, Ma, Luo, & Wang, 2011; Laurila, Vuorinen, & Kivilahti, 2005; M. Yang et al., 2010). At a lower reflow temperature of 200^{o}C, the formation of prism-like IMC at the interface shows that nucleation is the dominant factor. While at higher temperatures of 230^{o}C and 260^{o}C, the formation of scallop-like IMC at the interface suggests that grain growth is the dominant factor. A very thin layer of Cu_3Sn IMC is also found between the Cu_6Sn_5 and Cu substrate in all cases. The thickness of the Cu_3Sn layer increases with increasing reflow temperature, which is in accordance to thermodynamics.

It is also worth mentioning that there are some thickness variations for specimens reflowed at different temperatures. Pressure had to be applied to the joints during reflow to improve adhesion and minimize void formation. But the applied pressure caused the molten solder to flow out of the joint area, resulting in a lower thickness as seen for the sample reflowed at 260^{o}C (Figure 5.4(c)) . These variations will be taken into account during discussion in the next section.

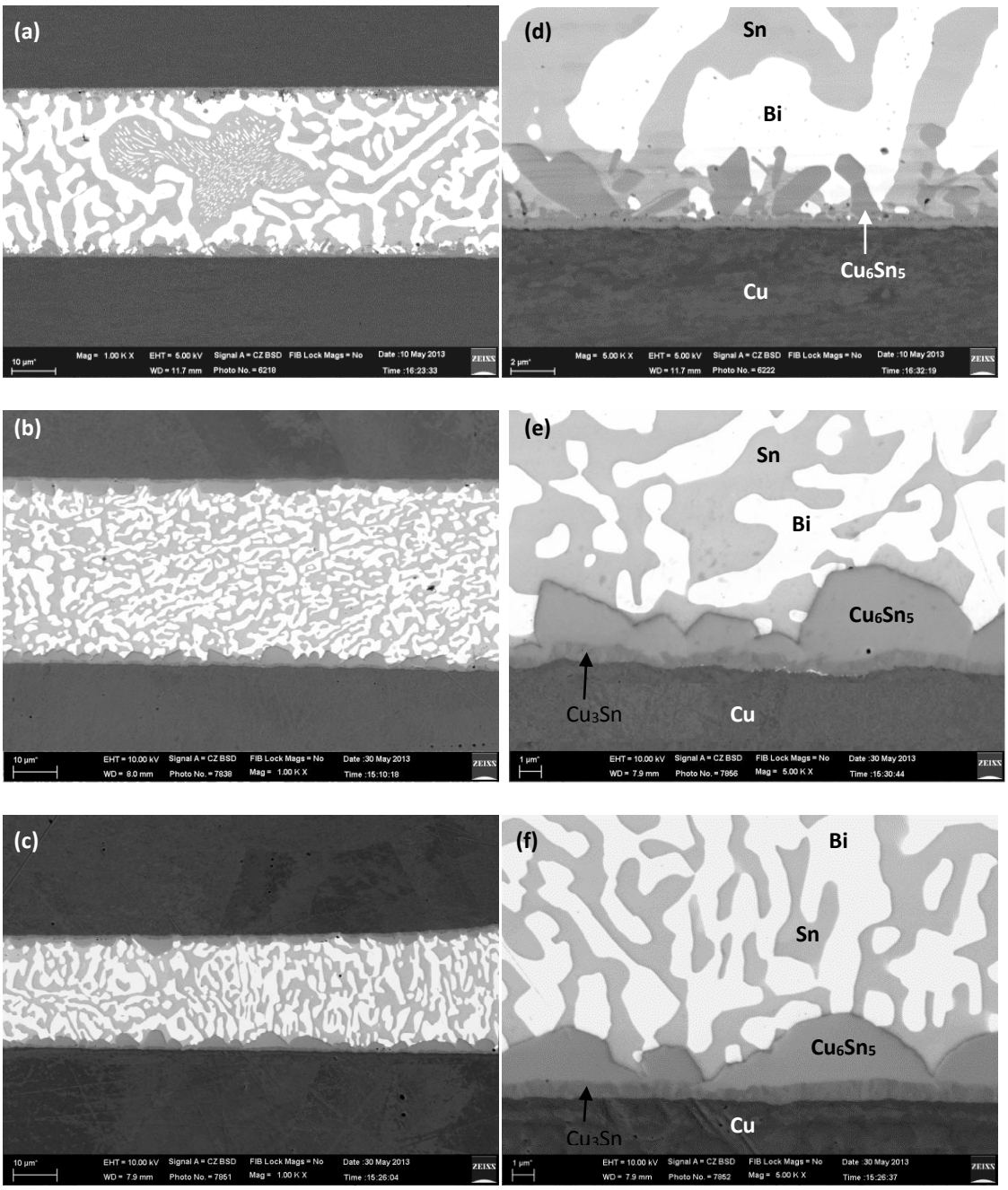

Figure 5.4 Cu/Sn-Bi/Cu joint reflowed at (a) 200ºC, (b) 230ºC, (c) 260ºC, with the magnified micrograph of IMC morphology shown in (d, e and f) respectively.

5.3.2 Effects of reflow temperature on shear strength of solder joints

The solder joints for lap shear tests were loaded to failure in a tensile mode at a strain rate of 4×10^{-4} /s. Figure 5.5(a) shows the representative shear stress-shear-strain curve of samples taken from positions numbered 2 to 6 (Figure 5.3). The elastic regime of the shear stress-shear strain curve of the solder joints is similar for all three reflow temperatures. This indicates that the shear modulus is not affected by varying the reflow

temperature which is expected as the modulus is a structure insensitive property. Beyond the elastic regime, work hardening occurs in the solder joints until the maximum shear strength is reached, at which fracture occurs.

The average maximum shear stress shown in Figure 5.5(b) is the average value from 15 samples for each reflow temperature, with the standard deviation shown as the error bar. It is found that the maximum shear stress increases with increasing reflow temperature. An ambiguity arises in that the shear strength of samples may have been influenced by solder thickness. It is known that a decrease in solder thickness results in an increase in maximum shear stress (Shen et al., 2005; L. M. Yang et al., 2012). The sample reflowed at 260^{o}C has a thickness lower than that of the sample reflowed at 230^{o}C. And the maximum shear stress of the sample reflowed at 260^{o}C is higher than the sample produced at 230^{o}C. Hence, the increased shear strength of the solder joint reflowed at 260^{o}C can be due to the reduced solder thickness. Yang et al. (2012) developed a numerical equation to relate the shear strength of the solder joints with the solder thickness. The maximum shear stress of a solder joint can be expressed as (L. M. Yang et al., 2012):

$$\tau_{max} = \frac{\tau_c}{1+ \lambda R} \qquad (5\text{-}1)$$

where τ_c and λ are constants that depend on the solder composition, substrate and soldering conditions, and R is the ratio of solder thickness to overlap length. The authors claimed that experimental data obtained in their work fitted exactly with this equation. In this work, the expected solder thickness is 50μm and the overlap length is 5 mm. The ratio R would be 0.01. If the solder thickness is reduced to 25μm after reflow, the ratio R becomes 0.005. Taking λ = 1.5 with reference to the work of Yang et al. (2012), the ratio R of 0.01 and 0.005 would give τ_{max} value of $\frac{\tau_c}{1.015}$ and $\frac{\tau_c}{1.0075}$

respectively. With τ_c values of Pb-free solder alloys lie typically between 30 – 60 MPa, the difference in ratios $\frac{\tau_c}{1.015}$ and $\frac{\tau_c}{1.0075}$ only yields a maximum shear stress difference of less than 0.5MPa. It is therefore seen that the thickness effect in the present case is very minimal. The thickness effect is only pronounced when the ratio R is greater than 1 (L. M. Yang et al., 2012). Also, the samples reflowed at 230°C is thicker than the sample reflowed at 200°C. Yet, the solder joints reflowed at 230°C has a remarkably higher shear strength compared to solder joints reflowed at 200°C. Hence, it can be inferred that in this work, the effect of thickness variation on shear stress values is negligible. Instead, the shear strength depends on τ_c and λ constants which vary with soldering conditions, i.e. the reflow temperature in this case.

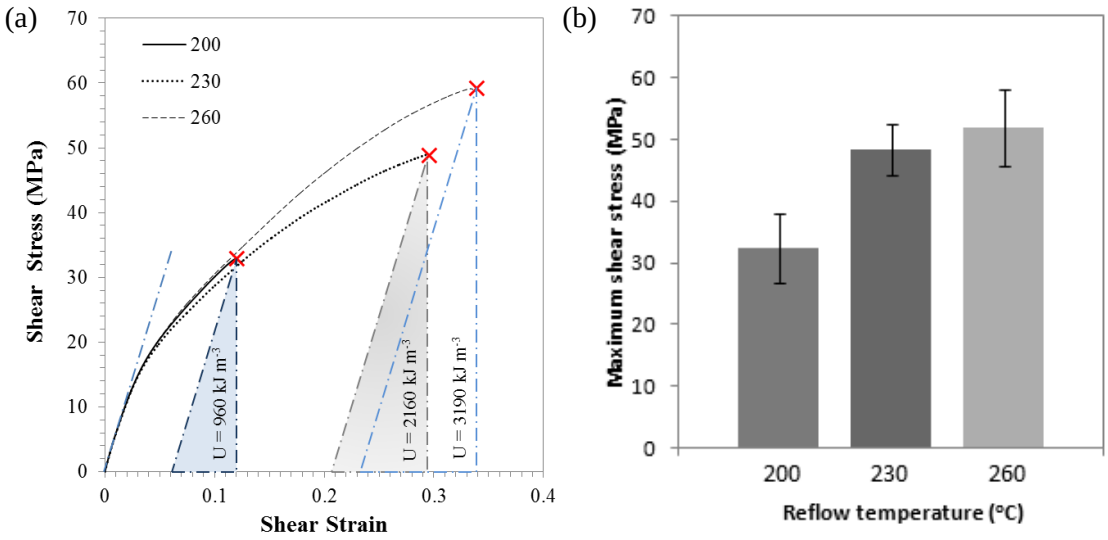

Figure 5.5 (a) Shear stress-shear strain curve of samples and (b) the average maximum shear stress taken from 15 tests.

During crack growth in metals, energy is expended by the formation of a new plastic zone at the tip of the advanced crack. The energy required for crack growth must be delivered as a release of the elastic energy. For stable crack growth, the energy release rate equals to the crack resistance of the material. If the energy release rate is larger than the crack resistance, crack instability occurs which leads to crack propagation and eventually fracture (Broek, 1996). Hence, the higher the elastic energy

release required for crack growth, the higher the crack resistance. The elastic energy release (per unit volume) required for crack propagation in Sn-Bi alloys, *U*, is calculated for each reflow temperature and is shown in Figure 5.5(a). A line parallel to the elastic zone of the curve is drawn from the fracture point to the x-axis. Another vertical line is extended from the fracture point to the x-axis to form a right-angled triangle. The area of the triangle indicates the elastic energy release per unit volume of solder. The elastic energy release increases by 225% (from 960 kJ m^{-3} to 2160 kJ m^{-3}) when reflow temperature is increased from 200^{o}C to 230^{o}C, indicating the increasing crack resistance of Sn-Bi solder joints. Sn-Bi solder joints reflowed at 260^{o}C yields a smaller increment in elastic energy release, 150% (from 2160 kJ m^{-3} to 3190 kJ m^{-3}), compared to joints reflowed at 230^{o}C. This suggests that the reflow temperature increment from 230^{o}C to 260^{o}C has a less profound effect on the crack resistance of the solder joints, compared to reflow temperature increment from 200^{o}C to 230^{o}C.

Table 5.1 shows the comparison of the shear properties of Sn-Bi/Cu lap shear solder joints reported in the literature. Values obtained in the present work are also shown in the last three rows of the table for comparison. Comparing the work by Raeder et al. (Raeder et al., 1994) and the present work (compare rows no. 1, 2 and 8), it is observed that at a same applied strain rate and same reflow temperature, the maximum shear stress value is rather comparable, regardless of the solder thickness and aging period. The work of Tomlinson and Fullylove (Tomlinson & Fullylove, 1992) employed a higher reflow temperature of 250^{o}C, and their reported shear strength and strain values are lower than in all other cases (rows no. 3 and 4). In their work, when strain rate was increased from 8.3 x 10^{-5} to 8.3 x 10^{-2}, a drop in maximum shear stress is observed. This opposes the normal trend where lower strain rate should lead to lower maximum shear strength due to creep and stress relaxation effects. The authors concluded that Sn-57Bi

joints often do not follow the general behaviour under different test conditions. Suh et al. (M. S. Suh et al., 2008) electrodeposited Sn-58Bi solder and reflowed the joints under a slightly different reflow temperature of 220°C, and applied a slightly lower strain rate of 3.3 x 10^{-4}/s compared to our work (rows no. 5-7). For aging period of less than 1 day, the maximum shear stress increased due to the bonding of prism-like IMC grains with higher surface area. As aging time increases, the IMC layer thickened and flattened which caused the reduction in strength. Generally, the shear strength values of Sn-Bi/Cu solder joints obtained in this work are comparable to literature reports.

Table 5.1 Comparison of shear properties of eutectic or near-eutectic Sn-Bi/Cu lap shear solder joints.

Row No.	**Solder preparation and thickness (μm)**	**Thermal history**	**Strain rate (s^{-1})**	**Maximum Shear Stress (MPa)**	**Reference**
1	Sn-58.5Bi solder foil, 250 μm	Reflow at 200°C, Aging at 80°C (3 days)	4 x 10^{-4}	30	(Raeder et al., 1994)
2	Sn-58.5Bi solder foil, 250 μm	Reflow at 200°C, Aging at 80°C (30 days)	4 x 10^{-4}	35 ± 1	
3	Sn-57Bi solder paste, 200 μm	Reflow at 250°C (1 min)	8.3 x 10^{-5}	25.3 ± 2.6	(Tomlinson & Fullylove, 1992)
4	Sn-57Bi solder paste, 200 μm	Reflow at 250°C (1 min)	8.3 x 10^{-2}	19.6 ± 4.2	
5	Electrodeposited Sn-58Bi solder, 20-25 μm	Reflow at 220°C	3.3 x 10^{-4}	41.9	(M. S. Suh et al., 2008)
6	Electrodeposited Sn-58Bi solder, 20-25 μm	Reflow at 220°C Aging at 80°C (1 day)	3.3 x 10^{-4}	47.8 ± 5.6	
7	Electrodeposited Sn-58Bi solder, 20-25 μm	Reflow at 220°C, Aging at 80°C (3 days)	3.3 x 10^{-4}	40.9 ± 5	
8	Electrodeposited Sn-59.8Bi solder, 39-42 μm	Reflow at 200°C (10mins)	4 x 10^{-4}	32.4 ± 5.6	Present work
9	Electrodeposited Sn-59.8Bi solder, 39-42 μm	Reflow at 230°C (10mins)	4 x 10^{-4}	48.4 ± 4.1	
10	Electrodeposited Sn-59.8Bi solder, 28-32 μm	Reflow at 260°C (10mins)	4 x 10^{-4}	52.0 ± 6.1	

5.3.3 Fracture surface analysis of solder joints

To investigate how the IMC morphology affects the shear strength of solder joints in this present work, Sn-Bi solder was chemically removed to reveal the IMC layer. Figure 5.6 shows the difference between IMC morphology of sample reflowed at 200^{o}C and 260^{o}C respectively. The prism-like IMC morphology (Figure 5.6(a)) may have provided a stronger binding effect to prevent the shearing at the interface. Yang et al. (2010) studied the Cu_6Sn_5 morphology transition under different thermal conditions for Sn-Ag/Cu system, and the effects of the transition on the shear strength of the joints. Three types of morphology were studied in their work: prism-like, scallop-like and layer-like. It is found that prism-like IMC binds stronger to the solder by penetrating into the solder matrix. The binding effect has increased the interfacial strength; hence the joints are more likely to fail in the bulk solder matrix. While for scallop-like and layer–like IMC structures, interfacial fracture is more dominant (M. Yang et al., 2010). From Figure 5.6(b), it is seen that higher reflow temperature imposes a coarsening and flattening effect on the IMC grains. The scallop-like IMC morphology is more prone to shearing and crack initiation (P. L. Tu et al., 1997; M. Yang et al., 2010). The Sn-Bi/Cu joints soldered at 230^{o}C and 260^{o}C are likely to fail at the solder/IMC interface. Studies on the fracture surface are expected to give more insight on the shear behaviour of the solder joints.

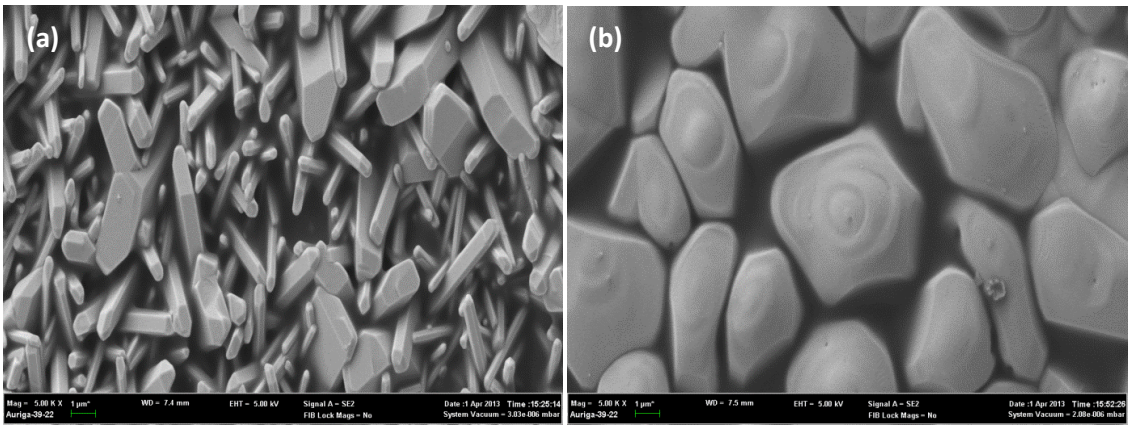

Figure 5.6 Cu_6Sn_5 IMC morphology of Sn-Bi/Cu joints soldered at (a) 200^{o}C and (b) 260^{o}C.

Figure 5.7(a) shows the representative micrograph of the fracture surface of solder joint reflowed at 200°C. The fracture pattern is parallel to the shear direction. Under high magnification, the fracture surface reveals the presence of elongated dimples (Figure 5.7(b)). This suggests that the fracture mode of this sample is ductile shear (Broek, 1996).The spherical features found at the fracture surface (indicated by arrows) are voids caused by entrapped gas within the solder. Such voids are found to appear in fracture surfaces of all joints reflowed at 200, 230 and 260°C. Elemental mapping was performed to determine the elemental distribution at the fracture surface. The Bi phase is mapped in green colour (Figure 5.7(c)) while Sn is mapped in red (Figure 5.7(d)). The composite map (Figure 5.7(e)) shows some yellowish regions seen which are merely the mixture of green and red colour, indicating the mixture of both Bi and Sn phases. The absence of Cu element in the elemental mapping data indicates no sign of exposed IMC from the elemental maps throughout the fracture surface. This can be related to the previous discussions on prism-like IMC morphology of joints reflowed at 200°C, where the high surface area of IMC grains binds strongly to the bulk solder and avoid shearing at the joint interface.

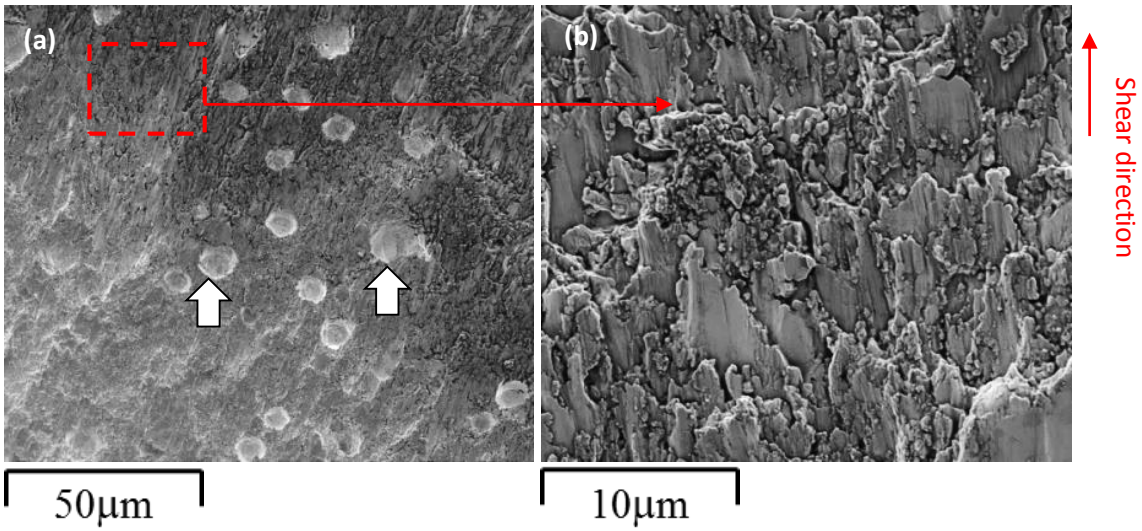

Figure 5.7(a) Micrograph (b) Magnified micrograph (c) Bi element mapping (d) Sn element mapping (e) composite mapping of fracture surface of joint reflowed at 200°C.

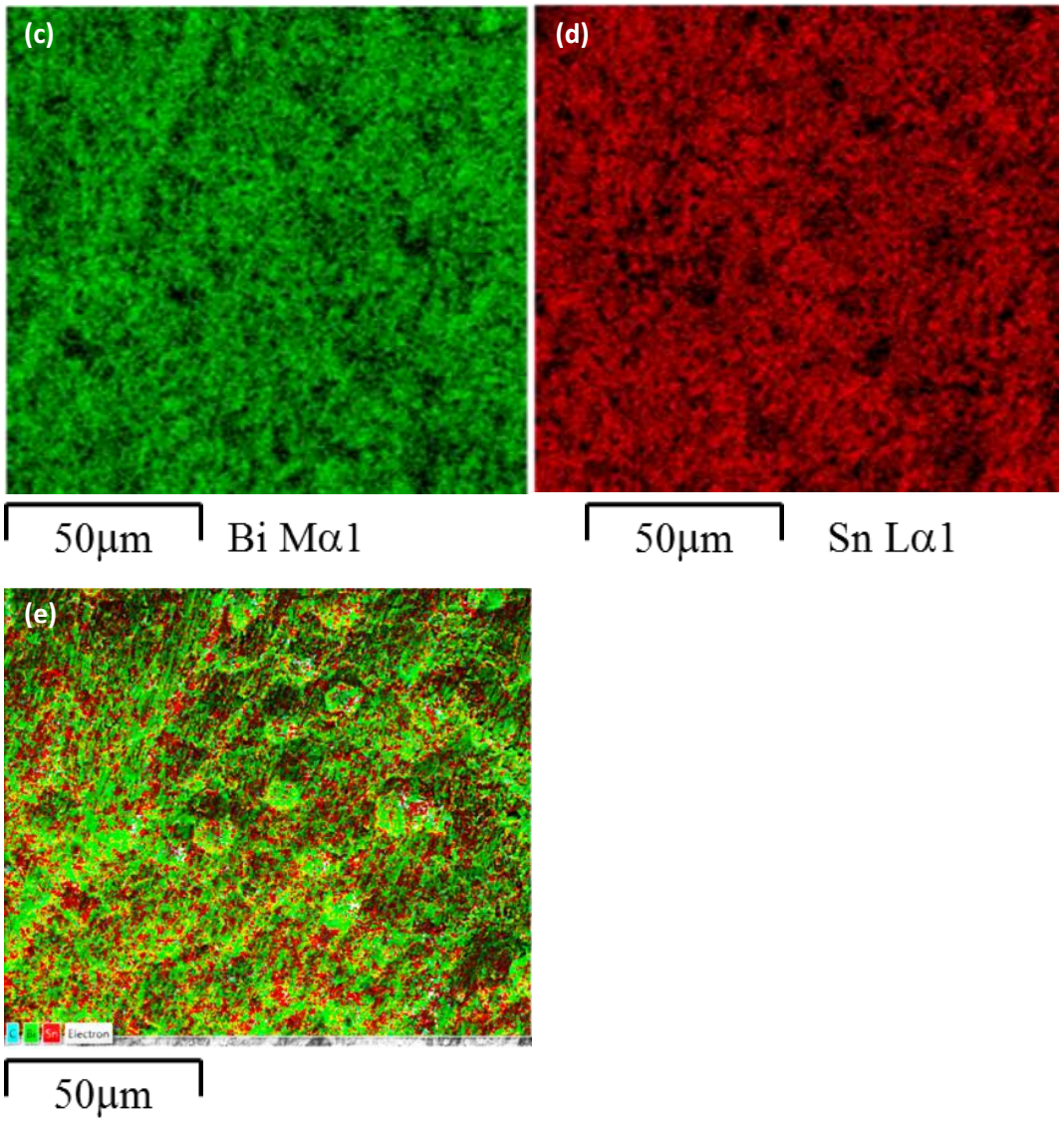

Figure 5.7 continued.

A representative micrograph of samples reflowed at 230°C show an irregular area with darker shade (Figure 5.8(a)). Such areas have been observed to cover about 25% of the 5 x 5 mm fracture surface area. These areas are irregular in shape and are not due to void formation caused by gas entrapment. Under higher magnifications, the irregular area with darker shade shows granular features (Figure 5.8(b)) and on areas with brighter shade shows fracture patterns following the shear direction (Figure 5.8(c)). For elemental mapping, Bi phase is mapped in green colour (Figure 5.8(d)), Sn is mapped in red colour (Figure 5.8(e)) and Cu is mapped in blue colour (Figure 5.8(f)). Shades of magenta colour are seen at the middle of the irregular area from the EDX composite

mapping micrograph in Figure 5.8(g). Basically, Cu is exposed at the area along with Sn, with low intensity of Bi counts as seen in the individual colour maps (indicated by arrows). This indicates there is interfacial fracture with exposure of flat and faceted Cu_6Sn_5 grains. The occurrence of interfacial fracture in samples reflowed at 230°C could be due to the transformation of IMC morphology from prism-like to scallop-like structure. Scallop-like IMC grains have a lower surface roughness and have less ability to resist shearing. However, in our work, interfacial fracture covers only about 25% of the fracture area, while the remaining area fails with ductile shear within the solder. Maximum shear stress values obtained (Figure 5.5) shows that there is a remarkable increase in shear strength and elastic energy release, *U*, when reflow temperature is increased from 200°C to 230°C. It may be inferred that the propagation of fracture from the interface to the bulk solder, and vice versa, has increased the shear strength and *U*.

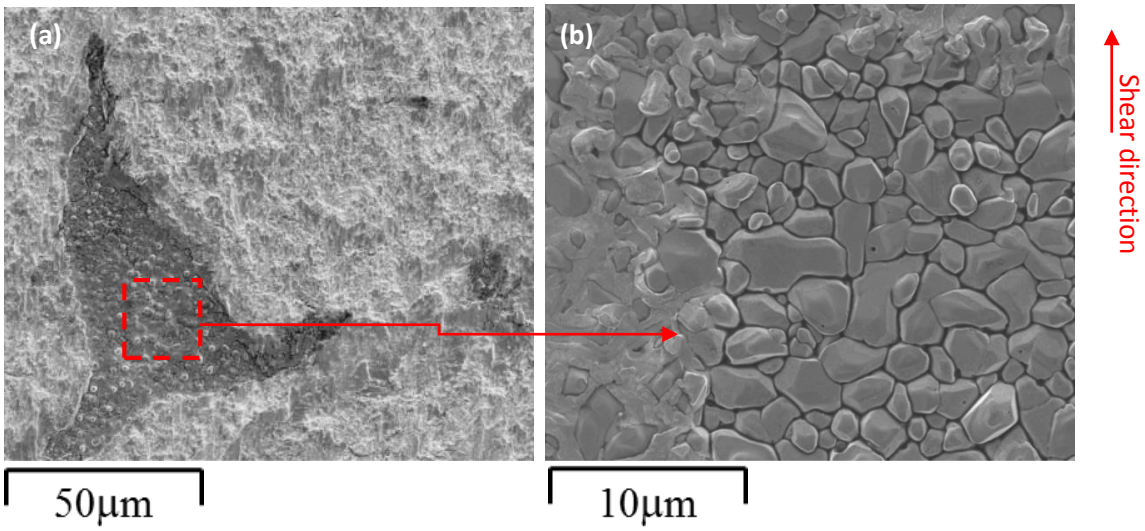

Figure 5.8 (a) Micrograph (b),(c) Magnified micrograph (d) Bi element mapping (e) Sn element mapping (f) Cu element mapping (g) composite mapping of fracture surface of joint reflowed at 230°C.

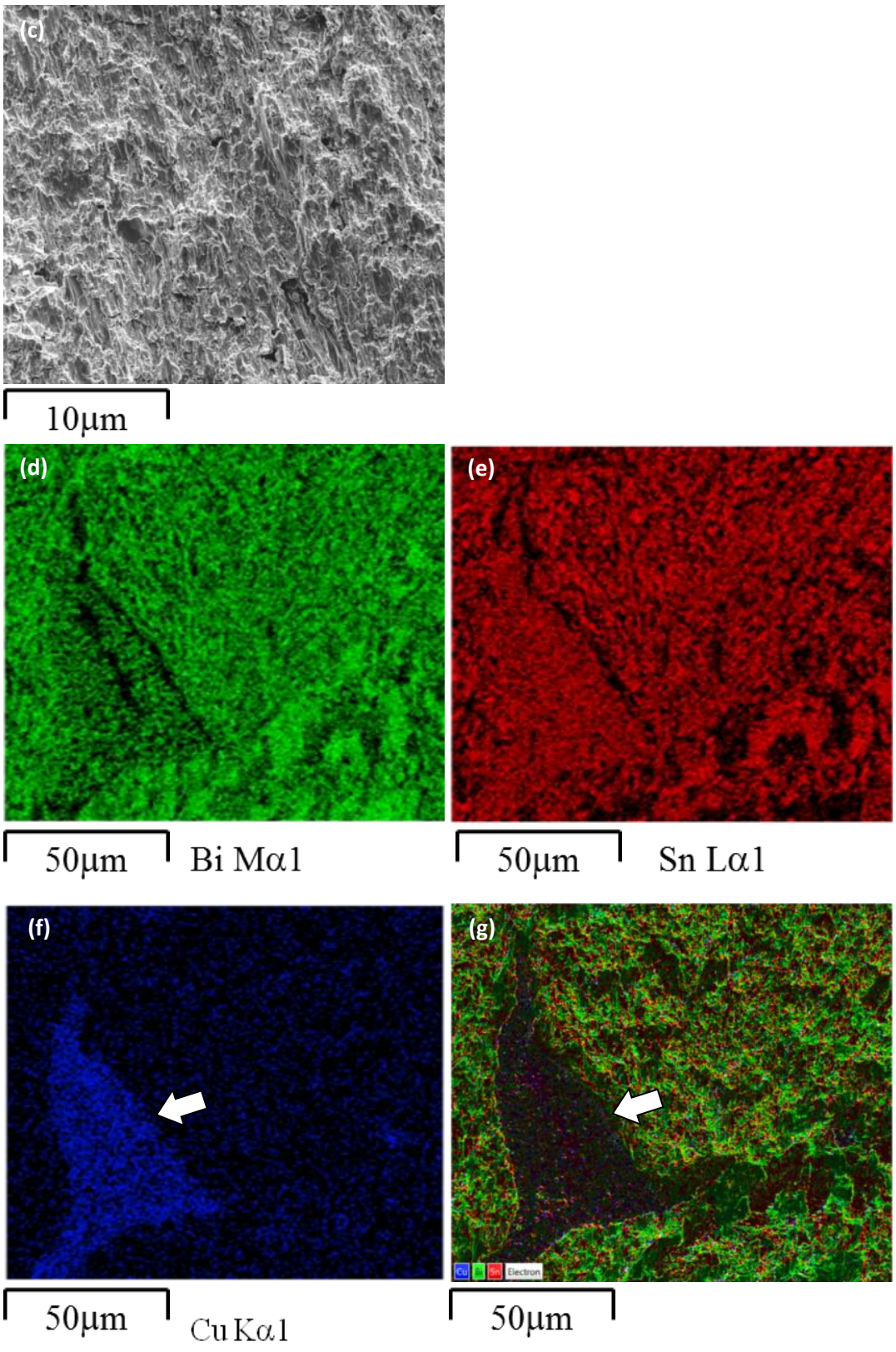

Figure 5.8 continued.

Figure 5.9(a) depicts fractograph of solder joint reflowed at 260°C. It is notable that the surface consists of sharp edged features, some irregular areas (similar to joints reflowed at 230°C), and the fracture patterns deviated from the shear direction. Fracture paths at different depths are observed from the magnified micrograph (Figure 5.9(b)). Figure 5.9(c) shows a magnified view of fracture features that are parallel to the shear direction, but at the lower left corner features showing deviation from the shear direction are observed.

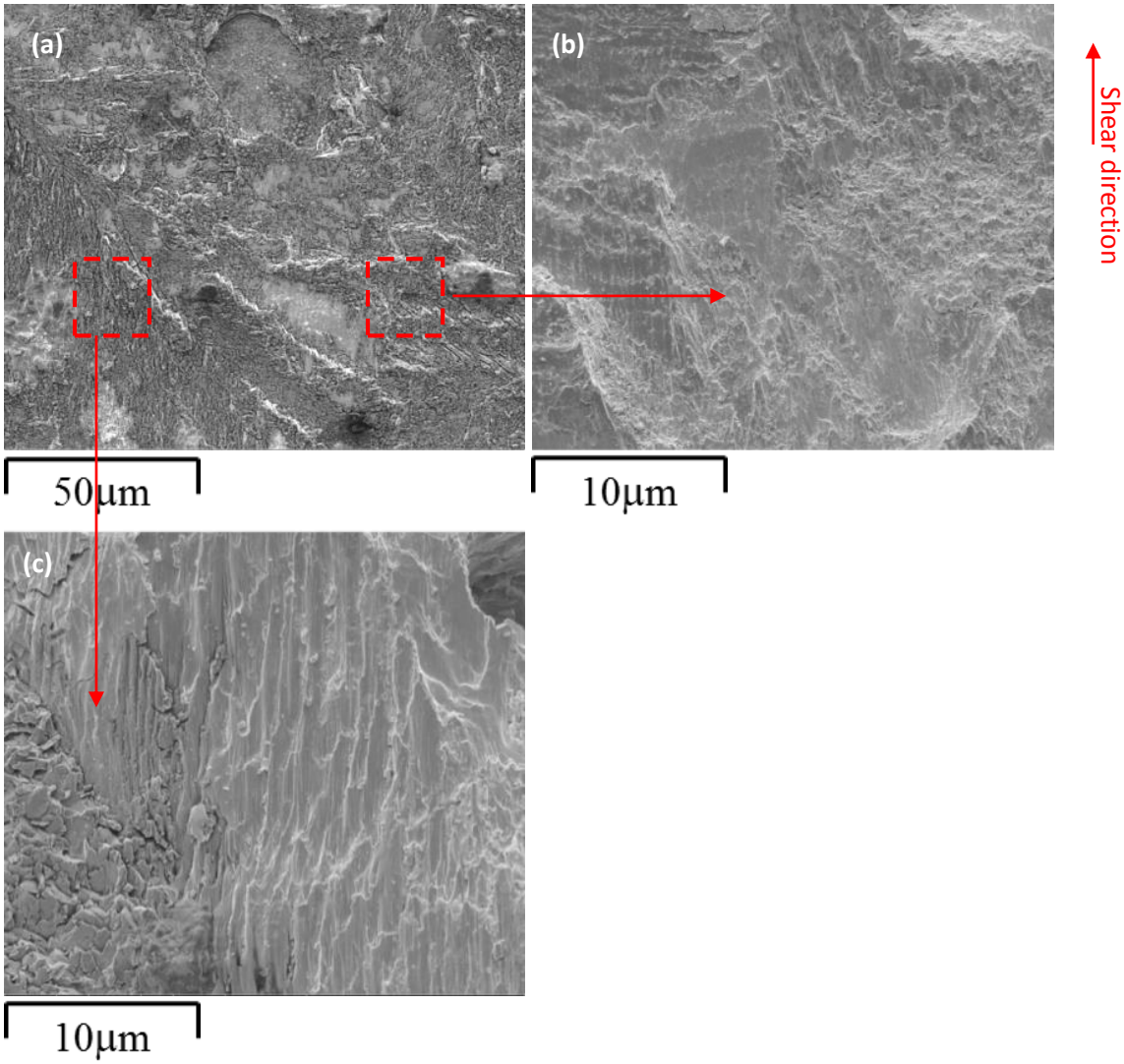

Figure 5.9 (a) Micrograph (b),(c) Magnified micrograph (d) Bi element mapping (e) Sn element mapping (f) Cu element mapping (g) composite mapping of fracture surface of joint reflowed at 260°C.

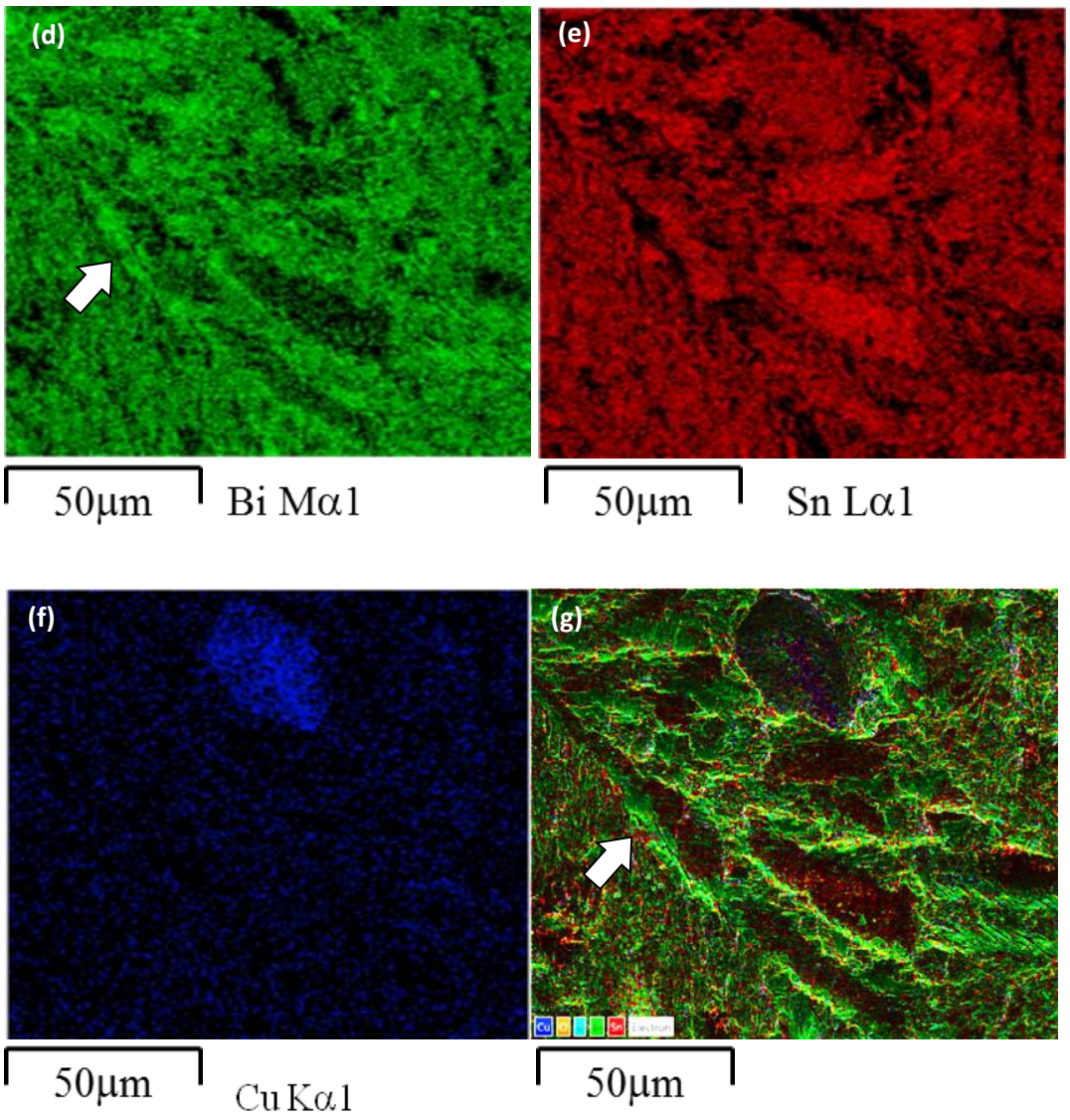

Figure 5.9 continued.

The EDX mapping of the fracture surface shows the elements present at each parts of the surface. The sharp edged features are Bi-rich phases (mapped in green) (Figure 5.9(d)) and are deviated from the shear direction, while Sn-rich phases (mapped in red) (Figure 5.9(e)) are found to follow the original shear direction. The main difference in fracture behaviour for the joints reflowed at 260^{o}C compared to previous cases (200^{o}C and 230^{o}C) is that the Bi-rich phase is seen to serve as a boundary to prevent the Sn-rich phase from sliding through during shear (indicated by arrows). At high reflow temperature, Bi-rich phase has much higher tendency to coarsen. It is

reported that this coarsening effect can have adverse effects on the reliability of the solder joints because the Bi-rich phase is more brittle than the Sn-rich phase (Felton et al., 1993; Huang et al., 2000; Miao et al., 2000; Raeder et al., 1994). However, in this work, Bi-rich phases do not seem to coarsen with increasing reflow temperature (Figure 5.4) and the maximum shear stress is higher compared to lower reflow temperatures. The increased reflow temperature may have caused changes in shear strength related τ_c and λ constants. These constant are claimed to vary with different soldering conditions and microstructural changes, but the exact trend is not known yet (L. M. Yang et al., 2012). On the other hand, it is apparent that the deviation in shear direction prolonged the fracture path of the joints, hence resulting in a higher *U* value.

The cross sectional views of the fractured solder joints were examined to provide a better insight into the fracture mode. Figure 5.10 shows the cross sectional view of a representative fracture site of solder joints reflowed at 200^{o}C. The joints are observed to have failed within the bulk solder with very slight changes in fracture path. This is consistent with earlier suggestions, where samples reflowed at 200^{o}C tends to fail within the bulk solder. This could be due to the prism-like IMC morphology formed at 200^{o}C bonds stronger to the solder matrix due to higher surface area. The crack initiation and propagation then occurs within the bulk solder. The ease of crack propagation, without much change in fracture path, resulted in a relatively lower *U* value.

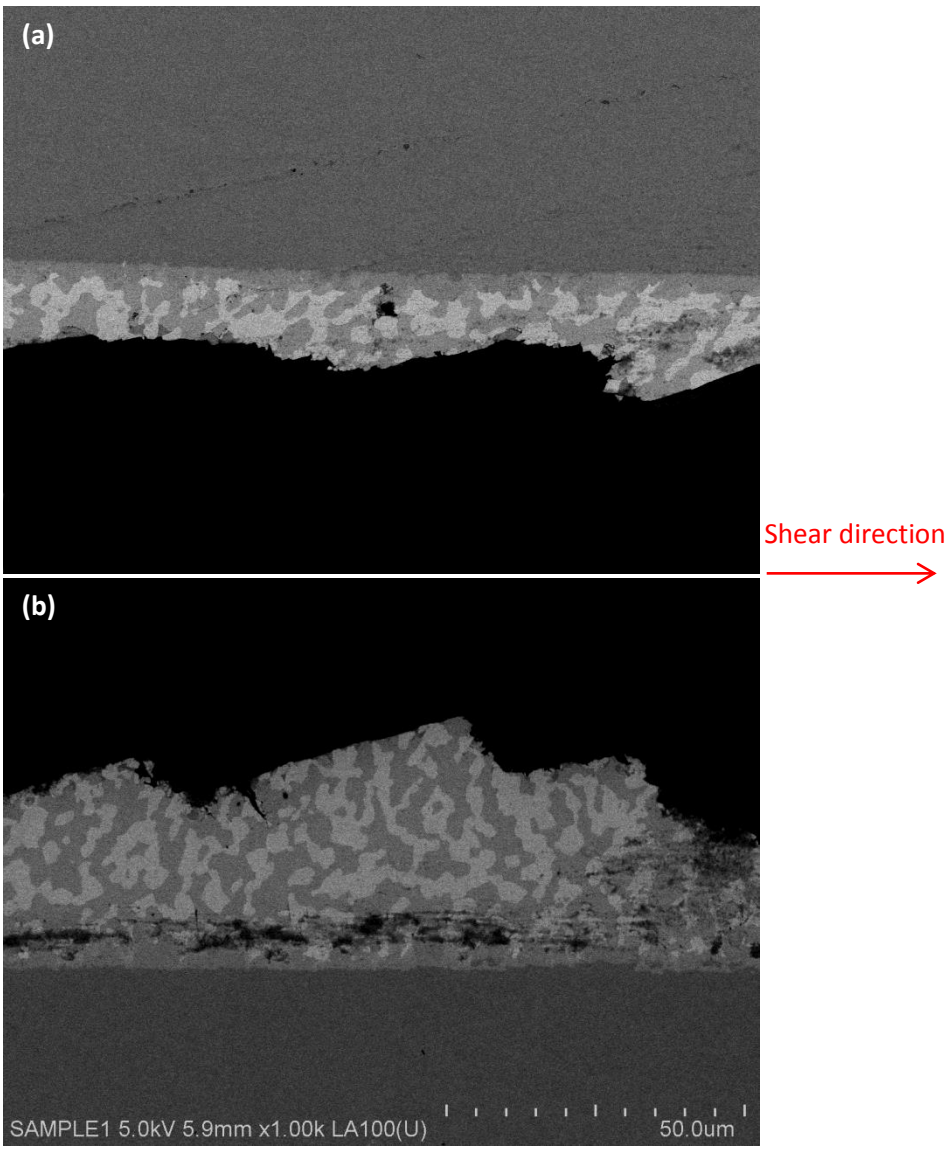

Figure 5.10 Cross sectional FESEM view of fractured solder joints reflowed at 200°C (a) top half (b) bottom half (strain rate 4 x 10^{-4}/s).

Figure 5.11 shows the cross sectional view of solder joints reflowed at 230°C after loaded to failure at an applied shear strain rate of 4 x 10^{-4}/s. Figure 5.11(a) is the micrograph taken at the edge of one of the failed samples. The scallop-like IMC grains became preferred crack initiation sites due to their low shear resistance (P. L. Tu et al., 1997; M. Yang et al., 2010). However, the crack propagation path changes when Bi-rich (light color) phases are encountered (indicated with arrow). The micrographs of failed joints (Figure 5.11(b) and 5.11(c)) shows that the fracture path tends to propagate from

bulk solder to IMC, and vice versa. This mode of propagation of fracture is suggested to give rise to the higher *U* value for these samples.

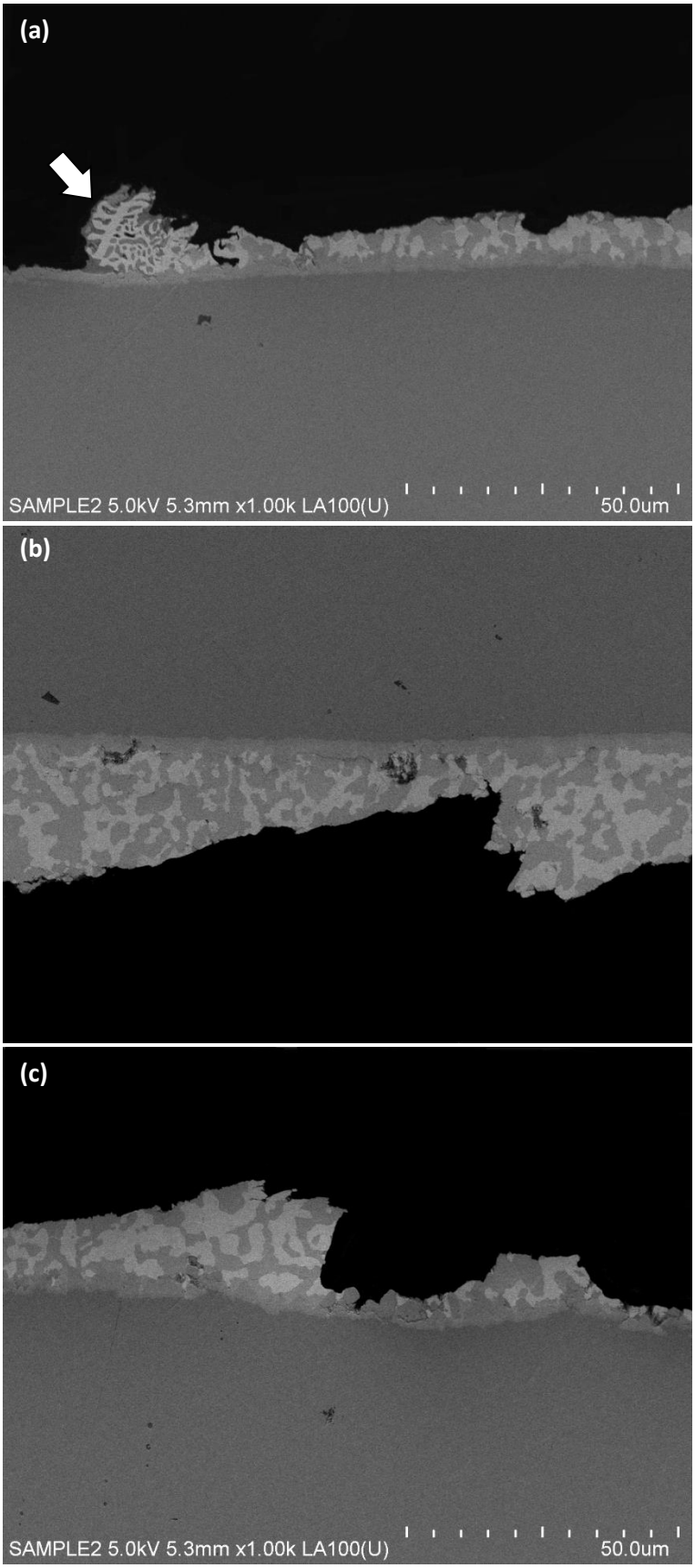

Figure 5.11 Cross sectional FESEM view of fractured solder joints reflowed at 230°C (a) at the edge of bottom half (b) top half (c) bottom half (strain rate 4 x 10^{-4}/s).

A representative fracture site of failed solder joints reflowed at 260°C is shown in Figure 5.12. Similar to the samples reflowed at 230°C, the samples reflowed at 260°C also shows propagation of fracture path from bulk solder to IMC and vice versa. This could be due to the same scallop-like IMC morphology formed at higher reflow temperatures. These IMC grains became preferred crack initiation sites, and fracture propagates along the IMC layer until some point. Abrupt changes in fracture path are observed for the solder joints reflowed at 260°C (indicated with arrow).

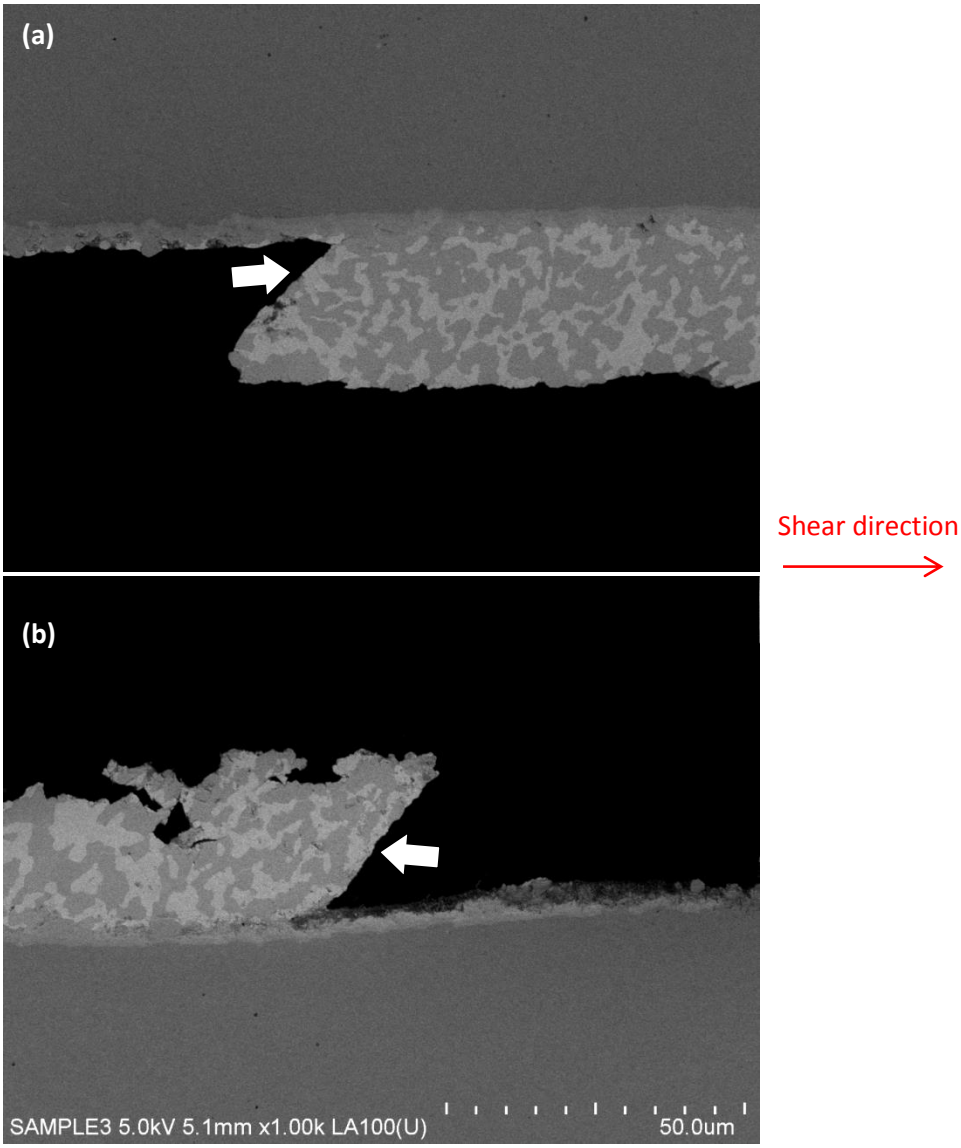

Figure 5.12 Cross sectional FESEM view of fractured solder joints reflowed at 260°C (a) top half (b) bottom half (strain rate 4 x 10^{-4}/s).

Micrographs taken at another representative fracture site of solder joints reflowed at 260°C shows the mixture of bulk solder and interfacial fracture. It can be seen in Figure 5.13(a) that the fracture proceeds along the Bi-rich phase within the bulk solder. When the Bi-rich phase in this eutectic structure approached the solder/IMC interface, the fracture path also propagates towards the IMC (indicated with arrow no.1). The magnified view where the crack propagates to the interface is shown in Figure 5.13(b). Fracture then proceeds along the solder/IMC interface for a short distance, before the fracture path propagates back into the solder matrix. This change in fracture path is seen to occur when the crack encounters another Bi-rich phase (indicated with arrow no.2, magnified view in Figure 5.13(c)). This phenomenon is observed only in solder joints reflowed at 230°C and 260°C.

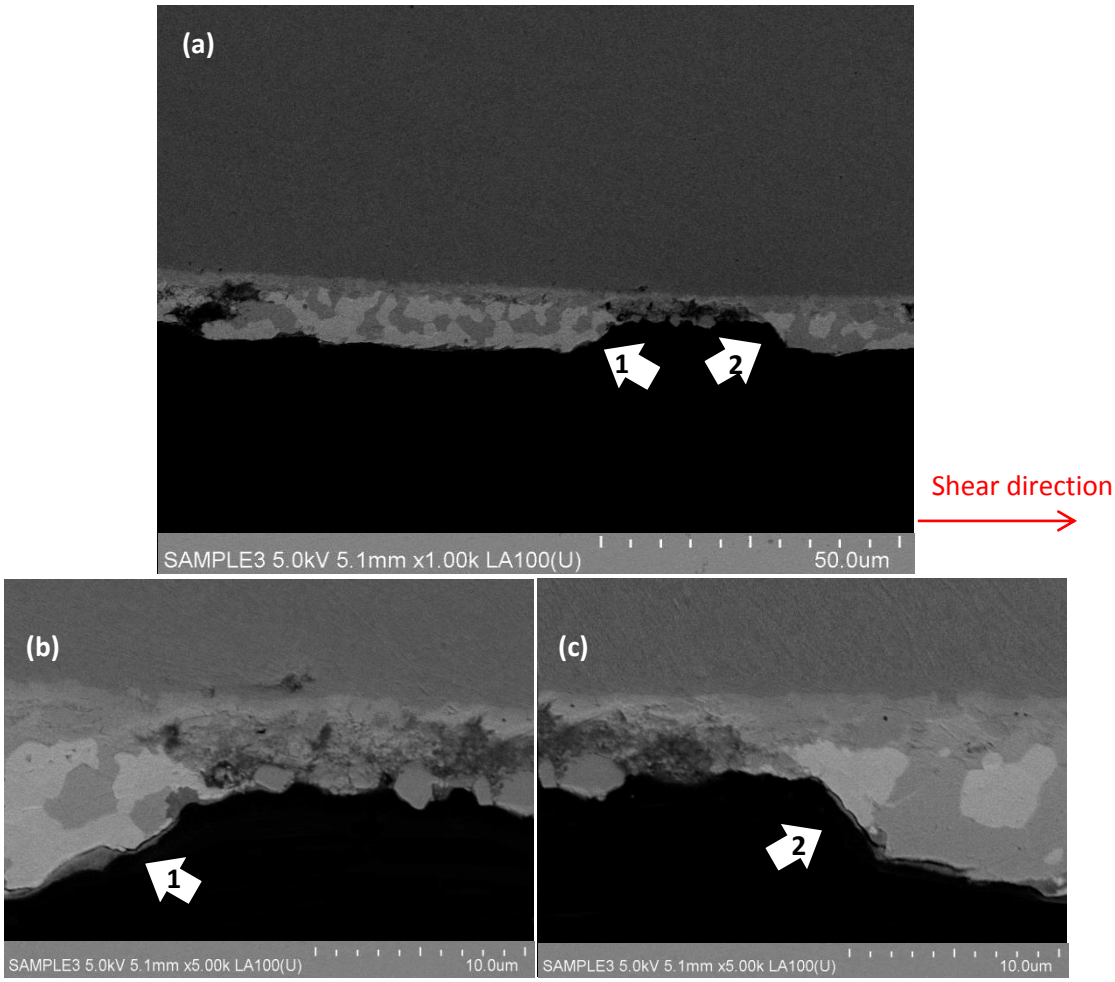

Figure 5.13 (a) Representative fracture site of solder joint reflowed at 260°C (b), (c) magnified view of crack propagation.

The trend observed from the shear stress-strain curves and fractography suggests that the fracture behaviour of these Sn-Bi/Cu joints is dependent on the reflow temperature and IMC morphology. A schematic diagram of possible fracture path is shown in Figure 5.14. The schematic representation of joints reflowed at 200°C (Figure 5.14(a)) shows that the prism-like IMC layers, having a higher surface area, bounds with the bulk solder more effectively and avoid fracture along the interface. The flat fracture surface with dimpled features and the absence of Cu in elemental mapping (Figure 5.7) indicate that the joints are sheared through the bulk solder without significant deviation in fracture path. The smooth fracture path of solder joints reflowed at 200°C indicates poorer crack resistance, hence resulting in a lower shear strength and *U* value.

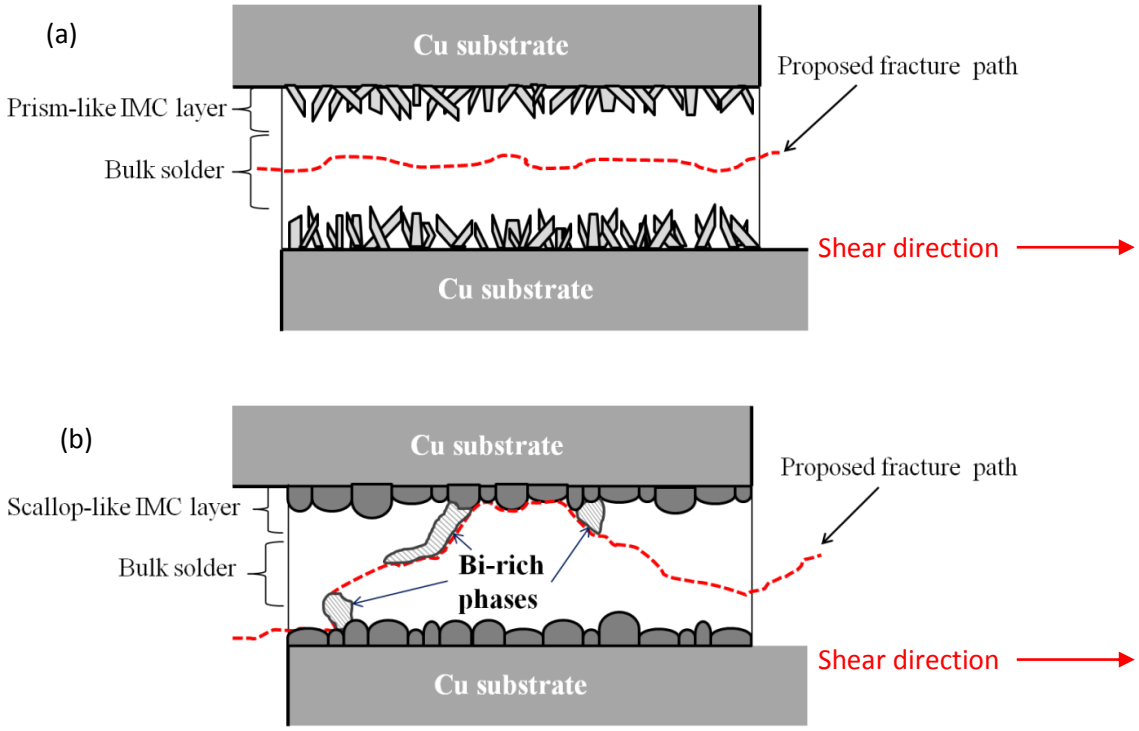

Figure 5.14 Proposed fracture propagation (a) within bulk solder for joints reflowed at 200°C, and (b) with mixture of interfacial and bulk solder shearing for joints reflowed at 230°C and 260°C (not to scale).

Figure 5.14(b) is the schematic proposed fracture path for solder joints reflowed at 230^{o}C and 260^{o}C; where both reflow temperatures yield scallop-like IMC morphology. The scallop-like structure has lower shear resistance which promotes interfacial fracture (P. L. Tu et al., 1997; M. Yang et al., 2010). In an earlier work, it has been reported that the eutectic Sn-Bi alloy show age-hardening effect when aged at high temperature of 100^{o}C (Miyazawa & T., 1999). According to the Sn-Bi phase diagram (Hassam, Dichi, & Legendre, 1998), the eutectic Sn-Bi alloy exists in a metastable condition consisting supersaturated Sn-rich solid solution crystals in the eutectic matrix. The age-hardening effect is attributed to the precipitation of hard Bi out of the supersaturated Sn-rich phase. It may be suggested that similar hardening effect could be achieved when this alloy is reflowed and soaked at a higher temperature. The Bi-rich phases (shown in Figure 5.14(b)) provide a hardening and blocking effect, similar to that of a second phase particle and interstitial hardening effect. This hardening effect increases the crack resistance of the solder joints, thus the crack propagation direction deviates from the original shear direction as can be seen from the fractographs in Figure 5.9 and Figure 5.13. According to the Sn-Bi phase diagram (Figure 5.15), Bi has 21% solubility in Sn phases. The Bi-rich phases may have hardened at higher reflow temperatures due to the precipitation of hard Bi out of Sn phases (Miyazawa & T., 1999). There might be small Bi precipitates in the Sn-rich phase which provide the hardening effect to effectively deviate the fracture path. From the observations, it may be suggested that cracks are prone to initiate at the scallop-like IMC interface. However, the eutectic Sn-Bi alloy may have hardened when reflowed at higher temperatures. This leads to crack propagation from solder/IMC interface to bulk solder when the crack tip encountered Bi-rich phase. The diversion of fracture path resulted in a higher elastic energy release and higher shear strength of solder joints reflowed at higher temperatures.

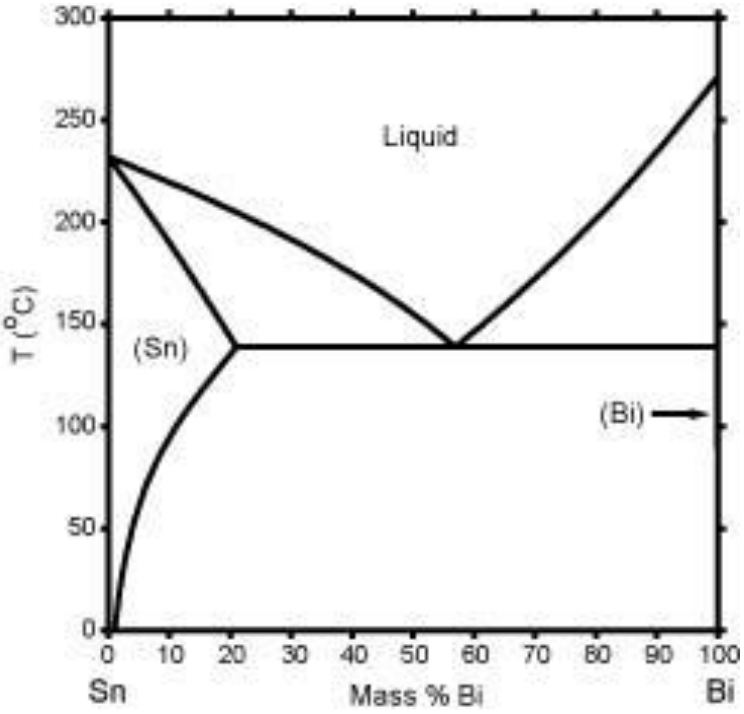

Figure 5.15 Equilibrium phase diagram of Sn-Bi system (Phase Diagrams & Computational Thermodynamics, National Institute of Standards and Technology (NIST) website, Retrieved 30 Jan 2015, from http://www.metallurgy.nist.gov/phase/solder/bisn.html)

5.4 Chapter conclusions

The shear strength and fracture behaviour of electroplated Sn-Bi solders on Cu substrates were investigated in this work. Cross sectional observations revealed that different interfacial IMC morphology was obtained at different reflow temperature. A reflow temperature of 200ºC yields prism-like interfacial IMC morphology; while 230ºC and 260ºC yield scallop-like IMC morphology. The maximum shear stress and elastic energy release (crack resistance) increases with increasing reflow temperature. Fractography of the failed joints showed that the fracture mechanism changes from dimpled fracture of bulk solder for joints reflowed at 200ºC, to mixture of interfacial and bulk solder fracture for joints reflowed at 230ºC and 260ºC. The difference in fracture behaviour is attributed mainly to the different reflow temperature and interfacial IMC morphology. For solder joints with prism-like IMC morphology, the

higher surface area of IMC resulted in stronger bonding near the interface, hence fracture occurs rather smoothly across the bulk solder. Scallop-like IMC grains having less resistance to shearing are suggested to be crack initiation sites. Solder joints with scallop-like IMC are prone to fail at the solder/IMC interface first, but the Bi-rich phase near the interface provides hardening effect and deviate the fracture path. The crack propagation from solder/IMC interface to bulk solder and vice versa resulted in a higher shear strength and elastic energy release.

CHAPTER 6

CONCLUSIONS AND RECOMMENDATIONS

6.1 Conclusions

In this work, investigations on electrodeposition of Sn-Bi solder alloys focuses on three main parts: (1) To study the effects of HQ and gelatin as electrolyte additives on the electrochemical behaviour of Sn-Bi plating solutions, (2) To optimize plating parameters to obtain eutectic Sn-Bi solder films from MSA-based plating baths, and (3) To evaluate the shear behaviour of electroplated eutectic Sn-Bi/Cu solder joints.

Polarization studies are conducted to investigate the effects of HQ and gelatin addition on the chemistry of the Sn-Bi plating bath. Without additives, the deposition potentials of Sn and Bi are 429 mV apart. HQ suppressed deposition current density of Sn. It also suppressed the hydrogen discharge reaction to more electronegative potentials. This is suggested to be related to the edge adsorption effect of HQ on the electrode surface. This suppression effect is eliminated upon the agitation of the solution. The deposition potential of Bi is polarized slightly by the addition of gelatin, where the deposition potential gap is reduced to 405 mV. On the other hand, gelatin caused a stronger suppression of current density and hydrogen evolution reaction compared to HQ during Sn-Bi deposition. This may be attributed to the large amount of amide nitrogen atoms available in the structure of gelatin, which are capable of adsorbing on electrode surfaces (Brown & Hope, 1995). The synergistic effects of HQ and gelatin resulted in huge shift of Bi deposition potential and strong suppression of hydrogen evolution reaction, where the potential difference between the two elements is decreased to 255 mV. This combination of additives has also improved the MSA-based Sn-Bi plating bath stability by minimizing the oxidation of ions present in the bath. A

composition estimation method is suggested from the polarization and galvanostatic studies conducted.

FESEM micrographs of electrodeposits obtained from the Sn-Bi+5g/L HQ+2g/L gelatin plating bath shows that the surface features becomes finer with increasing current density. However at high current densities (>20 mA cm^{-2}), large outward growing crystals formed on the surface of deposits. At high current densities, gelatin may undergo acid hydrolysis and decompose at a faster rate. The depletion of additives causes breaking of adsorption bonds. Nucleation and growth of deposits thus takes place preferentially at active sites without adsorption bonds. The content of Bi in the electrodeposits decreased with increasing current density, which is in accordance to thermodynamics. The Sn-Bi alloy compositions obtained at different current densities showed a similar trend with the compositions estimated from polarization curves. Near eutectic Sn-60.7wt.%Bi electrodeposits were obtained at an applied current density of 18 mA cm^{-2}.

Near eutectic Sn-Bi/Cu solder joints are reflowed at 200^{o}C, 230^{o}C and 260^{o}C. Prism-like IMC morphology is obtained at reflow temperature of 200^{o}C, while scallop-like IMC is formed at 230^{o}C and 260^{o}C. The maximum shear stress and elastic energy release, *U* increased with increasing reflow temperature. The fracture mode of the solder joints is dependent on the reflow temperature and IMC morphology. The solder joints reflowed at 200^{o}C failed with dimpled fracture within the bulk solder, without much change in fracture path. This is suggested to be related to the high surface area of prism-like IMC grains, which provided stronger binding effect to avoid failure at the solder/IMC interface. On the other hand, solder joints reflowed at 230^{o}C and 260^{o}C failed with mixture of interfacial and bulk solder fracture. Scallop-like IMC has lower

shear resistance which promotes crack initiation at the solder/IMC interface. However, when the crack tip encountered Bi-rich phase, changes in fracture path is observed. This may be attributed to the hardening of Bi-rich phases with increasing reflow temperature. Instead of shearing directly across the bulk solder, the fracture path is found to propagate from the interface to bulk solder and vice versa. The prolonged fracture path resulted in higher maximum shear stress and higher *U* value.

6.2 Recommendations for future work

6.2.1 Characterization of Bi-complexing ligands

It has been reported in this work that the addition of HQ and gelatin into the MSA-based Sn-Bi plating bath have successfully reduced the deposition potential gap between Sn and Bi. This reduction is attributed to the shift in deposition potential of Bi towards the more electronegative direction, which is suggested to be due to the synergestic complexing effect of HQ and gelatin. The actual complexing ligands are rather complicated to be identified. Till then, no reports on the characterization of Bi-complexing ligands are available. It is recommended that studies on the formation of complexing ligands from HQ and gelatin, as well as other electrolyte additives used in earlier works (e.g. EDTA, citrate ions) can be conducted.

The characterization of Bi-complexing ligands may be attempted using immobilized metal-ion affinity chromatography (IMAC) combined with electrospray ionization mass spectrometry (ESI-MS). Characterizations of Cu-complexing ligands have been studied using this combination (Ross, Ikonomou, & Orians, 2003). The IMAC technique works by flowing of the filtered sample solution through a chelating column in which the ion of interest (e.g. Bi^{3+}) is attached. Compounds having affinity with the metal ions (e.g. Bi-complexing ligands) will retain while the rest of the sample

solution passes through the column. The compound will then be subjected to mass spectrometric analysis. The electrospray ionization (ESI) process uses electrical energy to assist the transfer of ions from solution into the gaseous phase before they are subjected to mass spectrometric analysis (Ho et al., 2003).

6.2.2 Solder bump electrodeposition

The application of the plating bath developed in this work on solder bump deposition should be studied. With photolithography patterning process, the electrodeposition technique is capable of producing fine geometry solder bumps. Typically, an under bump metallization (UBM) coated Si wafer is prepared as electroplating substrate. A Ti-layer is deposited on top of the UBM to serve as solder dam against molten solder during reflow (Jung, Jung, & Zhou, 2006). Photoresist (PR) is spin-coated, cured and developed for patterning purpose. The thickness of PR is dependent on the desired solder bump height. The Ti solder dam exposed is etched away and solder electroplating is performed. Upon stripping of PR, a mushroom shape solder bump is formed. Reflow of the solder will result in a rounded bump. Issues on solder bump electrodeposition include alloy composition and thickness/coverage inconsistency. Also, with reduction in pitch size to produce fine geometry solder bumps, the throwing power of the plating solution has to be controlled so that the all PR via can be filled efficiently. These issues have to be studied and improved by optimization of applied current density and correct usage of additives.

6.2.3 Mechanical properties of lead-free solder joints

As solder joints are subjected to mechanical loading during service, fatigue resistance and shear strength are crucial properties to be considered. Besides the lap shear test used in this work, ball shear is also another method to investigate shear behaviour of solder

joints. Yang et al. (2011) investigated the Cu_6Sn_5 IMC morphology transition with different soldering conditions and its effect on mechanical properties of Sn-3.5Ag solder bump attachments. At higher ball shear height (further away from substrate), the joint strength depend primarily on the microstructure of solder matrix. In the case of lower shear height, the IMC morphologies are found to affect the joint strength, where deeply extruded prism-type IMC showed greater strength than scallop-type and layer-type IMC (M. Yang et al., 2010). The effects of Ag content in SAC solder balls on their shear strength are studied by Kim et al. (2003). It is found that large Ag_3Sn platelets formed in alloys with Ag content higher than 3.2 wt.%. These large Ag_3Sn platelets determine the fracture pattern of solder balls and induce serious degradation of joints if they are present near the IMC layer (K. S. Kim, Huh, & Suganuma, 2003). Roh et al. (2014) studied the bump shear strength of electroplated Sn-Bi micro bumps and found that the shear strength increased with increasing reflow time. The fracture mode of the solder bumps have changed from ductile to quasi-ductile with increasing reflow time (Roh, Jung, & Kim, 2014).

From the few case studies mentioned, it can be seen that there are lots of parameters that determine the shear behaviour of solder balls. The shear values obtained for lead-free solder alloys may vary although the alloy composition is almost similar. The values may differ due to variations in processing parameters such as solder deposition techniques, reflow and aging conditions, substrate materials, bump and pitch sizes etc. Many testing parameters such as shear height and shear speed are also not standardized. It would be worthwhile to study the shear behaviour of a few lead-free solder alloy systems under the same testing parameters but varying thermal conditions. The different shear behaviour at different thermal conditions would give a rough guide on the correct alloy to be used under a specific service condition.

References

Abtew, M., & Selvaduray, G. (2000). Lead-free Solders in Microelectronics. *Materials Science and Engineering R, 27*, 95-141.

Anderegg, G., Arnaud-Neu, F., Delgado, R., Felcman, J., & Popov, K. (2005). Critical evaluation of stability constants of metal complexes of complexones for biomedical and environmental applications. *Pure and Applied Chemistry, 77*, 1445-1495.

Arici, M., Nazir, H., & Aksu, M. L. (2011). Investigation of Sn-Zn electrodeposition from acidic bath on EQCM. *Journal of Alloys and Compounds, 509*(5), 1534-1537. doi: DOI 10.1016/j.jallcom.2010.10.161

Artaki, I., Noctor, D., Mather, J., Schroeder, S., Napp, D., Desantis, C., . . . Handwerker, C. (1999, 1-3 Feb 1999). *Research trends in lead-free soldering in the US: NCMS Lead-Free Solder Project.* Paper presented at the Environmentally Conscious Design and Inverse Manufacturing, 1999. Proceedings. EcoDesign '99: First International Symposium On.

Bi, J., Jiang, J., Hu, A., Li, M., Mao, D., & Suga, T. (2009, 10-13 Aug. 2009). *Fine pitch and high density Sn bump fabrication.* Paper presented at the Electronic Packaging Technology & High Density Packaging, 2009. ICEPT-HDP '09. International Conference on.

Bicelli, L. P., Bozzini, B., Mele, C., & D'Urzo, L. (2008). A Review of Nanostructural Aspects of Metal Electrodeposition. *International Journal of Electrochemcal Science, 3*(4), 356-408.

Bonafede, S., Huffman, A., & Palmer, W. D. (2006). Layer Structure and Thickness Effects on Electroplated AuSn Solder Bump Composition. *IEEE Transactions on Components and Packaging Technologies, 29*(3), 604-609.

Bradley, E., Handwerker, C. A., Bath, J., Parker, R. D., & Gedney, R. W. (2007). *Lead-Free Electronics: iNEMI Projects Lead to Successful Manufacturing*. New Jersey: John Wiley & Sons Inc.

Brenner, A. (1963). *Electrodeposition of alloys: principles and practice*: Academic Press.

Broek, D. (1996). *Elementary engineering fracture mechanics*. Dordrecht [u.a.]: Kluwer.

Brown, G. M., & Hope, G. A. (1995). Sers Study of the Adsorption of Gelatin at a Copper Electrode in Sulfuric-Acid-Solution. *Journal of Electroanalytical Chemistry, 397*(1-2), 293-300.

Cabruja, E., Bigas, M., Ullan, M., Pellegrini, G., & Lozano, M. (2007). Special bump bonding technique for silicon pixel detectors. *Nuclear Instruments and Methods*

in Physics Research Section A: Accelerators, Spectrometers, Detectors and Associated Equipment, 576(1), 150-153. doi: http://dx.doi.org/10.1016/j.nima.2007.01.143

Chen, H.-Y., Chen, C., Wu, P.-W., Shieh, J.-M., Cheng, S.-S., & Hensen, K. (2008). Effect of Polyethylene Glycol Additives on Pulse Electroplating of SnAg Solder. *Journal of Electronic Materials, 37*(2), 224-230. doi: 10.1007/s11664-007-0290-6

D1002-10, A. S. (2010). Standard Test Method for Apparent Shear Strength of Single-Lap-Joint Adhesively Bonded Metal Specimens by Tension Loading (Metal-to-Metal). West Conshohocken, PA: ASTM International, .

Datta, M., Osaka, T., & Schultze, J. W. (2005). *Microelectronic Packaging* (Vol. 3). Florida, USA: CRC Press.

Djurfors, B., & Ivey, D. G. (2001). Pulsed electrodeposition of the eutectic Au/Sn solder for optoelectronic packaging. *Journal of Electronic Materials, 30*(9), 1249-1254.

Duffy, J. I. (1981). *Electroplating technology: recent developments*: Noyes Data Corp.

Ezawa, H., Miyata, M., Honma, S., Inoue, H., Tokuoka, T., Yoshioka, J., & Tsujimura, M. (2001). Eutectic Sn–Ag Solder Bump Process for ULSI Flip Chip Technology. *IEEE Transactions on Electronics Packaging Manufacturing, 24*(4), 275-281.

Felton, L. E., Raeder, C. H., & Knorr, D. B. (1993). The Properties of Tin-Bismuth Alloy Solders. *Jom-Journal of the Minerals Metals & Materials Society, 45*(7), 28-32.

Field, S., & Weill, A. D. (1951). *Electro-plating: a survey of modern practice including the analysis of solutions*: Pitman.

Fukuda, M., Imayoshi, K., & Matsumoto, Y. (2001). Effect of polyoxyethylenelaurylether on electrodeposition of Pb-free Sn-Bi alloy. *Electrochimica Acta, 47*(3), 459-464.

Fukuda, M., Imayoshi, K., & Matsumoto, Y. (2002). Effects of Thiourea and Polyoxyethylene Lauryl Ether on Electrodeposition of Sn-Ag-Cu Alloy as a Pb-Free Solder. *Journal of The Electrochemical Society, 149*(5), C244-C249. doi: 10.1149/1.1463404

Gernon, M. D., Wu, M., Buszta, T., & Janney, P. (1999). Environmental benefits of methanesulfonic acid: Comparative properties and advantages. *Green Chemistry*, 127-140.

Gu, L. Y., Qu, L., Ma, H. T., Luo, Z. B., & Wang, L. (2011). Effects of Soldering Temperature and Cooling Rate on the as-Soldered Microstructures of

Intermetallic Compounds in Sn-Ag/Cu Joint. *2011 12th International Conference on Electronic Packaging Technology and High Density Packaging (Icept-Hdp)*, 342-345.

Han, C. (2009). *Electrodeposition of Pb-free, Sn-based Alloy Solder Films.* Doctor of Philosophy, University of Alberta, Edmonton, Alberta.

Han, C. F., Liu, Q., & Ivey, D. G. (2009). Electrochemical composite deposition of Sn-Ag-Cu alloys. *Materials Science and Engineering B-Advanced Functional Solid-State Materials, 164*(3), 172-179.

Hassam, S., Dichi, E., & Legendre, B. (1998). Experimental equilibrium phase diagram of the Ag–Bi–Sn system. *Journal of Alloys and Compounds, 268*, 199-206.

He, A., Liu, Q., & Ivey, D. G. (2007). Electrodeposition of tin: a simple approach. *Journal of Materials Science: Materials in Electronics, 19*(6), 553-562. doi: 10.1007/s10854-007-9385-3

Ho, C. S., Lam, C. W., Chan, M. H., Cheung, R. C., Law, L. K., Lit, L. C., . . . Tai, H. L. (2003). Electrospray ionisation mass spectrometry: principles and clinical applications. *Clin Biochem Rev, 24*(1), 3-12.

Hou, P., Han, D.-x., Niu, L., & Lin, H.-b. (2006). Electrochemistry of Hydroquinone Derivatives at Metal and Iodine-modified Metal Electrodes. *Chemical Research in Chinese Universities, 22*(4), 493-499. doi: http://dx.doi.org/10.1016/S1005-9040(06)60149-9

Hu, X., Li, Y., Li, K., & Min, Z. (2013). Effect of Bi Segregation on the Asymmetrical Growth of Cu-Sn Intermetallic Compounds in Cu/Sn-58Bi/Cu Sandwich Solder Joints During Isothermal Aging. *Journal of Electronic Materials, 42*(12), 3567-3572.

Hua, F., Mei, Z., & Glazer, J. (1998). *Eutectic Sn-Bi as an alternative to Pb-free solders.* Paper presented at the Electronic Components & Technology Conference, 1998. 48th IEEE.

Huang, M. L., Wu, C. M. L., Lai, J. K. L., & Chan, Y. C. (2000). Microstructural evolution of a lead-free solder alloy Sn-Bi-Ag-Cu prepared by mechanical alloying during thermal shock and aging. *Journal of Electronic Materials, 29*(8), 1021-1026. doi: DOI 10.1007/s11664-000-0167-4

Ishii, T., Aoyama, S., & Tokumitsu, M. (2001). Fabrication of 0.95Sn-0.05Au Solder Micro-Bumps for Flip-Chip Bonding. *Journal of Electronic Materials, 30*(6), L25-L27.

Joseph, S., Phatak, G., Gurunathan, K., Seth, T., Amalnerkar, D. P., & Kutty, T. R. N. (2006). Electrochemical co-deposition of ternary Sn–Bi–Cu films for solder bumping applications. *Journal of Applied Electrochemistry, 36*(8), 907-912. doi: 10.1007/s10800-006-9164-5

Joseph, S., & Phatak, G. J. (2008). Effect of surfactant on the bath stability and electrodeposition of Sn–Ag–Cu films. *Surface and Coatings Technology, 202*(13), 3023-3028. doi: http://dx.doi.org/10.1016/j.surfcoat.2007.11.002

Joseph, S., & Phatak, G. J. (2010). Effect of additives on the co-electrodeposition of Sn–Ag–Cu lead-free solder composition. *Materials Science and Engineering: B, 168*(1-3), 219-223. doi: 10.1016/j.mseb.2010.01.017

Joseph, S., & Phatak, G. J. (2011). Investigations on thiourea content in ternary Sn–Ag–Cu bath using electrochemical studies. *Journal of Applied Electrochemistry, 42*(1), 47-57. doi: 10.1007/s10800-011-0370-4

Jung, S. W., Jung, J. P., & Zhou, Y. (2006). Characteristics of Sn–Cu Solder Bump Formed by Electroplating for Flip Chip. *IEEE TRANSACTIONS ON ELECTRONICS PACKAGING MANUFACTURING, 29*(1), 10-16.

Kim, H. S., Yi, S. H., Song, J. H., Jeon, S. S., Kim, B. T., Lim, A. H., & Yook, J. M. (2014). High Speed Electrochemical Deposition Bath for Sn-Ag Alloy and Evaluation of Micro Solder Bump Plated on Ni-Coated Si Wafer. *Meeting Abstracts, MA2014-02*(16), 889.

Kim, J. H., Suh, M. S., & Kwon, H. S. (1996). Effects of plating conditions on the microstructure of 80Sn-20Pb electrodeposits from an organic sulphonate bath. *Surface & Coatings Technology, 78*(1-3), 56-63.

Kim, J. Y., Yu, J., Lee, J. H., & Lee, T. Y. (2004). The effects of electroplating parameters on the composition and morphology of Sn-Ag solder. *Journal of Electronic Materials, 33*(12), 1459-1464. doi: 10.1007/s11664-004-0087-9

Kim, K. S., Huh, S. H., & Suganuma, K. (2003). Effects of intermetallic compounds on properties of Sn–Ag–Cu lead-free soldered joints. *Journal of Alloys and Compounds, 352*, 226-236.

Kiumi, R., Takeda, S., Yoshioka, J., Kuriyama, F., & Saito, N. (2005, 31 May-3 June 2005). *Composition control for lead-free alloy electroplating on flip chip bumping.* Paper presented at the Electronic Components and Technology Conference, 2005. Proceedings. 55th.

Kloeser, J., Heinricht, K., Jung, E., Lauter, L., Ostmann, A., Aschenbrenner, R., & Reichl, H. (2000). Low cost bumping by stencil printing: process qualification for 200 mu m pitch. *Microelectronics Reliability, 40*(3), 497-505.

Knepper, T. P. (2003). Synthetic chelating agents and compounds exhibiting complexing properties in the aquatic environment. *TrAC Trends in Analytical Chemistry, 22*(10), 708-724. doi: http://dx.doi.org/10.1016/S0165-9936(03)01008-2

Kohl, P. A. (1982). The High-Speed Electrodeposition of Sn Pb Alloys. *Journal of The Electrochemical Society, 129*(6), 1196-1201.

Kühlkamp, P. (2011). Lead (Pb) – Free Plating for Electronics and Avoidance of Whisker Formation, 2011

Kunihiro, T., Morimitsu, M., & Matsunaga, M. (2000). Comparison of platinum with IrO2–Ta2O5 system for the stannous ion consumption in methane sulfonic acid baths with and without catechol. *Journal of Applied Electrochemistry, 30*(3), 359-364. doi: 10.1023/a:1003997303650

Laurila, T., Vuorinen, V., & Kivilahti, J. K. (2005). Interfacial reactions between lead-free solders and common base materials. *Materials Science & Engineering R-Reports, 49*(1-2), 1-60. doi: DOI 10.1016/j.mser.2005.03.001

Lee, B. J., Oh, C. S., & Shim, J. H. (1996). Thermodynamic assessments of the Sn-In and Sn-Bi binary systems. *Journal of Electronic Materials, 25*(6), 983-991. doi: Doi 10.1007/Bf02666734

Lee, J.-Y., Kim, J.-W., Chang, B.-Y., Tae Kim, H., & Park, S.-M. (2004). Effects of Ethoxylated α-Naphtholsulfonic Acid on Tin Electroplating at Iron Electrodes. *Journal of The Electrochemical Society, 151*(5), C333-C341. doi: 10.1149/1.1690289

Lee, Y.-G., Park, J.-G., Lee, C.-W., & Jung, J.-P. (2011). Electrodeposition of the Sn-58 wt.%Bi layer for low-temperature soldering. *Metals and Materials International, 17*(1), 117-121. doi: 10.1007/s12540-011-0216-y

Lien, C.-H., Hu, C.-C., Tsai, Y.-D., & Shan-Hill Wang, D. (2012). Preferred Orientation Control of Bi Deposits Using Experimental Strategies. *Journal of The Electrochemical Society, 159*(4), D260. doi: 10.1149/2.103204jes

Lin, K. L., & Liu, Y. C. (1999). Manufacturing of Cu/electroless nickel/Sn-Pb flip chip solder bumps. *Ieee Transactions on Advanced Packaging, 22*(4), 575-579.

Low, C. T. J., & Walsh, F. C. (2008a). Electrodeposition of tin, copper and tin–copper alloys from a methanesulfonic acid electrolyte containing a perfluorinated cationic surfactant. *Surface and Coatings Technology, 202*(8), 1339-1349. doi: 10.1016/j.surfcoat.2007.06.032

Low, C. T. J., & Walsh, F. C. (2008b). The influence of a perfluorinated cationic surfactant on the electrodeposition of tin from a methanesulfonic acid bath. *Journal of Electroanalytical Chemistry, 615*(2), 91-102. doi: 10.1016/j.jelechem.2007.11.031

Low, C. T. J., & Walsh, F. C. (2008c). The stability of an acidic tin methanesulfonate electrolyte in the presence of a hydroquinone antioxidant. *Electrochimica Acta, 53*(16), 5280-5286. doi: 10.1016/j.electacta.2008.01.093

Malik, M. A., Hashim, M. A., Nabi, F., AL-Thabaiti, S. A., & Khan, Z. (2011). Anti-corrosion Ability of Surfactants: A Review. *International Journal of Electrochemical Science, 6*(6), 1927-1948.

Mallik, M., Mitra, A., Sengupta, S., Das, K., Ghosh, R. N., & Das, S. (2014). Effect of Current Density on the Nucleation and Growth of Crystal Facets during Pulse Electrodeposition of Sn–Cu Lead-Free Solder. *Crystal Growth & Design, 14*(12), 6542-6549. doi: 10.1021/cg501440a

Martyak, N. M., & Seefeldt, R. (2004). Additive-effects during plating in acid tin methanesulfonate electrolytes. *Electrochimica Acta, 49*(25), 4303-4311. doi: http://dx.doi.org/10.1016/j.electacta.2004.03.039

Medvedev, G. I., Makrushin, N. A., & Dubenkov, A. N. (2003). Electrodeposition of Tin-bismuth alloy from sulfate bath containing organic additives. *Protection of metals, 39*(4), 381-384.

Mei, Z., & Morris, J. W. (1992). Characterization of eutectic Sn-Bi solder joints. *Journal of Electronic Materials, 21*(6), 599-607. doi: 10.1007/bf02655427

Meudre, C., Ricq, L., Hihn, J.-Y., Moutarlier, V., Monnin, A., & Heintz, O. (2014). Adsorption of gelatin during electrodeposition of copper and tin–copper alloys from acid sulfate electrolyte. *Surface and Coatings Technology, 252*(0), 93-101. doi: http://dx.doi.org/10.1016/j.surfcoat.2014.04.050

Miao, H. W., Duh, J. G., & Chiou, B. S. (2000). Thermal cycling test in Sn-Bi and Sn-Bi-Cu solder joints. *Journal of Materials Science-Materials in Electronics, 11*(8), 609-618. doi: Doi 10.1023/A:1008928729212

Miric, A. Z., & Grusd, A. (1998). Lead-free alloys. *Soldering & Surface Mount Technology, 10*(1), 19-+. doi: Doi 10.1108/09540919810203793

Miyazawa, Y., & T., A. (1999). *Microstructural Change and Hardness of Lead Free Solder Alloys.* Paper presented at the First International Symposium On Environmentally Conscious Design and Inverse Manufacturing (EcoDesign '99), Tokyo, Japan.

Moon, K. W., & Boettinger, W. J. (2004). Accurately determining eutectic compositions: The Sn-Ag-Cu ternary eutectic. *JOM, 56*(4), 22-27. doi: DOI 10.1007/s11837-004-0068-8

Moon, K. W., Boettinger, W. J., Kattner, U. R., Handwerker, C. A., & Lee, D. J. (2001). The effect of Pb contamination on the solidification behavior of Sn-Bi solders. *Journal of Electronic Materials, 30*(1), 45-52. doi: DOI 10.1007/s11664-001-0213-x

Morris, J. R., & Wojcik, T. (1991). Stencil Printing of Solder Paste for Fine-Pitch Surface Mount Assembly. *Ieee Transactions on Components Hybrids and Manufacturing Technology, 14*(3), 560-566.

Motulla, G., Kasulke, P., Heinricht, K., Ostmann, A., Zakel, E., Reichl, H., . . . Kloser, J. (1997, 16-18 April 1997). *A LOW COST BUMPING PROCESS FOR FLIP CHIP-TECHNOLOGY USING ELECTROLESS NICKEL BUMPING AND*

SOLDER BALL PLACEMENT. Paper presented at the International Electronics Manufacturing Technology Symposium, Tokyo, Japan.

Neveu, B., Lallemand, F., Poupon, G., & Mekhalif, Z. (2006). Electrodeposition of Pb-free Sn alloys in pulsed current. *Applied Surface Science, 252*(10), 3561-3573. doi: 10.1016/j.apsusc.2005.05.024

Persson, I. (2010). Hydrated metal ions in aqueous solution: How regular are their structures? *Pure and Applied Chemistry, 82*(10), 1901-1917.

Qin, Y., Wilcox, G. D., & Liu, C. (2008, 1-4 Sept. 2008). *Electrodeposition of Sn-Ag solder alloy for electronics interconnection.* Paper presented at the Electronics System-Integration Technology Conference, 2008. ESTC 2008. 2nd.

Qin, Y., Wilcox, G. D., & Liu, C. (2010). Electrodeposition and characterisation of Sn–Ag–Cu solder alloys for flip-chip interconnection. *Electrochimica Acta, 56*(1), 183-192. doi: 10.1016/j.electacta.2010.08.102

Raeder, C. H., Felton, L. E., Tanzi, V. A., & Knorr, D. B. (1994). The Effect of Aging on Microstructure, Room-Temperature Deformation, and Fracture of Sn-Bi/Cu Solder Joints. *Journal of Electronic Materials, 23*(7), 611-617. doi: Doi 10.1007/Bf02653346

Raub, E., & Müller, K. (1967). *Fundamentals of metal deposition*: Elsevier Publishing Cy.

Rinne, G. A. (1997, 18-21 May 1997). *Solder bumping methods for flip chip packaging.* Paper presented at the Electronic Components and Technology Conference, 1997. Proceedings., 47th.

Roh, M.-H., Jung, J. P., & Kim, W. (2014). Microstructure, shear strength, and nanoindentation property of electroplated Sn–Bi micro-bumps. *Microelectronics Reliability, 54*(1), 265-271. doi: http://dx.doi.org/10.1016/j.microrel.2013.09.016

Ross, A. R. S., Ikonomou, M. G., & Orians, K. J. (2003). Characterization of copper-complexing ligands in seawater using immobilized copper(II)-ion affinity chromatography and electrospray ionization mass spectrometry. *Marine Chemistry, 83*(1–2), 47-58. doi: http://dx.doi.org/10.1016/S0304-4203(03)00095-1

Ruythooren, W., Attenborough, K., Beerten, S., Merken, P., Fransaer, J., Beyne, E., . . . Celis, J. P. (2000). Electrodeposition for the synthesis of microsystems. *Journal of Micromechanics and Microengineering, 10*(2), 101-107.

Saban, M. D., Scott, J. D., & Cassidy, R. M. (1992). Collagen Proteins in Electrorefining: Rate Constants for Glue Hydrolysis and Effects of Molar Mass on Glue Activity. *Metallurgical Transactions B, 23*(B), 125-133.

Salager, J. L. (2002). Surfactants Types and Uses *TEACHING AID IN SURFACTANT SCIENCE & ENGINEERING* (Vol. #E300-A): FIRP.

Schlesinger, M., & Paunovic, M. (2010). *Modern electroplating* (5th ed.). Hoboken, NJ: John Wiley & Sons Inc.

Schowanek, D., McAvoy, D., Versteeg, D., & Hanstveit, A. (1996). Effects of nutrient trace metal speciation on algal growth in the presence of the chelator [S,S]-EDDS. *Aquatic Toxicology, 36*(3–4), 253-275. doi: http://dx.doi.org/10.1016/S0166-445X(96)00807-7

Sekar, R., Eagammai, C., & Jayakrishnan, S. (2010). Effect of additives on electrodeposition of tin and its structural and corrosion behaviour. *Journal of Applied Electrochemistry, 40*(1), 49-57. doi: DOI 10.1007/s10800-009-9963-6

Sharma, A., Bhattacharya, S., Das, S., & Das, K. (2014). Influence of current density on surface morphology and properties of pulse plated tin films from citrate electrolyte. *Applied Surface Science, 290*(0), 373-380. doi: http://dx.doi.org/10.1016/j.apsusc.2013.11.088

Shen, Y. L., Chawla, N., Ege, E. S., & Deng, X. (2005). Deformation analysis of lap-shear testing of solder joints. *Acta Materialia, 53*(9), 2633-2642. doi: http://dx.doi.org/10.1016/j.actamat.2005.02.024

Sidhu, R. S., & Chawla, N. (2008). Thermal Fatigue Behavior of Sn-Rich (Pb-Free) Solders. *Metallurgical and Materials Transactions A-Physical Metallurgy and Materials Science, 39A*, 799-810.

Siewert, T. A., & Handwerker, C. A. (2002). Test Procedures for Developing Solder Data. In N. T. G. o. L.-F. A. a. Reliability (Ed.), (Vol. 960-8, pp. 44). WASHINGTON: National Institute of Standards and Technology.

Soriaga, M. P., White, J. H., Song, D., & Hubbard, A. T. (1984). Adsorption and orientation of aromatic compounds at smooth polycrystalline platinum electrodes: The effect of halide electrolytes. *Journal of Electroanalytical Chemistry and Interfacial Electrochemistry, 171*(1–2), 359-363. doi: http://dx.doi.org/10.1016/0022-0728(84)80128-X

Stavila, V., Davidovich, R. L., Gulea, A., & Whitmire, K. H. (2006). Bismuth(III) complexes with aminopolycarboxylate and polyaminopolycarboxylate ligands: Chemistry and structure. *Coordination Chemistry Reviews, 250*(21–22), 2782-2810. doi: http://dx.doi.org/10.1016/j.ccr.2006.02.032

Suganuma, K. (2001). Advances in lead-free electronics soldering. *Current Opinion in Solid State & Materials Science, 5*(1), 55-64.

Suganuma, K. (2003). *Lead-Free Soldering in Electronics: Science, Technology, and Environmental Impact*: Taylor & Francis.

Suh, M.-S., Park, C.-J., & Kwon, H.-S. (2006). Effects of plating parameters on alloy composition and microstructure of Sn–Bi electrodeposits from methane sulphonate bath. *Surface and Coatings Technology, 200*(11), 3527-3532. doi: 10.1016/j.surfcoat.2004.08.162

Suh, M. S., Park, C. J., & Kwon, H. S. (2008). Growth kinetics of Cu-Snintermetallic compounds at the interface of a Cu substrate and 42Sn-58Bi electrodeposits, and the influence of the intermetallic compounds on the shear resistance of solder joints. *Materials Chemistry and Physics, 110*(1), 95-99. doi: DOI 10.1016/j.matchemphys.2008.01.021

Sun, W., & Ivey, D. G. (1999). Development of an electroplating solution for codepositing Au-Sn alloys. *Materials Science and Engineering B-Solid State Materials for Advanced Technology, 65*(2), 111-122.

Suraski, D., & Seelig, K. (2001). The current status of lead-free solder alloys. *IEEE TRANSACTIONS ON ELECTRONICS PACKAGING MANUFACTURING, 24*(4), 244-248. doi: Doi 10.1109/6104.980031

Survila, A., & Bražinskienė, D. (2007). Inhibition activity of ethyleneglycol and its oligomers on tin electrode. *Journal of Solid State Electrochemistry, 11*(1), 65-70. doi: 10.1007/s10008-005-0070-2

Survila, A., Mockus, Z., Kanapeckaite, S., Brazinskiene, D., & Juskenas, R. (2012). Surfactant Effects in Cu-Sn Alloy Deposition. *Journal of The Electrochemical Society, 159*(5), D296-D302. doi: Doi 10.1149/2.084205jes

Survila, A., Mockus, Z., Kanapeckaite, S., Jasulaitiene, V., & Juskenas, R. (2009). Codeposition of copper and tin from acid sulphate solutions containing polyether sintanol DS-10 and benzaldehyde. *Journal of applied electrochemistry, 39*(10), 2021-2026.

Survila, A., Mockus, Z., Kanapeckaitė, S., & Samulevičienė, M. (2005). Effect of sintanol DS-10 and halides on tin(II) reduction kinetics. *Electrochimica Acta, 50*(14), 2879-2885. doi: http://dx.doi.org/10.1016/j.electacta.2004.11.034

Tan, A. C. (1993). *Tin and solder plating in the semiconductor industry : A technical guide*. London: Chapman & Hall.

Tomlinson, W. J., & Fullylove, A. (1992). Strength of Tin-Based Soldered Joints. *Journal of Materials Science, 27*(21), 5777-5782. doi: Doi 10.1007/Bf01119737

Tsai, Y.-D., & Hu, C.-C. (2009a). Composition Control of Lead-Free Sn–Bi Deposits Using Experimental Strategies. *Journal of The Electrochemical Society, 156*(2), D58. doi: 10.1149/1.3035824

Tsai, Y.-D., & Hu, C.-C. (2009b). Composition Control of Sn–Bi Deposits: Interactive Effects of Citric Acid, Ethylenediaminetetraacetic Acid, and Poly(ethylene

glycol). *Journal of The Electrochemical Society, 156*(11), D490. doi: 10.1149/1.3224861

Tsai, Y.-D., & Hu, C.-C. (2011). Composition and Microstructure Control of Tin-Bismuth Alloys in the Pulse Plating Process. *Journal of The Electrochemical Society, 158*(8), D482. doi: 10.1149/1.3594733

Tsai, Y.-D., Hu, C.-C., & Lin, C.-C. (2007). Electrodeposition of Sn–Bi lead-free solders: Effects of complex agents on the composition, adhesion, and dendrite formation. *Electrochimica Acta, 53*(4), 2040-2047. doi: 10.1016/j.electacta.2007.09.002

Tsai, Y.-D., Lien, C.-H., & Hu, C.-C. (2011). Effects of polyethylene glycol and gelatin on the crystal size, morphology, and Sn2+-sensing ability of bismuth deposits. *Electrochimica Acta, 56*(22), 7615-7621. doi: 10.1016/j.electacta.2011.06.077

Tu, K. N., & Thompson, R. D. (1982). Kinetics of interfacial reaction in bimetallic Cu□Sn thin films. *Acta Metallurgica, 30*(5), 947-952. doi: http://dx.doi.org/10.1016/0001-6160(82)90201-2

Tu, P. L., Chan, Y. C., & Lai, J. K. L. (1997). Effect of intermetallic compounds on the thermal fatigue of surface mount solder joints. *IEEE Transactions on Components Packaging and Manufacturing Technology Part B-Advanced Packaging, 20*(1), 87-93. doi: Doi 10.1109/96.554534

Tzeng, G. S., Lin, S. H., Wang, Y. Y., & Wan, C. C. (1996). Effects of additives on the electrodeposition of tin from an acidic Sn(II) bath. *Journal of Applied Electrochemistry, 26*(4), 419-423. doi: 10.1007/bf00251327

Venkatasamy, V., Riemer, S., & Tabakovic, I. (2011). Electrodeposition of eutectic Sn96.5Ag3.5 films from iodide–pyrophosphate solution. *Electrochimica Acta, 56*(13), 4834-4840. doi: http://dx.doi.org/10.1016/j.electacta.2011.03.050

Vianco, P. T. (2000). Lead (Pb)-Free Solder Applications. U.S.: Sandia National Laboratory.

Vittal, R., Gomathi, H., & Kim, K.-J. (2006). Beneficial role of surfactants in electrochemistry and in the modification of electrodes. *Advances in Colloid and Interface Science, 119*(1), 55-68. doi: http://dx.doi.org/10.1016/j.cis.2005.09.004

Xiao, G. W., Gong, J. F., Yau, E. W. C., Chan, P. C. H., Lee, R. S. W., & Yuen, M. M. F. (2003, May 27-30, 2003). *Optimization of Electroplating, Stencil Printing, Ball Placement Solder-Bumping Flip-Chip Process Technologies.* Paper presented at the Electronic Components and Technology Conference, New Orleans, Louisiana USA

Yaakup, S., Zakaria, H. S., Hashim, M. A., & Isnin, A. (2008). TIN-BASED LEAD-FREE SOLDER BUMPS FOR FLIP-CHIP APPLICATION. *Solid State Science and Technology, 16*(2), 99-108.

Yan, H., Sone, M., Mizushima, A., Nagai, T., Abe, K., Ichihara, S., & Miyata, S. (2004). Electroplating in CO2-in-water and water-in-CO2 emulsions using a nickel electroplating solution with anionic fluorinated surfactant. *Surface and Coatings Technology, 187*(1), 86-92. doi: http://dx.doi.org/10.1016/j.surfcoat.2004.01.009

Yang, L. M., Zhang, Q. K., & Zhang, Z. F. (2012). Effects of solder dimension on the interfacial shear strength and fracture behaviors of Cu/Sn-3Cu/Cu joints. *Scripta Materialia, 67*(7-8), 637-640. doi: DOI 10.1016/j.scriptamat.2012.07.024

Yang, M., Li, M., Wang, L., Fu, Y., Kim, J., & Weng, L. (2010). Cu6Sn5 Morphology Transition and Its Effect on Mechanical Properties of Eutectic Sn-Ag Solder Joints. *Journal of Electronic Materials, 40*(2), 176-188. doi: 10.1007/s11664-010-1430-y

Yen, Y.-W., Liou, W.-K., Chen, C.-M., Lin, C.-K., & Huang, M.-K. (2011). Interfacial reactions in the Sn–xBi/Au couples. *Materials Chemistry and Physics, 128*(1–2), 233-237. doi: http://dx.doi.org/10.1016/j.matchemphys.2011.03.004

Zeng, K., & Tu, K. N. (2002). Six cases of reliability study of Pb-free solder joints in electronic packaging technology. *Materials Science & Engineering R-Reports, 38*(2), 55-105. doi: Pii S0927-796x(02)00007-4

Doi 10.1016/S0927-796x(02)00007-4

Zhang, J., An, M., & Chang, L. (2009). Study of the electrochemical deposition of Sn–Ag–Cu alloy by cyclic voltammetry and chronoamperometry. *Electrochimica Acta, 54*(10), 2883-2889. doi: http://dx.doi.org/10.1016/j.electacta.2008.11.015

Zhang, J., An, M., Chang, L., & Liu, G. (2008). Effect of triethanolamine and heliotropin on cathodic polarization of weakly acidic baths and properties of Sn–Ag–Cu alloy electrodeposits. *Electrochimica Acta, 53*(5), 2637-2643. doi: 10.1016/j.electacta.2007.10.038

Zhang, Q. K., Zou, H. F., & Zhang, Z. F. (2011). Influences of Substrate Alloying and Reflow Temperature on Bi Segregation Behaviors at Sn-Bi/Cu Interface. *Journal of Electronic Materials, 40*(11), 2320-2328. doi: 10.1007/s11664-011-1742-6

Zhang, Y., & Abys, J. A. (1999). A unique electroplating tin chemistry. *Circuit World, 25*(1), 30-37.

Zhao, J., Cheng, C.-q., Qi, L., & Chi, C.-y. (2009). Kinetics of intermetallic compound layers and shear strength in Bi-bearing SnAgCu/Cu soldering couples. *Journal of Alloys and Compounds, 473*, 382-388.

Zou, H. F., Zhang, Q. K., & Zhang, Z. F. (2012). Interfacial microstructure and mechanical properties of SnBi/Cu joints by alloying Cu substrate. *Materials Science and Engineering: A, 532*(0), 167-177. doi: http://dx.doi.org/10.1016/j.msea.2011.10.078

LIST OF PUBLICATIONS AND PAPERS PRESENTED

Publications

Goh, Y., Haseeb, A.S.M.A., & Sabri, M.F.M. (2013). Effects of hydroquinone and gelatin on the electrodeposition of Sn–Bi low temperature Pb-free solder. Electrochimica Acta, 90, 265-273. *(2013 JCR Science Edition Quartile 1, Impact factor 4.086)*

Goh, Y., Haseeb, A.S.M.A., & Sabri, M.F.M. (2013). Electrodeposition of lead-free solder alloys. Soldering and Surface Mount Technology, 25(2), 76-90. *(2013 JCR Science Edition Quartile 2, Impact factor 0.688)*

Goh, Y., Lee, S.F., & Haseeb, A.S.M.A. (2013). Formation of Sn–Bi solder alloys by sequential electrodeposition and reflow. Journal of Materials Science: Materials in Electronics, 24(6), 2052-2057. *(2013 JCR Science Edition Quartile 2, Impact factor 1.966)*

Patent Filing

Haseeb, A.S.M.A., Goh, Y., & Sabri, M.F.M. Electrodeposition Bath and Method of Electrodepositing Tin-Bismuth Alloy (PI 2013700972). Filed 11 June 2013.

Awards

ASQED 2012 Best Paper Award for the paper title: Effects of thiourea and gelatin on the electrodeposition of Sn-Ag solder alloy, 4th Asia Symposium on Quality Electronic Design.

Emerald Literati Awards 2014, Outstanding Paper Award Winner for Soldering & Surface Mount Technology journal, paper title: Electrodeposition of lead-free solder alloys.

Conference Proceedings

Chiew, Y.H., Haseeb, A.S.M.A., Goh, Y., & Lee, S.F. (2012) Effects of Sn Concentration and Current Density on Sn-Bi Electrodeposition in Additive Free Plating Bath. Proceedings of the 4th Asia Symposium on Quality Electronic Design (pp. 286-290). DOI 10.1109/ACQED.2012.6320517.

Goh, Y., Haseeb, A.S.M.A., & Sabri, M.F.M. (2011). Electrodeposition of Lead-Free Solder For Green Electronics. Proceedings of the 3rd International Congress on Green Process Engineering (pp. 34-42). Kuala Lumpur, Malaysia.

Goh, Y., Haseeb, A.S.M.A., & Sabri, M.F.M. (2012). Effects of hydroquinone and gelatin on the electrodeposition of SnBi low temperature Pb-free solder. Proceedings of the 4th Asia Symposium on Quality Electronic Design (pp. 306-312). DOI 10.1109/ACQED.2012.6320521.

Goh, Y., Haseeb, A.S.M.A., & Sabri, M.F.M. (2014). Electrochemical studies on the effects of additives during Sn-Bi plating. Paper presented at the International Union of Materials Research Societies – International Conference on Electronic Materials, Taipei, Taiwan.

Goh, Y., Haseeb, A.S.M.A., Liew, H.L. & Sabri, M.F.M. (2013). Deformation and Fracture Behaviour of Electroplated Sn-Bi/Cu Solder Joints. Proceedings of the 15th International Conference on Electronic Materials and Packaging (SIT-0132). Seoul, Korea.

Goh, Y., Lee, S.F., & Haseeb, A.S.M.A. (2012). Effects of stacking sequence of electrodeposited Sn and Bi layers on reflowed Sn-Bi solder alloys. Proceedings of the 35th International Electronic Manufacturing Technology Conference (pp. 1-6). DOI 10.1109/IEMT.2012.6521792.

Koh, K.X., Haseeb, A.S.M.A., Arafat, M.M., & Goh, Y. (2012). Effects of Mn nanoparticles on wettability and intermetallic compounds in between Sn-3.8Ag-0.7Cu and Cu substrate during multiple reflow. Proceedings of the 4th Asia Symposium on Quality Electronic Design (pp. 297-301). DOI 10.1109/ACQED.2012.6320518.

Lee, S.F., Haseeb, A.S.M.A., & Goh, Y. (2012). Formation of Sn-Bi alloys through sequential electrodeposition. Proceedings of the 4th Asia Symposium on Quality Electronic Design (pp. 160-163). DOI 10.1109/ACQED.2012.6320493.

Lee, X.W., Goh, Y., & Haseeb, A.S.M.A. (2012). Effects of thiourea and gelatin on the electrodeposition of Sn-Ag solder alloy. Proceedings of the 4th Asia Symposium on Quality Electronic Design (pp. 291-296). DOI 10.1109/ACQED.2012.6320518.